UNIVERSITY OF LIVERPOOL

IN VITRO AND COMPUTATIONAL MODELLING OF DRUG DELIVERY IN THE EYE FOR THE TREATMENT OF RETINAL PATHOLOGIES

Thesis submitted in accordance with the requirements of the

University of Liverpool for the degree of Doctor in Philosophy
by

Alys Elisabeth Davies

January 2019

Doctor of Philosophy Declaration

I hereby declare that this dissertation is a record of work carried out at the Institute of Ageing and Chronic Disease at the University of Liverpool during the period of November 2014 to January 2019.This dissertation is original in content except where otherwise stated.

January 2018

Alys Elisabeth Davies

ABSTRACT

Posterior segment diseases such as proliferative vitreoretinopathy and diabetic retinopathy have the potential to cause irreversible visual impairment. Delivery of therapeutic drugs to this region of the ocular globe poses many challenges owing to different anatomical and physiological constraints. There are some conditions that require drug treatment over prolonged periods of time and there is scope for the development of an extended drug delivery device to combat the burden of current treatment methods. Models can be a fast, inexpensive method of understanding the release profiles of therapeutics from such systems in an attempt to avoid toxic/ineffective treatment. Well designed, validated models could help speed the development of novel drug delivery systems and, if standardised, allow comparison between different technologies. Here the aim was to develop models of the drug clearance mechanisms in the posterior segment of the eye and test their ability to model drug transport behaviour from one potential drug delivery system.

A static in vitro model of the outer blood retinal barrier (OBRB) was developed using a human retinal pigmented epithelium cell line, ARPE-19 cells, cultured on ammonium plasma treated expanded polytetrafluoroethylene (ePTFE) transwell membranes and used to evaluate the permeability of different molecular weight dextran molecules. Using COMSOL Multiphysics computational fluid dynamics (CFD) software, computational models of the transport of dextrans across this barrier within a dynamic microfluidic environment, the Kirkstall Ltd QV600 culture chamber, were developed and corresponding in vitro experiments were carried out in order to validate the simulations. This was then repeated for the release of ibuprofen (ibu) from a silicone oil (SiO) tamponade. Two other in vitro models; a spherical eye model and an eye-on-a-chip (EOC) device were also used to investigate different drug clearance mechanisms that are present in the eye in an attempt to gain a full understanding of the release dynamics of this potential delivery system.

In order to build accurately described computer models, experimental data was obtained from simple experiments in each of the different *in vitro* models used to determine key input parameters. Within the Kirkstall QV600, transepithelial electrical resistance (TEER) and immunocytochemistry (ICC) showed increased barrier function of the ARPE-19 cells cultured under medium flow up to a flow rate of 200µL/min. At 400µL/min, there was decreased functionality and clusters of the epithelial mesenchymal transition marker, αSMA, appeared. Utilising permeability and diffusion coefficients derived from the static *in vitro* experiments,

transport of dextrans across unseeded ePTFE membranes were able to be simulated to within 15% error of the corresponding dynamic *in vitro* results. The introduction of cells increased this error to a maximum 30%. Simulating the release of ibu from SiO within the same dynamic environment produced results again, within a 15% error of the *in vitro* data. This was able to be repeated when investigating the other clearance mechanism in the spherical eye model. Within the EOC, the percentage release of ibu was equivalent after 7 days, however the release profile over days 1, 2 and 3 was not comparable.

The predicted results from the computational models showed good agreement with the results obtained from the benchtop experiments and the computer models showed that it is possible to investigate a vast range of parameters in a more time and cost efficient manner. Using a variety of models to investigate drug release from the ibu-SiO device provided a more comprehensive understanding of how both the anterior and posterior clearance mechanisms found within the posterior segment of the eye, affect the transport of the drug.

Computational modelling can be a fast and cost-effective method to assist in the development of novel drug delivery devices. This study presents the design and development of three distinct yet complementary CFD models used to investigate the release of ibuprofen from silicone oil. The accuracy of these simulations was validated using data from corresponding in vitro experiments to produce models which can be used as valuable predictive tools.

ACKNOWLEDGEMENTS

I would first like to thank my supervisors Dr Victoria Kearns and Professor Rachel Williams for giving me the opportunity to undertake my PhD studies and for their continued guidance, support and encouragement throughout the past 4 years. I would also like to thank Dr Serban Pop from the University of Chester, for his invaluable support and guidance throughout this PhD study.

Secondly I would like to thank everyone in Dr. Anderson Shum's lab at the University of Hong Kong, in particular Joseph Chan, who all taught me so much and made me feel very welcome during my time there.

Special thanks go to all the staff and students in the Department of Eye and Vision Science for their support and friendship over the past 4 years, particularly Sam, Steph, Aruni and Jess.

Finally, I have to thank my family and friends. Everyone at the TLC for looking after me for so many years. Chloe, who is always there to remind me that I can do anything. My boys who are always there when I need a hug. And most importantly my mum and dad, everything I have achieved is a result of their belief in me.

Contents

LIST OF FIGURES

CHAPTER 1

CHAPTER 2

LIST OF TABLES

CHAPTER 1

CHAPTER 2

LIST OF EQUATIONS

LIST OF ABBREVIATIONS

5-FU	5-Flurouracil
ABS	Acrylonitrile Butadiene Styrene
AMD	Age-Related Macular Degeneration
aTRA	all-trans Retinoic Acid
AUC	Area Under Curve
BCNU	1,3-bis(2-chloroethyl)-nitrosourea
BM	Bruchs Membrane
BSA	Bovine Serum Albumin
CFD	Computational Fluid Dynamics
CO_2	Carbon Dioxide
COX	Cyclooxygenase
DAPI	4',6-Diamidino-2-Phenylindole, Dilactate
ddH_20	Distilled Water
EDTA	Ethylenediaminetetraacetic Acid
EMT	Epithelial-Mesenchymal Transition
EOC	Eye-On-a-Chip
ePTFE	expanded Polytetrafluoraethylene
ERD	Exudative Retinal Detachment
ERM	Epiretinal Membrane
FCS	Foetal Calf Serum
FD	FITC Dextran
FEA	Finite Element Analysis
FITC	Fluoracine Isothiocyanate
HRA	Human Retinal Astrocyte
HREC	Human Retinal Endothelial Cell
hRPE	human Retinal Pigemented Epithelium
HUVEC	Human Umbilical Vein Endothelial Cell
IBRB	Inner Blood Retinal Barrier
ibu	Ibuprofen
ILM	Inner Limiting Membrane
IPL	Inner Plexiform Layer
NBF	Neutral Buffered Formalin
NSAID	Non-Steroidal Anti-inflammatory Drug
OBRB	Outer Blood Retinal Barrier
OLI	Outer Limiting Layer
OPL	Outer Plexiform Layer
PBS	Phosphate Buffered Saline
PDE	Partial Differentiation Equation
PDMS	Polydimethylsiloxane
PET	Polyethylene Terephthalate
PIV	Particle Image Velocimetry
PMMA	Polymethylmethacralate
PTFE	Polytetrafluoraethylene

PVD	Posterior Vitreal Detachment
PVR	Proliferative Vitreoretinopathy
RA	Retinoic Acid
RD	Retinal Detachment
RPE	Retinal Pigemented Epithelium
RRD	Rhegmatogenous RD
RSC	Reduced Serum Culture Medium
SiO	Silicone Oil
TAA	Triamcinolone Acetonide
TCP	Tissue Culture Plastic
TEER	Transepithelial Electrical Resistance
TRD	Tractional Retinal Detachement
ZO-1	Zonula Occuldin-1
ZO-2	Zonula Occuldin-2
αSMA	alpha-Smooth Muscle Actin

CHAPTER 1

INTRODUCTION

1.1 THE EYE - STRUCTURE AND FUNCTION

The eye (***Figure 1-1***) is a specialised structure in the body which is responsible for the conversion of light signals into neural signals, which can then be transformed into visual images. It can be divided into two segments, the anterior segment (the region from the front of the cornea to the lens containing the aqueous humour) and the posterior segment (extending from the lens to the optic nerve and containing the gel-like fluid called the vitreous humour). The supporting wall of the eye, the sclera, is an opaque, connective tissue layer which provides mechanical protection and maintains the shape of the eye. Anteriorly, the sclera joins to the transparent cornea where light is able to enter the eye. Posteriorly it joins to the optic nerve. Beneath this outer layer (sclera and cornea) lies the uveal layer of the eye, comprised of the iris, ciliary body and choroid, each of which serve different functions. The iris forms a central circular opening, the pupil, which controls the amount of light that enters the eye. The ciliary body attaches to the lens and anchors it via the suspensory ligaments to focus light onto the retina via muscular adjustment in a process known as accommodation. The choroid is a vascularised layer that acts as the primary region of nutrient and gas exchange for the underlying retina. The innermost layer includes the neural sensory retina and the retinal pigment epithelium (RPE) and is the layer of the eye which is responsible for the conversion of light signals [1, 2]. The neural retina and RPE layer are further discussed in section 1.1.1.

In order to produce an image, light follows a specific pathway through these many structures. Entering the eye initially through the cornea, light is partially refracted due to its convex shape. From there, the light passes through the aqueous humour and the pupil onto the lens where it is further refracted in order to focus the rays onto the macula region of the retina, containing the fovea – a region of densely packed neural cells. Here the light signal is processed and the neural signal is sent down the optic nerve to the visual cortex where it is further processed [1, 2].

The Human Eye

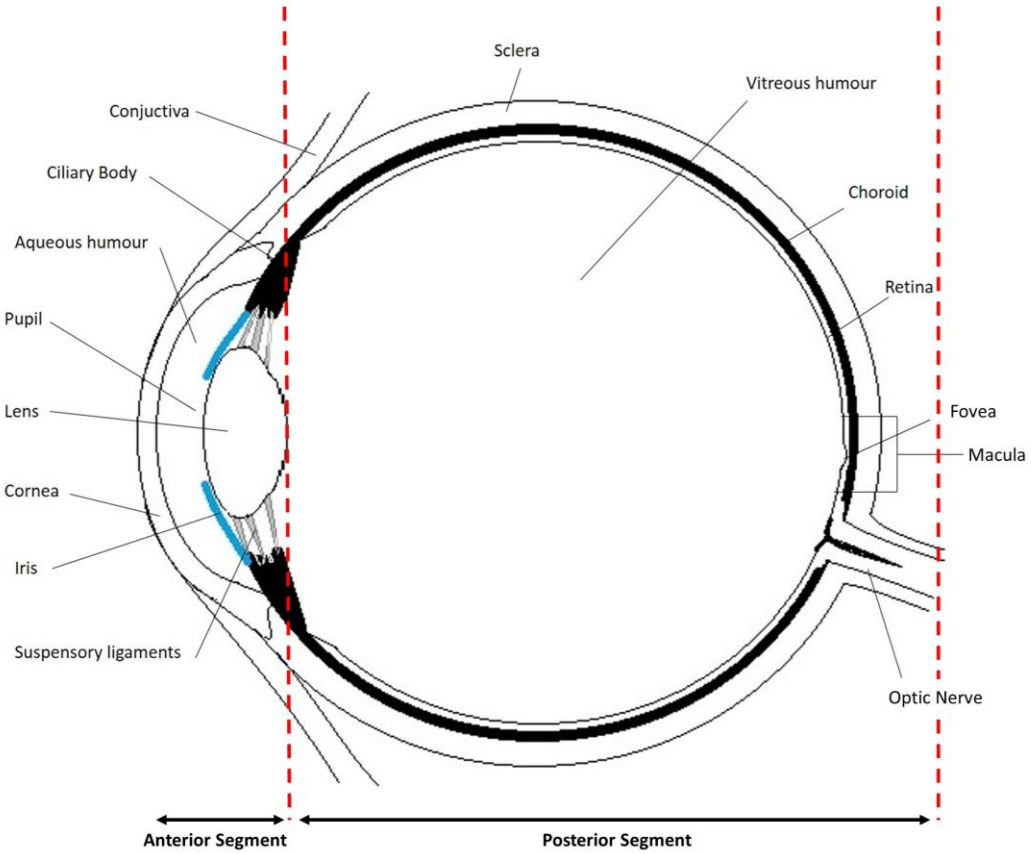

Figure 1-1. An illustration of the structure of the human eye.

1.1.1 THE RETINA – STRUCTURE AND FUNCTION

The retina is the neural layer of the eye which is responsible for transforming visual light stimuli into electrical signals which can be transmitted to, and interpreted by the brain. It is the innermost layer onto which the light received is focussed in order to produce an image. Extending round from the edge of the optic nerve head, it reaches to the ora serrata where it is joined to the ciliary body and the non-photosensitive region begins. On the sagittal plane it is bound by the vitreous and joined to the choroid via the Bruch's membrane. One of the key features of the retina is the macula, an important structure for visual acuity and colour vision [3].

Being the photosensitive region of the eye, the retina has a very complex structure and is made up of ten layers which can crudely be described as two distinct regions; the photosensitive region, comprised of an inner stratified layer of neural elements, and the retinal pigment epithelium layer. Moving from anterior to posterior the photosensitive

region is made up of the following layers: the inner limiting membrane (ILM), the nerve fibre layer, ganglion cell layer, the inner plexiform layer (IPL), the inner nuclear layer, the outer plexiform layer (OPL), the outer nuclear layer, the outer limiting layer (OLL) and the photoreceptor layer. This neurosensory layer terminates posteriorly with the photoreceptor cells, those cells which capture the light, beneath which lies the retinal pigment epithelium (RPE). The majority of these layers contain the cell bodies, processes and synapses of the neurosensory cells of the retina including the ganglion cells, bipolar cells, amacrine cells, horizontal cells and Müller cells which all have a role in the modification and integration of the electrical signal before it is sent down the optic nerve. It is the integrity and interaction of these layers which can determine the quality of our vision [3, 4].

The outermost layer of the neurosensory retina is the photoreceptor layer and in the human eye, two types of photoreceptor cell exist: rods and cones. The rods are responsible for vision in low light conditions and are used to detect brightness and contrast. These cells are distributed throughout the retina however they are predominantly found in the peripheral regions. Within the human eye, approximately 100 million rod cells exist and these slender cells have long outer segments, adjacent to the RPE, which house stacks of disc membranes containing the visual pigment rhodopsin. Rhodopsin is a sensory protein which is highly sensitive to light and it is this sensitivity which enables vision in dim conditions [5].

Cone cells are responsible for colour vision and high spatial resolution. Fewer numbers of these cells exist in the human eye in comparison to the rods, with approximately 6.5 million cells occurring predominantly within the macular region of the retina. As previously mentioned, the macula is a key region of the neurosensory retina located near the centre of the human retina and is responsible for central, high resolution vision. Within the macula sits the fovea and this region contains the highest density of cone cells within the retina with no rods residing in the fovea. Cone cells occur in three spectrally distinct types: red, green and blue sensitive cones, each containing different visual pigments. These visual pigments absorb photons of light causing phototransduction of the light energy to electrical energy which can be transmitted to the brain. Red cones are responsible for the absorption of long wavelengths of light, green for medium and blue cones absorb short wavelengths [5].

Once the photoreceptors absorb the light entering the eye, a biochemical change occurs which synaptically sends a signal to the bipolar cells within the neurosensory retina. The signal is modified by the horizontal and amacrine cells which surround the photoreceptors

before it is ultimately relayed to the ganglion cells and into the brain to form a representation of the environment.

The photoreceptors are the outermost layer of the neurosensory retina, behind which lies a hexagonally packed, cuboidal, continuous monolayer of epithelial cells known as the retinal pigment epithelium (RPE). These cells exist between the photoreceptor cells and the Bruch's membrane and are vital in maintaining homeostasis within the retina. The RPE is responsible for the supply of nutrients in, and the removal of waste products out of the inner retinal cells via the choroidal blood network, the choriocapillaris [4].

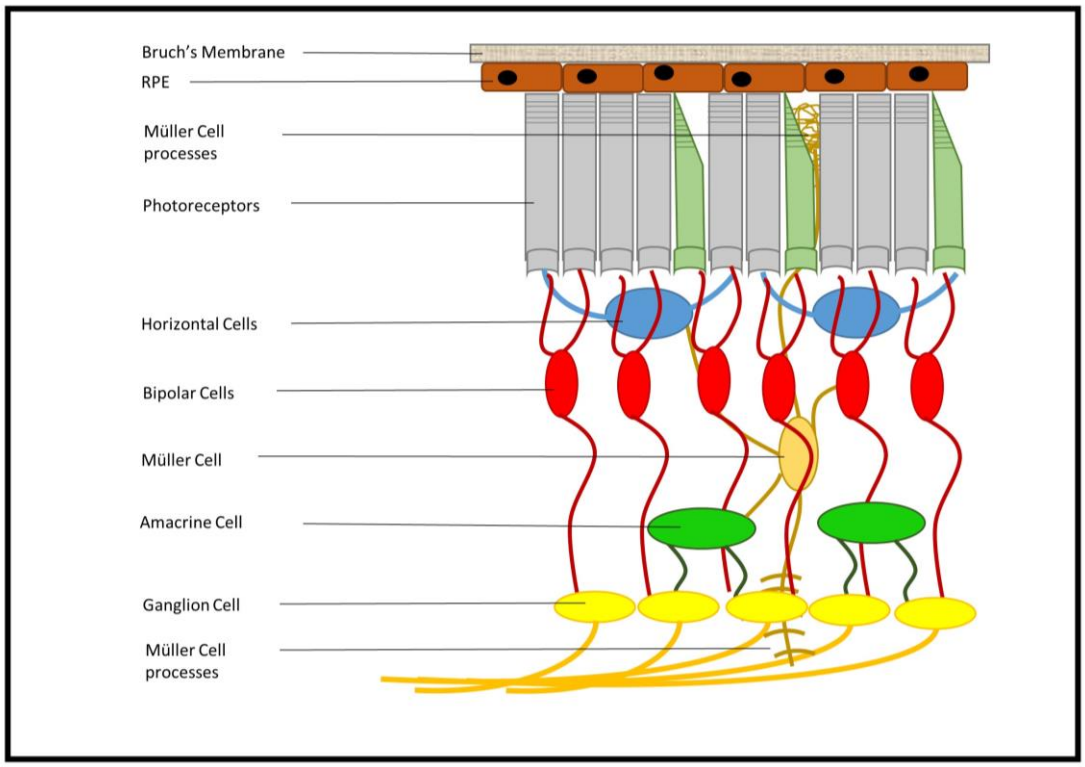

Figure 1-2: Organisation of the retina.

1.1.2 THE RETINAL PIGMENT EPITHELIUM

The RPE is a highly specialised monolayer of pigmented cells located between the neurosensory retina and the vascular choroid. It has been reported that approximately 3.5 – 6 million RPE cells exist within the human eye and, for the majority of adult life, this population remains stable in the absence of disease. The cells exhibit the cobblestone like appearance typical of epithelial cell layers and form a highly polarised monolayer, with microvilli on the apical side which interact with the photoreceptors of the neurosensory retina and the basal side forming firm attachment with the underlying Bruch's membrane.

RPE cells carry out several major functions at the back of the eye which include: (1) transport of nutrients and ions, (2) absorption of scattered light entering the eye and protection against photo-oxidation, (3) isomerisation of key molecules involved in the visual cycle, (4) phagocytosis of membranes shed by photoreceptors and (5) secretion of factors which maintain the structural integrity of the retina [6, 7].

Transport occurs in two directions across the RPE, outward flux of electrolytes and water from the subretinal space into the choroid and inward flux of nutrients from the blood to the photoreceptors. Due to intense metabolic turnover that occurs in the photoreceptors and also the natural level of intraocular pressure, a large amount of water can reside in the subretinal space which must be constantly removed into the choriocapillaris. This water is eliminated by the RPE cells [8, 9]. In the other direction, the RPE takes up nutrients such as glucose and retinol, and delivers these to the photoreceptors to maintain their function [10].

Due to the frequent, direct light to which the retina is exposed, it is at high risk of photo-oxidative stress. This stress leads to damage of the photoreceptor outer segments, whose membrane discs therefore require constant renewal. The role of the RPE in this renewal process is to phagocytose damaged photoreceptor outer segments which have been shed. This process, however, leads to the release of free radicals into an already highly photo-oxidative environment. The RPE plays a vital role in counterbalancing the high oxidative stress by absorbing and filtering the light that enters the eye using their pigment, melanin, to protect other cells within the tissue [11].

RPE cells are essential in the visual cycle as they are responsible for the metabolism of retinoids. Light transduction begins when light is absorbed by chromophores in the photoreceptor cells. This absorption leads to a conformational change of the chromophore 11-*cis*-retinal into all-*trans*retinal. In order to be reactivated by another photon, there must be a reisomerisation back to 11-*cis*-retinal, however, photoreceptors lack the enzymes needed for this conversion therefore the metabolism takes place in the RPE after which 11-*cis*-retinal is redelivered to the photoreceptors [12].

The RPE serves as the interface between the neural retina and the choriocapillaris. The cells of the epithelium are adjoined by tight junctions which form a partial seal that retards transepithelial diffusion. These cells in combination with their underlying basement

membrane, Bruch's membrane (BM) form the outer blood retinal barrier (OBRB). This barrier disconnects the eye from the blood stream, establishing immune privilege [13].

1.1.3 THE BLOOD RETINAL BARRIER

The blood retinal barrier is responsible for the maintenance of the neural retina environment through the regulation of nutrient delivery, ion concentrations and preventing access of circulatory factors such as immune cells and antibodies [14]. It consists of both an inner blood retinal barrier (IBRB) and an outer blood retinal barrier (OBRB). The IBRB is composed of the retinal endothelial cells which line the retinal microvasculature and regulates transport across the retinal capillaries. The OBRB comprises the RPE and Bruch's membrane and regulates transport between the choriocapillaris and the neural retina (***Figure 1-3***)[15].

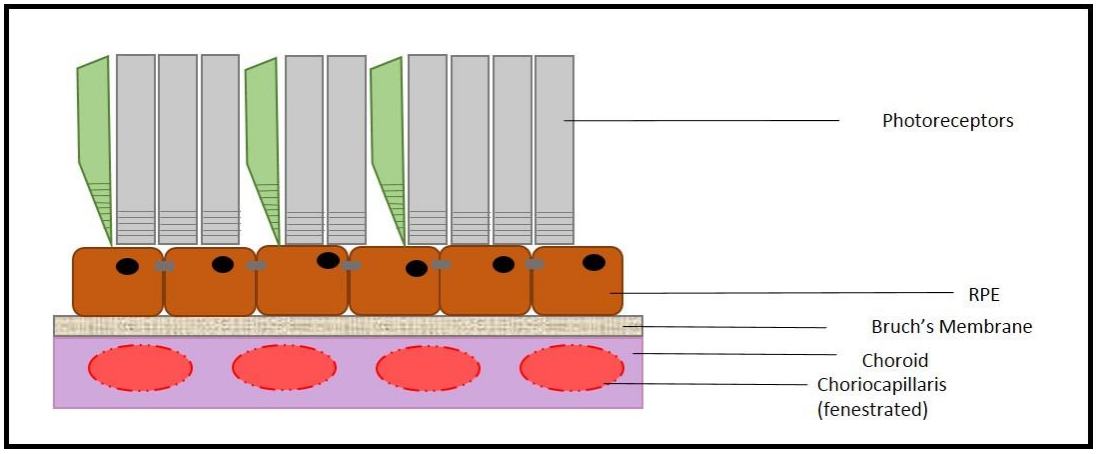

Figure 1-3: Schematic of the outer blood retinal barrier.

Bruch's Membrane

The Bruch's membrane (BM) is an acellular structure which is comprised of five layers of extracellular matrix and lies between the RPE layer and the choroid. The layers include: the basement membrane of the RPE, an inner collagen fibre layer, an elastic fibre layer, an outer collagen fibre layer and the basement membrane of the choriocapillaris endothelium. As the layers suggest, the composition of the BM is predominantly collagen and elastin fibres. Other molecules that are present include fibronectin and laminin. The average thickness of the BM is between 2-5µm with the region in the macula being thinner and more porous than the surrounding areas. The primary function of the BM is structural, however, it also facilitates transport of nutrients and gases between the choroidal circulation and the RPE [16].

Choroid

The choroid is a tissue in the eye which predominantly serves as the vascular supply to the outer retina. It is composed of blood vessels, fibroblasts, melanocytes and supporting collagenous and elastic connective tissue. As well as supplying oxygen and nutrients to the outer retina, it is also believed to be involved in thermoregulation of the surrounding tissues. Within the choroid is a thin sheet formed by a network of capillaries. This sheet is known as the choriocapillaris. Due to the highly metabolic nature of the RPE and outer retinal layer, extensive molecular exchange occurs between these cells and the choriocapillaris. To aid in this demand, the walls of the choriocapillaris vessels are fenestrated to allow easier passage of molecules [17].

Both the IBRB and the OBRB are formed by the presence of zonulae occludens (tight junctions) between either the adjacent endothelial cells (IBRB), or the adjacent RPE cells (OBRB). Tight junctions are multi-protein junctional complexes which are composed of a network of sealing strands that prevent paracellular transport [18]. Two major groups of proteins of tight junctions are claudins and occludins. Occludins are thought to have a pivotal role in maintaining the polarity of RPE cells by preventing the diffusion of integral membrane proteins from the apical to the basal surface. They interact with other proteins such as zonula occluden-1 (ZO-1) and -2 (ZO-2) to form complexes with the actin cytoskeleton which helps to regulate cell proliferation [19]. Claudins are thought to have a role in the selectivity of the tight junction and it has been shown that overexpression of Claudin-1 in kidney cells increases the transepithelial electrical resistance and reduces fluorescein isothiocynate conjugated dextran flux across the cell monolayer, suggesting it has a strong influence on the barrier function of epithelial cells [20, 21].

When trauma or disease occur within the RPE layer of the OBRB, a local breakdown in the barrier function of this structure occurs which can lead to circulatory factors entering the immune privileged region of the eye. This can ultimately lead to further ophthalmic complications and disease.

1.2 THE RETINAL PIGMENT EPITHELIUM IN DISEASE

The dysfunction of RPE plays a central role in the pathogenesis of many retinal diseases which can ultimately lead to vision loss or impairment. Disorders which occur in the RPE can mostly

be categorised into three mechanistic actions: degenerative, dystrophic and proliferative. Degenerative and dystrophic diseases will briefly be discussed here, however the main emphasis will be on proliferative disease of the RPE with respect to migration and dedifferentiation.

Degenerative and dystrophic diseases involving the RPE: The RPE is formed during early development and, in the absence of disease, remains as a stable population throughout normal life undergoing minimal proliferation. It is also a highly metabolic cell layer, continuously ingesting debris from the neural retina and expelling waste products. As we age, accumulation of debris can occur within the RPE making it less efficient and eventually leading to degeneration of the tissue. The most common degenerative disease that occurs which involves the RPE is age-related macular degeneration (AMD) [22]. As the name suggest, AMD is a disease that can develop as we age and is characterised by a breakdown of the macula (central portion of the retina). There are two types of AMD that occur: neovascular and geographic atrophy. When geographic atrophy occurs, accumulated waste products aggregate on the Bruch's membrane (BM) and form drusen, fatty deposits, which can impede the attachment of the RPE to the BM and deprive the RPE of oxygen and nutrients, causing degeneration of the RPE. In neovascular AMD, neovascularisation occurs in the choroid which produces fragile, leaky blood vessels that can haemorrhage into the subretinal space, again impeding attachment of the RPE. This degeneration then leads to lack of functionality and prevents the RPE from performing its role in homeostasis of the neural retina, leading to degeneration of the photoreceptors within the macula and eventually loss of central vision [23-25]. AMD is a leading cause of visual impairment in the developed world and approximately 35,000 people develop neovascular AMD each year in the UK alone. The most common treatment is intravitreal injection of either aflibercept or ranibizumab. In 2015/16 the cost associated with the use of these drugs in the NHS was estimated to be approximately £450 million [26].

An example of a dystrophic disease is retinitis pigmentosa, a rare, inherited condition which arises from genetic abnormalities within the RPE cells causing altered cellular morphology and function. This disease can present itself in the early stages of life and progressively narrows a person's field of view over the course of their lifetime. [27].

Proliferative diseases involving the RPE: As previously mentioned, the monolayer of RPE cells reside in a highly differentiated, mitotically inactive state in healthy eyes. However,

these cells will dedifferentiate and become mobile, proliferative cells in response to trauma or inflammation [28]. Robust proliferation of RPE cells in humans is relatively uncommon but when it does occur it can result in pathologic epithelial-mesenchymal transition (EMT), whereby the epithelial cells lose their differentiated phenotypes and convert to more mobile, mesenchymal-like cells. Dedifferentiation and proliferation of RPE cells can depend on several factors including: condition of the underlying BM, size of injury, and interaction with cytokines and growth factors. It is possible for a fibrotic wound healing response to be triggered following retinal trauma; in this case, RPE cells will proliferate and migrate into the vitreous and form epiretinal membranes which contract and distort the natural architecture of the retina. This is seen in pathologies such as proliferative vitreoretinopathy (PVR), a complication of retinal detachment, which will be discussed further in section 1.2.2.

1.2.1 RETINAL DETACHMENT

Retinal detachment (RD) is a potentially blinding condition whereby the neural retina becomes detached from the underlying RPE. By definition, there are three types of RD: rhegmatogenous RD (RRD), exudative RD (ERD) and tractional RD (TRD) (***Figure 1-4***). Of these three, RRD is the most common and occurs where there is a tear in the retina. There are approximately 12 cases of retinal detachment per 100,000 people each year in the UK and it is classified as one of only a few ophthalmic emergencies [29] [30].

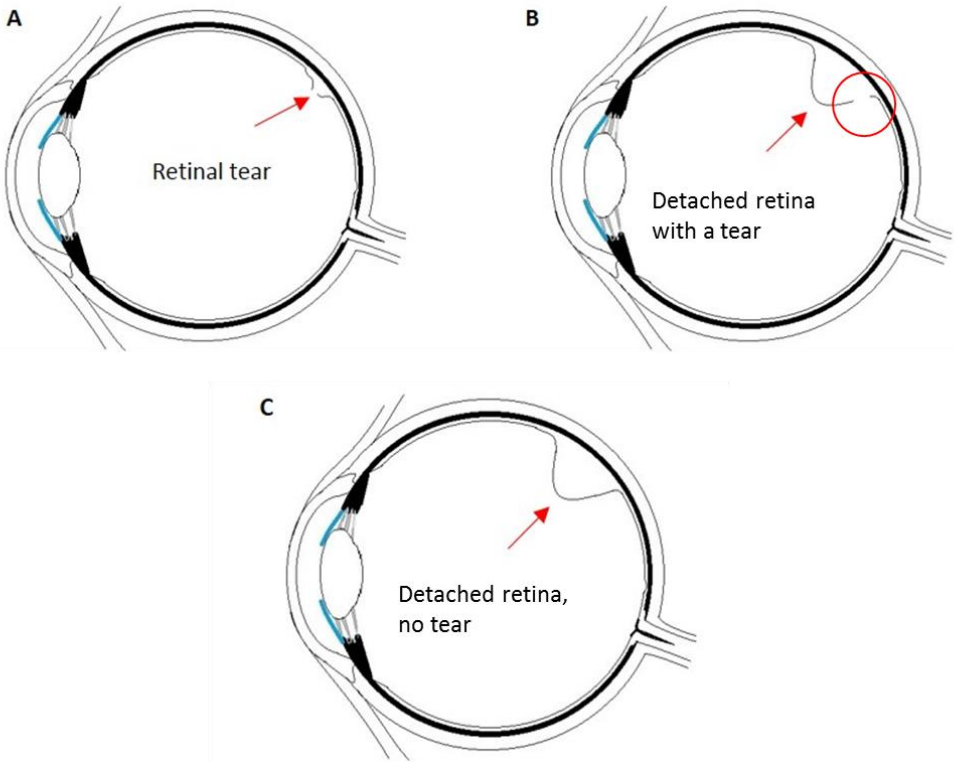

Figure 1-4: Diagram of retinal detachment. (A) Retinal tear, (B) rhegmatogenous retinal detachment, (C) exudative and tractional retinal detachment.

Breaks in the retina can occur for a number of reasons such as trauma, complications of diabetes, inflammatory eye diseases or myopia [31, 32]. Ageing can also increase the risk of RRD due to thinning of the retina and breakdown of the collagen network of the vitreous. The vitreous is the transparent gel-like structure which occupies the posterior segment of the eye. Over 97% of the vitreous is water with the remaining composition consisting of a network of collagen and glycoproteins such as hyaluronic acid. In non-diseased eyes it attaches to the optic nerve, retina and back of the lens. Predominantly, it acts as a shock absorber from mechanical trauma, as well as allowing circulation of metabolites through the eye and maintaining the positioning of the retina and lens [33]. With age, the consistency of the vitreous becomes more fluid-like and it begins to shrink due to collapsing of the collagen network. The average age of presentation is 60 years of age [30]. In severe cases, the vitreous can become detached from the retina resulting in posterior vitreous detachment (PVD). When this happens, movement of the eye can result in the vitreous and retina moving relative to one another, leading to tractional forces between the two that can cause tears in

the retina. Vitreous humour is then able to penetrate the subretinal space and accumulate underneath the retina which can lead to further separation from the RPE [34].

In the case of ERD and TRD, retinal detachment happens without the occurrence of a tear in the retina. ERD is usually a result of a breakdown within the blood retinal barrier, when fluid leaks into the subretinal space from retinal vessels. The accumulation of this fluid forces the retina away from the RPE. In TRD, contractile membranes form on the neural retina which pull the retina away from the RPE by traction forces. TRD usually occurs as a complication of other conditions such as diabetic retinopathy or proliferative vitreoretinopathy [35, 36].

1.2.2 PROLIFERATIVE VITREORETINOPATHY

Proliferative vitreoretinopathy (PVR) is a condition that can happen following a break in the retina. It is a modified form of a wound healing response with respect to inflammation, proliferation and formation of scar tissue and results in epi- and subretinal membranes on the surface of the neural retina [37].

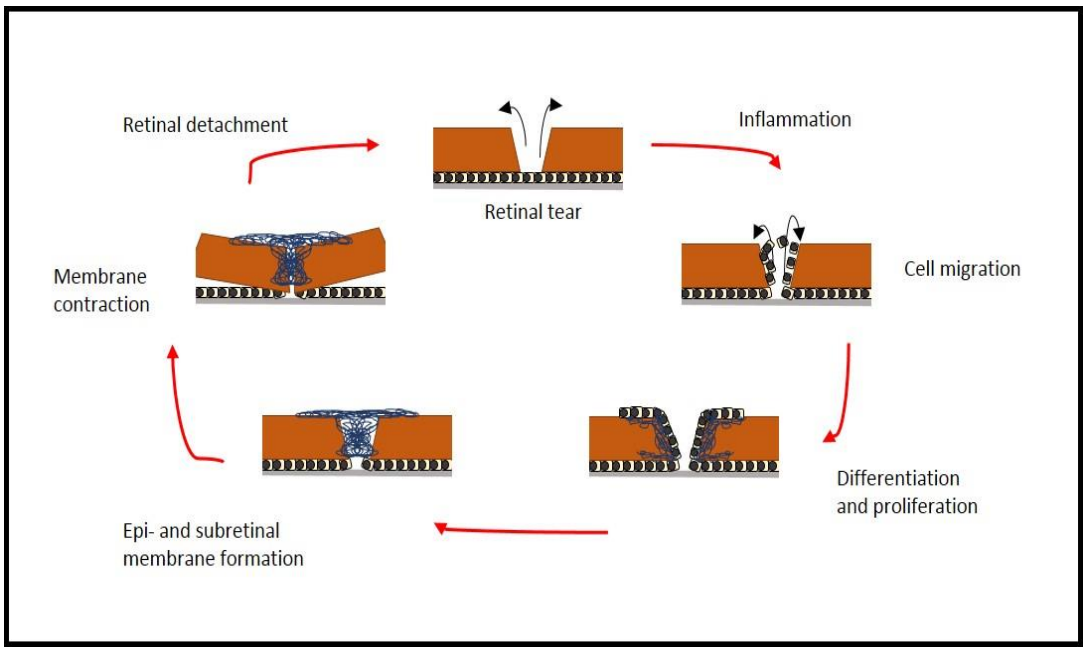

Figure 1-5: Diagram of the proliferative vitreoretinopathy cycle following a retinal tear. Adapted from [38].

PVR can manifest itself in two ways: traumatic PVR and idiopathic PVR. Traumatic PVR occurs in patients with perforating ocular injuries which involve the posterior segment or following ocular surgery [39]. Idiopathic PVR is a complication observed in approximately 5-10% of severe cases of RRD and is the leading cause of failure in RRD surgery [40] .

RRD causes a breakdown in the blood retinal barrier. Loss of contact, and therefore loss of signalling, between adjacent RPE cells triggers their proliferation and dedifferentiation in an attempt to repair the defect [41]. The tear also exposes the RPE to cytokines and inflammatory factors which are normally excluded from these cells due to the immune privilege in the eye. As the cells dedifferentiate, they undergo a process called epithelial-mesenchymal transition (EMT) in which they adopt a more fibroblastic phenotype and become more migratory and proliferative [42]. The abnormal wound healing response and continual inflammation contributes to the formation of epiretinal membranes (ERM). These ERM have been shown to consist of a number of different cell types, predominantly RPE cells, however there are also fibroblasts, myofibroblasts and immune cells present. The fibroblasts and myofibroblasts are thought to play a key role in the contractile phase of PVR which occurs once the membranes have invaded the vitreo-retinal surface of the retina. These membranes contract and distort the retina which ultimately leads to TRD [43].

1.3 CURRENT TREATMENTS

1.3.1 RETINAL DETACHMENT TREATMENTS

Numerous treatment options exist to combat RD, all of which aim to reattach the neural retina to the RPE and repair any tears that are present. RD is described as an ophthalmic emergency and so it is crucial that treatment is urgent in order to achieve a successful outcome. The type of procedure is dependent on a number of factors including severity, location and type of RD [44].

1.3.1.1 PNEUMATIC RETINOPEXY

Pneumatic retinopexy (PR) is a procedure to treat RRD which uses laser photocoagulation or cryotherapy in addition to injection of a gas bubble to seal small tears in the retina and prevent progression of the RD [45]. The gas bubble is injected into the vitreous cavity and serves to force the retina back against the RPE layer. The RPE will then remove any subretinal fluid which may have accumulated [46]. The choice of gas used is either air or a perfluorocarbon gas such as sulphur hexafluoride, perfluoropropane or perfluoroethane. Air is more rapidly absorbed by the surrounding tissues in comparison with the other available gases and is therefore not suitable for long term support of retinal reattachment. PR is usually reserved for patients with RD in the superior segment of the retina as the head must

maintain a set position over a period of approximately 2 weeks. For this reason, PR is not an appropriate treatment method for all patients due to the restriction of head movement which is required to achieve successful reattachment of the retina [47, 48].

1.3.1.2 Scleral Buckle Surgery

Scleral buckle surgery involves suturing a piece of silicone, natural rubber or hard plastic onto the sclera in an attempt to push, or 'buckle', the sclera inwards, towards the middle of the eye. This buckling effect relieves tractional forces on the retina and allows it to settle back against the RPE. The buckle may be applied to just the area behind the detachment or a circumferential band can be placed to encircle the eye, depending on the size of the break. As with PR, laser photocoagulation or cryotherapy can be used in conjugation with a scleral buckle to seal the tear. This treatment method is more invasive than PR, but has higher success rates (approximately 85% anatomic success versus 65% in PR) [49, 50].

1.3.1.3 Vitrectomy/ Tamponade Placement

The most common course of treatment for severe or complicated cases of retinal detachment is a vitrectomy followed by the insertion of a tamponade agent in to the vitreous cavity. During surgery, the vitreous humour is removed whilst the eye is simultaneously filled with saline to maintain the pressure. After this, a silicone oil or gas tamponade is inserted to fill replace the saline. The tamponade prevents the migration of any aqueous within the vitreous cavity to the wound site, excluding inflammatory factors and cytokines and initiating retinal reattachment.

The effectiveness of a tamponade is dictated by its ability to maintain contact with the retina and displace any aqueous away from the retinal surface [51]. There are a number of properties which influence this, such as specific gravity, interfacial tension and viscosity [52]. Hydrophobic materials are used as they form a bubble within the aqueous in order to minimise surface contact with the aqueous. This also prevents any of the tamponade material migrating through the wound, instead providing a plug effect. There are a number of materials that are available as tamponade agents which are currently used clinically, and they are either gas or oil based.

Gas tamponades include materials such as air or perfluorocarbon gases. The major disadvantage of some gas tamponades is they have a short residency time due to diffusion

of the gas into surrounding tissues, leading to a reduced tamponade effect. This residency time can be increased depending on which gas is used however, this can also affect the expansion of the gas within the vitreous cavity following insertion. Perfluoropropane, for example, has a residency time of approximately 7 weeks, however can expand by as much as 100% following insertion. This expansion can cause increased pressure on structures such as the optic nerve and ultimately cause more damage [53]. As with pneumatic retinopexy, there is also a requirement for patients to maintain a constant head position for the majority of time over approximately 2-3 weeks. This can contribute to the lack of success of gas tamponades due to poor patient compliance [54].

Unlike gas tamponades, silicone oil (SiO) tamponades are permanent and do not dissipate over time. This does however require further follow-up surgery to remove the tamponade once treatment has concluded. SiO is transparent, chemically inert within the vitreous cavity and has a high interfacial surface energy. These properties, in combination with its low toxicity and highly hydrophobic nature, make it a useful material as a tamponade agent. Silicone oils are often used in cases where RD or tears are very complicated or when PVR is present (see section 1.2.2) [55].

Both silicone oils and tamponade gases have very low specific gravities and therefore float on the aqueous within the eye. This can lead to less successful treatment of inferior retinal detachments, although SiO has still been shown to be effective. Heavy-than-water tamponades, such as heavy silicone oils (Densiron®) and perfluorocarbon liquids, have now been developed and provide a more successful treatment option in these cases [56, 57].

A disadvantage of SiO is that forces at the interface between the oil and aqueous, which are often caused by movements of the eye, can cause break-up of the SiO into droplets. In the presence of surfactants or cellular debris, these droplets can stabilise and form emulsions. Emulsions pose two threats in that they can reduce the effectiveness of the tamponade and also initiate an inflammatory response, if the droplets are small enough to be engulfed by macrophages [58, 59]. Additionally, it is possible for the SiO to migrate into the anterior chamber which has been shown to lead to glaucoma [60]. The tendency for SiO to emulsify is a product of its rheological properties. The lower the shear viscosity of the oil, the lower the shear force required to disperse the bulk oil into droplets. Silicone oils which are currently used clinically have viscosities ranging from 1000 centistokes (c.st) to 5000 c.st and the choice is often down to preference of the surgeon, although there are distinct

advantages and disadvantages of both high and low viscosity oils. High viscosity oils, such as 5000c.st, are very stable and reduce the risk of emulsification, however, 1000 c.st oils are often used as they offer ease of manual injection and removal. The difference in anatomical success and visual acuity following either 1000 c.st or 5000 c.st oil placement was investigated by Scott et al. who showed no significant difference between the two oils [61].

Although there are disadvantages associated with using SiO as a tamponade agent, they are greatly outweighed by the advantages in terms of patient comfort and conformity. It removes the need for restricted head movement and allows recovery during normal day-to-day activity over the long term. Also, modified silicone oils (such as Siluron XTRA, Fluoron) have been developed incorporating physical properties such as shear thinning, making them easy to inject manually but providing resistance against emulsification *in situ* [62].

1.3.2 PROLIFERATIVE VITREORETINOPATHY TREATMENT

Surgical methods are often applied in the treatment of proliferative vitreoretinopathy (PVR), this is due to the limitations involved in the use of pharmacological agents. The aim of PVR surgery is to reduce the tractional forces of the epi- and subretinal membranes and repair the break in the retina. This is often achieved using a combination of the surgical procedures described above (section 1.3.1). Given the complexity of PVR, the risk of retinal redetachment is high following surgery. There are currently some pharmacological approaches to managing PVR, however an understanding of how different pharmacological agents could potentially target different phases of the disease could provide a more successful approach.

1.3.2.1 DRUG TREATMENTS IN PVR

A variety of drugs have been investigated in the prevention/reduction of PVR. Mostly they can be grouped into either anti-proliferative or anti-inflammatory drugs, however, some studies have investigated the use of anti-growth factors and anti-oxidants also.

Anti-proliferative drugs: Following a break in the BRB and the subsequent inflammation, proliferation ensues, therefore drugs which inhibit the cell cycle and suppress cell proliferation have been investigated to target this initial phase of PVR. Those which have been extensively include: 5-fluorouracil (5-FU), daunorubicin, α-tocopherol and retinoic acid (RA). 5-FU is one of the most thoroughly investigated dugs for use in PVR [63, 64]. It was

originally developed as an anti-cancer drug but has been shown to reduce fibroblastic proliferation. One disadvantage of 5-FU is that it has a very short half-life and is rapidly eliminated from the vitreous ($t_{1/2}$ = 3.5 hours for 1 mg), therefore multiple doses are required. This can lead to complications from increased risk of infection and danger of administering toxic levels. Borhani et al. developed a sustained release device which administered 5-FU in a rabbit model of PVR which showed a 100% efficiency in preventing tractional RD [65].

Anti-inflammatory drugs: Some of the first agents tested in the treatment of PVR were corticosteroids. Corticosteroids are anti-inflammatory drugs which are used in a vast range of medical conditions and act to suppress inflammation at the early stages of its initiation [66]. Triamcinolone acetonide (TAA) showed success in early animal experiments with an approximately 64% reduction in recurring RD following intravitreal injection of the drug [67]. However in humans, although it has been shown to potentially reduce breakdown within RPE, the success of the animal experiments has not been observed. A human study conducted by Chen et al. assessed the role of low-dose triamcinolone as an adjunctive therapy with a vitrectomy and silicone oil tamponade which appeared to be safe and effective [68]. Other corticosteroids that have been investigated in animal models include: methylprednisolone, and methotrexate. Methylprednisolone reduced the incidence of RD following PVR and minimised infiltration of cells into the vitreous whereas methotrexate had no beneficial effect [69, 70].

1.3.2.2 IBUPROFEN

2-(4-Isobutylphenyl)propionic acid, also known as ibuprofen (ibu), is a non-steroidal anti-inflammatory drug (NSAID) often used to treat pain, fever and inflammation. In the context of PVR, it is yet to be studied, however, its characteristic action of reducing inflammation could make it a suitable candidate to be investigated further. A paper published by Cauldbeck et al. proposes its use in the treatment of the disease but it is yet to be investigated in a PVR model [71]. The mechanism of action of ibuprofen is not greatly understood, however it has been shown to be a non-selective inhibitor of the enzyme, cyclooxygenase (COX), which is required for the synthesis of prostaglandins, active lipid compounds which promote inflammation [72]. Ibuprofen was chosen to be investigated in this study due to its potential applications as a PVR treatment but also because it is soluble in silicone oil and the concentration is easily detectable in relevant media using established techniques.

1.4 OCULAR DRUG DELIVERY

Due to the unique anatomical and physiological structure of the eye, delivery of drugs to the posterior segment poses a major challenge. There are a number of both static and dynamic barriers which must be overcome in order to achieve a therapeutic dose at the target location. Here, the major routes of ocular drug administration will be discussed.

1.4.1 TOPICAL

Topical administration of drugs in the eye involves application of eye drops to the surface of the eye at the cornea. The usefulness of topical administration in the treatment of posterior segment diseases such as PVR is limited due to poor bioavailability. It has been estimated that only 5% of topically applied drugs penetrate the cornea and reach intraocular tissues and this approach typically does not yield a therapeutic dose in posterior tissues [73]. Much of the loss of drug occurs rapidly following application as a result of tear fluid turnover and subsequent drainage, furthermore, the corneal epithelium presents a significant barrier to solute flux in to the cornea. Additionally, the use of many topical drugs requires strong patient compliance which can often be a cause of failure in such treatments. Despite the shortcomings of this technique, topical eye drops are still widely prescribed due to their non-invasive nature but predominantly for anterior segment conditions [74].

1.4.2 SYSTEMIC

It is possible for drugs to reach the retinal/choroidal tissue via the blood circulation through systemic administration either orally or intravenously. The availability of drugs in tissues of the posterior segment is limited due to the presence of tight junctions in the BRB which control the movement of large molecules from the blood into the retina, as previously discussed (section 1.1.3). This can lead to a need to administer high doses of the drug which can have negative side effects on non-target tissues [75]. This is not a conventional administration route for PVR drug treatment but there has been a trial which studied oral administration of 13-cis retinoic acid for PVR. They suggest that at their stated dose and duration of treatment, orally administered 13-cis retinoic acid could reduce the risk of PVR following RD surgery [76].

1.4.3 INTRAVITREAL INJECTION

The quickest and most direct route to administering drug solution to the posterior segment is via intravitreal injection. This is currently the most common approach used for drug therapies in posterior diseases. The benefit of this method is that it bypasses the BRB and directs the drug to the site of action. However, the majority of intravitreal drugs that are used have a short half-life in the vitreous, and require frequent repeat injection to maintain a therapeutic level. This requirement increases the risk of complication due to the invasive nature of the technique and can lead to injuries such as lens damage or endopthalmitis (inflammation of intraocular tissues) [77].

1.4.4 OCULAR IMPLANTS

In recent times there has been a surge in research looking to develop implantable sustained-delivery drug devices to overcome the problems associated with the traditional administration techniques described above. There have been a number of diverse approaches utilised in the development of such devices, ranging from biodegradable and non-biodegradable drug-loaded biomaterials, to scleral plugs, to polymeric drug matrices, each of which can provide unique mechanisms of drug release depending on requirement [78]. Implantable drug delivery devices are thought to present a number of advantages over current techniques, these are outlined in Table 1-1 [79, 80]. These devices are not without risk however, and can also lead to complications associated with invasive surgeries. It has also been reported that implantable ocular drug delivery devices can caused increased intraocular pressure which cause damage to tissues such as the optic nerve [81].

Advantages of Implantable Drug Delivery Devices

Delivery close to target site, minimising off target effects
Direct delivery allows for less total drug to be delivered, reducing the risk of possible side-effects
Sustained release removes risk of lack of patient compliance
Bypasses BRB allowing use of macromolecules
Can offer molecular protection for drugs which are unstable *in vivo*

Table 1-1: Advantages of ocular drug delivery devices [79, 80].

1.4.5 CURRENT RESEARCH IN PVR DRUG DELIVERY DEVICES

Ideally, pharmacological intervention for PVR would occur over a course of 6-8 weeks as this is the time over which the disease process occurs, therefore a sustained-release drug delivery device would be valuable tool for use in this disease. Some of the technologies that are suitable for use following a vitrectomy which have been investigated include injectable liposome and microsphere suspensions. Liposomes are membrane-like vesicles which are composed of concentric phospholipid bilayers containing aqueous compartments. These vesicles can either encapsulate hydrophilic drugs within the aqueous or combine hydrophobic drugs in to the membrane and act as a reservoir [82]. Drugs that have been investigated as liposomal formulations in rabbit PVR models include: 5-FU [83], cytarabine [84] and daunomycin [85], and in each case the half-life of the drug within the vitreous was significantly increased when the liposomal formulation was used in comparison with administration of free drug. Microspheres are micron-sized, drug containing polymer matrices which are suspended in a liquid medium. Drug dissolves through the matrix and out of the polymer which may or may not simultaneously degrade. Microspheres loaded with 5-FU [86] and retinoic acid [87] have been studied both *in vitro* and *in vivo* in PVR models and shown gradual release of drug over time periods up to 30 days, for the case of RA.

It seems as though there is an opportunity to exploit the tamponade agents used in the treatment of RD and PVR to administer an adjunctive therapy as a drug delivery device whilst simultaneously repairing retinal wounds. Silicone oil (SiO) is most commonly used as a vitreous replacement in PVR surgery and its lipophilic nature means there are a number of lipophilic compounds which are readily dissolved in it and can utilise the material as a reservoir. Chung et al. were the first to investigate the drugs dissolved in SiO as a treatment in PVR. They evaluated lipophilic 1,3-bis(2-chloroethyl)-nitrosourea (BCNU) in terms of its solubility and stability in SiO, its release into aqueous and antiproliferative properties *in vitro* as well as in a rabbit PVR model [88, 89]. BCNU is not a suitable drug for the treatment of PVR and is normally reserved for cancer treatment, however this work has led to further drugs such as RA [90] and 5-FU [91] being investigate as possible candidates for this delivery method. Ibuprofen is a lipophilic drug by nature, but it is able to be dissolved in SiO, a non-lipid based oil. Given this and its anti-inflammatory effects, it is possible that is has applications in this drug delivery system to treat PVR. This study will investigate ibuprofen

release from silicone oil, with a focus on its transport and clearance away from the oil reservoir.

1.5 OCULAR DRUG ELIMINATION PATHWAYS

With respect to ocular drug delivery and clearance, the eye can be visualised as four compartments: the anterior chamber, vitreous cavity, tear film cul-de-sac and periocular space. The route of both administration and elimination alters moving through these compartments [92].

Following topical administration of drugs, the majority of the dose is washed out immediately via the blinking mechanism. Upon installation, drug compounds combine with the lacrimal fluid present on the ocular surface. Normally, lacrimal fluid turnover occurs at just 1µL/min, however, the excess fluid is rapidly removed through the nasolacrimal duct [93]. Once in the nasal cavity, drugs and metabolites are able to be removed via systemic absorption. Systemic absorption also occurs in the conjunctival sac, the narrow pocket where the conjunctiva meets the eyelid. This sac is able to hold approximately 30µL of the typical 70µL volume of eye drop normally administered but has a rich capillary bed which is able to absorb drugs and metabolites and remove them systemically [94]. The dose that remains in the lacrimal fluid following this early elimination permeates across the cornea into the anterior chamber.

Once in the humour of the anterior chamber, drugs can be easily transported to structures such as the iris and ciliary body. Drug elimination in the anterior chamber primarily occurs via two mechanisms: aqueous humour outflow through the Schlemm's canal and through the blood flow in the anterior uvea [95]. Aqueous humour is produced by the ciliary body and travels from the posterior chamber in to the anterior chamber through the pupil. In the anterior chamber, it flows out in to the Schlemm's canal through the trabecular meshwork and is subsequently absorbed by the episcleral vasculature. Flow of aqueous humour is thought to occur at a rate of 3-5µL/min [96]. Elimination of drugs via the uveal blood flow is dependent on the ability of the drug to penetrate the endothelium of the blood vessels. This causes lipophilic drugs to be cleared more readily by this mechanism than hydrophilic drugs as they move more freely across the endothelial cell membranes. Once in the blood flow, elimination is estimated to occur at approximately 20µL/min [97].

Drugs administered intravitreally, whether via injection or implant, are cleared via two routes, either anteriorly or posteriorly. Nearly all compounds can be eliminated via the anterior route (described above). Once the drug has diffused across the vitreous, it enters the aqueous of the posterior chamber, where it is transported in to the anterior chamber and cleared either out through the Schlemm's canal or in to the uveal blood flow [98]. Alternatively, posterior elimination occurs through permeation across the posterior blood-ocular barriers such as the outer and inner BRB. This route requires either adequate passive permeability of agents, generally very low molecular weight or lipophilic substances, or active transport of molecules by the cells present in the barrier. This is the reason for larger or hydrophilic molecules generally exhibiting longer half-lives in the vitreous [99].

This study will investigate *in vitro* models of drug transport and clearance through the aqueous outflow and posterior drug elimination pathways used to remove drugs that are administered intravitreally.

1.6 IN VITRO MODELS OF OCULAR DRUG TRANSPORT

In vitro models have been used for many years to establish a basic mechanistic understanding of a system in a relatively simple, quick and reproducible manner. Additionally, *in vitro* models allow more combinations of parameters to be tested which can be unachievable in *in vivo* models. Models have applications in basic science, toxicological and pharmaceutical studies and are often heavily involved in the early discovery phases of drug development. Frequently these cells are based around either primary or immortalised cell lines, and in the context of ocular models, both have been heavily used [100]. In recent times there has been a focus on developing more biologically representative *in vitro* models by building them up in a 3-dimensional (3D) environment, incorporating more the one cell type as well as biomaterials to establish more realistic cell signalling environments [101]. *In vitro* models of both healthy and diseased ocular tissues have been reported for the cornea [102], conjunctiva [103], inner and outer BRB [104, 105] and vitreous body [106]. Vitreoretinal and BRB models will be discussed here.

1.6.1 MODELS OF THE BLOOD RETINAL BARRIER

In section 1.1.3, the structure of both the inner and outer BRB was discussed. The inner BRB contains the complex tight junctions of the retinal vasculature endothelial cells and is

designed to limit non-specific transport from the microvasculature to the cells of the retina. It is thought the main contributing components to this barrier are the retinal endothelial cells, the pericytes which reside around the outside of the blood vessels, and the extracelluar matrix surrounding both, however, other cell types such as retinal astrocytes may also be involved [107]. Breakdown of this barrier is common in pathologies such as diabetic retinopathy, therefore extensive research has been done to model the breakdown of this barrier and understand the factors that influence conditions such as the permeability of the retinal endothelium in the hope of discovering new treatment strategies [108].

Beharry et al. developed a 3-dimensional (3D) co-culture model of the inner blood retinal barrier to investigate ocular drug delivery development. In this model, primary human retinal endothelial cells (HREC) were cultured together with primary human retinal astrocytes (HRA) on hydrogel scaffolds in an attempt to create a more representative biomimetic model of the dynamic inner BRB in comparison to a traditional 2-dimensional culture [109]. They then used this model to assess the response of the HRECs to drugs for use in the treatment of retinopathy and reported that the HRECs response to the drugs showed less variability when cultured in their *in vitro* model in comparison with a single cell type 2D culture [109].

In vitro study of the outer blood retinal barrier is well reported. As with the inner BRB, these models have often been used to investigate the permeability of drugs and compounds across the RPE or look to model disease of the OBRB. In order to obtain a true model of the OBRB, the main structures need to be incorporated. These being the RPE, BM and choroidal endothelium. Hamilton et al. developed a trilayer *in vitro* model of the OBRB using an immortalised human RPE cell, ARPE-19, and human umbilical vein endothelial cells (HUVEC) cultured either side of amniotic membrane. This model was able to maintain the polarisation of the ARPE-19s whilst simultaneously forming a fenestrated endothelial phenotype in the HUVECs and was planned to be used to study age-related macular degeneration [104]. Other models of the OBRB have used alternative cell sources and BM materials, such as primary human RPE cells and. Skottman et al. describe an OBRB model which used human embryonic stem cell derived retinal pigment epithelium cells and human retinal microvasculature endothelial cells either side of polyethylene terephthalate (PET) membrane. They suggest that co-culture of the two cell types together drastically improves the barrier functionality of the RPE cells and that this model would be useful in investigating OBRB drug transport [110].

Although many of the *in vitro* models of the OBRB that have been reported include the main structures within the tissue, few include a flow mechanism to model the blood flow within the choroid. This flow mechanism is particularly important when investigating the clearance of drugs across the BRB as it causes systemic removal of permeated drugs. Yeste et al. describe a system which comprises the co-culture of human retinal endothelial cells and ARPE-19s in a microfluidic culture system. This system compartmentalises the cells and they therefore do not create a single construct and the transepithelial electrical resistance of each of the cells was measured independently and no drug permeability studies were conducted [111]. Another microfluidic chip device was reported by Chen et al. who investigated the co-culture of ARPE-19s and HUVECs in a microfluidic model of choroidal angiogenesis. Within this model, glucose was transported to the cells within the flow of the media but the actual transport mechanisms were not the parameter of interest [112].

The lack of studies regarding *in vitro* modelling of the effects of posterior systemic clearance of drugs in the eye leaves scope for this mechanism to be investigated further. This study will look to produce a relevant *in vitro* model of this clearance pathway using ARPE-19 cells, synthetic BM and a blood flow system.

1.6.2 MODELS OF AQUEOUS OUTFLOW CLEARANCE

There have been few studies that have looked to develop an *in vitro* model of aqueous outflow to investigate the transport of molecules which follow this anterior clearance pathway [113]. One model, the PK-Eye model, was developed by Awaad et al. and was designed as a flow model for use in preclinical drug development. The model uses a Perspex eye model with both an anterior and posterior chamber which are separated by a dialysis membrane. The model was used to estimate the intraocular residency time of the drugs, ranibizumab, bevacizumab and triamcinolone acetonide. The drugs were administered to the posterior chamber of the model and the flow was introduced through the front of the posterior chamber with the outlet positioned at the front of the anterior chamber. With this model they were able to produce results for the clearance of drugs which showed good agreement with similar studies which used animal trials to investigate the mechanism [114].

To the best of my knowledge there are no other *in vitro* models of aqueous outflow drug clearance. As with dynamic OBRB models, there is scope for this to be investigated further as this mechanism is of equal importance in terms of intravitreal drug clearance. In this study,

an *in vitro* model of aqueous outflow will be investigated using a spherical eye model which was originally designed to study the emulsification of silicone oils as discussed in section 1.3.1.3.

1.7 COMPUTER MODELLING IN DRUG DELIVERY

Over the past two decades, significant advances in information technology and computer systems have made complex mathematical modelling of processes, such as drug delivery, more available. Novel drug delivery systems can now be optimised *in silico* with great accuracy and the ease of application has only increased. Computer science and simulation of pharmacokinetic behaviour is becoming an integral part of pharmaceutical research and development due to the significant reduction in cost and time they can offer. Professor Takeru Higuchi was the first describe drug release from an ointment based matrix using a mathematical equation [115] and this study began the trend of using mathematical equations to explain drug release and pharmaceutical dosing. Models used to describe such processes can be divided into two categories: empirical/semiempirical or mechanistic. Empirical models are purely descriptive mathematical equations based on no real physical, chemical or biological phenomena. This kind of description can for example be used to compare the release profiles of drugs in respect to a specific parameter such as apparent release rate constant [116]. Mechanistic modelling is based around real phenomena, such as diffusion or degradation. These models can be used to determine system specific parameters and provide an understanding of the underlying mechanisms of drug delivery within the system. Mechanistic approaches allow for quantitative analysis and prediction of the effects of the specified input parameters which makes unknown, desired properties theoretically predictable [117].

1.7.1 THE FINITE ELEMENT METHOD

Finite element analysis (FEA) is a computational tool used to simulate and analyse physical problems. The laws of physics and the characterisation of phenomena such as diffusion, as described in time and space, are often solved using partial differential equations (PDE). These complex PDEs are often not solvable analytically and approximations of the equations have to be built based on discretisations. Discretisation involves approximating the PDEs with numerically solvable equations, which in turn, produces solutions which are an

approximation of the PDE. Finite element analysis is used to compute these approximations [118].

When a model body is discretised, it is divided into an equivalent system made up of many smaller units, elements. These elements are interconnected at points which are common to two or more other elements (nodes) and/or boundary lines.

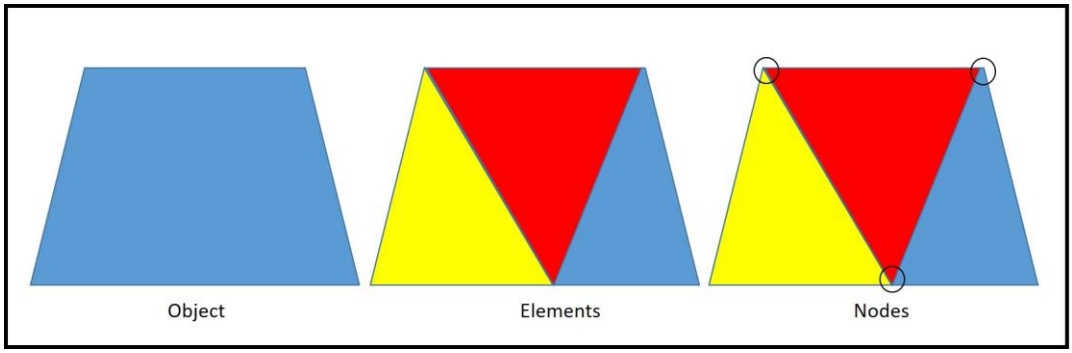

Figure 1-6: Discretisation in finite element analysis.

The assembly of the complete set of elements that divide the object is known as the mesh. Rather than solve the PDEs which describe the object as a whole, it is assumed that the field variable in question, for example concentration of drug, acts through each element in a predefined manner which could be a linear, quadratic or high order function. The number of elements must adequately approximate the variable distribution across the body as a whole [119]. If the mesh is too coarse, the resolution of the distribution becomes insufficient. If the mesh is too fine, it becomes computationally intensive and requires much more time to solve. The ordinary differential equations are solved for each individual element based on their location within the mesh. These elemental solutions are then assembled into a solution for the variable field across the entire body of the object [120].

The advantages of FEA is that it provides a comprehensive description of the variable field and can be used to predict behaviours of systems to minimise experimental burden. It also allows accurate analysis of critical design parameters and can increase the rate of the developmental process whilst minimising failures. FEA has applications across many engineering disciplines including electrical, mechanical, fluid and chemical engineering and has been used previously in studies investigating the design of drug delivery devices. There are a number of software packages that are commercially available such as ANSYS, SimScale and COMSOL Multiphysics, each of which have different benefits in terms of user friendliness and analytical power [121].

COMSOL Multiphysics is a FEA solver and simulation software package used in solving various physical and engineering problems. It was initially developed for use in structural mechanics but now provides a number of application-specific sub modules such as: acoustics, chemical engineering, microfluidics and heat transfer. The major benefit of using COMSOL over other FEA software is that it has a user-friendly interface and allows the problems with multiple physics interfaces to be solved. It provides professionally predefined modelling interfaces as well as allowing to user to define their own PDEs, it also has the capability to be integrated with other computer software such as computer aided design software which can be used to import problem specific geometries [122].

1.7.2 THE EQUATIONS OF FLUID DYNAMICS

This study aimed to produce computer simulations of drug clearance in *in vitro* models of the eye. The two clearance mechanisms of interest are those which are experienced by intravitreally administered drugs, so anterior clearance via aqueous outflow and posterior clearance by transport through the BRB and away via the systemic circulation. Both of these pathways involve convective fluid flow to influence the distribution of drug. For this reason, the models were built using computational fluid dynamics descriptions.

Computational fluid dynamics (CFD) is a branch of fluid dynamics which uses methods such as FEA described above, to solve problems that involve fluid flow. COMSOL Multiphysics provides a physics module to solve for the equations of fluid dynamics and has been used in many studies where fluid flow is present in the model, such as flow through pipes and design of microfluidic devices.

The fundamental basis of almost every CFD problem are the Navier-Stokes equations [123]. These equations govern the motion of fluids and are the fluid equivalent of Newton's second law of motion:

$$F = ma$$

Equation 1-1: Newton's second law of motion.

which shows Force, F, is a product of the mass, m, of an object and its acceleration, a. In the case of fluids though there are additional forces present between the layers of the fluids and

fluids also transfer energy differently to solids all of which is taken into account with the Navier-Stokes equations, which can be written as:

$$\rho\left(\frac{\partial \boldsymbol{u}}{\partial t} + \boldsymbol{v}.\nabla \boldsymbol{v}\right) = -\nabla \mathrm{p} + \nabla.\mathbf{T} + \mathbf{f}$$

Equation 1-2: Navier Stokes equation.

The left-hand side of the equation describes the product of the density of the fluid and the acceleration that is experienced by the particles within the fluid. This side of the equation is analogous to the ma side of Newton's second law of motion, where **u** is the velocity vector. The right-hand side of the equation incorporates the forces which are responsible for the particle acceleration: the pressure gradient p, the viscous shear stresses, T and volume forces, f, which for the purposes of the models in this study are due to gravity, which makes f equal to the product of the gravity constant, g, and the density of the fluid.

The continuity equation is the law that describes how mass cannot be created nor destroyed and represents the mass conservation of the system. In the case of fluid dynamics it states that the rate at which mass enters a system is equal to the rate at which mass leaves a system plus the accumulation of mass within the system. In the case of incompressible fluids, such as the culture medium used in these models which will maintain a constant density, this mass continuity equation simplifies to a volume continuity equation:

$$\nabla.\boldsymbol{u} = 0$$

Equation 1-3: Volume continuity equation

This equation states that the volume dilation rate of the fluid is zero, therefore the fluid will alter its velocity based on the geometry of the pipe [124].

The models in this study need to provide solutions not only for the velocity of the fluid field within the system but also the concentration field of drug ibuprofen both in the silicone oil and once it is released. To do this a diffusion equation will be implemented:

$$\frac{\partial c_i}{\partial t} + \nabla.(-D\nabla c_i) + \boldsymbol{u}.\nabla c_i = R_i$$

Equation 1-4: Diffusion equation for transport of diluted species.

This equation models diffusion and convection and solves the mass conservation equation for one or more chemical species c_i. D is the diffusion coefficient which is based on the molecular size of the chemical species and can be calculated theoretically, **u** is the velocity vector and R_i is the reaction rate expression.

The first term on the left side of equation 1-4 corresponds to the accumulation of the species. The second term accounts for the diffusive transport, accounting for the interaction between the dilute species and the solvent. The third term on the left side of describes the convective transport due to a velocity field **u**. This field can be expressed analytically or obtained from coupling this physics interface to one that computes fluid flow, such as Laminar Flow. For the case of these models, the solutions from the laminar flow study can be used as the velocity field in this mass balance equation [125].

1.7.3 FINITE ELEMENT ANALYSIS OF DRUG DELIVERY WITHIN THE EYE

Finite element analysis has be used to produce a number of simulations which look to predict the behaviour of novel drug delivery devices. The studies that have been conducted investigated devices such as transdermal patches [126], microneedles [127], hydrogel matrices [128] and nanoparticles [129], all of which aimed to understand the release and transport profiles of the loaded drug through the system.

There have been several studies carried out that specifically model drug delivery and kinetics in the posterior segment of the eye, including systemic delivery methods, intravitreal injection and ocular implants. The diffusion and convection of drugs across ocular tissues has been investigated by Balachandran and Barocas who designed a model to identify the barriers to the diffusion of drugs following transcleral administration [130]. Similarly, Jooybar et al. developed a computer simulation using COMSOL Multiphysics which investigated the transport of drugs through the eye following intravitreal injection. This study examined the effects that needle gauge had on the injected drug bolus and how that subsequently affected the drug distribution through the eye [131]. Other studies have looked to simulate drug distribution following implantation of a drug delivery device, including polymer gel implants, scleral patches and controlled release implants [132-134]. These models all simulate drug delivery within computer built geometries of the eye and although they can provide useful information regarding the drug kinetics in the eye, experimentally these results cannot be validated *in vivo* due to the invasive nature of the techniques that would be required to do

so. Much of the work carried out is based on experimental work conducted by Palestine and Brubaker who investigated the kinetics of fluorescein in the human eye [135]. In order for the sophistication of these models of drug delivery in the eye to be improved, more experimental data is required to provide a greater database for FEA validation. For this reason it could be useful to build predictive models of *in vitro* devices used in the development of novel drug delivery devices as they are able to be validated using data from benchtop experiments. Although these models will not provide an approximation of what will occur once the device is administered in the eye, it may make the discovery phase development process more efficient. This is the rationale behind the use of computational models in this study. They may be able to reduce the number of time intensive and costly experiments that would be required in the development of an ibu-SiO drug delivery system by predicted the behaviour of the device under a range of experimental parameters. There are obvious limititaions to computational models, namely the solution will always be an approximation and the accuracy of the results produced is a relfection of the quality and accuracy of the user implemented parameters and boundary conditions. However, they still have the power to be a useful predictive tool.

1.8 HYPOTHESIS, AIMS AND OBJECTIVES

Hypothesis

Computer models built using experimentally derived parameters from simple *in vitro* experiments would be able to accurately predict the release behaviour of ibuprofen from silicone oil in more complex *in vitro* experiments across a number of model designs

Aims and Objectives:

Aim 1: To develop an experimentally validated *in silico* model which can be used to predict the release and transport profiles of compounds across an equivalent *in vitro* model of the outer blood retinal barrier.

> Objective 1: To develop a simple, yet relevant *in vitro* model of the OBRB and use this model to define key parameters needed for the *in silico* model.

Objective 2: To build an *in silico* model of an equivalent *in vitro* model of posterior drug clearance across the OBRB.

Objective 3: To validate the *in silico* model using data from *in vitro* experiments and use the *in silico* model to predict ibuprofen release from silicone oil within the i*n vitro* model.

Aim 2: To develop experimentally validated *in silico* models which can be used to predict the release and transport of ibuprofen from a silicone oil reservoir within equivalent *in vitro* models of both the aqueous outflow pathway and an eye-on-a-chip microfluidic device.

Objective 1: To build *in silico* models of equivalent *in vitro* models of aqueous outflow drug clearance of ibuprofen from silicone oil within a spherical eye model and release of ibuprofen from silicone oil in an eye-on-a-chip device.

Objective 2: To validate the *in silico* models using data from *in vitro* experiments and use the *in silico* models to predict ibuprofen release from silicone oil within the i*n vitro* models.

Objective 3: To determine the effects that exposure to simulated saccadic movements has on the release profiles of ibuprofen within these *in vitro* models.

CHAPTER 2

MODELLING THE OUTER BLOOD RETINAL BARRIER

2.1 AIM AND OBJECTIVES

AIM

To design complimentary *in vitro* models and computer simulations for use in the study of molecule permeation across the outer blood-retinal barrier.

OBJECTIVES

- Develop and optimise a relevant *in vitro* model of the RPE – Bruch's Membrane – Choroidal blood flow complex.
- Study the permeability of this barrier model *in vitro* and investigate the diffusion of different size molecules across it.
- Develop, optimise and validate a complimentary CFD model of the *in vitro* model.
- Determine whether the CFD model can be used to predict molecule concentrations across the *in vitro* model.

2.2 IN VITRO MODEL OF THE OUTER BLOOD RETINAL BARRIER

In vitro models can be a valuable tool in understanding biological systems particularly in drug development and toxicology. Knowledge of parameters such as barrier permeability and diffusion coefficients, is of crucial importance when studying the movement of potential therapeutic treatments across epithelial tissues. Many existing *in vitro* models do not sufficiently mimic the many different environmental and dynamic factors associated with these physiological barriers. However, with the rapid rise in microfluidic technologies for cell culture which has occurred over recent years, the creation of dynamic *in vitro* models has become more accessible.

2.2.1 THE KIRKSTALL QV600 CELL CULTURE SYSTEM

The Kirkstall QV600 cell culture chamber (***Figure 2-1***) is a novel system which has been designed to allow surface cultures of cells which are found in an air-liquid interface environment *in vivo*, for example skin, respiratory epithelium or corneal cells.

The media flow culture platform perfuses volumes of media in the range of millilitres, potentially allowing a more physically relevant perfusion model to be designed for this study in comparison with traditional microfluidic devices. The external dimensions of the chamber are 40mm in height and 30mm in diameter meaning it can be used with transwell inserts already commercially available. The chamber and the tubing are made from PDMS and a pump is required to generate the fluid flow. It was initially designed as an air-liquid interface culture system whereby a hanging transwell insert hangs in the top half of the chamber and medium is perfused through the bottom half. This split chamber design (***Figure 2-2***) allows for independent control of fluid flow across either side of the transwell membrane and the placement of the inlet and outlet ports mean that the media flow is maintained at a consistent level. Moving the height of the media reservoir in relation to the chamber can manipulate the pressure gradient across the system, altering the level of media flow based on whether the cells require an air-liquid interface or complete submersion in media.

Being a new technology, previous studies using this system are limited. However, there are examples where the QV600 has been used to study permeability across epithelial models [136] and to build dynamic 3D models to study disease [137]. For the purposes of investigating the outer blood retinal barrier, this system provides many of the necessary

properties for a representative model as outlined in section 1.6. Kirkstall Ltd also manufacture two other cell culture chambers which are not air-liquid interface chambers but are designed for fully submerged cultures which expose the apical surface of the cells to fluid flow. These chambers, the QV500 and QV900, have been used in studies using cardiac cells [138], liver hepatocytes [139] and fibroblasts [140] however these are not relevant in this study.

The main aim of this study was to investigate the movement of molecules and drugs across an RPE-Bruch's Membrane model from an implantable drug reservoir within the vitreous cavity, and their subsequent clearance via a flow system. Simple modification of the QV600 chamber provides these features in an *in vitro* model that can be used to study this drug clearance pathway (***Figure 2-3***, ***Figure 2-4***).

The Kirkstall QV600 Cell Culture Chamber

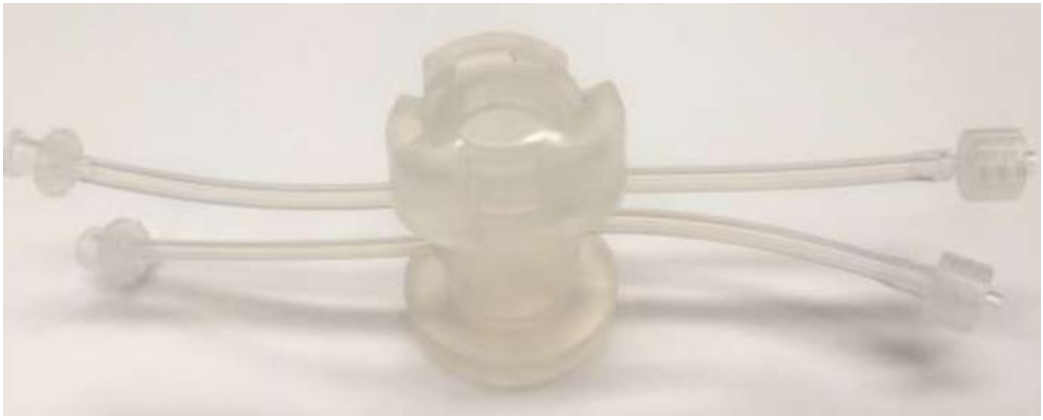

Figure 2-1: Kirkstall QV600 cell culture chamber.

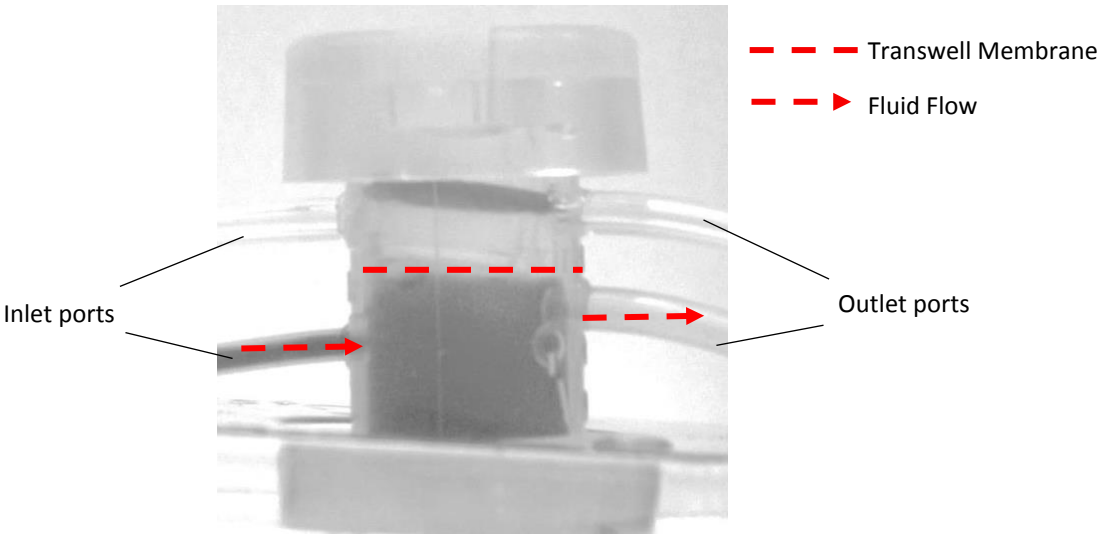

Figure 2-2: Kirkstall QV600 cell culture chamber, side view.

Comparison of In Vivo Structure vs In Vitro Model

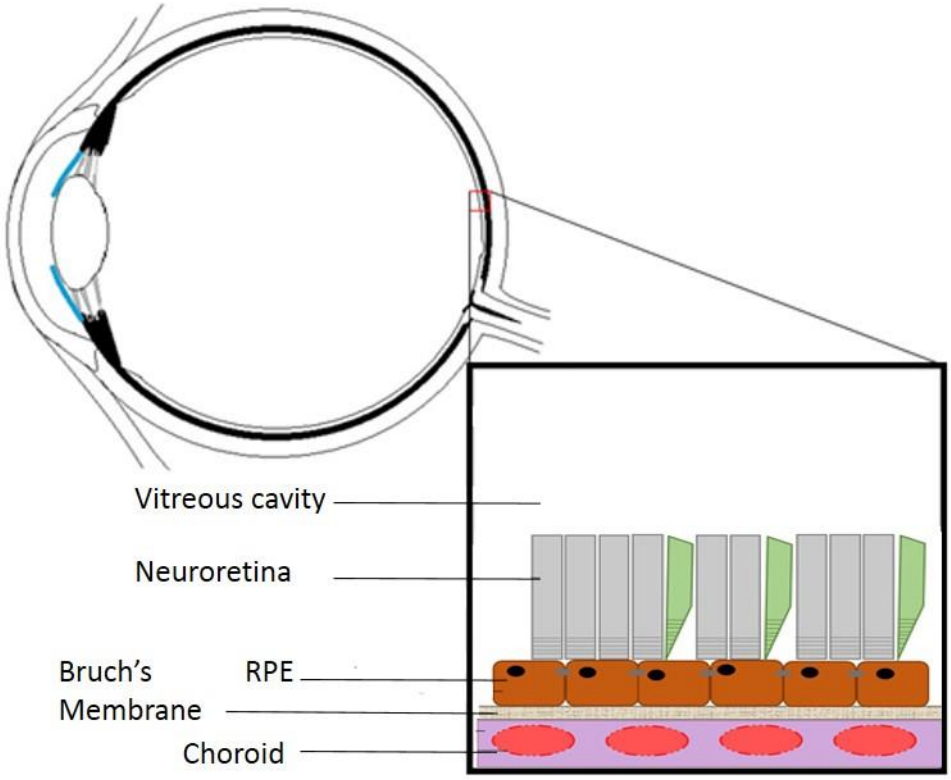

Figure 2-3: Schematic of the outer blood retinal barrier in vivo showing the structures drugs must travel through to reach the bloodstream from the vitreous cavity.

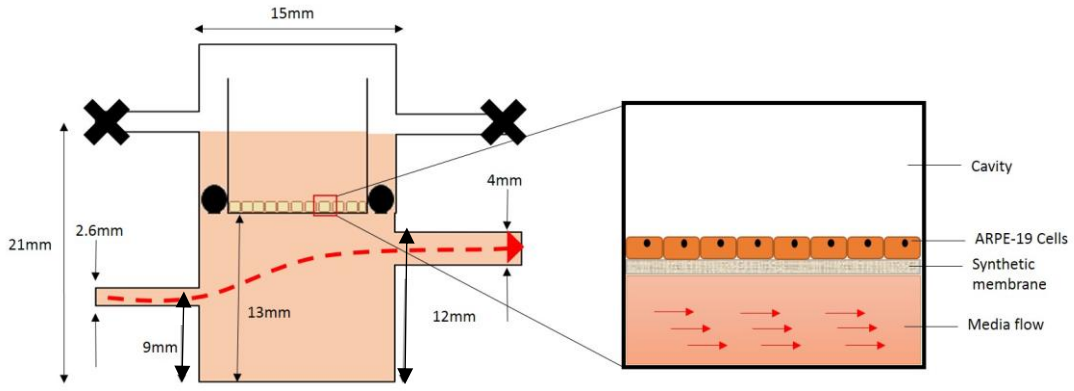

Figure 2-4: Schematic of the Kirkstall QV600 cell culture chamber showing analogous structures to those shown in Figure 2-3. Red arrows indicate culture media flow.

2.2.2 MATERIALS AND METHODS

2.2.2.1 MODIFICATION OF THE KIRKSTALL QV600 CHAMBER FOR OUTER BRB STUDIES

The Kirkstall QV600 culture system with its novel split chamber design, could be modified to allow a static fluid reservoir on the apical side of the cells with dynamic media flow on the basal side. This media flow was used as an analogy to choroidal blood flow, one of the clearance mechanisms in the posterior segment of the eye. Choroidal blood flow rates *in vivo* have been reported to peak up to approximately 10µL/min during systole with the maximum blood velocity reaching 45mm/s [3]. However, given the dimensional differences between choroidal arteries and the QV600 chamber, the flow velocities will be significantly different for equal flow rates. For this reason a range of flow rates was investigated in these studies. The flow was generated via a peristaltic pump connected to a reservoir of fresh perfusion medium. To create a drug implant reservoir on the apical side of the membrane, the inlet and outlet ports to the top half of the chamber were sealed.

The Bruch's Membrane was modelled using commercially available transwells as a substitute. These transwell inserts are provided as 12mm diameter membranes set in a standing transwell mould, they are further described in section 2.2.2.4. For use in the QV600 system, a silicone O-ring was placed around the outer wall of the transwell prior to the sterilisation step described in section 2.2.2.4. This O-ring was used to create a seal within the chamber between the apical and basal sides of the transwell membrane and allowed the insert to sit a specified level within the chamber. However, the pressure generated by the force of closing the lid of the chamber following the insertion of the transwell caused the transwell to become dislodged and produced variability in the position of the membrane across the different experiments. To overcome this problem, a transwell mount design was developed to ensure each transwell would sit at the same level in each experiment. The mounts were produced from acrylonitrile butadiene styrene (ABS) via additive manufacture and were designed to have no impact on the flow of the medium (***Figure 2-5***).

To complete the model, a retinal pigment epithelium cell line, ARPE-19, was seeded onto the apical side of the transwell membranes and the cells were allowed to develop into a confluent monolayer prior to insertion into the QV600 chamber.

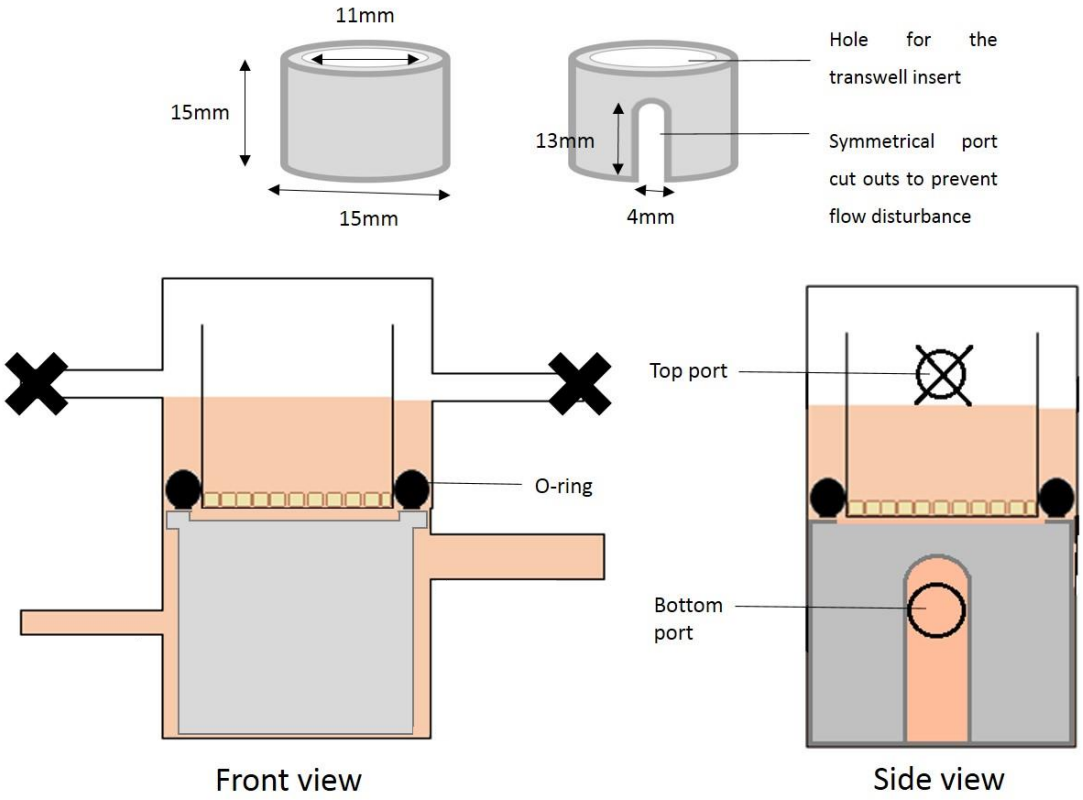

Figure 2-5: ABS mount design and position within chamber.

2.2.2.2 CULTURE OF HUMAN RETINAL PIGMENT EPITHELIAL CELL LINE (ARPE-19 CELLS)

The ARPE-19 cell line (ATCC® Number: CRL-2302™) is a well-established, spontaneously arisen adult retinal pigment epithelium cell line from the normal eyes of a 19 year old male donor who died in a motor vehicle accident. In culture, these cells are able to form stable monolayers with a distinctive cobblestone morphology and functional polarity. They display the normal phenotype of RPE cells found *in vivo* and express RPE-specific markers hence making them a useful model in assessing RPE permeability and drug interaction [141, 142]. A recent study has also shown that they are able to become repigmented in long term cultures [143].

The ARPE-19 cells were maintained in complete culture medium, a 1:1 (vol/vol) mixture of DMEM/F-12 containing cell culture supplements (***Table 2-1***), in a humidifying incubator at 37^{o}C with 5% carbon dioxide (CO_2) as recommended by ATCC. The cells were grown in 75cm^2 flasks (Greiner 658175) and the media was replenished three times a week. Once the cells had reached approximately 80% confluency in the flask, the culture medium was removed and the cells were washed in 10ml of phosphate buffered saline solution (PBS) (Thermo

Scientific Oxoid BR0014G; 1 tablet per 100ml distilled water (dH_2O)). After adding 5mL of 1x Trypsin-ethylenediaminetetraacetic acid (EDTA) solution (Sigma T4171; 2mL of stock solution (as provided) mixed with 18mL sterile PBS) and incubating the cells for five minutes at 37^{o}C, they rounded and detached from the flask. To prevent protein digestion, 5mL of complete culture medium was added to the Trypsin-EDTA and the solution was transferred to a 30mL universal tube. The mixture was then centrifuged (Thermo Scientific Heraeus Multifuge x1) at 1500 x g for five minutes. The supernatant in the tube was removed and the cell pellet was resuspended in 1mL of complete culture medium. A sample of this suspension was taken and further diluted 1:10 in complete culture medium in a micro-centrifuge tube before being counted with haemocytometer. The cells were then seeded into culture containers at cell densities and medium volumes appropriate for the subsequent experimental needs. All cells used in experiment were between passage 22 and passage 30.

2.2.2.3 CRYOPRESERVATION AND RETRIEVAL OF CELLS

Spare flasks of ARPE-19 cells were frozen down and stored in liquid nitrogen until needed. Cells were trypsinised and centrifuged as above and the pellet was resuspended in freezing media (***Table 2-2***) at room temperature. This cell suspension was transferred into cryogenic vials (flask/vial ratio 1:3) and slowly frozen in a Mr Frosty™ Cryo 1^{o}C freezing container (Thermo Scientific, 5100-0001) containing isopropanol (Sigma I9516) which has a cooling rate of approximately 2^{o}C/min. The container was stored in a -80^{o}C freezer overnight. The cryogenic vials were then transferred into liquid nitrogen for long term storage. The presence of dimethyl sulfoxide in the freezing media prevents its rapid cooling as it is a cryoprotective agent which reduces the freezing point. This is necessary to reduce the risk of ice crystal formation which can cause cell death [144].

When required, the cells were retrieved from the liquid nitrogen and thawed via immersion in a 37^{o}C for one to two minutes. The cell suspension was transferred to a 30ml universal tube, 9ml of culture media was added and the solution was thoroughly mixed. The cell solution was then centrifuged at 1500 x g for five minutes, resuspended in 1ml of culture media and transferred into a 75cm^2 flask. A further 9ml of culture media was added to the flask which was then maintained inside a humidifying incubator (37^{o}C, 5% CO_2). The media was replenished after 24hrs and then three times a week thereafter.

2.2.2.4 CULTURE SUBSTRATE AND PLASMA TREATMENT

As mentioned in section 1.1, the Bruch's membrane (BM) is an integral structure in maintaining the outer BRB. To develop a relevant *in vitro* model of the outer BRB, a suitable replacement for the BM must be used to support the growth of an ARPE-19 cell monolayer. A number of studies have looked to identify suitable synthetic materials for use in the replacement of BM with some of the necessary physical properties being porosity, bio-stability and mechanical strength [145, 146].

Polytetrafluoroethylene (PTFE), also known as Teflon®, is a synthetic fluoropolymer which was discovered in 1938 and was widely used in wiring as insulation. In 1969, it was found that by heating and stretching PTFE, a porous membrane could be formed, known as expanded PTFE (ePTFE). The unique physical and chemical properties of ePTFE have made it a leading biomaterial used in many medical applications such as synthetic vascular grafts, sutures and ligaments [147-149]. ePTFE has many properties which make it appropriate as a BM replacement. It has well-established biocompatibility, porosity, flexibility and bio-stability, however, 'as-received' ePTFE is hydrophobic in nature and therefore does not promote the adhesion and formation of cell layers [146, 150].

Commercially available expanded modified polytetrafluoroethylene (ePTFE) culture inserts (Merck Millipore, PICM01250) were used for all permeability and cell culture experiments. The inserts are provided as 12mm diameter standing well inserts with a pore size of 0.4µm and a membrane thickness of approximately 50µm, making them suitable for use in 24 well plates and the Kirkstall QV600 system. These membranes are subjected to proprietary treatment by the manufacturer to increase the hydrophilicity, however they still recommend coating with protein prior to seeding attachment dependent cells such as ARPE-19 cells. It is believed that the long term behaviour of RPE cells grown on synthetic substrates will be affected by the stability of their surrounding basement membrane. Deposition of ECM by cells has been shown to be affected by surface topography therefore coating the membranes with synthetic proteins prior to seeding could promote abnormal deposition of matrix by the cells thus affecting the ability to form a polarised monolayer [146, 151].

Previous studies have shown that the use of plasma technology allows modification of the surface of ePTFE to achieve greater hydrophilicity. This technique allows the fibrous, porous architecture of the material akin to the natural BM to be maintain whilst enhancing cell

attachment without requiring any additional ECM coating [146, 152]. Gas plasma treatment works by using an electrical charge to ionise gas within a vacuum chamber which creates plasma ions. These plasma ions react with molecular groups on the surface of the treatment sample and alter the surface chemistry of the material [153].

All the inserts used in the experiments were surface modified by ammonia gas (100% purity; BOC Ltd) plasma treatment using a helical resonator plasma system. The system was built in house and is formed from a 100-turn copper wire wound outside of a glass tube. The resonant frequency was <1W and the treatment time was 2 minutes at a gas pressure of $1.2x10^{-1}$mbar and flow rate of 85sccm as described previously [154, 155]. Immediately following treatment, the inserts were placed into distilled water to maintain the stability of the modification [156] and stored at room temperature until required for experiments. All inserts were U.V. sterilised (CL-1000 U.V. Crosslinker; UVP) for 5 minutes on either side immediately before use in cell culture.

Components of Complete Culture Medium

Name	Concentration	Source
Dulbecco's Modified Eagle Medium/Ham's Nutrient Mixture F-12 Formulation (1:1 mix) with L-Glutamine, 15mM HEPES and sodium bicarbonate		*Sigma (D8437)*
Penicillin/Streptomycin 10mg/ml streptomycin in 0.9% NaCl	1%	*Sigma (P0781)*
Foetal Calf Serum (FCS)	10%	*BioSera (S1900)*

Table 2-1: Components of complete culture media used to culture ARPE-19 cells.

Components of Freezing Medium

Name	Concentration	Source
Dulbecco's Modified Eagle Medium/Ham's Nutrient Mixture F-12 Formulation (1:1 mix) with L-Glutamine, 15mM HEPES and sodium bicarbonate		*Sigma (D8437)*
Dimethyl Sulfoxide Hybri-max	10%	*Sigma (D2650)*
Foetal Calf Serum (FCS)	10%	*BioSera (S1900)*

Table 2-2: Components of freezing media used in the cryopreservation of ARPE-19 cells.

Components of Reduced Serum Culture Medium

Name	Concentration	Source
Dulbecco's Modified Eagle Medium/Ham's Nutrient Mixture F-12 Formulation (1:1 mix) with L-Glutamine, 15mM HEPES and sodium bicarbonate		*Sigma (D8437)*
Penicillin/Streptomycin 10mg/ml streptomycin in 0.9% NaCl	1%	*Sigma (P0781)*
Foetal Calf Serum (FCS)	2%	*BioSera (S1900)*

Table 2-3: Components of reduced serum culture medium used in experimental cultures of ARPE-19 cells.

2.2.2.5 CELL SEEDING ONTO SUBSTRATES

Throughout these studies ARPE-19 cells were cultured on NH_3 treated ePTFE transwell insert membranes with tissue culture polystyrene (TCP) used as a control substrate. All experiments were conducted with a cell density of $2.6x10^4$cells/cm^2.

Cells were seeded onto TCP coverslips (ThermoFisher 174950) in a 24 well plate (Greiner 662160) and allowed to settle for one hour before an additional 1mL of complete culture media was added to maintain the cultures. The cells cultured on NH_3 treated ePTFE transwell were seeded on to the apical side of the membrane and the inserts were maintained in 24 well plates with 400µL of complete culture media on the apical side and 600µL of complete culture media on the basal side. Previous studies have shown that reducing the concentration of serum in culture media can prevent over-proliferation of the cells and maintain the polarised monolayer morphology which is vital to the barrier functionality [157, 158] Therefore, 24hr post-seeding, the serum content in the media was reduced to 2% FCS. All cultures were incubated at 37^{o}C with 5% CO_2 and cells were fed with fresh reduced serum culture medium (RSC) (***Table 2-3***) three times a week for all experiments.

2.2.2.6 EPITHELIAL BARRIER FORMATION AND FUNCTION

At days 2, 7, 10 and 14 post seeding the cell tight junction formation was assessed to determine the optimal time to allow for cell barrier formation. At each time interval, the media was removed from the cells and each sample was washed three times with PBS. The cells were then fixed in 10% neutral buffered formalin (NBF) (Sigma HT501128) for 10 minutes at room temperature. NBF is a fixative agent which cross-links proteins to preserve the natural architecture of the cellular components. Immunocytochemistry was used to visualise the presence of tight junctions within the samples, this method is further described in section 2.2.3.10.

In addition to immunocytochemical assessment, those cells cultured on ePTFE membranes were subjected to transepithelial electrical resistance (TEER) measurements to study the extent and integrity of the tight junction formation in the cell monolayer. This is a widely accepted quantitative method which has been used to determine barrier integrity in many epithelial and endothelial models. TEER uses Ohm's Law to determine the electrical resistance between the two sides of a cell monolayer grown on a semipermeable membrane, in this case the electrical resistance of the ARPE-19 monolayer on the ePTFE membrane. By

placing an electrode on either side of the membrane and applying an alternating current, the electrical resistance between the two electrodes can be measured.

The commercially available Epithelial Voltohmeter (EVOM) system with STX-2 electrodes (World Precision Instruments) was used for all TEER measurements. The electrodes were sterilised in 70% ethanol for 15 minutes, then washed in fresh sterile RSC media. Control background readings were taken from a transwell without cells on to determine the resistance of the membrane, the mean of these values was then subtracted from the values obtained from the samples with cells grown on. These values were then normalised per unit area (cm^2) of the membrane and the mean ± 1 standard deviation TEER values (Ω/cm^2) are presented.

2.2.2.7 CELL CULTURE IN THE PRESENCE OF FLOW

The bioreactor system was set up in a recirculating fluid series circuit (***Figure 2-6***). A reservoir bottle was connected to a single QV600 chamber, which was connected to the peristaltic pump (Parker, PF22X0103) and then reconnected to the initial reservoir bottle. This recirculating system allows continuous perfusion of media without the need to monitor and refresh the media supply. The chambers and tubing are made from poly(dimethylsiloxane) (PDMS) and the reservoir bottles and Luer connectors from polypropylene which allows them all to be sterilised via autoclaving prior to cell culture experiments.

Cells were cultured statically on the transwell membranes for 10 days prior to insertion into the perfusion system. This was to allow the monolayer to develop fully and form tight junctions before the cells were exposed to fluid flow. Cell morphology, viability and transepithelial electrical resistance (TEER) were also studied prior to their exposure to the fluid flow to provide comparison post-flow.

All parts of the system were assembled in a sterile, class II biosafety cabinet and the sterile ABS transwell mounts were inserted to the bottom of the chamber. The system was rinsed through with 30ml of sterile PBS for 20 minutes after which the system was primed with 30ml of fresh RSC medium and incubated at 37^{o}C with 5% CO_2 for 10 minutes. The system was returned to the class II cabinet, the inlet and outlets were clamped shut and the transwell membrane with the ARPE-19 cells were inserted into the chamber. The chamber was closed, the ports unclamped and the system was connected to the peristaltic pump at a predetermined flow rate and incubated at 37^{o}C, 5% CO_2 for 24 hours.

Control samples were also incubated at 37°C, 5% CO_2 for 24 hours and maintained statically on the membranes within a 24 well plate (Greiner 662160). The RSC media in the control plates was replenished at the same time as the bioreactor system was filled and cell morphology, viability and TEER were assessed alongside the flow samples.

After 24 hours, the transwell membranes were removed from the system and TEER measurements were taken from all of the samples. The media was then removed and the samples were washed 3 times in PBS. Samples were fixed in either 100% ice-cold methanol (Fisher Scientific, 11976961) or 10% neutral buffered formalin (NBF) (Sigma HT501128) to assess cell morphology and characteristic cell markers.

2.2.2.8 CALIBRATION OF THE PERISTALTIC PUMP

The Parker PF22X0103 peristaltic pumps used in these studies have two independent pump heads which are controlled via Vernier dials. In order to assign flow rates to the numbers on the dials, the pumps had to be calibrated to the specific configuration of the system. The bioreactor system was set up in a single pass fluid series circuit (***Figure 2-7***). A reservoir of fresh distilled water connected to a single QV600 chamber then connected to the peristaltic pump which circulated the water into a waste collection reservoir. The QV600 chamber was set up as per the cell culture experiment, with a transwell membrane without cells seeded, inserted atop an ABS mount. The system was primed with distilled water to expel all the air between the starting reservoir and the outlet into the waste reservoir. The pump was run for 5 minutes after which the water output was collected and the volume measured. For each speed, this was repeated 3 times and the mean was taken to calculate a flow rate in mL/min. To ensure reproducibility in flow rates across each experiment, the exact lengths of PDMS tubing was measured for each experimental circuit.

Experimental Setup for Flow Culture and Peristaltic Pump Calibration

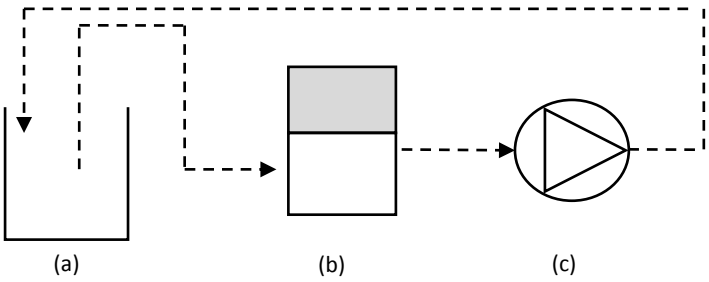

Figure 2-6: Flow culture experiment recirculating setup. Dotted line represents dynamic flow. (a) Media reservoir (b) QV600 chamber (c) peristaltic pump.

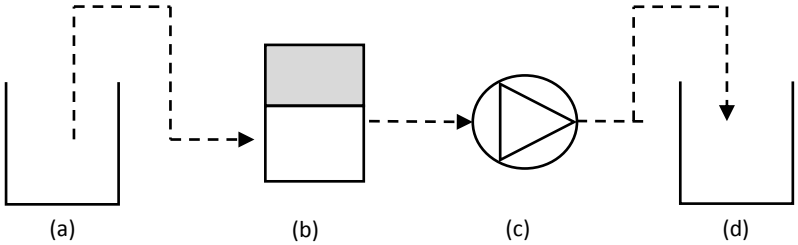

Figure 2-7: Flow culture experimental single pass setup. Dotted line represents dynamic flow. (a) Fresh media reservoir (b) QV600 chamber (c) peristaltic pump (d) waste collection reservoir.

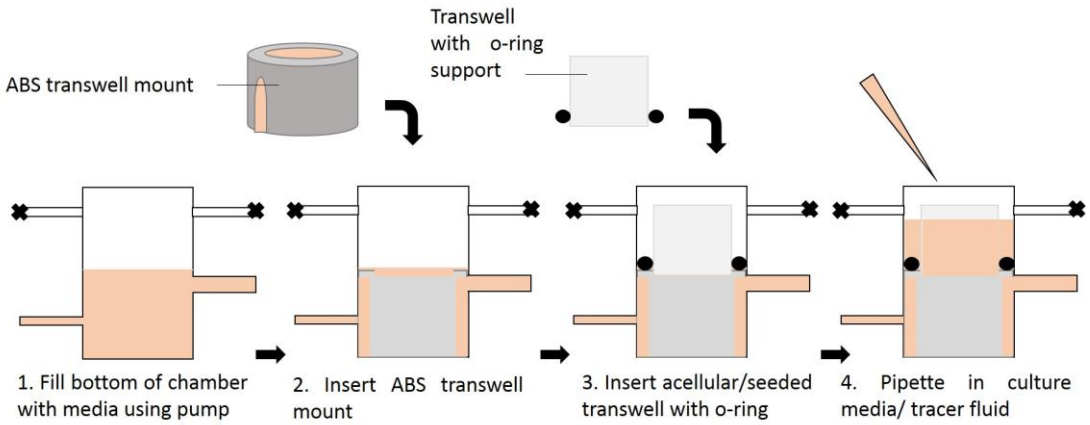

Figure 2-8: Schematic of experimental assembly process.

2.2.2.9 CELL METABOLIC ACTIVITY

Throughout these studies, cell metabolic activity was measured using a resazurin reduction assay which determines the mitochondrial activity of the cells. The cell permeable redox indicator begins as a deep blue coloured solution and in the presence of cells with active mitochondrial metabolism, is reduced to fluorescently active resorufin, which is pink in colour but fluoresces when exposed to green light. This can be quantified using a fluorescent plate reader with a $\lambda_{excitation}$ = 530nm, $\lambda_{emission}$ = 590nm filter set [159].

Resazurin assays were performed on cells prior to and post exposure to basal RSC media flow to assess the cell metabolic activity alongside the barrier formation studies as described previously. Again, this was to determine whether their exposure to flow had any effect on the metabolic activity of the cells. Resazurin salt (ThermoFisher, R12204) was dissolved in sterile PBS to a stock concentration of 0.1mg/mL, filtered to sterilise and stored at 4°C in the dark. At the point of assay, the stock solution was further diluted 1:10 in RSC media to a final concentration of 0.01mg/mL. At day 10 post seeding, a resazurin assay was performed on transwell inserts prior to insertion in the Kirkstall QV600 chamber. The RSC media was removed and 400µL of resazurin solution was added inside the transwell, with 600µL of RSC media added outside the transwell. The background fluorescence was measured using transwells containing no cells with 400µL of resazurin added inside and 600µL RSC media added outside of the transwell. The plates were then incubated for 2 hours at 37°C, 5% CO_2 in dark conditions. Post-incubation, 3x 100µL samples were taken from each well and transferred to a black 96-well plate (Corning, CC780). Resorfurin fluorescence was read using BMG Labtech FLUOROstar Optima plate reader ($\lambda_{excitation}$ = 530nm, $\lambda_{emission}$ = 590nm). The background fluorescence was deducted from all values and they were then normalised to the pre-flow controls and the values are reported as the mean ± 1 SD.

2.2.2.10 CELL NUMBER

At culture days 2, 7, 10 and 14 (n=9 for each treatment) the media was removed from the cells and they were washed three times in PBS. The cells were then fixed in 100% ice cold methanol (Fisher Scientific 11976961) for 5 minutes and washed again 3 times in PBS. Methanol is a fixative agent which also permeabilises the cells. The nuclei of the cells were stained using 4',6-Diamidino-2-Phenylindole, Dilactate (DAPI; Life Technologies D35741, 5mg/mL), diluted in 1:30,000 in PBS for 5 minutes at 37°C. DAPI forms a fluorescent complex

by attaching to adenine/tyrosine rich regions of DNA which can be visualised using a fluorescent microscope [160]. The samples were then washed again 3 times in PBS and then stored under 500µL of fresh PBS.

All samples were visualised using a Nikon Eclipse Ti-E microscope (Japan). To determine the cell number for each sample, five images from five different fields of view were taken from each well/substrate using a 10X objective and the number of nuclei per field of view were counted using the image analysis software ImageJ. The mean number of nuclei per view was used to calculate the mean number of cells/cm^2 for each sample. These values are presented as the mean ± SD, n=9.

2.2.2.11 Immunocytochemistry for Cell-Cell Junctions and Differentiation Markers

To evaluate cell-cell contact, a protein component of tight junctions, Zonula Occluden-1 (ZO-1) was stained and visualised using immunocytochemistry. At culture days 2, 7, 10 and 14, cells seeded on TCP coverslips in 24-well plates and in transwells were fixed in 10% NBF as described previously. The cells were then permeabilised with 0.1% Triton-X100 for 5 minutes at 4°C following three PBS washes. The samples were blocked in 10% goat serum (Sigma G9023) (diluted in PBS) for 30 minutes at 37°C. Blocking with a solution such as serum, which contains an abundance of charged proteins, reduces the non-specific binding of antibodies which give rise to background staining. The samples were then incubated with a primary rabbit anti-ZO-1 antibody (details in ***Table 2-4A***) diluted with 1% BSA solution, at 4°C overnight. Following three washes in wash buffer (0.1% PBS Tween 20) (Sigma P1379) the samples were incubated with an anti-rabbit secondary antibody (details in ***Table 2-4B***) for an hour at 37°C and then counterstained with DAPI. The transwell membranes were removed from the transwells by cutting around the edge of the membrane with a scalpel, in order to mount them onto microscope slides. All microscope slides were mounted using VECTASHIELD antifade mounting media (VECTOR Laboratories, H-1000) which prevents rapid photobleaching and preserves fluorescence in samples. Images were taken using a Zeiss LSM 800 laser confocal microscope.

The expression of alpha-smooth muscle actin (αSMA) was also evaluated. αSMA is biochemical marker and its expression in RPE cells is an indication of epithelial-mesenchymal transition. In stable, differentiated monolayer cultures, RPE cells will not express αSMA [161]. At each time point, the samples were washed three times in PBS and fixed in ice cold

methanol for 5 minutes at room temperature. Following three further washes in PBS, the samples were blocked in 10% goat serum (diluted in PBS) for 30 minutes at 37°C after which they were incubated with a mouse anti-αSMA antibody (details in table) diluted in 1% BSA, overnight at 4°C. The samples were washed three times with wash buffer and incubated for a further hour with an anti-mouse secondary antibody (details in table) at 37°C and counterstained with DAPI. Images were taken using a Zeiss LSM 800 laser confocal microscope. To ensure the specificity of the antibodies used, rabbit or mouse immunoglobulins (IgG) were used as an isotype control (details in table).

ZO-1 and αSMA expression were also evaluated in the experiments where the samples were exposed to flow. Cells were fixed and stained for each of the antibodies described above after their exposure to flow for each flow rate as well as the static controls.

Antibodies used to detect Cell-Cell Junctions and Differentiation Markers in ARPE-19 Cells

A

Primary Antibodies	Dilution	Source
Rabbit polyclonal anti-ZO-1	1:100	*Invitrogen (40-2200)*
Mouse monoclonal anti-alpha smooth muscle Actin	1:200	*abcam (ab7817)*

B

Secondary Antibodies	Dilution	Source
Goat anti-rabbit, Alexa Fluor 488	1:500	*Life Technologies (A-11034)*
Goat anti-mouse, Alexa Fluor 594	1:500	*Life Technologies (A-11032)*

Table 2-4: Primary (A) and secondary (B) antibodies used to detect cell-cell junctions and differentiation markers in ARPE-19 cells.

Fluorescein Isothiocynate Conjugated Dextrans used in Permeability Studies

FITC Dextran	**Molecular Weight (kDa)**	**Source**
FD4	4	*Sigma (FD4-100MG)*
FD40	40	*Sigma (FD40-100MG)*
FD70	70	*Sigma (FD70-100MG)*

Table 2-5: Different molecular weights of fluorescein isothiacynate conjugated dextrans used in the in vitro permeability studies.

2.2.2.12 STATIC TRANSPORT STUDIES TO DETERMINE BARRIER PERMEABILITY

A classic two compartment, zero flow model system was used to study the permeability of different sized molecules across the NH_3 treated, ePTFE membrane. Following plasma treatment, transwell inserts with ePTFE membranes were sterilised via UV treatment (5 minutes UV exposure on both sides) and inserted into a 24-well plate. The transwells were then either seeded with ARPE-19 cells or left unseeded. For seeded experiments, ARPE-19 cells were seeded on to transwell membranes at $2.6x10^{-4}$cells/cm^2 in complete culture medium as per previous experimental conditions. Day 1 post seeding, the medium was changed to reduced serum culture medium and the cells were allowed to grow for 10 days to ensure tight junction formation, this was also confirmed with TEER measurements. Transwells without cells were used immediately after sterilisation and soaked in RSC medium prior to the experimentation. Transport studies were done using fluorescently labelled dextrans with different molecular weights to obtain apparent permeability coefficients over a range of particle sizes.

Fluorescein isothiocynate (FITC) conjugated dextrans of different molecular weights (***Table 2-5***) were each diluted in PBS to yield stock solutions with a concentration of 1mg/mL. At the point of experimentation, the stock solutions were further diluted in RSC medium to create a tracer solution with a final concentration of 50µg/mL and filtered to sterilise. The media in the transwells was discarded and the inside and outside of each was washed with PBS. The apical compartment of the transwells was filled with 400µL of tracer solution, with 600µL of RSC medium added to the basal compartment and the plates were incubated at 37°C with 5% CO_2 in the dark. At time intervals of 1, 3, 8 and 24 hours, the unidirectional flux (apical to basal) of FITC-dextran was measured by taking three, 50µL samples from the basal compartment. An equal volume of fresh RSC medium was added to the basal compartment after sampling to replace the lost volume. The samples were kept at 4°C in the dark until all samples had been collected. The samples were transferred to a black 96-well plate and the fluorescence of each sample was measured using a fluorescence spectrophotometer (FluorSTAR Optima, BMG Labtech) with $\lambda_{excitation}$ = 492nm, $\lambda_{emission}$ = 520nm filter set. For each molecular weight of dextran a standard curve was generated by measuring the fluorescence of a serial dilution. The tracer solution was diluted 1:4 in RSC medium for 5 dilutions and triplicate 50µL samples were taken for each dilution and the fluorescence was measured as described previously. Experimental and standard curve samples were performed in triplicate

for each molecular weight. The time-dependent increase in FITC-dextran in the basal compartment is presented. Results are shown as the mean concentration at each time point ± 1 SD.

Under static conditions, the transmembrane flux of the dextran particles (J_D) is predominantly determined by diffusive forces and can be calculated using the quantity of dextran traversing the membrane in time t (dQ/dt) and the exposed area of the membrane (A):

$$J_D = \frac{dQ}{dt} A$$

Equation 2-1: Transmembrane Flux.

Flux can also be defined by the change in concentration through the thickness of the membrane (dC/dx) multiplied by the diffusion coefficient (D) of the membrane:

$$J_D = -D \frac{dC}{dx}$$

Equation 2-2: Relationship between flux and diffusion coefficient.

If we assume steady state flux through the membrane and that the concentration at the apical side of the membrane is equal to the donor concentration, $C_{A,}$ and the concentration at the basal side of the membrane is equal to the receptor concentration, C_B, then equation 2-1 can be written as:

$$J_D = D \frac{C_A - C_B}{h}$$

Equation 2-3: Intergrated equation for transmembrane flux.

where h is the thickness of the barrier. Using the concentration curves obtained from the two-compartment static transport studies, the transmembrane flux was calculated using equation 2-1. The calculated flux was then used to determine the diffusion coefficients for each molecular weight of dextran across both the seeded and unseeded NH_3 treated ePTFE membranes. The values obtained for the diffusion coefficients were then used as initial parameters in the computational models described in section 2.3.

The other input parameter required by the computational models is the permeability coefficient (K_P) of the membrane. This was also calculated from the data obtained from the two-compartment static transport studies.

If the amount of dextran traversing the membrane were an infinite dose, then the permeability coefficient (K_P) can be defined by the relationship:

$$K_P = \frac{Q}{At(C_A - C_B)}$$

Equation 2-4: Apparent permeability coefficient from time-dependent FITC-dextran concentration.

where C_A is the concentration of the dextran in the apical compartment and C_B is the concentration of dextran in the receptor compartment on the basal side of the membrane. Normally C_A can be simplified as the donor concentration and C_B can be simplified to 0. For each different molecular weight dextran used, the apparent permeability coefficient was calculated for both the ePTFE membrane with ARPE-19 cells and without ARPE-19 cells.

2.2.2.13 DYNAMIC TRANSPORT STUDIES

The experimental set-up was designed to emulate mass transport and drug clearance at the interface between the vitreous cavity and the outer blood retinal barrier therefore the system was arranged in a single pass series fluid circuit as described in section 2.2.2.7. This set up allowed the study of the movement of the dextran particles from a static reservoir, through the ePTFE membrane into a dynamic flow environment representative of the movement from the vitreous cavity, through the Bruch's membrane into the choroidal capillary network.

Initial experiments were conducted in the absence of ARPE-19 cells. The Kirkstall QV600 system was assembled as previously described in 2.2.2.7 but for a single pass, non-recirculating circuit. The system was rinsed with 30mL of sterile PBS for 20 minutes prior to being primed with 30mL of RSC media. Once the system was filled with media, the inlet and outlet tubes of the Kirkstall QV600 chamber were clamped shut and the ABS transwell mount was inserted after which the plasma treated ePTFE membrane transwell with the silicone O-ring was inserted. The apical compartment of the transwell was filled with 400µL of tracer solution, the chamber was sealed and the inlet and outlet were unclamped. The media was

then perfused through the system. At defined time points, samples were taken from the chamber on the basolateral side of the membrane. The inlet and outlet tubes were clamped shut and the transwell containing the tracer solution was removed. The remaining volume of media (2.5mL) in the Kirkstall QV600 chamber was removed using a syringe and the solution was homogenised. Three 100µL samples were taken from this solution and transferred to a black 96-well plate. The chamber was then refilled with 2.5mL of fresh RSC media, the transwell reinserted and resealed after which the tubes were unclamped and the flow was allowed to perfuse once more. This was repeated for each time point up to 24 hours. Once all the samples had been collected, the fluorescence of each was measured using a spectrophotometer (FluorSTAR Optima, BMG Labtech) with $\lambda_{excitation}$ = 492nm, $\lambda_{emission}$ = 520nm filter set. The concentration of FITC-dextran in each of the samples was determined by comparison with the standard curve for each molecular weight of FITC-dextran. Data are presented as the average concentration profile for the basolateral side of the membrane within the chamber. This procedure was repeated for each molecular weight of FITC-dextran at flow rates of 20uL/min, 200uL/min, 400µL/min and 2mL/min. Each experiment was repeated in triplicate and the results are shown as mean concentration ± 1 SD. For the 2mL/min experiment the systems were unable to be left overnight due to the risk of exhausting the media supply within the reservoir, therefore these experiments were conducted over 8 hours.

2.2.2.14 Static Release of Ibuprofen from Silicone Oil

The release of ibuprofen (ibu) from silicone oil (SiO) was measured over time to determine a static release profile. Ibu is a lipophilic drug and is also soluble in SiO, one of the reasons it was selected for use in these studies. An experimental concentration of 1mg of ibu (Tokyo Chemical Industry UK, I0415) was added to 1mL of 1000c.st Silicone oil (Fluoron GmbH) and the mixture was stirred for a minimum of 72 hours in a sealed flask. Following stirring, the ibu-SiO was filtered in a Class II biological safety hood to sterilise and remove any undissolved material before being stored at RT. The initial experimental set-up was designed to measure the release of ibu from SiO directly into RSC culture media at 37^{o}C with 1mL of the ibu-SiO on top of 500µl of RSC media in the well of a 24-well plate. At defined time points, three 100µl samples were taken from the RSC media, transferred to UV transparent cuvettes (UVette, Eppendorf) and the time-dependent increase in ibu concentration was measured using a UV spectrophotometer (SPECTROstar Nano, BMG Labtech) $\lambda_{absorption}$ = 264nm. Due to

the abundance of proteins and other molecules present in the RSC media, the absorption spectra of the ibuprofen in the samples produced undetectable results due to interference, therefore the experimental set up was altered to measure the release of ibu into PBS. As culture media was unable to be used, the release experiments could not be conducted in the presence of cells therefore it should be noted that all results presented for the release of ibuprofen are without the passage of the drug across an ARPE-19 monolayer. Similarly, initial experiments were designed to measure the release of ibuprofen from the SiO across the NH_3 treated EPTFE membrane, however a fluid-fluid interface was needed to allow movement of the drug from the oil phase to the aqueous phase. To overcome this, a small volume (100µL) of PBS was added to the donor compartment on the apical side of the transwell membrane with 300µL of SiO and 600µL of PBS added to the receptor compartment on the basal side of the membrane. Due to the transwell design and the differences in density between the PBS and the SiO, hydrostatic forces caused the level of the PBS phase on the apical side to alter during the timeframe of the experiment leading to inconsistences across replicates. The final experimental design therefore involved direct release of ibuprofen from the SiO into the PBS without crossing a membrane. In a well plate, 500µL of PBS was added with 1mL of ibu-SiO added on top. This was repeated in 12-well plates, 24-well plates and 48-well plates to investigate the effect of interfacial surface area on the release profile.

The concentration of ibuprofen present in each of the samples was determined by comparison with the standard curve. Concentration gradient effects were investigated with experiments being carried out with the PBS completely replaced following sample removal, or just the 150µl sample volume replaced with fresh PBS. Experiments were carried out in triplicate and results are presented as the mean cumulative release ± 1 SD.

2.2.2.15 Dynamic Release of Ibuprofen from Silicone Oil

The Kirkstall QV600 chamber was used to investigate the effects of dynamic flow on the release of ibu from SiO. Utilising the single pass, non-recirculating set up described in 2.2.2.13, the concentration of ibu in the bottom of the QV600 chamber was measured at defined time points, as previously described. As with the static experiments, release of ibu was measured into PBS. The Kirkstall QV600 chamber, tubing and peristaltic pump were assembled as previously described. The system was rinsed and primed with 30mL of fresh sterile PBS. The inlet and outlet ports were clamped shut and 2mL of 1mg/mL ibu-SiO was

added directly on top of the PBS. The clamps were removed and the flow was allowed to perfuse.

At set time intervals, the ports were clamped shut and the volume of PBS beneath the ibu-SiO in the QV600 chamber (2.5mL) was removed using a 25 gauge (25G) needle and syringe. Using a 25G needle allows the PBS to be removed from the chamber without removing any silicone oil as 1000 c.st SiO is too viscous to be drawn into the needle. The PBS removed was homogenised and three 50µL samples were added to individual UV-clear cuvettes and the UV light absorption of the samples was measured using a UV spectrophotometer (SPECTROstar, BMG Labtech) $\lambda_{absorption}$ = 264nm. The absorption of each of the samples was compared to a standard curve and the concentration of the ibu present in each sample was determined. Results are presented as mean concentration at each time point ± 1 SD.

2.2.2.16 STATISTICS

GraphPad Prism statistical analysis software was used to analyse all data.

Unpaired student t-test

- Concentration curve statistics of transport through NH_3 treated ePTFE and NH3 treated ePTFE seeded with ARPE-19 cells.

A significance level of $p < 0.05$ was set for these experiments.

One-way Analysis of Variance (ANOVA)

- Effects of dynamic flow on cell number.
- Effects of dynamic flow on cell viability.
- Effects of dynamic flow on TEER.

Dunnet's post hoc test was used. A minimum significance level of $P < 0.05$ was set for each experiment. D'Agostino & Pearson normality tests were used to confirm the normal distribution of the data.

2.2.3 RESULTS

2.2.3.1 CELL MORPHOLOGY AND EPITHELIAL BARRIER FORMATION

ARPE-19 cells seeded on both TCP coverslips and NH_3 treated ePTFE transwell membranes were investigated to determine the optimal culture time for the cells to develop tight junctions and exhibit the barrier properties necessary to study the transmembrane transport of molecules. Previous models of the outer BRB which used ARPE-19 cells report epithelial barrier functionality at time points ranging from 7 days to 4 weeks [104, 162, 163]. Cell number, immunocytochemistry and transepithelial electrical resistance were all used to evaluate the monolayer and epithelial barrier integrity.

Cell Number and Growth

The cell populations showed an increasing trend in cell number up until day 7 after which the number appeared to begin to plateau up to day 14 where the cells had reached confluence; this is a typical growth pattern for cells in culture [164]. Although both materials were initially seeded with a density of $2.6x10^4$ cells/cm^2, the increase in cell number was more rapid for those cells grown on TCP controls compared with the NH_3 treated ePTFE membranes however both surfaces displayed similar shaped curves but with the nuclei count on the ePTFE being lower at each time point (***Figure 2-9***). These differences however, were not statistically significant (Two-way ANOVA, Sidak post-hoc. F (3, 24)= 0.556, p= 0.65). The growth of the cells on TCP was also confirmed with phase contrast microscope images which appear to show approximately 80% confluency by day 7 and a confluent monolayer, with a cobblestone appearance typical of that seen in epithelial cell morphology, by day 10 (***Figure 2-9***). Due to the opacity of the NH_3 treated ePTFE membrane, images were not able to be obtained with a standard light microscope therefore the presence of an intact monolayer was confirmed via immunocytochemistry.

Expression of the Tight Junction Marker Zonula Occluden-1

The formation of junctional complexes which are typically found in epithelial cell types provides the necessary intercellular adhesion needed for the RPE cells to form a functional polarised monolayer. The monolayer formation was therefore verified by fluorescent staining of the tight junctional protein Zonula Occluden-1 (ZO-1). The use of ZO-1 in the identification of the presence of tight junctions within a culture is common and established

method [112, 162, 165, 166], however other tight junction protein components, such as occludin, can also be used.

The presence of ZO-1 was demonstrated from culture day 7 on both the NH_3 treated ePTFE and the TCP controls (***Figure 2-11***, ***Figure 2-12***). For both surfaces, the ZO-1 staining was localised at the cell-cell borders as expected, with the majority of the cell monolayer expressing the protein. Qualitatively, this expression was maintained across the monolayer at both the 10 day and 14 day time point on both surfaces suggesting that an intact, polarised monolayer had been formed.

Transepithelial Electrical Resistance

Transepithelial electrical resistance (TEER) was used to study the integrity of the tight junction formation within the monolayer, as described in section 2.2.2.6. Briefly, ARPE-19 cells were cultured on NH_3 treated ePTFE membranes and TEER measurements were conducted at each time interval: day 2, day 7, day 10 and day 14. Additionally, control membranes (NH_3 treated ePTFE membranes without cells) were used to determine the background resistance of the membranes which was then subtracted from the experimental group membranes containing cells. According to the suppliers (ATCC), ARPE-19 cells are able to reach a maximum TEER measurements of 50-100 $\Omega.cm^2$ in culture, however within the literature, measurements have been reported to be between 40 and 120 $\Omega.cm^2$ for intact monolayers depending on the culture surface [163, 167].

There was a sharp increase in the TEER of the ARPE-19 cells cultured on the NH_3 treated ePTFE membranes between day 2 and day 7. Following the increase, the TEER did continue to rise to a maximum of 59.4 ± 6.7 $\Omega.cm^2$ at day 10 however at a lower rate of increase. This is to be expected as the monolayer stabilises and the tight junctions mature. This value was maintained at day 14, when the TEER had appeared to plateau (***Figure 2-13***). These TEER values are consistent with the qualitative assessment of the presence of tight junctions within the cultures as shown by the cobblestone appearance of the cells and the positive staining indicating the expression of the protein ZO-1. Based on these results, it was decided that the cells would be cultured on the NH_3 treated ePTFE membranes for 10 days before conducting the transport studies in order to ensure the presence of an intact epithelial monolayer barrier.

Growth Curve of ARPE-19 Cells

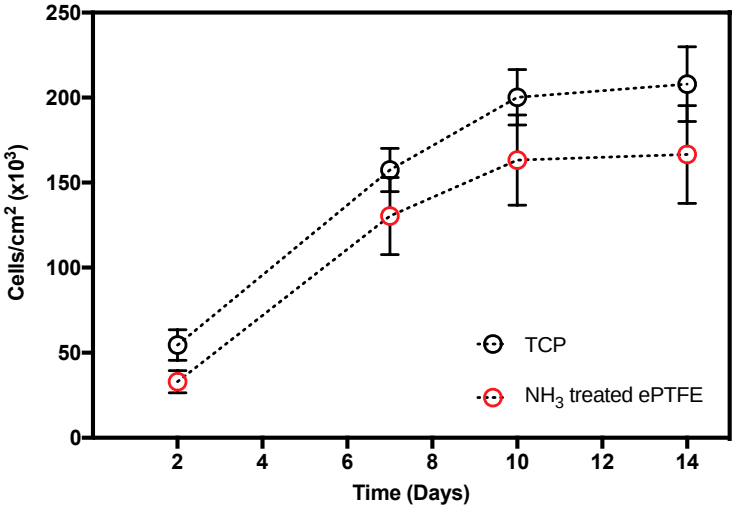

Figure 2-9: Growth curve of ARPE-19 cells on NH_3 treated ePTFE membranes vs TCP controls over 14 days in culture. Data are presented as mean cells/cm^2(x10^3) ± 1 SD, n=9.

Phase Contrast Images of ARPE-19 Cells

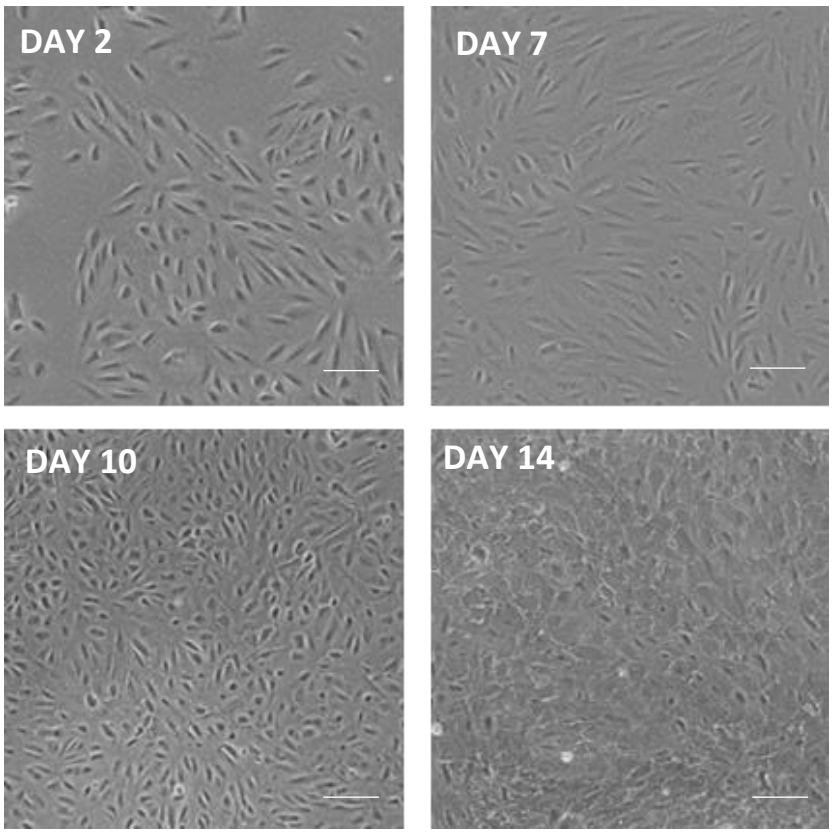

Figure 2-10: Phase contrast images of ARPE-19 cells cultured on TCP over 14 days. By day 7 in culture, cells had reached 80% confluency and by day 10 the cells had formed a complete monolayer. Scale bar = 50µm.

Expression of the Tight Junction Marker ZO-1 on TCP over 14 Days

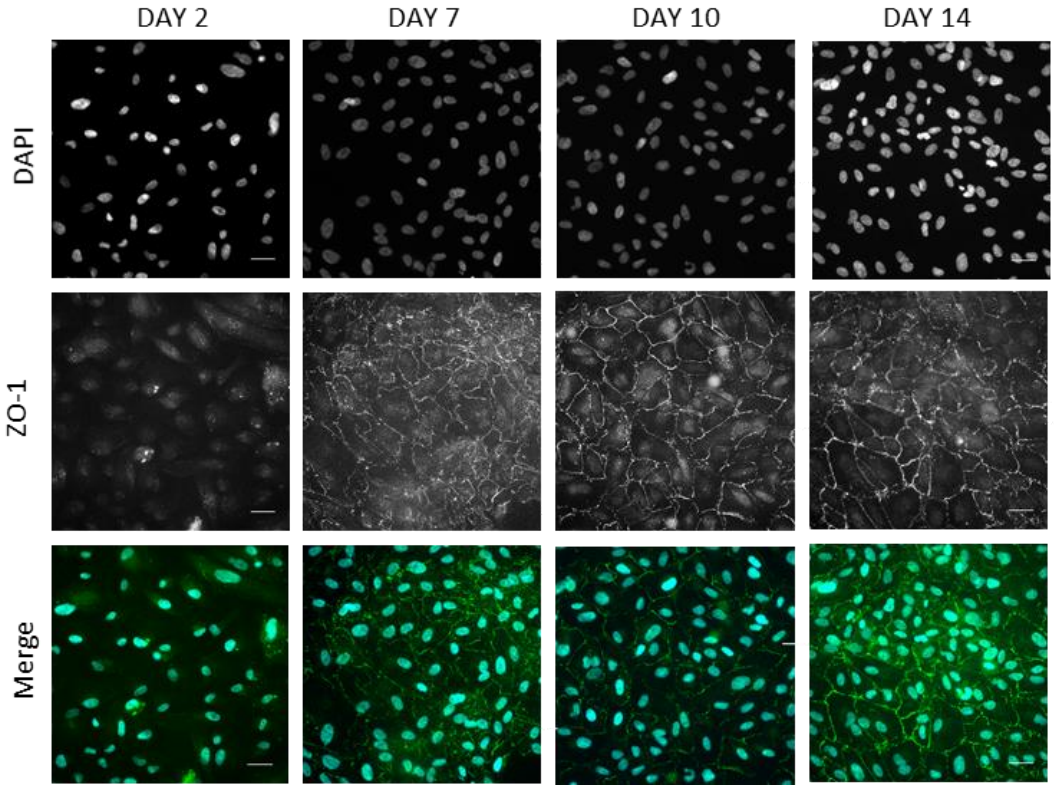

Figure 2-11: Expression of the tight junction protein, ZO-1, by ARPE-19 cells cultured on TCP over 14 days. Presence of ZO-1 was demonstrated using anti-ZO-1 staining with Alexa Fluor 488 conjugated secondary antibodies. From day 7, there is positive expression of ZO-1 at the cell borders. Scale bar = 50µm.

Expression of the Tight Junction Protein ZO-1 on NH_3 treated ePTFE over 14 Days

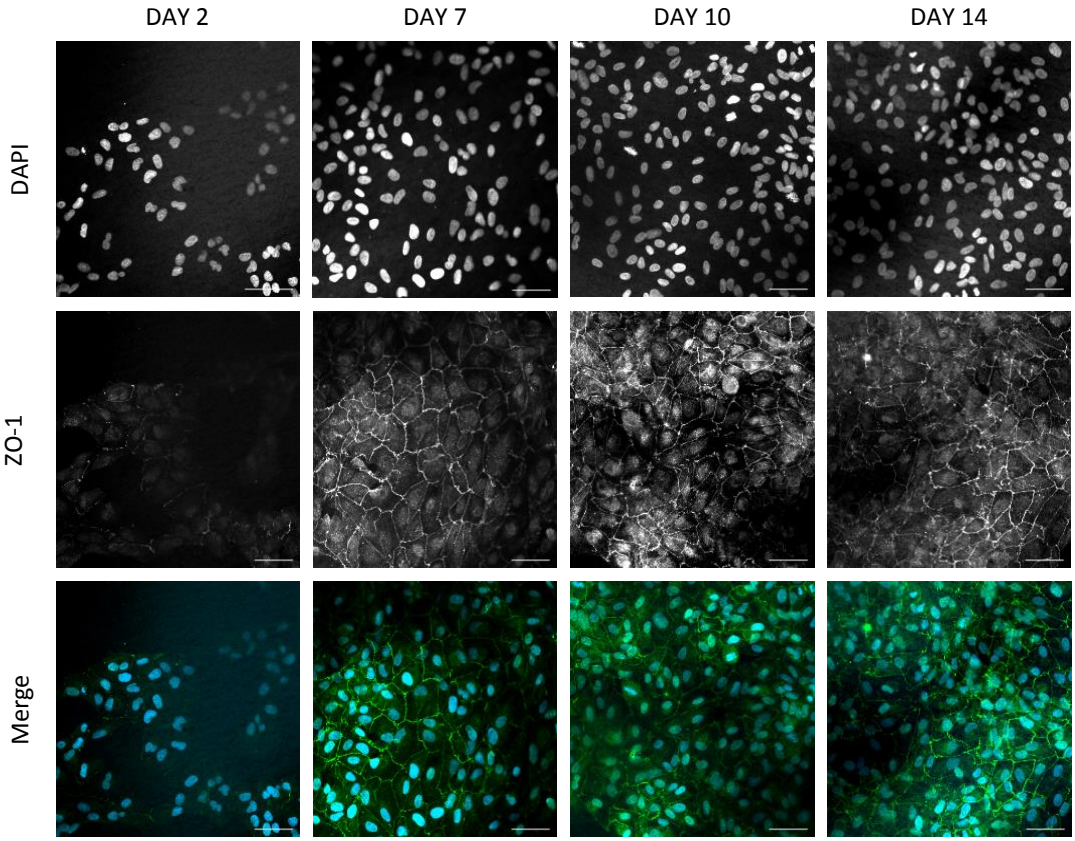

Figure 2-12: Expression of ZO-1 by ARPE-19 cells cultured on NH_3 treated ePTFE over 14 days. The presence of ZO-1 was demonstrated at the cell borders from day 7 onwards. Scale bar = 50µm.

Transepithelial Electrical Resistance of ARPE-19 Cells cultured on NH_3 treated ePTFE over 14 Days

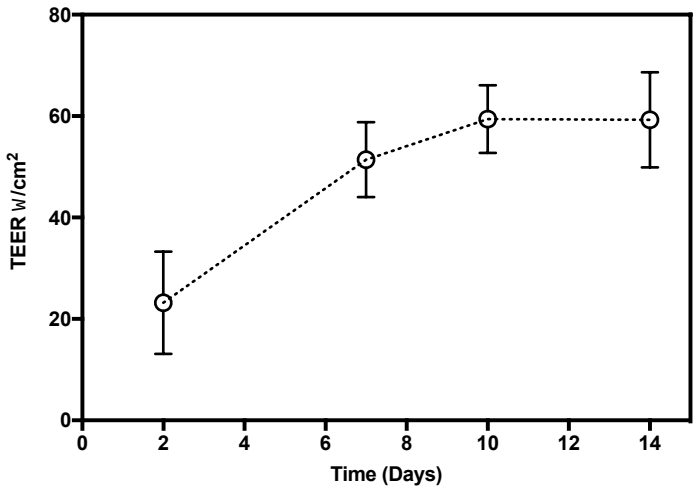

Figure 2-13: Transepithelial electrical resistance of ARPE-19 cells cultured on NH_3 treated ePTFE normalised to culture area. $\Omega.cm^2$ calculated as $\Omega.cm^2 = (\Omega_{cell} - \Omega_{control}) \times 0.6_{membrane\ area\ cm^2}$. Data presented as mean TEER ($\Omega.cm^2$) ± 1 SD, n=9.

2.2.3.2 Effects of Dynamic Flow on ARPE-19 Morphology and Function

Studies of ARPE-19 cells cultured in a dynamic flow environment are limited [168] and although the cells in the following experiments were not directly exposed to the fluid flow, it was necessary to determine their viability within this culture system prior to conducting any transport studies. Cells cultured in flow environments are exposed to shear stresses which are not observed in static cultures, therefore as the culture of ARPE-19 cells under flow is not well documented, their survival in this system is unknown. ARPE-19 cells were cultured on NH_3 treated ePTFE transwells for 10 days before being inserted into the Kirkstall QV600 cell culture chamber and set up in a recirculating perfusion system as described in section 2.2.2.7. The basolateral side of the transwells were then exposed to perfusion flow of RSC media at flow rates ranging from 20µL/min to 400µL/min for 24 hours.

As with the static cultures in the previous section, cell number, TEER and expression of the tight junction protein ZO-1 were used to assess the barrier integrity of the ARPE-19 monolayer before and after exposure to flow. Additionally, cell viability and expression of alpha-smooth muscle actin (αSMA) were evaluated to determine any detrimental effects on the monolayer caused by the presence of the flow.

Cell Number and Viability

Compared with the mean cell number obtained from the pre-flow cultures, there was no significant difference observed in either the static cultures or those cultured under flow for any flow rate. There was also no significant differences in mean cell number between those cells cultured statically for 24 hours and those exposed to flow at any of the flow rates used ($F(5, 48)=0.3877$, $p=0.85$) (***Figure 2-14***). The metabolic activity of the cells also appeared to be unaffected by their exposure to flow up to a flow rate of 200µL/min compared with their metabolic activity measured prior to the exposure. There was also no differences in metabolic activity shown between those cells cultured statically and those exposed to flow for 24 hours up to a flow rate of 200µL/min. However, the metabolic activity of the cells cultured under a flow rate of 400µL/min showed a significant decrease compared with both the static controls and the pre-flow values ($F(5, 138)=6.114$, $p<0.001$) (***Figure 2-15***). Given that there was no difference in cell number between the pre-flow and static controls and those cells exposed to 400µL/min flow, this suggests that the highest flow rate used had a negative effect on the metabolic activity of the cells.

Effect of Media Flow Rate on ARPE-19 Cell Number

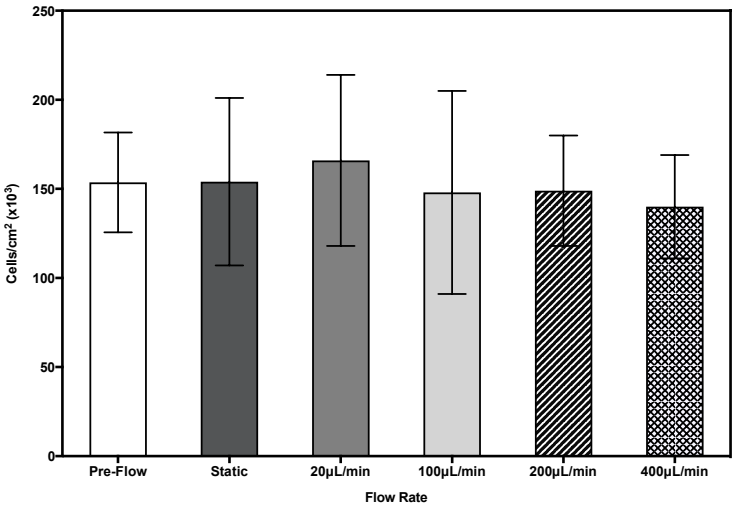

Figure 2-14: Mean cell number per cm² for ARPE-19 cells cultured on NH_3 treated ePTFE membranes prior to exposure to flow and following 24 hour exposure to different flow rates. There were no significant differences shown between any of the groups. Data presented as mean cell number/cm² ± 1 SD, n=9.

Effect of Media Flow Rate on ARPE-19 Cell Metabolic Activity

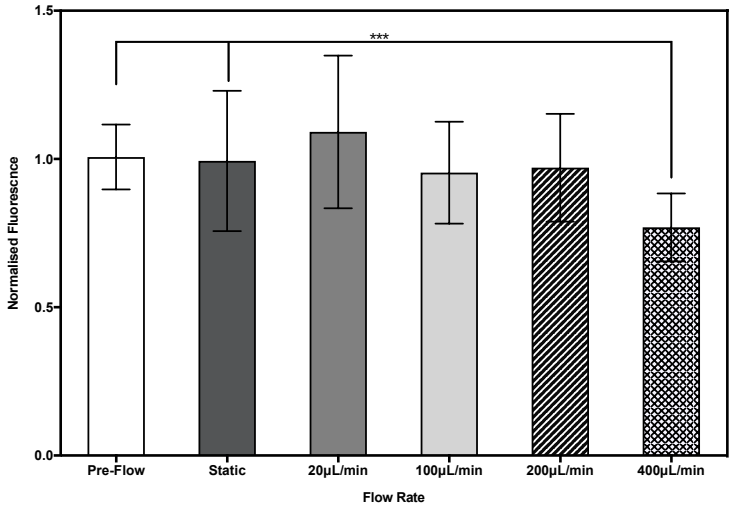

Figure 2-15: Normalised resorufin fluorescence of ARPE-19 cells cultured under different flow conditions. Values for each group are normalised to pre-flow control. Resorufin fluorescence was significantly decreased in cells cultured under 400µL/min compared with both the pre-flow fluorescence (p<0.001) and the cells grown in static conditions (p<0.001) suggesting a decrease in the metabolic activity of the cells. Data presented as mean resorufin fluorescence ± 1 SD, n=9; *** p < 0.001 (One-way ANOVA; Dunnett's post hoc test).

Expression of Tight Junction Protein ZO-1 and Mesenchymal Cell Marker αSMA

The ARPE-19 cells cultured for 10 days in RSC medium all stained positive for the tight junctional protein complex, ZO-1, at the cell-cell borders prior to their basal exposure to media flow. Following a further 24 hours in static culture, the expression of ZO-1 was maintained at the cell-cell contact points across the monolayer. This was also evident in the ARPE-19 cells which had been cultured in the Kirkstall QV600 chamber, exposed to media flow rates of 20, 100 and 200µL/min for 24 hours (***Figure 2-16***). Qualitatively, the basolateral exposure of the cells to media flow at lower flow rates has no effect on the expression of ZO-1 shown by a network of ZO-1 staining which can be seen across the whole surface area of the substrate, as was the case prior to any exposure to flow. Additionally, for the pre-flow, static, 20µL/min, 100µL/min and 200µL/min cultures, no positive staining was observed for the mesenchymal cell marker alpha-smooth muscle actin (αSMA). αSMA is widely recognised of an indication of fibrosis in ARPE-19 cells and its positive expression is used as indicator of epithelial-mesenchymal transition [169, 170]. In contrast, the ARPE-19 cells exposed to the highest flow rate of 400µL/min showed a more granulated appearance of ZO-1 expression, without clearly defined staining around the cell borders as seen in cells cultured under the other conditions. There were also clusters of cells across the monolayer which exhibited positive staining for αSMA (***Figure 2-16***).

Expression of ZO-1 and αSMA under different Flow Conditions

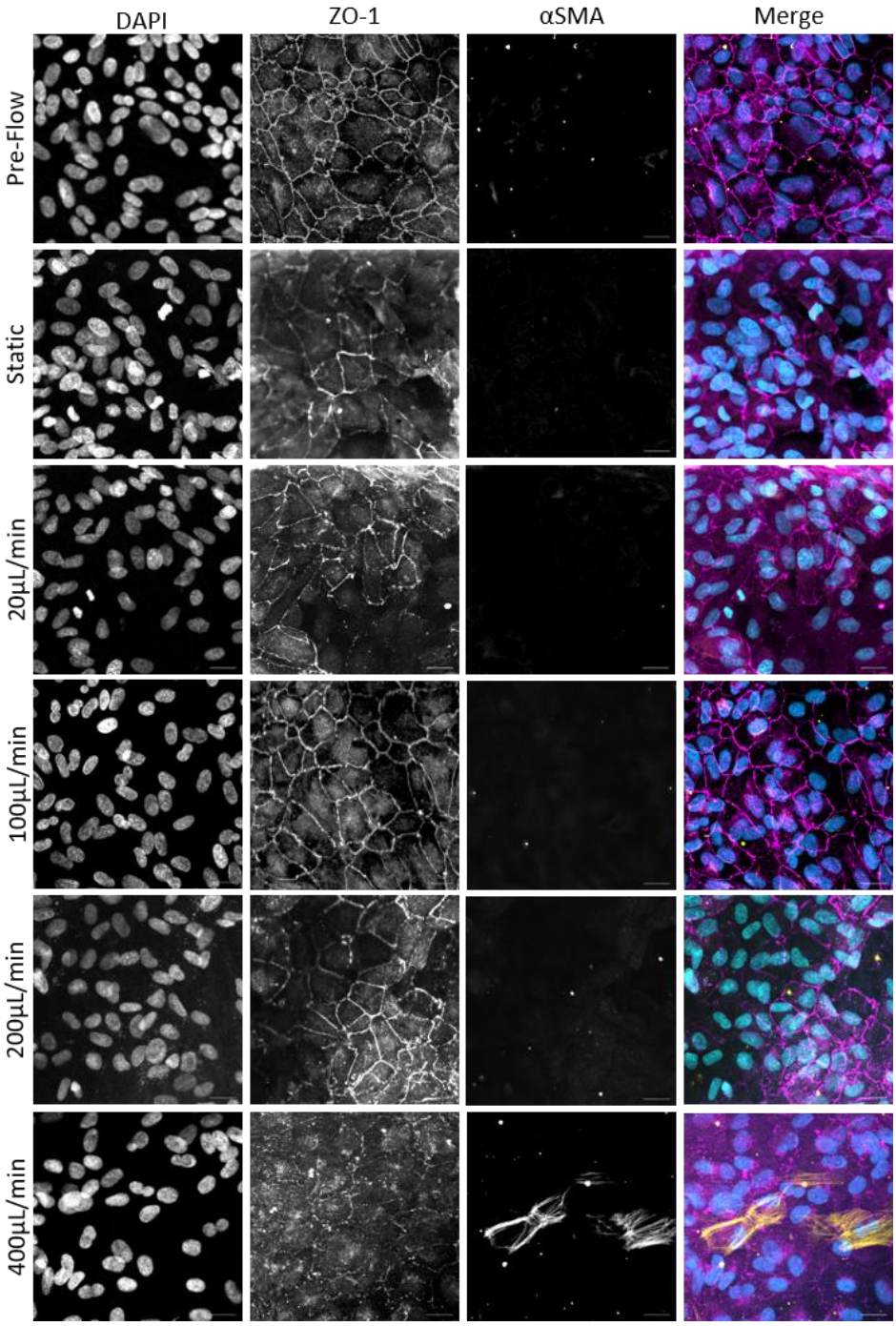

Figure 2-16: Expression of ZO-1 and αSMA in ARPE-19 cells exposed to different flow conditions for 24hrs. All cells were cultured for 10 days prior to exposure. Positive staining for ZO-1 was seen in all conditions, whereas the only positive staining for αSMA was seen in small clusters of cells exposed to 400µL/min flow. Scale bar = 20µm.

Transepithelial Electrical Resistance

Prior to the exposure of cells to flow, the mean TEER across ARPE-19 cells on all membranes was 60.3 ± 8.5 Ω.cm^2, as expected following 10 days in culture. A one-way ANOVA indicated a significant difference between the mean TEER values for different flow rates ($F(5, 54) = 23.12$, $p < 0.001$). Dunnett's post hoc test was used to analyse significance between flow rates. No significant change in TEER was observed in the cells cultured statically for a further 24 hours, in keeping with the result shown in section 2.2.4.1 which showed a plateau in TEER after day 10 in culture ($p = 0.93$). The results show that the cells exposed to static media for 24 hours had a mean TEER of 66.3 ± 8.4 Ω.cm^2. Compared with the static conditions, cells exposed to 20µl/min flow for 24 hours also showed no significant change in TEER ($p = 0.98$). For each flow rate higher than 20µL/min, there were statistically significant changes in the TEER values of the cell monolayers compared with the static controls (***Figure 2-17***)

Dunnett's post-hoc test revealed at flow rates 100µL/min and 200µL/min, results show a significant increase in TEER measurements in comparison with the static controls following 24 hour exposure (both $p < 0.001$). The cells exposed to 200µL/min flow showed the greatest increase in TEER, reaching a mean TEER of 93.0 ± 12.9 Ω.cm^2. The trend appears to be an increase in TEER with increasing flow rate, however, Dunnett's post hoc test also revealed the cells exposed to the highest flow rate of 400µl/min, showed a significant decrease ($p=0.0119$) in TEER compared with the static controls with the mean TEER value = 46.3 ± 9.5 Ω.cm^2 (***Figure 2-17***).

Comparing the TEER values for each group to their own pre-flow value, the greatest change was observed in the 200µL/min group where there was a 61.46% increase in TEER following exposure to flow. In comparison, the cells exposed to 400µL/min flow showed a 23.47% decrease in TEER compared to their pre-flow measurements. These results corroborate the qualitative observation from the immunocytochemistry images which showed less distinct positive staining for ZO-1 in the 400µL/min group, suggesting a breakdown in the intercellular junctional complexes.

Effect of Media Flow on TEER of ARPE-19 Cells cultured on NH_3 treated ePTFE Membranes

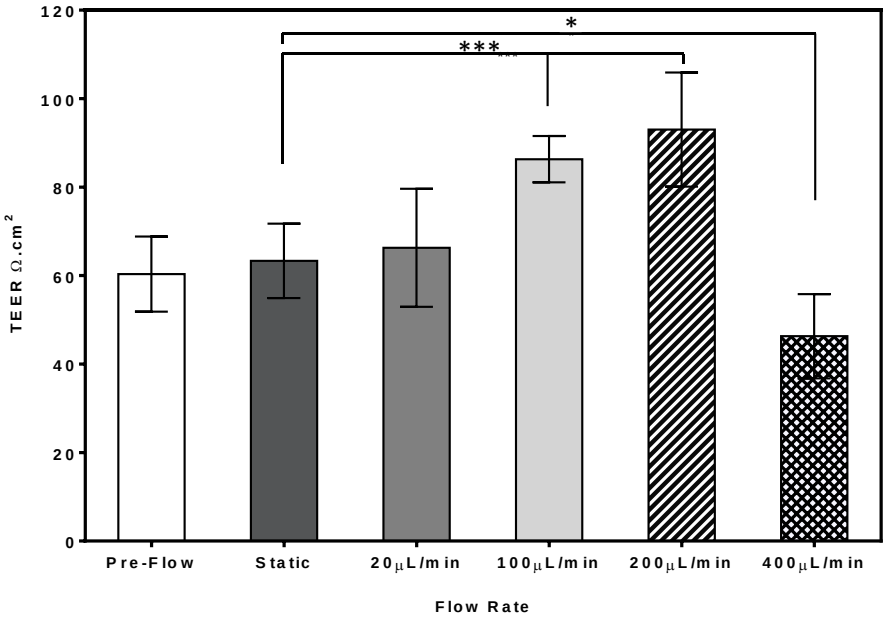

Figure 2-17: TEER values for ARPE-19 cells cultured under flow for 24hrs. All cells were cultured for 10 days prior to exposure. The 20µL/min showed no difference compared with the static control, however there was a significant increase (p<0.001) in both the 100µL/min and 200µL/min groups. The 400µL/min group showed significant decrease in TEER (p=0.0119) compared with static controls. Data presented as mean TEER Ω.cm² ± 1 SD, n=9; * p =0.0119, *** p < 0.001 (One-way ANOVA; Dunnett's post hoc test).

Changes in TEER of ARPE-19 Cells cultured under different Flow Conditions

Transepithelial Electrical Resistance Ω.cm²			
Flow Rate	Pre-flow	Post-flow	% Change
Static	58.4 ± 7.2	63.3 ± 8.4	+ 8.39
20µL/min	61.7 ± 1.9	66.3 ± 13.4	+ 7.46
100µL/min	63.5 ± 3.0	86.3 ± 5.2	+ 35.90
200µL/min	57.6 ± 4.5	93.0 ± 12.9	+ 61.46
400µL/min	60.5 ± 2.9	46.3 ± 9.5	- 23.47

Table 2-6: Changes in TEER of ARPE-19 cells following culture under different flow conditions. Values reported as mean TEER Ω.cm² ± 1 SD, n=9.

2.2.3.3 STATIC TRANSPORT OF DEXTRAN TO DETERMINE PERMEABILITY AND DIFFUSION COEFFICIENTS

NH_3 treated ePTFE membranes either seeded with ARPE-19 cells or left unseeded were used to study the transport of FITC-conjugated dextrans across the membranes. The unseeded membranes were used immediately following the sterilisation step, as described in section 2.2.2.12. The membranes seeded with ARPE-19 cells were cultured for 10 days when the monolayers were exhibiting maximum TEER values, after which the transport studies were conducted. FITC-conjugated dextran (FD) of different molecular weights were used to ascertain the diffusion and permeability coefficients of each size molecule across the membranes.

The initial concentration of FD in the donor solution on the apical side of the membrane was 50µg/mL in a volume of 400µL. Therefore the equilibrium concentration in the receptor compartment on the basal side of the membrane (volume: 600µL) was 20µg/mL. In the absence of cells, FD4 (4kDa dextran) had reached a concentration of 18.4±2.83µg/mL, 92% of the equilibrium concentration, in the receptor compartment by 8hrs and by the 24hr time point the concentration had reached 20±1.69µg/mL. FD40 also reached the equilibrium concentration by 24hrs in the absence of cells but the rate of passage was lower with the concentration in the receptor compartment only reaching 12.6±2.06µg/mL after 8hrs (fig 2-15). Similarly, FD4 and FD40 had both reached 20µg/mL at 24hrs in the presence of ARPE-19 cells, however the rate of passage was lower for both as expected (***Figure 2-18***).

Increasing the molecular weight to 70kDa, the amount of dextran transported through either the membrane or monolayer-membrane complex was decreased. In the absence of the cell monolayer, the concentration of FD70 in the receptor compartment reached a maximum of 14.98±2.6µg/mL at 24hrs, only 75% of the equilibrium concentration (***Figure 2-18***). The transport was further decreased in the presence of ARPE-19 cells with a maximum concentration of 12.12±2.58µg/mL reached at 24hrs (***Figure 2-18***).

Using the data from the curves and the equations described in section 2.2.2.12, diffusion and permeability coefficients for each molecular weight of dextran were calculated for both the unseeded and seeded membranes (***Table 2-7***, ***Table 2-8***).The highest permeability and diffusion coefficient was observed in the experiments using FD4 across the unseeded membranes with values of $1.34x10^{-5}$ cm/s and $1.23x10^{-6}$ cm^2/s. As expected, the value of both

coefficients decreases with increasing molecular weight of dextran. There is also a decrease in permeability and diffusion in the presence of the ARPE-19 monolayer.

Static Transport of Dextrans across NH_3 treated ePTFE Membranes

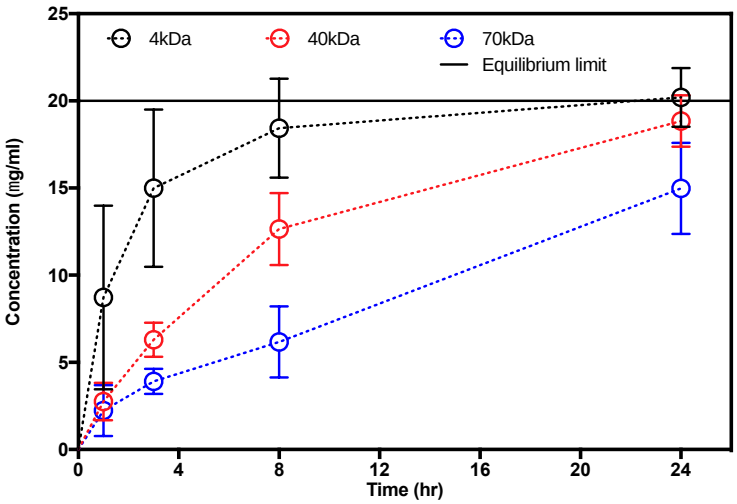

Figure 2-18: Passage of fluorescently labelled dextrans (FD) through NH_3 treated ePTFE membranes over time. Graph indicates concentration of different molecular weight FDs on basolateral side of the membrane at each time point (FD4, 4kDa, black) (FD40, 40kDa, red) (FD70, 70kDa, blue). Equilibrium limit shows maximum possible concentration of FD in basolateral compartment. n= 9.

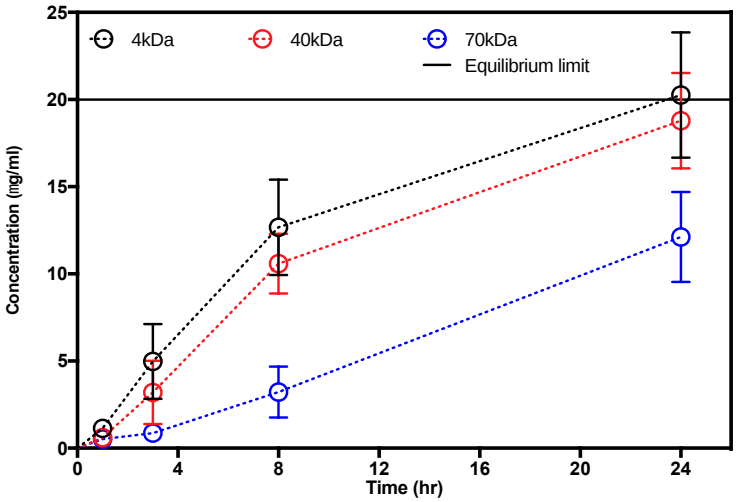

Figure 2-19: Passage of fluorescently labelled dextrans (FD) through NH3 treated ePTFE membranes, seeded with ARPE-19 cells, over time. Cells were cultured for 10 days prior to experimental use. Graph indicates concentration of different molecular weight FDs on basolateral side of the membrane at each time point (FD4, 4kDa, black) (FD40, 40kDa, red) (FD70, 70kDa, blue). Equilibrium limit shows maximum possible concentration of FD in basolateral compartment. n= 9.

Diffusion and Permeability Coefficients of Dextrans across NH_3 treated ePTFE Membranes

Molecular Weight	Diffusivity in RSC Medium (m^2/s)	Diffusion Coefficient across Barrier (m^2/s)	Permeability Coefficient of Barrier (m^2)
4kDa	$2.4x10^{-11}$	$1.22x10^{-11}$	$1.35x10^{-9}$
40kDa	$7.4x10^{-12}$	$8.90x10^{-12}$	$7.97x10^{-10}$
70kDa	$5.6x10^{-12}$	$4.89x10^{-12}$	$4.28x10^{-10}$

Table 2-7: Diffusion and permeability coefficients of different molecular weight dextrans across NH_3 treated ePTFE membranes. Coefficients calculated using data from static transport studies and the equations described in section 2.2.2.12.

Diffusion and Permeability Coefficients of Dextrans across NH_3 treated ePTFE Membranes seeded with ARPE-19 cells

Molecular Weight	Diffusivity in RSC Medium (m^2/s)	Diffusion Coefficient across Barrier (m^2/s)	Permeability Coefficient of Barrier (m^2)
4kDa	$2.4x10^{-11}$	$1.07x10^{-11}$	$8.80x10^{-10}$
40kDa	$7.4x10^{-12}$	$5.18x10^{-12}$	$5.90x10^{-10}$
70kDa	$5.6x10^{-12}$	$1.82x10^{-12}$	$2.23x10^{-10}$

Table 2-8: Diffusion and permeability coefficients of different molecular weight dextrans across NH_3 treated ePTFE membranes seeded with ARPE-19 cells. Coefficients calculated using data from static transport studies and the equations described in section 2.2.2.12.

2.2.3.4 DYNAMIC TRANSPORT AND CLEARANCE OF DEXTRAN WITHIN THE KIRKSTALL QV600 SYSTEM

Each experiment was performed using two transwells in separate perfusion systems, and this was repeated three times for each flow rate. The membranes seeded with ARPE-19 cells were exposed to basolateral flow rates of 20µL/min, 200µL/min and 400µL/min for 24 hours. The membranes without cells were exposed to the same flow rates and an additional flow rate of 2mL/min (8 hours for 2mL/min).

The initial donor concentration was equal to that of the static experiments (50µg/mL) and the measured concentration in the receptor compartment shows the mean concentration ± 1 SD in the receptor compartment at that instance in time, as the dextran is continuously cleared from the chamber by the flow.

<u>20µL/min</u>

For each molecular weight of dextran and irrespective of the presence of ARPE-19 cells, the concentration profiles for each condition exposed to 20µL/min appear to follow that of a typical single dose response (***Figure 2-20***). This is defined by a rise in concentration up to a maximum peak after which the concentration decreases with time as it is cleared away. As expected, given the diffusion and permeability coefficients, the concentration in the receptor compartment of chambers with ARPE-19 cells was lower compared with chambers absent of cells. This is reflected in the area under the curve values (AUC). The AUC value for a concentration vs time graph is an indication of the total amount of drug which has moved into the receptor compartment over the measured time. In the presence of ARPE-19 cells, the AUC was lower and the AUC decreased with increasing molecular weight of FD. The highest value for the AUC was seen with FD4 used across unseeded NH_3 treated ePTFE membranes (table 2-8), AUC = 16.63µg.hr/mL. In comparison, FD4 across NH_3 treated ePTFE membranes seeded with ARPE-19 cells 10 days prior to experimental use had an AUC 30% lower, AUC = 11.57µg.hr/mL.

The diffusion and permeability coefficients established in section 2.2.3.3 showed that as the molecular weight of FD increased, a greater difference in permeability and diffusion occurred between seeded and unseeded membranes. This was reflected in the percentage decrease in AUC. For FD40, the AUC for unseeded membranes = 15.89µg.hr/mL and for seeded membranes = 9.05µg.hr/mL, a 43% decrease (***Table 2-9***). The decrease between unseeded

and seeded membranes was greatest for FD70. The AUC for the unseeded membranes was 14.76µg.hr/mL and for the seeded membranes 6.04.µg.hr/mL, a reduction of 59%.

Peak concentration (C_{max}) was also significantly decreased in the presence of ARPE-19 cells for each molecular weight of FD ($p<0.001$ FD4, FD40) ($p=0.0013$ FD70). The fall in peak concentration was consistent across the different molecular weights, with the reduction being 32%, 33% and 35% for FD4, FD40 and FD70 respectively. As expected, the conditions which contributed to the highest C_{max} were FD4 through unseeded membranes, where the maximum concentration in the receptor compartment reached 1.72±0.15µg/mL. By comparison, FD70 through cell seeded membranes only reached a peak concentration of 0.87±0.22µg/mL.

Concentration Profiles of Fluorescently labelled Dextrans in Receptor Compartment of Kirkstall QV600 exposed to a Flow Rate of 20µL/min

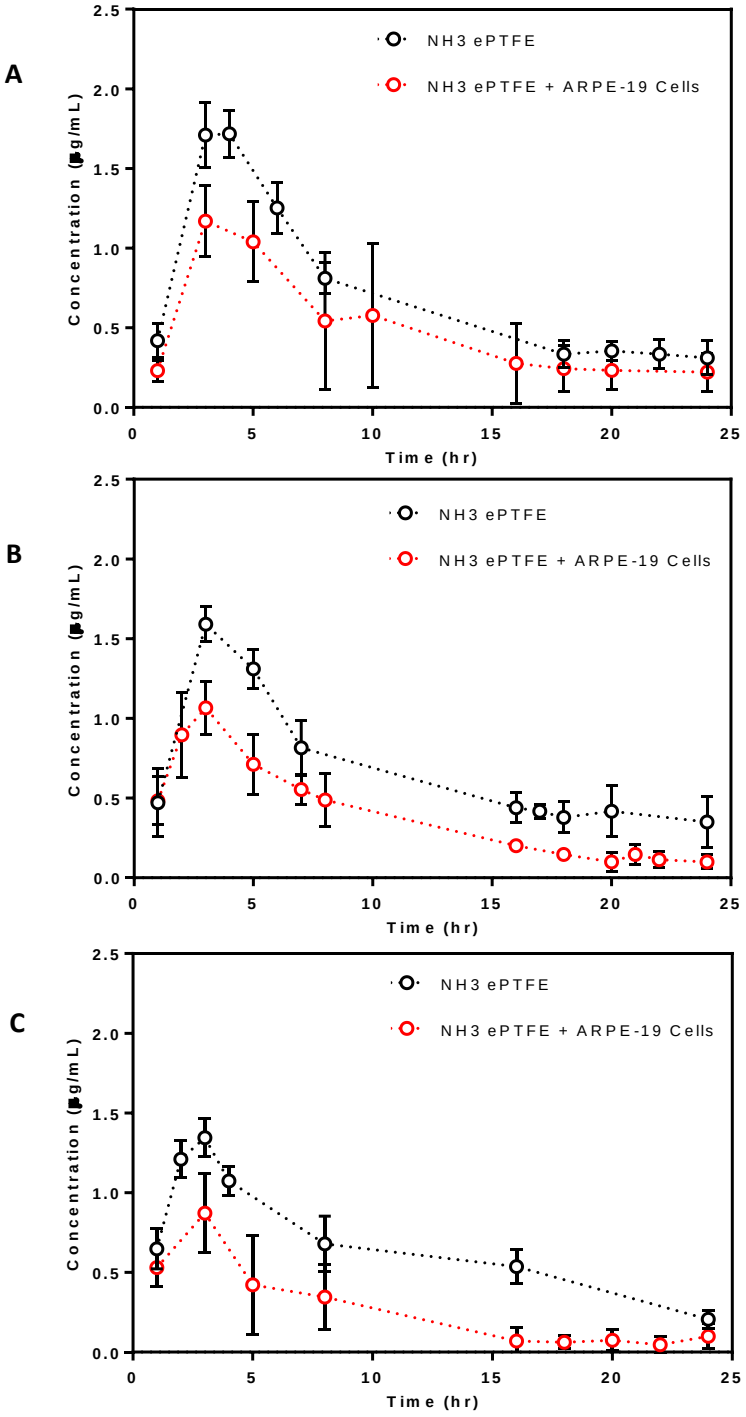

Figure 2-20: Concentration profiles of different molecular weight fluorescently labelled dextrans a) 4kDA, b) 40kDa and c) 70kDa in receptor compartment of Kirkstall QV600 chamber. Studies carried out on unseeded and seeded NH_3 treated ePTFE membranes. Experimental flow rate = 20µL/min. Data presented as mean ± 1 SD, n=6.

Concentration Curve Statistics for Dynamic Transport Studies at 20µL/min

	Area under Curve (AUC, µg.h/mL)	Peak Concentration (C_{max}, µg/mL)	Time of Peak Concentration (t_{max}, hr)	Average Concentration (C_{ave}, µg/mL)
NH_3 ePTFE	16.63	1.72±0.15	4	0.81
NH_3 ePTFE + ARPE-19 cells	11.57	1.17±0.22	3	0.50

Table 2-9: Concentration curve statistics for 4kDa fluorescently labelled dextran exposed to a flow rate of 20µL/min.

	Area under Curve (AUC, µg.h/mL)	Peak Concentration (C_{max}, µg/mL)	Time of Peak Concentration (t_{max}, hr)	Average Concentration (C_{ave}, µg/mL)
NH_3 ePTFE	15.89	1.59±0.11	3	0.69
NH_3 ePTFE + ARPE-19 cells	9.05	1.07±0.17	3	0.42

Table 2-10: Concentration curve statistics for 40kDa fluorescently labelled dextran exposed to a flow rate of 20µL/min.

	Area under Curve (AUC, µg.h/mL)	Peak Concentration (C_{max}, µg/mL)	Time of Peak Concentration (t_{max}, hr)	Average Concentration (C_{ave}, µg/mL)
NH_3 ePTFE	14.76	1.34±0.12	3	0.81
NH_3 ePTFE + ARPE-19 cells	6.04	0.87±0.25	3	0.28

Table 2-11: Concentration curve statistics for 70kDa fluorescently labelled dextran exposed to a flow rate of 20µL/min.

200µL/min

Unlike at 20µL/min, the concentration profiles of the dextran at 200µL/min show a burst release response with an exponential decay in concentration in the receptor compartment over time (***Figure 2-21***). As expected, in the presence of cells, the AUC values were much lower compared with those experiments absent of cells. The percentage decrease in AUC between the seeded and unseeded membranes followed the same trend as seen at 20µL/min, with a 28%, 48% and 52% decrease seen in FD4, FD40 and FD70 experiments respectively.

Statistically significant decreases in peak concentration (C_{max}) were seen between the seeded and unseeded membranes at 200µL/min for each molecular weight of dextran (p=0.004 FD4) (p<0.001 FD40, FD70). For FD4, C_{max}= 1.60±0.30µg/mL in the absence of cells. Comparatively, in the presence of cells C_{max} = 0.96±0.29µg/mL, a 40% decrease in peak concentration (***Table 2-12***). For the larger molecular weight dextrans, FD40 and FD70, the percentage decrease was much larger. FD40 showed a decrease of 75% from 0.81±0.12µg/mL to 0.20±0.09µg/mL and FD70 dropped from 0.13±0.02µg/mL to 0.05±0.01µg/mL, 62% (***Table 2-13***, ***Table 2-14***).

Concentration Profiles of Fluorescently labelled Dextrans in Receptor Compartment of Kirkstall QV600 exposed to a Flow Rate of 200µL/min

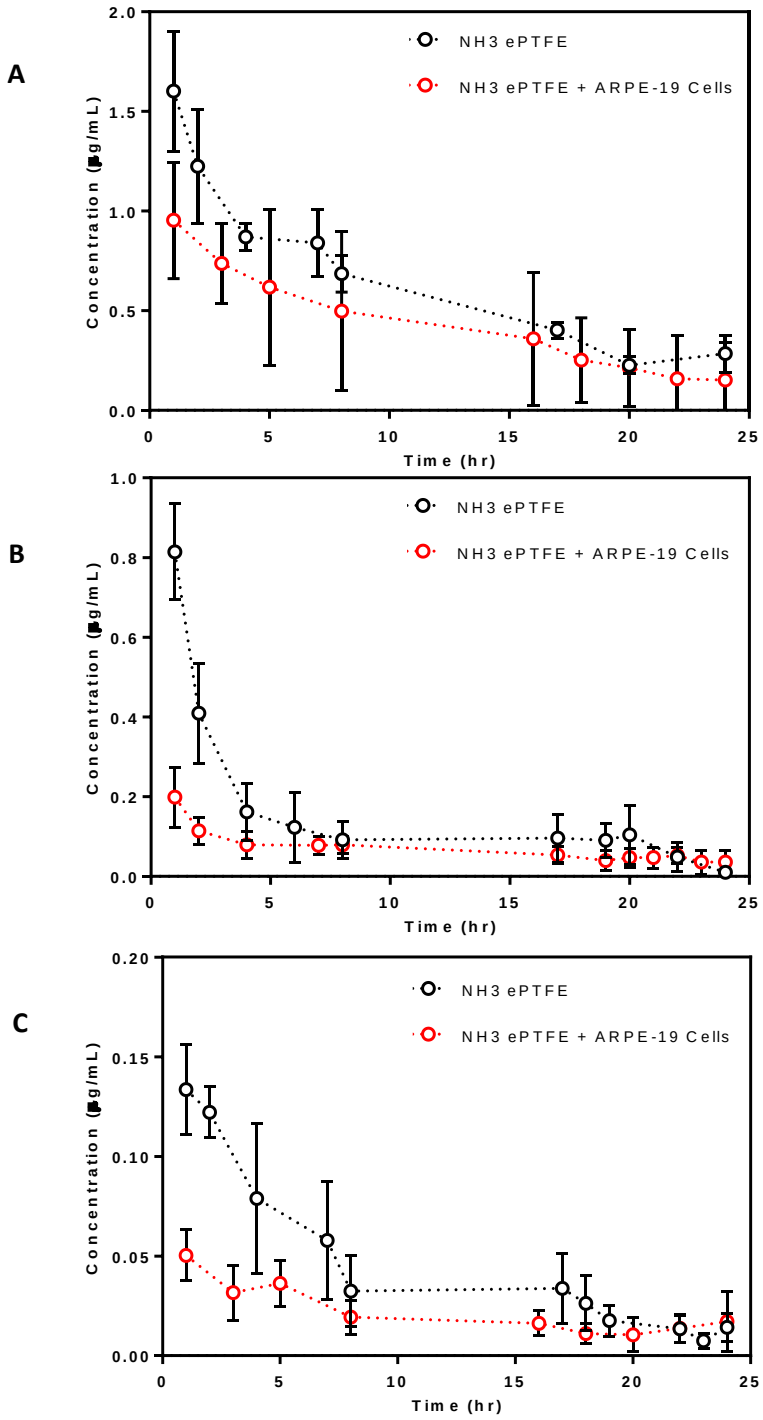

Figure 2-21: Concentration profiles of different molecular weight fluorescently labelled dextrans a) 4kDA, b) 40kDa and c) 70kDa in receptor compartment of Kirkstall QV600 chamber. Studies carried out on unseeded and seeded NH_3 treated ePTFE membranes. Experimental flow rate = 200µL/min. Data presented as mean ± 1 SD, n=6.

Concentration Curve Statistics for Dynamic Transport Studies at 200µL/min

	Area under Curve (AUC, µg.h/mL)	Peak Concentration (C_{max}, µg/mL)	Time of Peak Concentration (t_{max}, hr)	Average Concentration (C_{ave}, µg/mL)
NH_3 ePTFE	13.70	1.60±0.30	1	0.76
NH_3 ePTFE + ARPE-19 cells	9.91	0.96±0.29	1	0.43

Table 2-12: Concentration curve statistics for 4kDa fluorescently labelled dextran exposed to a flow rate of 200µL/min.

	Area under Curve (AUC, µg.h/mL)	Peak Concentration (C_{max}, µg/mL)	Time of Peak Concentration (t_{max}, hr)	Average Concentration (C_{ave}, µg/mL)
NH_3 ePTFE	3.03	0.81±0.12	1	0.20
NH_3 ePTFE + ARPE-19 cells	1.58	0.20±0.08	1	0.07

Table 2-13: Concentration curve statistics for 40kDa fluorescently labelled dextran exposed to a flow rate of 200µL/min.

	Area under Curve (AUC, µg.h/mL)	Peak Concentration (C_{max}, µg/mL)	Time of Peak Concentration (t_{max}, hr)	Average Concentration (C_{ave}, µg/mL)
NH_3 ePTFE	1.00	0.13±0.02	1	0.05
NH_3 ePTFE + ARPE-19 cells	0.48	0.05±0.01	1	0.02

Table 2-14: Concentration curve statistics for 70kDa fluorescently labelled dextran exposed to a flow rate of 200µL/min.

400µL/min

Qualitatively, the shapes of the concentration curves at 400µL/min showed little difference to those at 200µL/min, however, the differences between the seeded and unseeded membranes were not as distinct (***Figure 2-22***). FD4 was the only molecular weight to decrease in AUC for both the seeded and unseeded membranes compared to 200µL/min, with FD40 and FD70 both displaying an increase in comparison to the lower flow rate. FD40 and FD70 also showed instances where the curves for the seeded and unseeded membranes cross, indicating time points at which the passage of dextran was greater in the seeded experiments compared with the unseeded.

FD4 had shown a percentage decrease in AUC of 30% and 28% for 20µL/min and 200µL/min respectively, however, at 400µL/min the AUC for the unseeded membranes was 11.27µg.hr/mL and for the seeded membranes AUC = 11.32µg.hr/mL, an increase of 0.4% (***Table 2-15***). Similarly, there was little percentage difference between the AUC using FD40. For the unseeded membranes AUC = 6.80µg.hr/mL and for the seeded membranes AUC = 6.78µg.hr/mL, a decrease of 0.29% (***Table 2-16***). Only FD70 showed a percentage decrease comparable to the lower flow rates with the AUC dropping 54% from 2.42µg.hr/mL unseeded to 1.11µg.hr/mL seeded.

FD4 also showed an increased C_{max} in the presence of cells compared with the unseeded membranes. At 400µL/min, the highest observed C_{max} was FD4 through seeded membranes, C_{max} = 1.81±0.25µg/mL, a 7.7% increase on the peak concentration observed in the unseeded membranes, C_{max} = 1.68±0.4µg/mL although this difference was not deemed statistically significant. FD40 and FD70 showed differences in peak concentration similar to those seen at 20µL/min although the values were lower in comparison to the lowest flow rate, however, only FD70 showed a significant ($p<0.001$) decrease in C_{max} from 0.19±0.02µg/mL to 0.12±0.02µg/mL.

Concentration Profiles of Fluorescently labelled Dextrans in Receptor Compartment of Kirkstall QV600 exposed to a Flow Rate of 400µL/min

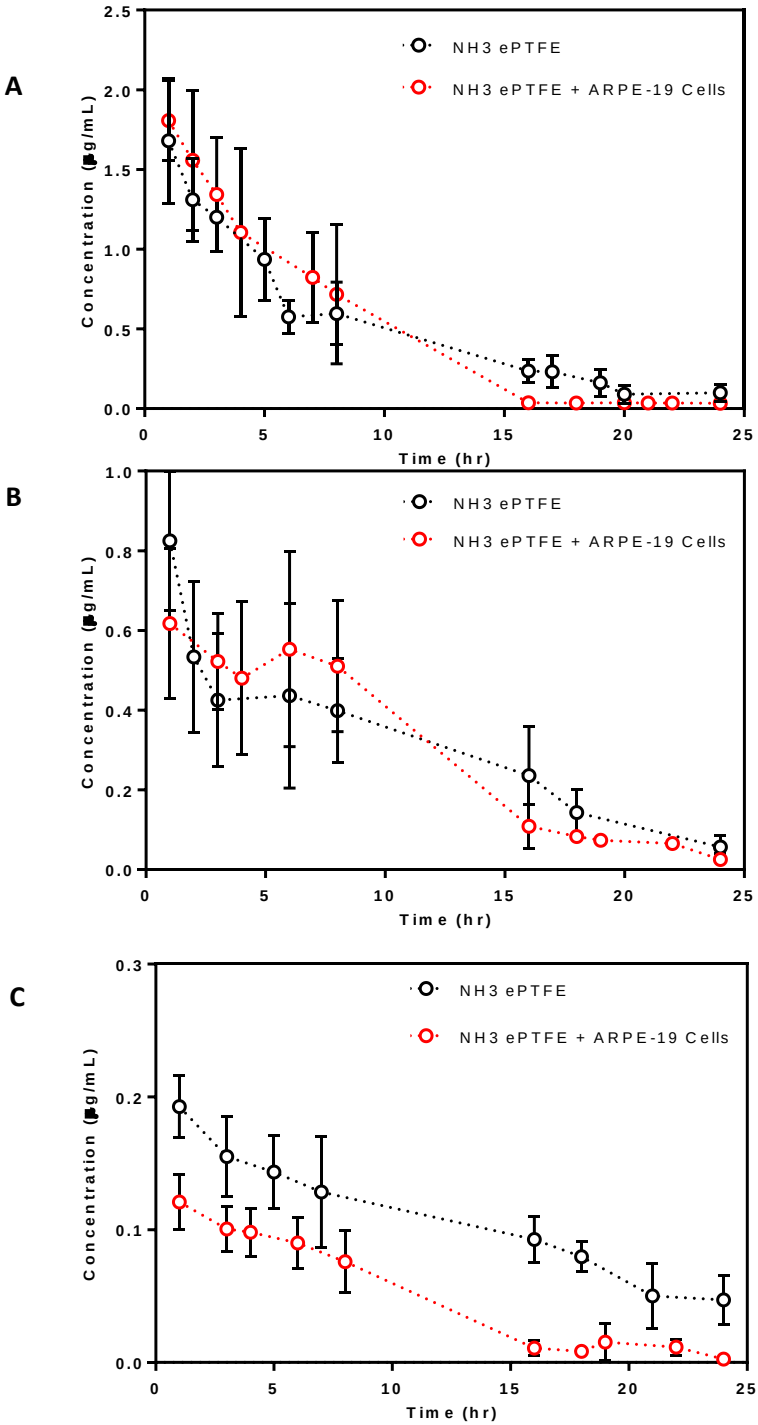

Figure 2-22: Concentration profiles of different molecular weight fluorescently labelled dextrans a) 4kDA, b) 40kDa and c) 70kDa in receptor compartment of Kirkstall QV600 chamber. Studies carried out on unseeded and seeded NH_3 treated ePTFE membranes. Experimental flow rate = 400µL/min. Data presented as mean ± 1 SD, n=6.

Concentration Curve Statistics for Dynamic Transport Studies at 400µL/min

	Area under Curve (AUC, µg.h/mL)	Peak Concentration (C_{max}, µg/mL)	Time of Peak Concentration (t_{max}, hr)	Average Concentration (C_{ave}, µg/mL)
NH_3 ePTFE	11.27	1.68±0.40	1	0.65
NH_3 ePTFE + ARPE-19 cells	11.32	1.81±0.25	1	0.63

Table 2-15: Concentration curve statistics for 4kDa fluorescently labelled dextran exposed to a flow rate of 400µL/min.

	Area under Curve (AUC, µg.h/mL)	Peak Concentration (C_{max}, µg/mL)	Time of Peak Concentration (t_{max}, hr)	Average Concentration (C_{ave}, µg/mL)
NH_3 ePTFE	6.80	0.82±0.18	1	0.38
NH_3 ePTFE + ARPE-19 cells	6.78	0.62±0.19	1	0.30

Table 2-16: Concentration curve statistics for 40kDa fluorescently labelled dextran exposed to a flow rate of 400µL/min.

	Area under Curve (AUC, µg.h/mL)	Peak Concentration (C_{max}, µg/mL)	Time of Peak Concentration (t_{max}, hr)	Average Concentration (C_{ave}, µg/mL)
NH_3 ePTFE	2.42	0.19±0.02	1	0.11
NH_3 ePTFE + ARPE-19 cells	1.11	0.12±0.02	1	0.05

Table 2-17: Concentration curve statistics for 70kDa fluorescently labelled dextran exposed to a flow rate of 400µL/min.

2mL/min

The results from section 2.2.3.2 show detrimental effects on the ARPE-19 cells exposed to the highest flow rate of 400µL/min, therefore only unseeded NH_3 treated ePTFE membranes were used in the 2mL/min studies. Also, the increased risk of leakage and lack of appropriate media reservoirs meant that the 2mL/min experiments could only be conducted over 8 hours as opposed to 24 hours. This shorter time frame however, still allows the observation of the initial passage characteristics of the dextran particles to be observed. The peak and average concentrations observed in the receptor compartment were greatly reduced for each of the molecular weights compared with the lower flow rates. This is reflected in the AUC of each. As expected, the AUC and C_{max} decreased with increasing molecular weight (***Table 2-18***, ***Table 2-19***, ***Table 2-20***) and qualitatively the curves became flatter as the molecular weight increased suggesting a shift from burst release to steady release across the membrane (***Figure 2-22***)

Concentration Profiles of Fluorescently labelled Dextrans in Receptor Compartment of Kirkstall QV600 exposed to a Flow Rate of 2mL/min

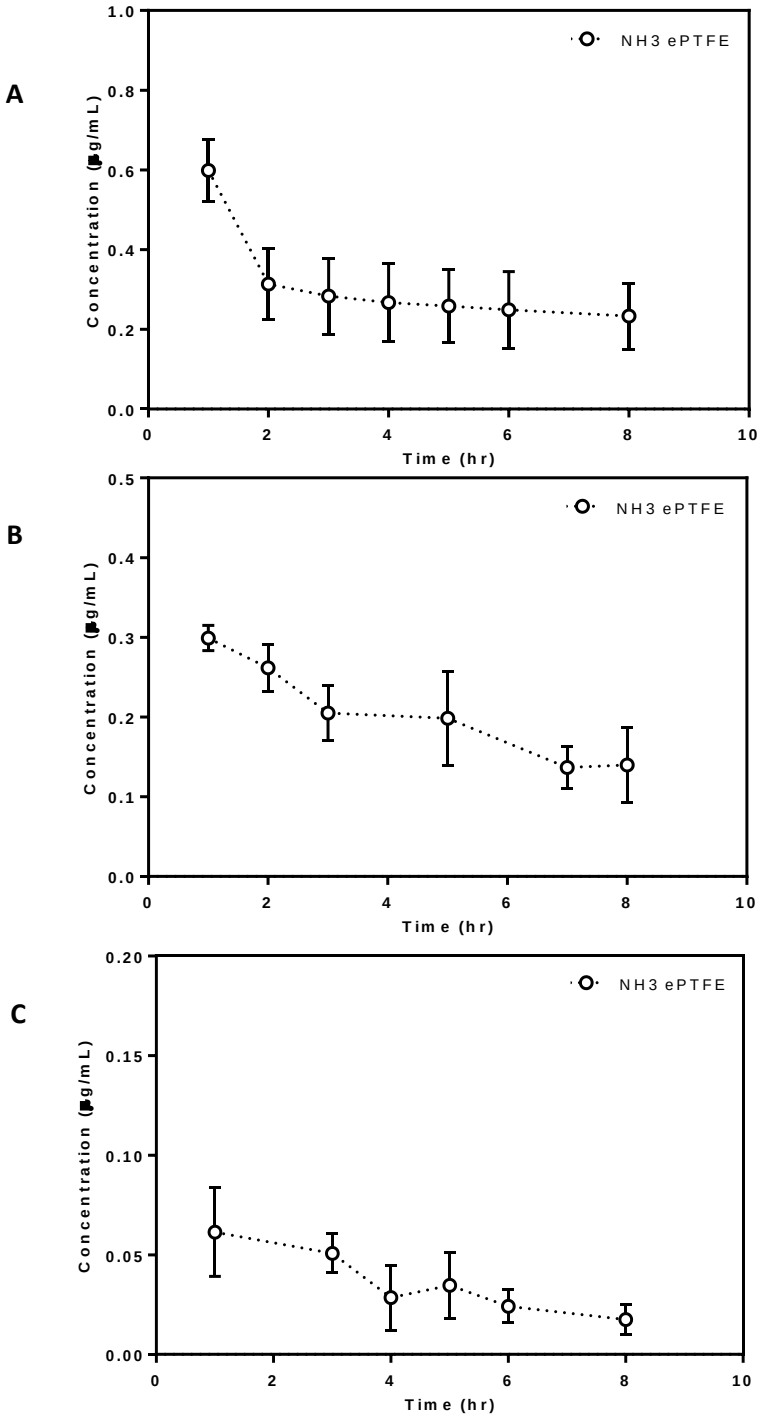

Figure 2-23: Concentration profiles of different molecular weight fluorescently labelled dextrans a) 4kDA, b) 40kDa and c) 70kDa in receptor compartment of Kirkstall QV600 chamber. Studies carried out on unseeded NH_3 treated ePTFE membranes. Experimental flow rate = 2mL/min. Data presented as mean ± 1 SD, n=6.

Concentration Curve Statistics for Dynamic Transport Studies at 2mL/min

	Area under Curve (AUC, µg.h/mL)	Peak Concentration (C_{max}, µg/mL)	Time of Peak Concentration (t_{max}, hr)	Average Concentration (C_{ave}, µg/mL)
NH_3 ePTFE	2.03	0.60±0.08	1	0.31

Table 2-18: Concentration curve statistics for 4kDa fluorescently labelled dextran exposed to a flow rate of 2mL/min.

	Area under Curve (AUC, µg.h/mL)	Peak Concentration (C_{max}, µg/mL)	Time of Peak Concentration (t_{max}, hr)	Average Concentration (C_{ave}, µg/mL)
NH_3 ePTFE	1.39	0.30±0.02	1	0.21

Table 2-19: Concentration curve statistics for 40kDa fluorescently labelled dextran exposed to a flow rate of 2mL/min.

	Area under Curve (AUC, µg.h/mL)	Peak Concentration (C_{max}, µg/mL)	Time of Peak Concentration (t_{max}, hr)	Average Concentration (C_{ave}, µg/mL)
NH_3 ePTFE	0.25	0.06±0.02	1	0.04

Table 2-20: Concentration curve statistics for 70kDa fluorescently labelled dextran exposed to a flow rate of 2mL/min.

2.2.3.5 RELEASE OF IBUPROFEN FROM SILICONE OIL UNDER STATIC CONDITIONS

The abundance of proteins within culture medium can cause interference in the UV-Vis absorbance spectrum of ibuprofen, therefore measurement of concentration in such samples is unachievable via this method. Other methods of measuring the concentration in culture medium are available, such as radio-labelling of the ibuprofen and quantifying using a scintillation counter, however such methods were outside the scope of this project. Ibuprofen release was, therefore, measured into PBS instead. The release of ibuprofen (ibu) from SiO was investigated with PBS being replenished every 24 hours or left standing over 3 days. Percentage cumulative release was used to allow comparison between the two conditions. The effect of interfacial contact area between the aqueous PBS phase and the ibu-SiO was also investigated by using equal volumes of both in different size well plates (1mL ibu-SiO), 500µL PBS.

Ignoring meniscus formation caused by surface tension between the two phases, the interfacial contact area of the ibu-SiO and PBS in a 12-, 24- and 48-well plate = 3.85, 1.91 and 0.95cm^2 respectively. This reduction in contact area was reflected in the cumulative release of ibu over 72 hours. In the first 24 hours there was a burst release of ibu observed in each of the well plates with the initial release being greater as the contact area increased. In the 12-well plate, 58.1±3.82% of the ibu was released after 24 hours compared with just 32.0±4.58% in the 48-well plate. There were negligible differences observed between the continuous and replenished conditions after 24 hours, these effects were more apparent over time (***Figure 2-24***).

After 72 hours, 98.5±3.68% of the ibu was released from the oil in a 12-well plate when the PBS was replenished every 24 hours, compared with 84.0±5.52% in the samples where the PBS was unchanged. Similar differences were seen in the 24-well plates however the cumulative release was lower in both conditions by comparison. Only 82.0±5.25% ibu was released from the SiO after 72 hours when the PBS was replenished; this was further reduced to 71.5±5.70% when the PBS was unchanged. The lowest cumulative release was seen in the 48-well plates however the difference between the replenished and continuous conditions was not as great. Following 72 hours, 57.7±2.58% of ibu was released when the PBS was replenished and 52.4±2.175 was released when the PBS was left to stand but in both conditions, the cumulative percentage released after 72 hours was still lower than that released in the 12-well plate after 24 hours (***Figure 2-24***).

Continuous Release vs Replenished Release Profiles of Ibuprofen from Silicone Oil 1000 with different Interfacial Contact Areas

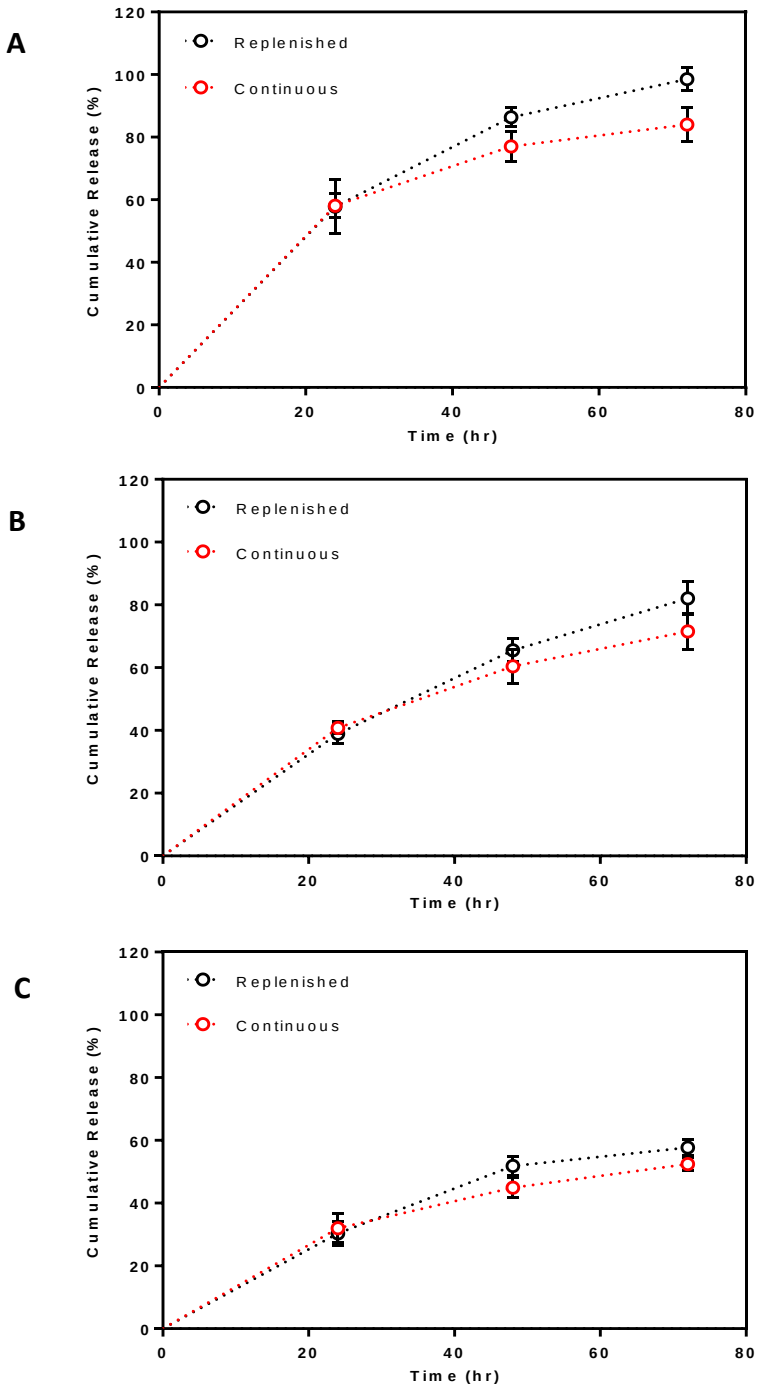

Figure 2-24: Release profiles of ibu from SiO in different size well plates (a) 12-well, (b) 24-well, (c) 48-well. Release presented as cumulative percentage release of ibu into PBS over time for PBS replenished every 24 hrs (black) and left to continuously stand (red). Data presented as mean ± 1 SD, n=9.

2.2.3.6 RELEASE AND TRANSPORT OF IBUPROFEN FROM SILICONE OIL UNDER FLUID FLOW

As with the static release experiments, ibu-SiO was in direct contact with PBS. Fresh PBS was continuously perfused through the system at different flow rates and the concentration of ibuprofen released into the PBS was measured. The differences in receptor compartment concentration profile (***Figure 2-25***) seen for ibu-SiO exposed to varying flow rates were similar to that seen in the dynamic transport of fluorescently labelled dextran in section 2.2.3.4 with a different response seen at 20µL/min compared to the higher flow rates.

At the lowest flow rate, 20µL/min, the concentration in the compartment rose to a peak over the first 8 hours after which there was a small drop in concentration by 16 hours followed by a plateau up to 24 hours. The higher flow rates however, showed an initial spike in concentration after 1 hour, followed by a steep elimination phase over the following 23 hours. Peak concentration was highest after 1 hour at 200µL/min, C_{max} = 0.162±0.04µg/mL compared with 0.128±0.02µg/mL and 0.004±0.0004µg/mL for 20µL/min and 2mL/min respectively.

Concentration Profiles of Ibuprofen released from Silicone Oil into Receptor Compartment of Kirkstall QV600 exposed to different Flow Rates

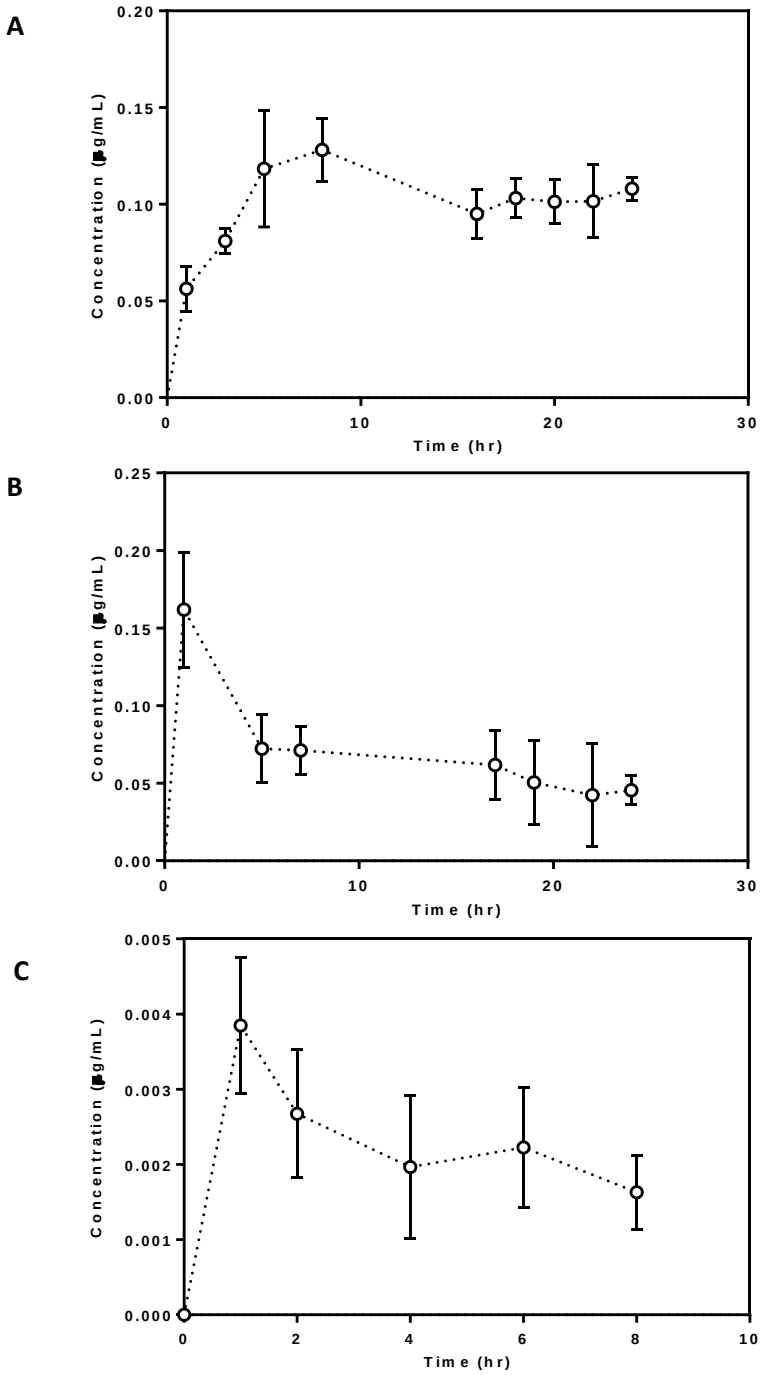

Figure 2-25: Concentration profiles of ibuprofen released from Silicone Oil into receptor compartment of Kirkstall QV600 chamber exposed to flow rates (a) 20µL/min, (b) 200µL/min and (c) 2mL/min. Data presented as mean ± 1 SD, n=6.

Concentration Curve Statistics for Dynamic Release of Ibuprofen

Flow Rate	Area under Curve (AUC, µg.h/mL)	Peak Concentration (C_{max}, µg/mL)	Time of Peak Concentration (t_{max}, hr)	Average Concentration (C_{ave}, µg/mL)
20µL/min	2.41	0.13±0.02	8	0.10
200µL/min	1.62	0.16±0.04	1	0.07
2mL/min	0.02	0.004±0.0004	1	0.002

Figure 2-26: Concentration curve statistics for ibuprofen released from Silicone Oil exposed to flow rates of 20µL/min, 200µL/min and 2mL/min.

2.3 COMPUTATIONAL MODEL OF OUTER BLOOD RETINAL BARRIER

All of the computational analysis in this study was conducted using COMSOL Multiphysics software. COMSOL is a computational fluid dynamics software package which uses finite element analysis to calculate complex fluid flow solutions. As discussed in section 1, the finite element analysis method can crudely be described as a three phase process: (1) *pre-processing*, where the subject geometry is divided into a discrete mesh of finite elements with defined material properties and boundary conditions and allows mathematical analysis of each element individually, (2) *Solution,* where the program uses a matrix of partially differentiated equations defined by the model to solve for defined values and (3) *Post-processing,* where the user is able to extract and evaluate the solved quantities and uses various techniques to examine the validity of the model.

Utilising the permeability and diffusion coefficients determined from the data compiled in section 2.2, representative computational models of the transport and release experiments for both the dextran and ibuprofen were able to be built using the COMSOL software. By building a model using experimentally derived data and boundary conditions it is possible to predict and optimise the conditions of the drug release studies which will ultimately provide a more time and cost effective method for the development of the novel silicone oil tamponade drug delivery method.

2.3.1 METHODS

2.3.1.1 PHYSICAL AND MATHEMATICAL DESCRIPTION OF MODEL USED FOR DEXTRAN TRANSPORT STUDIES

The model built was based on a two-dimensional (2D) projection of the Kirkstall QV600 cell culture chamber using COMSOL Multiphysics finite element analysis software. Using the schematic diagrams provided by Kirkstall Ltd, the input geometry was built within the software (***Figure 2-27***).

The model itself consists of two parts. One part uses the laminar flow interface to compute the velocity flow and pressure fields of the single-phase fluid flow that occurs across the QV600 chamber. The second part uses the transport of diluted species interface which is able to calculate the concentration field of a dilute solute in a solvent, i.e. the fluorescently labelled dextrans diluted in culture medium. These two physics interfaces were applied across the three domains defined in the geometry: the donor compartment, the ePTFE membrane or ePTFE membrane/ARPE-19 cell complex, and the receptor compartment (***Figure 2-27***). The model was run to simulate both the absence and presence of cells using alterations in both the geometry and permeability boundary conditions that will be described in later sections.

Modelling Laminar Flow

Fluid flow can only be described as laminar if a parameter known as the Reynolds number remains below a critical value [171]. Above this critical value, disturbances in the flow occur which leads to turbulent flow patterns. The Reynolds number can be defined as the ratio of viscous forces and inertial forces within a fluid which is subjected to bounding surface forces, such as flowing through a pipe. Mathematically it can be defined as:

$$Re = \frac{\rho u L}{\mu}$$

Equation 2-5: Reynolds number

where ρ is the density of the fluid, u is the velocity of the fluid, L is a linear dimension (i.e. diameter of a pipe) and μ is the viscosity of the fluid. Although it is dependent on the model, it is generally accepted that the critical Reynolds number for flow through a pipe ≤ 2000 is appropriate for most applications [172].

The viscosity and density of the culture medium used in the model were measured experimentally (2.3.2.1) and found to be 0.754mPa.s and 0.955kg/m^3 respectively. When applied to equation 2-5 for each flow rate used in the model, the critical value for Reynolds number was not exceeded, making a laminar flow physics interface appropriate for this model.

The equations solved for by the laminar flow are the Navier-Stokes equations for the conservation of momentum and the continuity equation for conservation of mass. These are described in section 1.7.2.

An additional physics node was included in modelling the transport of FD through the membrane into basolateral medium flow. Including fluid and matrix properties incorporates the Brinkman equations which define the behaviour of a fluid moving through a porous matrix, in this case the ePTFE membrane [173]. Similar to the Navier-Stokes equation for momentum, this particular model take into account the dissipation of kinetic energy experienced by the fluid moving through a porous matrix, through means of viscous shear. Including these additional equations allows the movement of the fluid on the apical side of the membrane to influence the distribution of the FD in that domain. This node was only applicable to the membrane part of the model and were therefore only applied to that domain.

Geometry input for Kirkstall Dextran Experiments

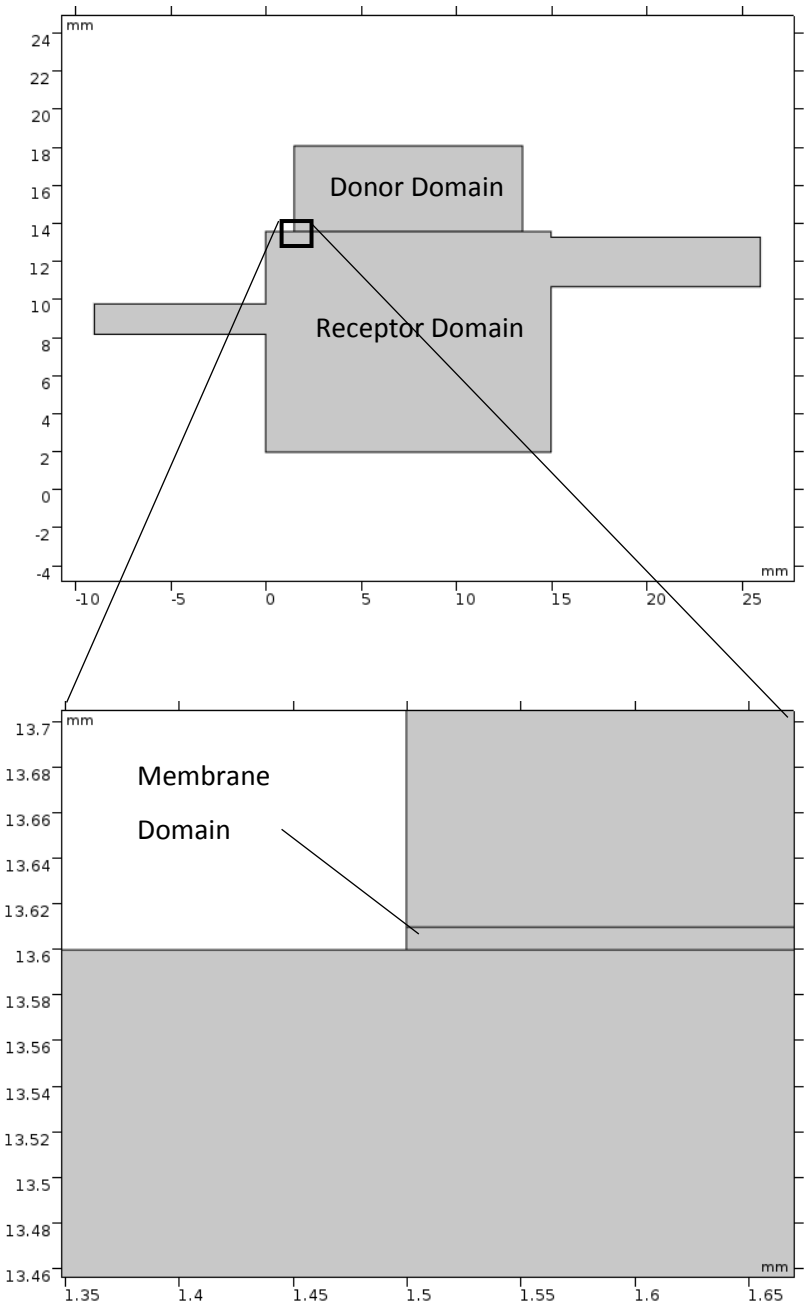

Figure 2-27: Input geometry for Kirkstall QV600 dextran simulations.

Modelling Transport of Diluted Species

The transport of diluted species physics node solves for the concentration field of a diluted solute within a solvent. This includes movement of the species via diffusion using Fick's Law, as well as transport via convection in the fluid flow field. The diluted species node assumes that the concentration of the solvent is more than 90mol% of the solution and that the presence of the solute has no impact on the density and viscosity of the solvent, making it an appropriate selection for this model.

The model implements a diffusion equation:

$$\frac{\partial c_i}{\partial t} + \nabla.(-D\nabla c_i) + \boldsymbol{u}.\nabla c_i = R_i$$

Equation 2-6: Diffusion equation for transport of diluted species.

This equation models diffusion and convection and solves the mass conservation equation for one or more chemical species c_i. D is the diffusion coefficient which is based on the molecular size of the chemical species and can be calculated theoretically, **u** is the velocity vector and R_i is the reaction rate expression which in the case of this study is a sink condition. The details of this equation were discussed in section 1.7.2.

2.3.1.2 Input Parameters for Dextran Transport Studies

The majority of the input parameters required for the model were defined by the experimental conditions described in the *in vitro* experiments; these are outlined in ***Table 2-21***. Parameters were either experimentally defined or had been determined by the experiments carried out in section 2.2, for example the diffusion coefficients and permeability coefficients which were deduced from the static transport experiments.

Input Parameters for Kirkstall QV600 Dextran Transport Simulations

Parameter	Value
Diffusion coefficient of FD in RSC medium (4kDa, 40kDa, 70kDa)	2.39 x10^{-11}, 0.74 x10^{-11}, 0.56 x10^{-11} m^2/s
Diffusion coefficient of FD across ePTFE (4kDa, 40kDa, 70kDa)	1.2x10^{-6}, 8.9x10^{-8}, 4.9x10^{-8} m^2/s
Diffusion coefficient of FD across ePTFE ARPE-19 complex (4kDa, 40kDa, 70kDa)	1.1x10^{-7}, 5.2x10^{-8}, 1.8x10^{-8} m^2/s
Initial concentration of FD in donor domain	50 µg/mL
Initial concentration of FD in membrane domain	0 µg/mL
Initial concentration of FD in receptor domain	0 µg/mL
Flow rate	20,200,400,2000 µL/min
Permeability coefficient of ePTFE (4kDa, 40kDa, 70kDa)	1.4x10^{-5}, 8.0x10^{-6}, 4.3x10^{-6} cm/s
Permeability coefficient of ePTFE ARPE-19 complex (4kDa, 40kDa, 70kDa)	8.8x10^{-6}, 5.9x10^{-6}, 2.2x10^{-6} cm/s
Porosity of ePTFE membrane	0.3
Density of RSC medium at 37°C	994.12 kg/m^3
Dynamic viscosity of RSC medium at 37°C	0.636 mPa.s

Table 2-21: Input parameters for Kirkstall QV600 dextran transport simulations.

2.3.1.2.1 Rheology

The viscosity and density of RSC medium were unknown parameters which had to be experimentally derived. The dynamic viscosity of a range of fluids including RSC medium, were measured using a TA Instruments Rheolyst AR 1000N controlled-stress rheometer (TA Instruments, UK) and concentric cylinder geometry. The viscosity of each fluid was determined from the gradient of a shear stress versus shear strain plot. All viscosity measurements with this rheometer were conducted at 21°C. Due to unavailability of the equipment, repeats of the measurements at 37°C were unable to be obtained using the TA Instruments rheometer, therefore these measurements were conducted using a Rheosense Inc µVISC rheometer (Rheosense Inc., USA) with a 100N load cell. The 21°C viscosities were also measured with the Rheosense Inc µVISC rheometer to ensure consistency between the equipment. The rheometer provides a value for the viscosity as opposed to the TA Instruments machine which provides the shear stress of the fluid over a range of shear rates. All measurements were conducted in triplicate and the results are presented as the mean viscosity ± 1 SD.

A handheld density meter (Anton Parr) was used to measure the density of the fluids at both 21°C and 37°C. The fluids were heated to the relevant temperatures in a water bath and samples of each were measured using the density meter. The measurements were repeated in triplicate and the results are presented as mean ± 1 SD.

2.3.1.3 Boundary Conditions for Dextran Transport Studies

Laminar Flow

A no slip boundary condition was applied to the walls of the geometry (***Figure 2-28***); this is the default boundary condition in modelling solid walls and means the velocity of the fluid in relationship to the velocity of the wall is zero [174]. In this case, the adhesion forces at the wall are stronger than the fluid's cohesion forces. Hence, in terms of a stationary wall, as is the case for the walls of the QV600 chamber, **u** = 0.

The inlet was applied to the left-hand wall of the inlet tube of the QV600 chamber (***Figure 2-30***). A range of inlet flow rates was investigated to coincide with the flow rates used in the *in vitro* experiments: 20µL/min, 200µL/min, 400µL/min, and 2mL/min. The outlet was applied to the right-hand wall of the outlet tube of the chamber (***Figure 2-29***). The outlet

condition was a pressure condition defined as a function of the density of the fluid and gravity. The value of this function is close to zero, however defining the value as a function rather than 0 allows proper convergence of the model.

In addition to the wall, inlet and outlet conditions, a volume force was applied to the entire geometry which applies the effects of gravity to each domain.

Transport of Diluted Species

Two transport of diluted species nodes were used in the transport of dextran simulations. One for the donor and receptor domains and one for the membrane domain. This separate node for the membrane domain allowed the difference in diffusion in that domain to be accounted for.

For the donor and receptor domains, a no flux boundary condition was applied to the exterior boundaries of the geometry on the same edges as the no slip conditions for laminar flow (***Figure 2-28***). This no flux condition prevents any mass flow across those boundaries. An outflow condition was applied to the outlet (***Figure 2-29***) to account for transport of FD out of the domain by the fluid motion. At the boundaries where the two domains meet the membrane domain, a pointwise constraint was applied to compute the transfer of mass across the membrane out of the donor domain into the receptor domain. The pointwise constraint was a function of the two concentrations at the boundaries which were defined by the diffusive and convective movements of the FD through the domains and computed the flux across the boundaries based on the concentration of FD and the diffusion coefficient for each domain.

The second transport of diluted species node applied similar boundary conditions as above but across the membrane domain, therefore accounting for the difference in diffusion coefficient across the membrane. A no flux condition was applied on the exterior wall boundaries of the membrane. No outflow condition was applied because the concentration species was not leaving the system at any point in the domain. The same function for the pointwise constraint was applied to the boundaries which were shared with the other two domains to compute the passage of the FD across these boundaries through the membrane. The dimensions of the membrane domain were altered depending on whether the presence of the cells was being modelled or not. In the presence of cells, the membrane domain was 70μm in height and the appropriate diffusion coefficient of the domain was used, as

described in table ***Table 2-21***. In the absence of the cells, the domain was reduced to 50µm and the diffusion coefficient was altered to account for their absence.

Boundary Selections for Kirkstall QV600 Dextran Transport Studies

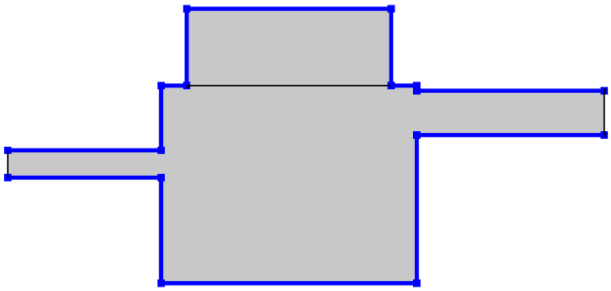

Figure 2-28: Exterior boundary walls highlighted with no slip laminar flow condition and no flux transport condition.

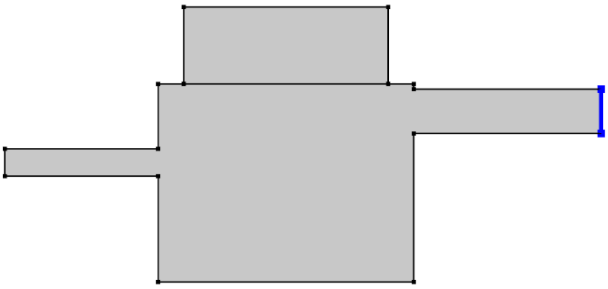

Figure 2-29: Outlet boundary highlighted with pressure defined outlet condition for laminar flow and mass outflow condition for transport.

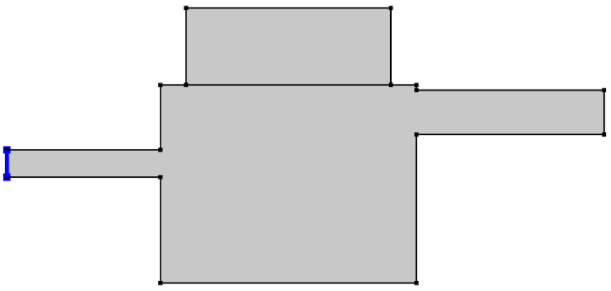

Figure 2-30: Inlet boundary highlighted with flow rate defined fluid inlet condition for laminar flow.

2.3.1.4 MESH USED FOR DEXTRAN TRANSPORT STUDIES

The mesh was created within the COMSOL software and was generated by the software to be controlled by the physics of the system. It comprised of free triangular elements with boundary layers at the no slip walls. The total number of elements in the mesh was 38267 with a greater refinement of elements at the membrane domain where the solution requires most accuracy (***Figure 2-31***)

A grid independence analysis was conducted to ensure the mesh was refined enough to produce accurate results. Firstly, the velocities along a line from the centre of the inlet to the centre of the outlet were plotted for varying numbers of mesh elements from an extremely fine mesh of 108814 elements to an extremely coarse mesh of 18005 elements. Additionally, the velocities at two points in the centre of the chamber were further evaluated and the percentage difference in velocity at these two points compared to the most refined mesh was plotted. A percentage difference of ≤5% of the most refined mesh was deemed fine enough. This was reached at 38267 elements and all further simulations were carried out with this mesh.

Mesh generated for Kirkstall QV600 Dextran Transport Studies

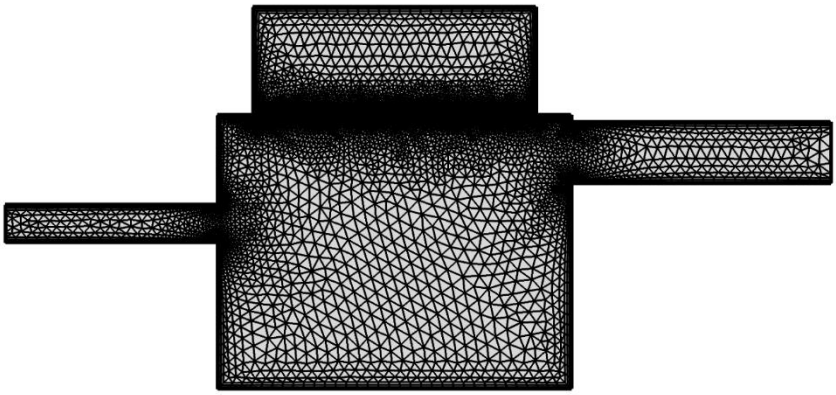

Figure 2-31: Mesh generated for Kirsktall QV600 chamber used in dextran transport simulations. Mesh consists of 38267 elements with a combination of free triangular elements and layered quadrilateral elements at the no slip boundaries.

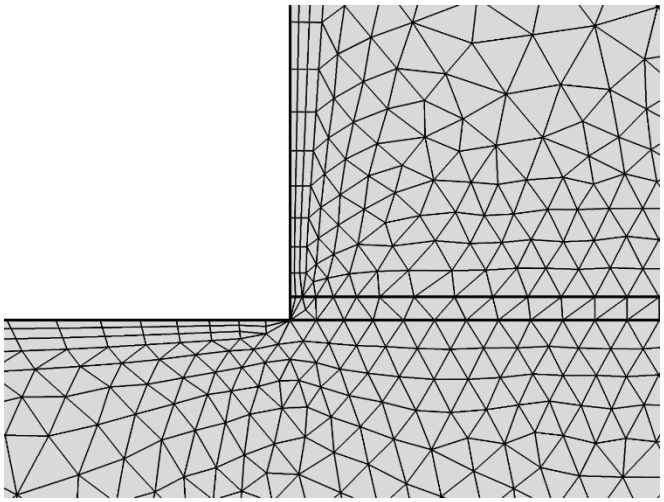

Figure 2-32: Mesh zoomed into membrane domain showing refinement of the mesh at the membrane domain and the changes in element shape at the boundaries.

2.3.1.5 PHYSICAL AND MATHEMATICAL DESCRIPTION OF IBUPROFEN RELEASE STUDIES

The model was built based on the same Kirkstall QV600 chamber geometry described previously. The difference between the ibuprofen release studies and the dextran transport studies was the ibuprofen release studies require the model to simulate the interaction of two immiscible fluid phases: the aqueous PBS phase and the 1000 c.st silicone oil phase. This model also removes the membrane domain as the movement of drug was directly from the oil into PBS. As with the model described in section 2.3.1.1, the simulation model consists of two parts: a laminar flow solution and a transport of diluted species solution. These physics nodes produce solutions based on the equations previously described with some differences in the mesh design based on the requirement of a two phase model.

Modelling Laminar Flow

To model the two-phase nature of the model, the same laminar flow physics was used however this was in addition to a moving mesh physics interface. The laminar flow moving mesh physics node solves the same equations for velocity and pressure fields but also tracks the movement of the interface between two immiscible fluids by allowing deformation of the mesh during the solution.

A free mesh deformation is prescribed to the domains either side of the interface, the oil domain and the PBS receptor domain. These are the regions where the mesh is allowed to deform. The inlet and outlet tubes of the geometry are prescribed a fixed mesh as only one of the fluid phases moves through these parts of the geometry. The mesh is also prescribed zero displacement at the exterior boundary walls to prevent collapsing of the solid wall boundaries. Those walls which are in contact with the fluid-fluid interface are prescribed free deformation of the mesh parallel to the exterior wall boundaries but with zero perpendicular displacement, again to prevent collapsing the solid exterior walls.

The additional equation solved for in the laminar flow, moving mesh interface is the Navier slip equation [175]. This condition is applied to the boundaries which are in contact with the fluid-fluid interface and it is appropriate for the two-phase flow model. This condition adds a frictional force, **F**, at a stationary wall which allows the interface to move against the wall.

$$\boldsymbol{F}_{fr} = -\frac{\mu}{\beta}\boldsymbol{u}$$

Equation 2-7: Navier slip frictional force.

Where β is the slip length, which is a function of the element size of the mesh. The fluid-fluid interface node also takes into account the interfacial tension of the two fluids and the contact angle between the wall and the fluids.

Due to the nature of the two-phase model, a stationary solution for the velocity field could not be solved because of the movement at the interface, therefore a time-dependent solution was obtained over 9 seconds, at which point the flow stabilised. The solution for the stabilised flow field was used as the velocity field input for the transport of diluted species solutions.

Modelling Transport of Diluted Species

The transport of diluted species follows the same principles as described in section 2.3.1.1. The solution for the transport is simpler for the release of ibuprofen because the concentration species only moves through two domains and not through a fluid matrix domain therefore the movement is purely diffusion and convection in the two different fluids. An additional expression for the partition coefficient is included in the mass transport between the two phases. The partition coefficient is a measure of the difference in solubility of a compound in the two different phases and describes the ratio of concentrations of the compound in the two phases when equilibrium has been reached across the interface.

To satisfy the convective terms of the mass balance equation, the solution for the laminar flow, moving mesh physics node was used to describe the velocity field in the model in order to solve for the concentration field of the ibuprofen across the model.

2.3.1.6 Modelling Static Ibuprofen Release in Well Plates

In addition to the modelling the dynamic release of ibuprofen from silicone oil within the Kirkstall QV600 chamber, the release was also investigated in static well plate models. Models were built to represent 12, 24 and 48-well plates and the transport of diluted species physics, input parameters and boundary conditions used for the solution were identical to

those used for the dynamic release models, however these models do not require the laminar flow physics as they were static.

2.3.1.7 Input Parameters for Ibuprofen Release Studies

The input parameters were either experimentally defined or calculated. The values for the partition coefficient of ibuprofen and the interfacial tension of 1000 c.st silicone oil and PBS were taken from the literature. All of the input parameters used are detailed in ***Table 2-22***.

Input Parameters for Ibuprofen Release Studies

Parameter	Value
Diffusion coefficient of ibuprofen in 1000c.st silicone oil	3.35 x10^{-11} m^2/s
Diffusion coefficient of ibuprofen in PBS	2.27 x$10^{-13}$$m^2/s$
Partition coefficient of ibuprofen	2.2 [176]
Initial concentration of ibuprofen in oil phase	1 mg/mL
Initial concentration of ibuprofen in aqueous phase	0 µg/mL
Flow rate	20,200,400,2000 µL/min
Interfacial tension 1000c.st silicone oil/PBS	50 mN/m
Wall contact angle of fluid interface	1.3 rad
Density of PBS at 37°C	996.31 kg/m^3
Dynamic viscosity of PBS at 37°C	0.61 mPa.s
Density of silicone oil at 37°C	967 kg/m^3
Dynamic viscosity of silicone oil at 37°C	790 mPa.s

Table 2-22: Input parameters for Kirkstall QV600 ibuprofen release studies.

2.3.1.8 BOUNDARY CONDITIONS FOR IBUPROFEN RELEASE STUDIES

Laminar Flow

A no-slip condition was applied to the exterior boundary walls as with the transport of dextran studies (***Figure 2-33***). However, those walls in contact with the fluid-fluid interface were assigned a Navier slip condition (***Figure 2-34***). This condition allows the fluid-fluid interface to move along the wall. Additionally, the top boundary of the oil phase, parallel to the fluid-fluid interface, was assigned a slip condition (***Figure 2-35***). This slip condition allows the deformation of the mesh to continue throughout the phase whilst still applying a no penetration condition, meaning the model allows the movement of the mesh without fluid leaving that domain.

The inlet and outlet conditions were as previously describes and the same flow rates were investigated as with the dextran transport studies: 20µL/min, 200µL/min, 400µL/min and 2mL/min. A volume force was also implemented across the entire geometry to account for gravity in the system.

Transport of Diluted Species

Two transport of diluted species nodes were used to investigate the release of ibuprofen from the silicone oil: one for the oil phase and one for the aqueous phase. As in the previous model, a no-flux condition was applied on the exterior boundary walls of the geometry. An outflow condition was applied to the right-hand wall of the outlet port of the chamber to allow the removal of ibuprofen via the fluid flow field. The appropriate diffusion coefficients as described in table ***Table 2-22*** were applied to each fluid domain and a pointwise constraint was applied at the fluid-fluid interface. This pointwise constraint takes into account the concentration at the interfaces and solves for the mass flux across that boundary using a function of the concentration gradient and the partition coefficient.

Boundary Selections for Kirkstall QV600 Ibuprofen Release Studies

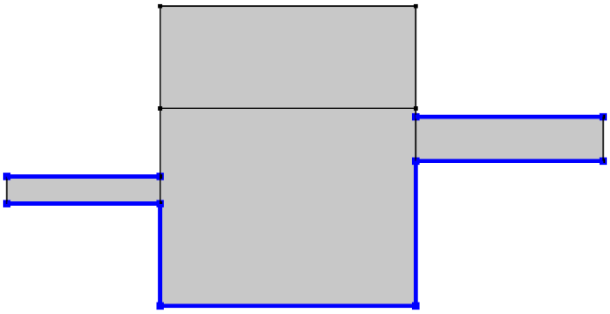

Figure 2-33: Exterior boundary walls highlighted with no slip laminar flow condition.

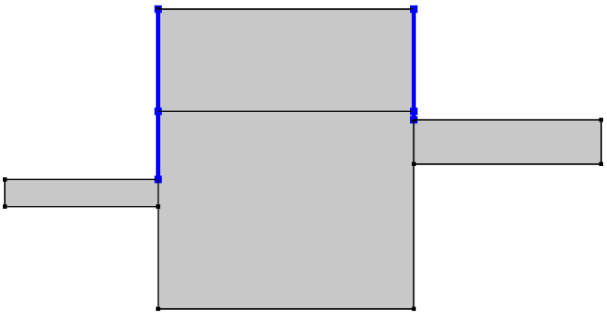

Figure 2-34: Boundaries in contact with fluid-fluid interface with Navier slip laminar flow condition.

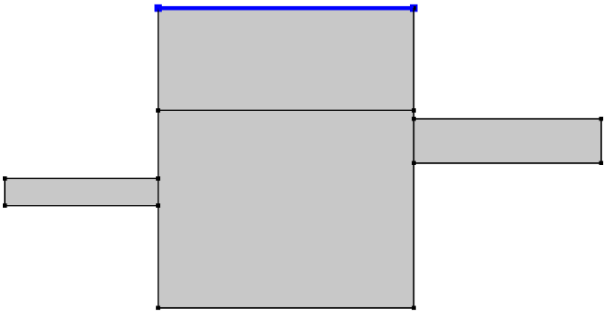

Figure 2-35: Oil phase boundary with slip laminar flow condition.

2.3.1.9 MESH USED FOR IBUPROFEN RELEASE STUDIES

For the static release studies in the well plate, the mesh was made up of 1732 free triangular elements (***Figure 2-36***). A grid independence test was carried out to ensure the mesh was refined enough to produce accurate results. The concentration at two points within the well was compared across a range of increasingly finer meshes to evaluate the accuracy of the results compared with the finest mesh. A percentage error of 5% or less compared with the finest mesh was deemed sufficiently accurate. This was achieved at 1732 elements and this mesh was used for all well plate simulations.

As previously discussed, the model for dynamic release of ibuprofen used a moving mesh which undergoes deformation at the fluid-fluid boundary and allows the interface between the two phases to be tracked. The mesh was generated by the software to be controlled by the physics of the system and consisted of 2258 free triangular elements (***Figure 2-37***). Again, a grid independence test was carried out. The velocity at the points within the centre of the chamber were compared across a range of mesh element numbers from an extremely coarse mesh of 345 elements to an extremely fine mesh of 3481 elements. The percentage different in velocity at the two points compared with the most refined mesh was used to evaluate the accuracy of the results. A percentage error of 5% or less was deemed accurate enough. This was reached at 2258 elements and this mesh was used for all the following simulations.

Mesh generated for Ibuprofen Release Studies

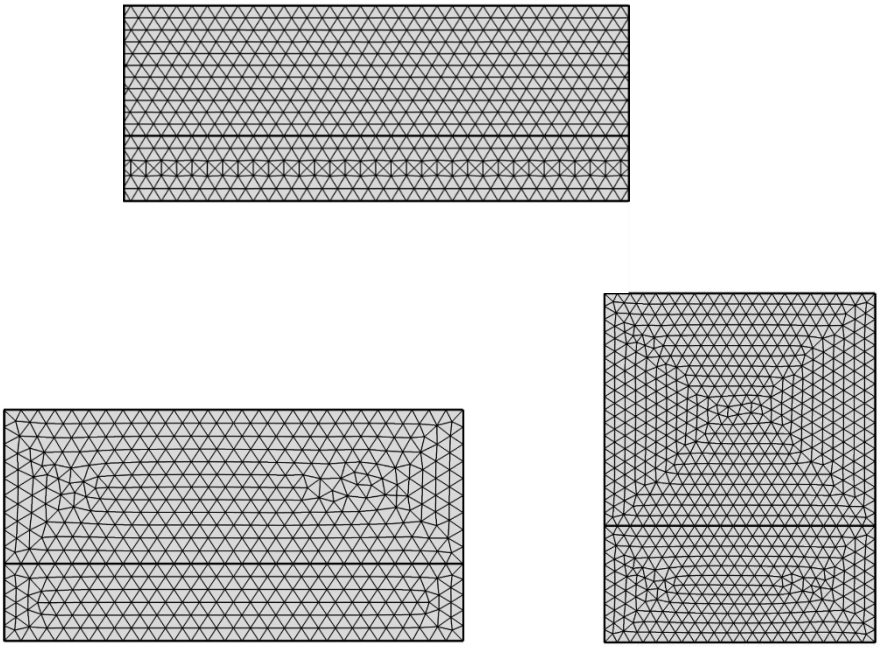

Figure 2-36: Mesh generated for (a) 12-well plate, (b) 24-well plate, (c) 48-well plate used in ibuprofen release experiments. Mesh consists of 1732 free triangular elements.

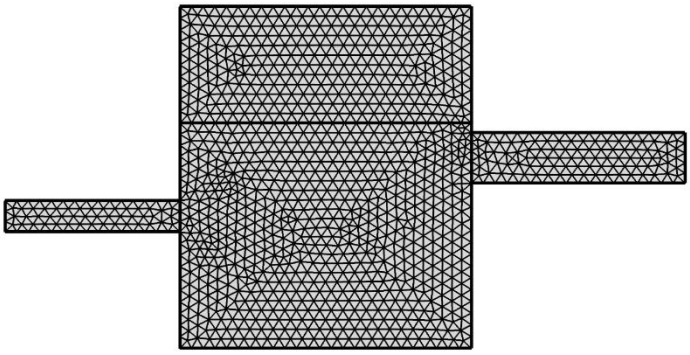

Figure 2-37: Mesh generated for Kirsktall QV600 chamber used in ibuprofen release simulations. Mesh consists of 2258 free triangular elements.

2.3.2 RESULTS

2.3.2.1 RHEOLOGICAL EVALUATION OF FLUIDS

The viscosities of a range of fluids used in *in vitro* experiments were investigated to determine the values of the viscosities required to input into the computer model to build an accurate simulation. Initial studies used a TA Instruments Rheolyst stress-controlled rheometer at 21^{o}C. The results from these studies showed minimal differences between all of the fluids measured and water with the exception of 10% BSA solution which had a viscosity 50% higher than the other fluids (***Figure 2-38***). The fluids of greatest interest to this study were DMEM-F12 2% FCS and PBS. These two fluids were used in the Kirkstall QV600 chamber and in the release studies. The viscosities of these two fluids were required for the input parameters of the model, the other fluids were used for reference. The TA Instruments Rheolyst rheometer measured the viscosities of DMEM-F12 2% FCS and PBS as 0.89 and 0.86 mPa.s respectively.

Evaluation of the viscosities at 37^{o}C was unable to be carried out using the TA Instruments Rheolyst rheometer, therefore a different rheometer was used to obtain these data. The Rheosene Inc µVISC measures viscosity in a similar stress-controlled system however, it is less sophisticated and provides less data regarding the shear stress across a range of strains. It provides an instantaneous value for viscosity. The viscosities of the fluids were measured at 21^{o}C again (***Figure 2-39***) with the µVISC system to ensure the values produced were comparable to the Rheolyst system. The differences in the values of viscosities produced between the two machines were ≤5%, this was deemed an acceptable difference and so the measurements at 37^{o}C were carried out using the µVISC rheometer (***Table 2-23***). As expected, increasing the temperature to 37^{o}C saw a decrease in viscosity across all of the fluids. The highest viscosity fluid remained 10% BSA which decreased from 1.463 mPa.s to 0.934 mPa.s. PBS, 1% BSA and DMEM-F12 2% FCS all decreased in viscosity but remained within 5% of the value for water, 0.650 mPa.s (***Figure 2-40***). These values were then able to be used as input parameters for the computer model.

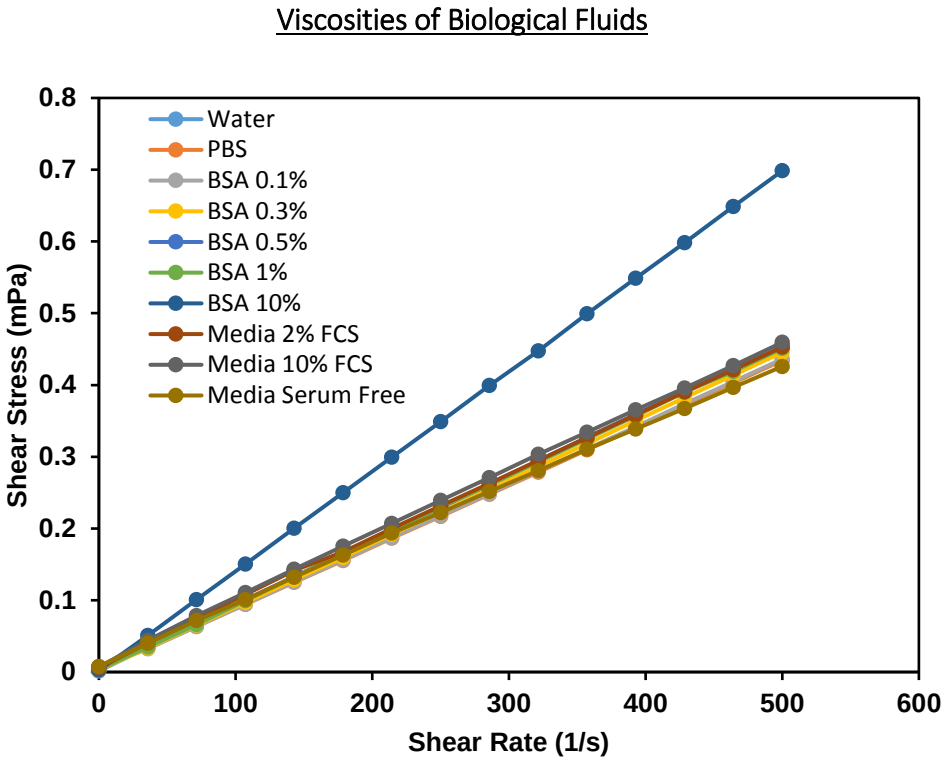

Figure 2-38: Shear stress vs shear strain relationship of biological fluids. Measured using TA Instruments Rheolyst rheometer at 21°C. Data presented as mean shear stress, n=3.

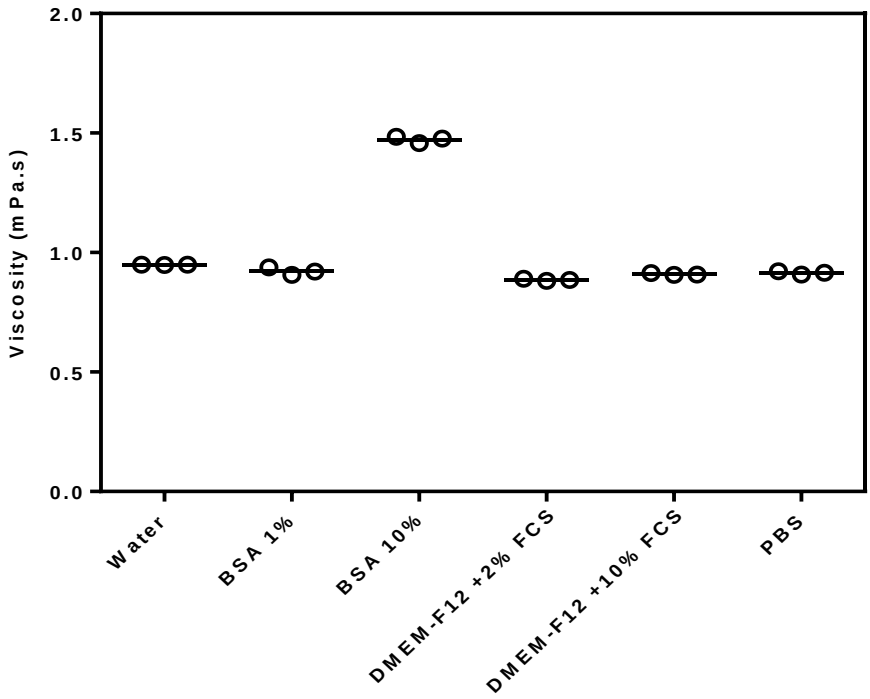

Figure 2-39: Viscosities of biological fluids at 21°C. Measured using Rheosense Inc. µVISC. Each data point represents one measurement, line = mean, n=3.

Viscosities of Biological Fluids

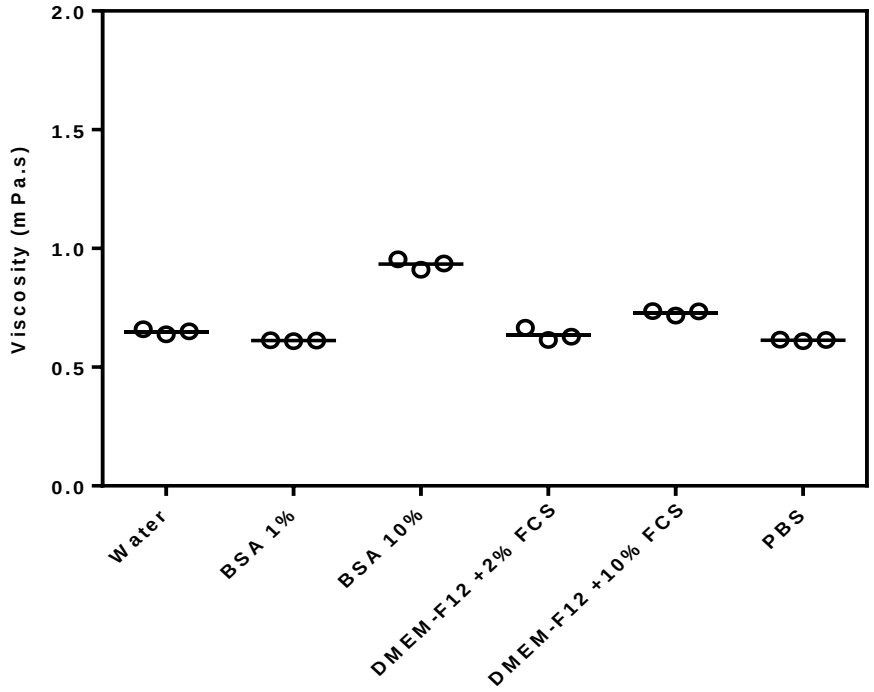

Figure 2-40: Viscosities of biological fluids at 37°C. Measured using Rheosense Inc. µVISC. Each data point represents one measurement, line = mean, n=3.

Solution	Viscosity (mPa.s) at 21°C using TA Instruments Rheolyst	Viscosity (mPa.s) at 21°C using Rheosense Inc. µVISC	Viscosity (mPa.s) at 37°C using Rheosense Inc. µVISC
Water	0.907	0.948	0.650
PBS	0.861	0.915	0.613
BSA 1%	0.898	0.922	0.612
BSA 10%	1.393	1.473	0.934
DMEM-F12 +2% FCS	0.886	0.886	0.636
DMEM-F12 +10% FCS	0.896	0.909	0.730

Table 2-23: Rheological measurements of viscosities of biological fluids at 21°C and 37°C using different rheometers.

2.3.2.2 GRID INDEPENDENCE TESTS

A grid independence test was carried out for each geometry to assure the meshes that were generated were fine enough to produce accurate results.

Dynamic transport of dextran in Kirkstall QV600

The transport of dextran simulations used a steady state solution for the velocity field within the chamber, i.e. only the final stable velocity field was obtained. In this instance, the velocities along a line from the centre of the inlet to the centre of the outlet were analyzed for increasingly refined meshes to determine the effects of the mesh element density (***Figure 2-41***). At the highest velocities, within the inlet and outlet ports, refining the mesh serves to smooth the velocity curve however the difference in velocities between the meshes is not dissimilar. At the lower velocities within the centre of the chamber, the effects of mesh refinement are more noticeable. The difference between the most refined mesh of 108814 elements and the least refined mesh of 18005 was up to 20mm/s at points along the line.

Two specific points within the geometry were also evaluated and the point at which the mesh element density reached velocity results with <5% error in comparison to the most refined mesh were assumed to satisfy the accuracy of the model. For these simulations, this was reached at 38267 elements (***Figure 2-42***).

Static release of ibuprofen from silicone oil in well plates

Given there was no velocity field to evaluate in the static release experiments, the concentration at two points within the geometry was evaluated. Again, when the concentration at those two points reached a percentage error of <5% in comparison to the most refined mesh, the mesh satisfied requirement. For the static release experiments this was reached at 1732 elements (***Figure 2-43***).

Dynamic release of ibuprofen from silicone oil in Kirkstall QV600

The velocity field for the ibuprofen release studies was a time-dependent solution due to the need to track the moving interface of the two fluids. Therefore measuring the velocity along a line is difficult because it is always changing with time. For this reason, the velocity at two points within the geometry was evaluated at the final time point of the solution, 9 seconds,

as this was the time at which a stable flow had been developed. The <5% error was used again as the limit of accuracy. This was achieved at 2258 elements (***Figure 2-44***).

Grid Independence Test for Dextran Transport in Kirkstall QV600 Studies

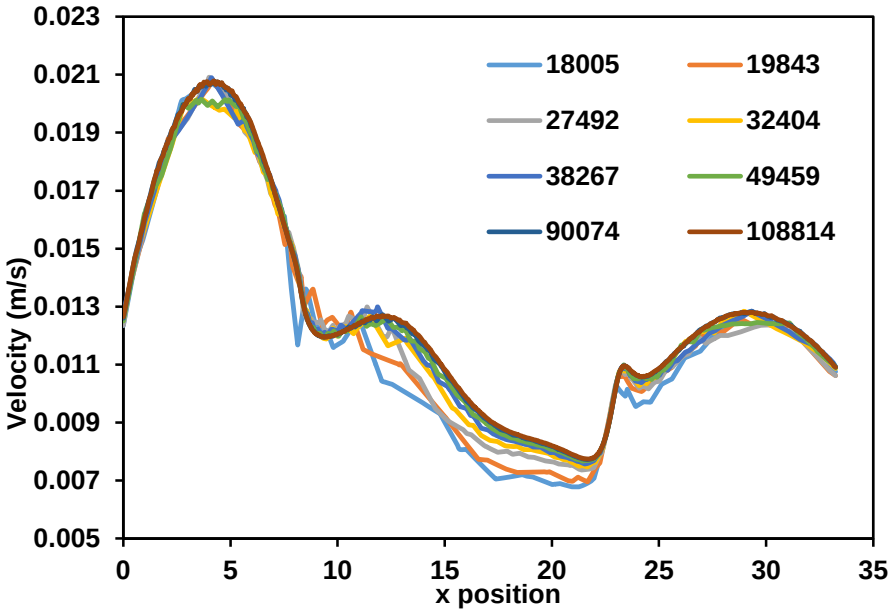

Figure 2-41: Fluid velocity in Kirkstall QV600 chamber along a line from the centre of the inlet to the centre of the outlet for different mesh densities. Legend indicates number of elements in the mesh.

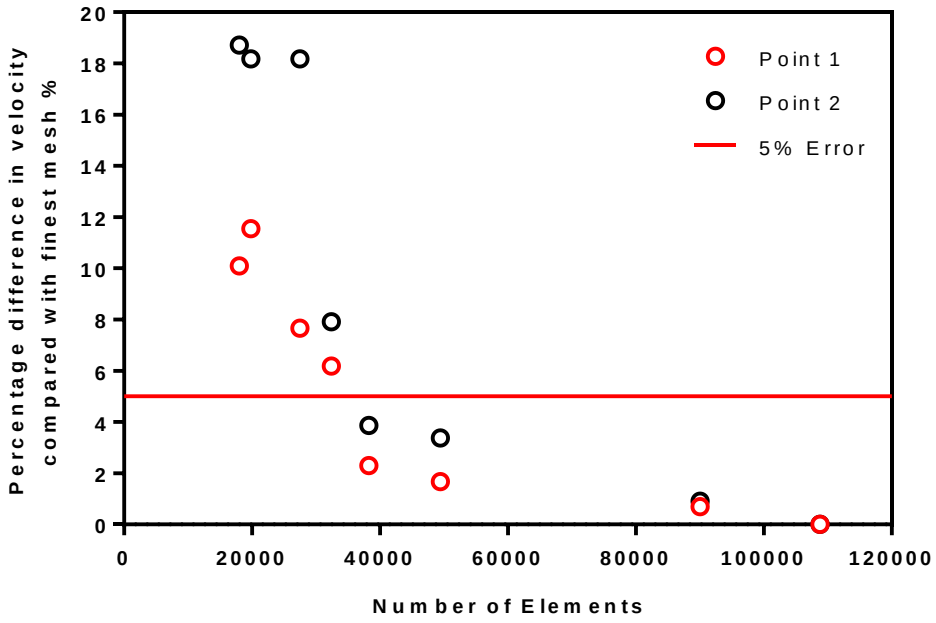

Figure 2-42: Percentage difference in velocity at two points in the centre of the chamber compared with the finest mesh (108814 elements). A <5% error was deemed to be acceptable mesh density.

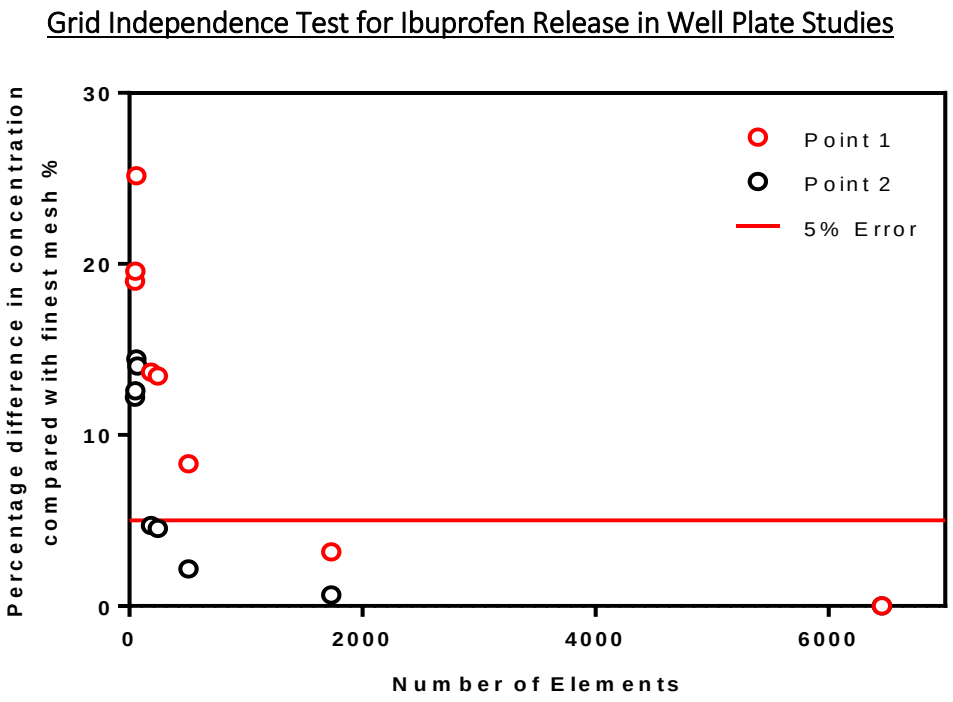

Figure 2-43: Percentage difference in concentration at two points in the centre of the well compared with the finest mesh (6458 elements). A <5% error was deemed to be acceptable mesh density.

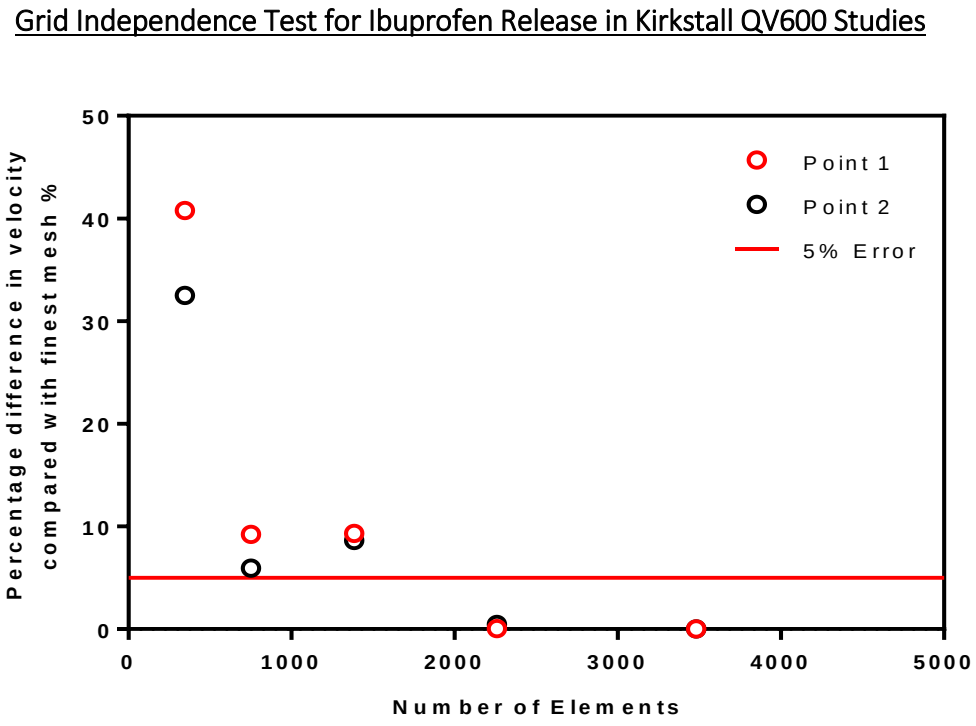

Figure 2-44: Percentage difference in velocity at two points in the centre of the Kirkstall QV600 chamber compared with the finest mesh (3481 elements). A <5% error was deemed to be acceptable mesh density.

2.3.2.3 DEVELOPMENT OF VELOCITY FIELDS IN THE DEXTRAN TRANSPORT STUDIES

The inlet flow rates investigated in these studies were 20µL/min, 200µL/min, 400µL/min and 2000µL/min. For flow rates 20, 200 and 400µL/min the velocity fields produce similar patterns (***Figure 2-45***). A parabolic flow out from the inlet tube and in to the outlet tubes with considerably lower velocities in the main well of the chamber. Each of these flow rates shows areas of recirculating flow trapped in the corners of the receptor compartment on the inlet side, with these areas increasing in size as the inlet flow rate increased. The streamlines show that at the lowest flow rate, 20µL/min, the flow in the main chamber has little effect on the velocity field in the donor compartment of the chamber. As the flow rate increases, the flow profile of the donor compartment becomes more uniform as fluid from the main well penetrated through the membrane and caused fluid flow in the donor compartment. This phenomenon is most obvious in the highest inlet flow rate simulation, 2ml/min. In the donor compartment of this simulation, a parabolic flow regime is observed. The velocities in the main well of the chamber are also considerably higher than in comparison with lower inlet flow rates. Another feature of this high flow rate is the development of a dominating stream of fluid from the inlet tube to the outlet port and large area of recirculating fluid beneath this stream which occurs in the majority of the chamber volume.

Velocity Fields of Different Flow Rates in the Kirkstall QV600 Dextran Transport Studies

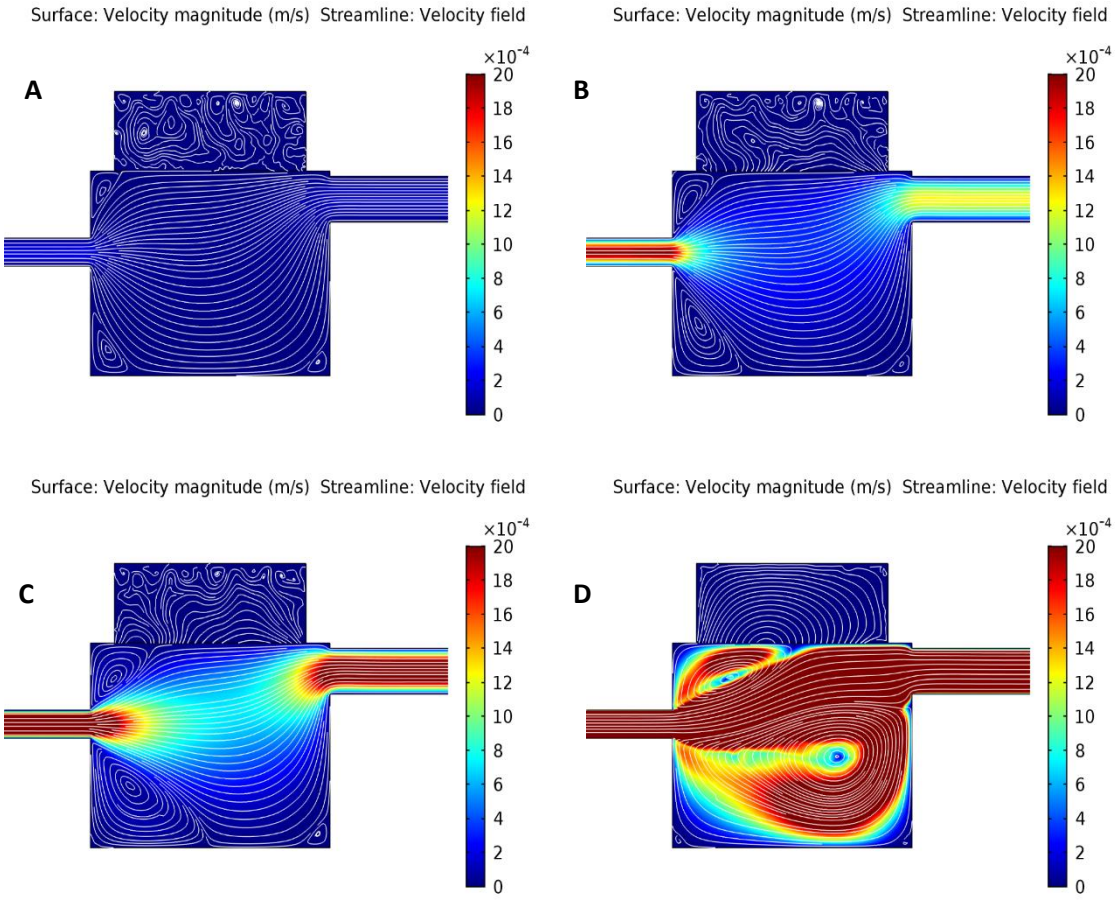

Figure 2-45: Velocity fields for different inlet flow rates used in the Kirkstall QV600 chamber geometry for dextran transport studies. Inlet flow rates: (a) 20µL/min, (b) 200µL/min, (c) 400µL/min and (d) 2mL/min. Colour scale bar indicates velocity (m/s). Streamlines show velocity field.

2.3.2.4 CONCENTRATION PROFILES OF DEXTRAN IN THE KIRKSTALL QV600 CHAMBER

The concentration profiles which were obtained from the simulations were reliant on the coefficients which were acquired from the *in vitro* experiments. As discussed in section 2.2.3.2, the presence of the fluid flow had varying effects on the efficiency of the ARPE-19 cell monolayer as a barrier to compound transport. This was apparent in the results for the computational solutions which showed greater accuracy in the simulations which modelled the membranes without cells in comparison to those which modelled their presence.

At 20µL/min, the computational solution produced the same concentration profile as seen in the *in vitro* results. The profile again showed similarities to a single dose response curve. For the unseeded membranes, the simulated results for AUC for each molecular weight of dextran was within 15% of the *in vitro* results, with the percentage error being 13.4, 10.0 and 3.6% for FD4, FD40 and FD70 respectively. The error seen in the maximum concentrations of the receptor domain were smaller still with the differences being 2.3, 6.7 and 0.8% respectively. There were some discrepancies in the time at which the maximum concentration was reached. For FD4, the simulation predicted the maximum concentration would be reached after 3 hours, however, the experimental results showed this to be after 4 hours. Similarly, for FD40, the simulation predicted the T_{max} to be after 4 hours, however the experiment showed it to be after 3 hours (***Figure 2-46***, ***Table 2-24***, ***Table 2-25, Table 2-26***)

The seeded membranes showed greater differences in both AUC and C_{max} values. The simulation showed an over-estimation in the concentration profile in the domain. The AUC was higher in the simulation for each molecular weight. The differences were 19.5, 28.3 and 14.2% for FD4, FD40 and FD70 respectively. There appears to be no correlation between the molecular weight of the dextran and the accuracy of the model. The error in C_{max} was also greater in the seeded membranes, particularly for FD4 and FD40. The simulation predicted the C_{max} of these two molecular weights to reach 18.9 and 12.3% higher respectively. The simulated result for FD70 was only 1.2% higher in comparison to the *in vitro* result (***Figure 2-47***, ***Table 2-27***, ***Table 2-28***, ***Table 2-29***)

At the higher flow rates, the simulated results were able to mirror the change in release profile exhibited *in vitro* which showed a shift to a burst release response followed by an exponential decay in concentration over time (***Figure 2-48***, ***Figure 2-49***, ***Figure 2-50***, ***Figure***

2-51, ***Figure 2-52***). Again for 200µL/min, 400µL/min and 2mL/min the results produced from the acellular studies were within a 15% difference of the *in vitro* data for AUC, with no correlation between molecule size or flow rate and simulation accuracy. The largest differences in simulation and experimental agreement were seen in both the AUC and C_{max} results on the cell seeded studies at 200µL/min. For the largest molecular weight FD used, FD70, the error in AUC between the two data sets was 57%. Similarly, the predicted C_{max} was 46% different to the observed *in vitro* value (***Table 2-35***). At 400µL, the simulation was able to predict AUC and C_{max} for both cellular and acellular studies to within 30% and at 2mL/min, this was reduced to 15% (2mL/min studies only conducted in acellular conditions).

Simulation vs Experimental Concentration Profiles of Dextrans in Receptor Compartment of Kirkstall QV600 exposed to 20µL/min Flow without ARPE-19 cells

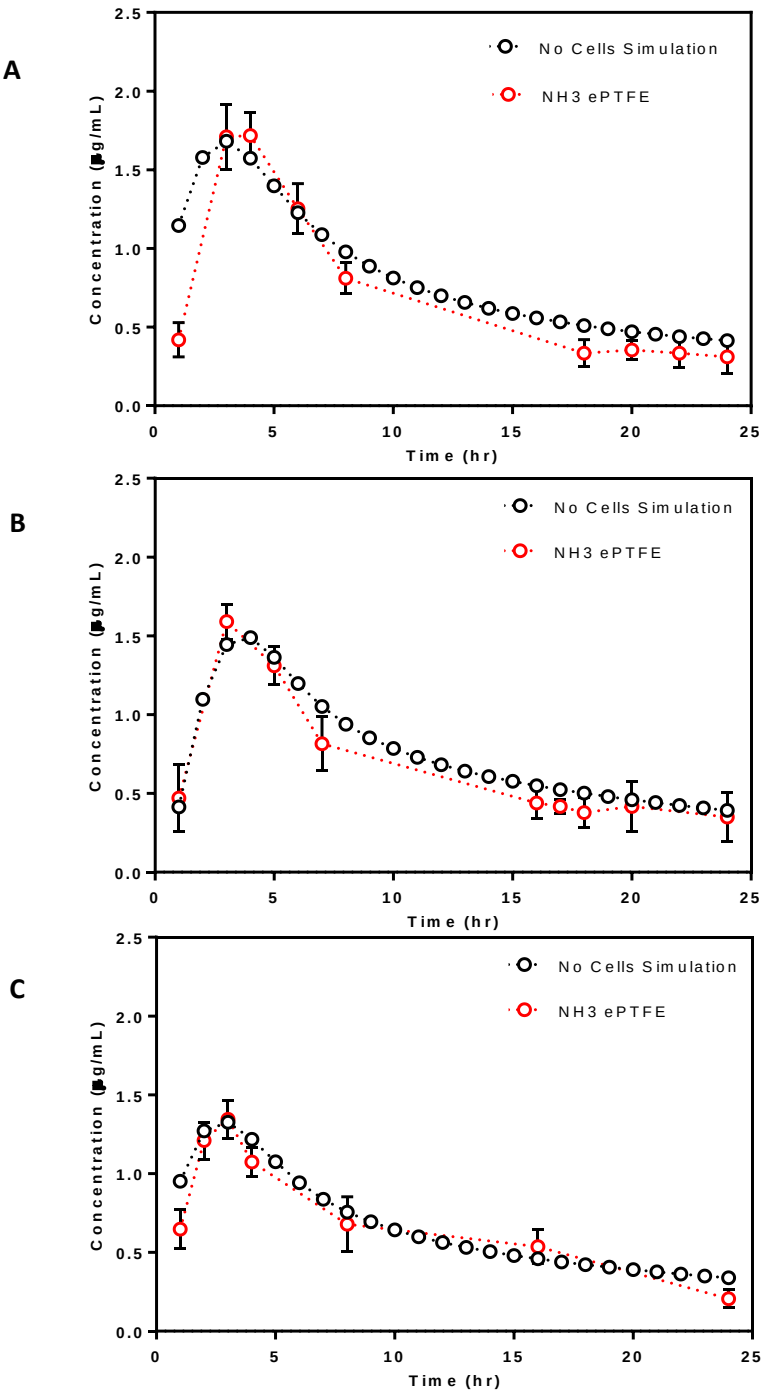

Figure 2-46: Concentration profiles of different molecular weight fluorescently labelled dextrans a) 4kDA, b) 40kDa and c) 70kDa in receptor compartment of Kirkstall QV600 chamber. Studies carried out experimentally (red) and simulated (black) on unseeded NH_3 treated ePTFE membranes. Experimental flow rate = 20µL/min. Data presented as mean ± 1 SD, n=6.

Simulation vs Experimental Concentration Profiles of Dextrans in Receptor Compartment of Kirkstall QV600 exposed to 20µL/min Flow with ARPE-19 cells

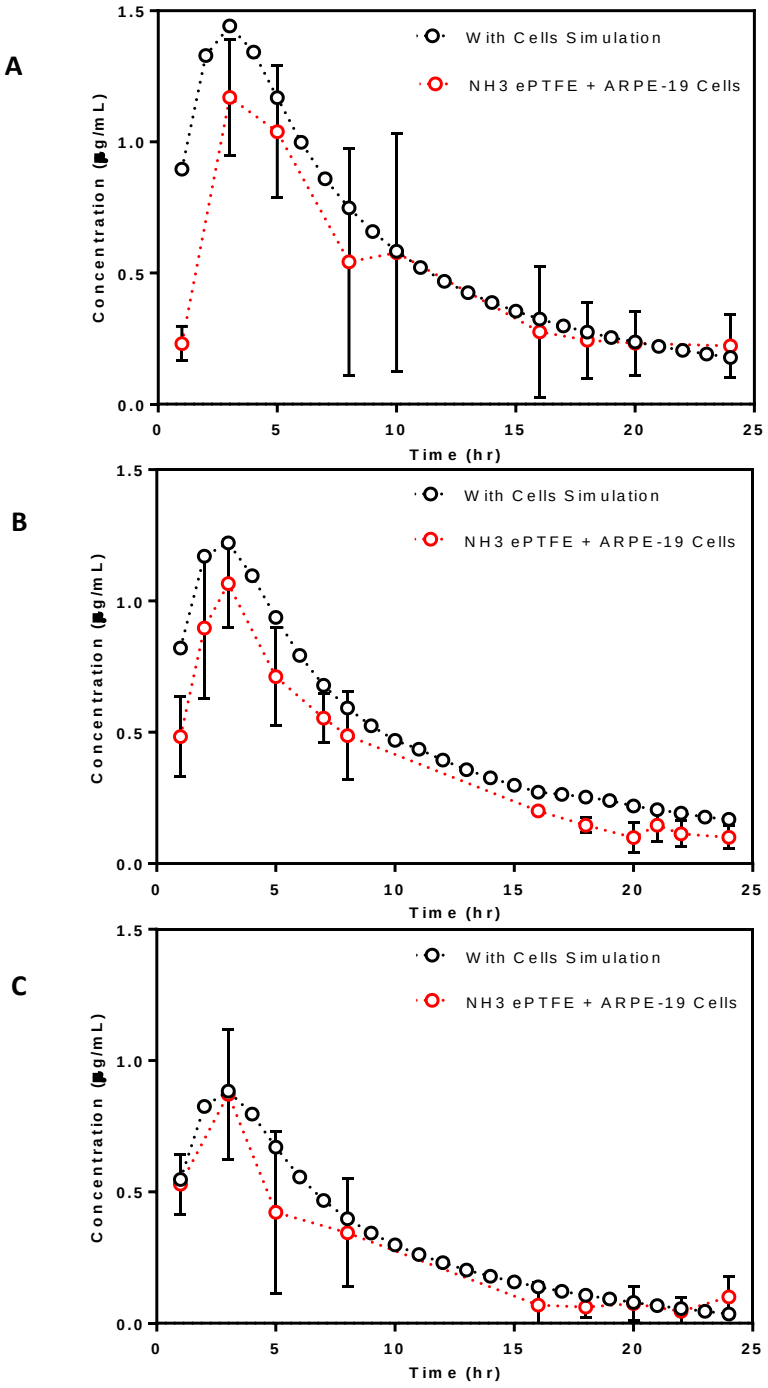

Figure 2-47: Concentration profiles of different molecular weight fluorescently labelled dextrans a) 4kDA, b) 40kDa and c) 70kDa in receptor compartment of Kirkstall QV600 chamber. Studies carried out experimentally (red) and simulated (black) on seeded NH_3 treated ePTFE membranes. Experimental flow rate = 20µL/min. Data presented as mean ± 1 SD, n=6.

Concentration Curve Statistics for Simulated vs Experimental Dextran Transport Studies across Unseeded Membranes at 20µL/min

	Area under Curve (AUC, µg.h/mL)	Peak Concentration (C_{max}, µg/mL)	Time of Peak Concentration (t_{max}, hr)	Average Concentration (C_{ave}, µg/mL)
Experimental	16.63	1.72±0.15	4	0.81
Simulation	19.20	1.68	3	0.83

Table 2-24: Concentration curve statistics for 4kDa fluorescently labelled dextran transport across unseeded NH_3 treated ePTFE membranes exposed to a flow rate of 20µL/min.

	Area under Curve (AUC, µg.h/mL)	Peak Concentration (C_{max}, µg/mL)	Time of Peak Concentration (t_{max}, hr)	Average Concentration (C_{ave}, µg/mL)
Experimental	15.89	1.59±0.11	3	0.69
Simulation	17.65	1.49	4	0.75

Table 2-25: Concentration curve statistics for 40kDa fluorescently labelled dextran transport across unseeded NH_3 treated ePTFE membranes exposed to a flow rate of 20µL/min.

	Area under Curve (AUC, µg.h/mL)	Peak Concentration (C_{max}, µg/mL)	Time of Peak Concentration (t_{max}, hr)	Average Concentration (C_{ave}, µg/mL)
Experimental	14.76	1.34±0.11	3	0.81
Simulation	15.30	1.33	3	0.66

Table 2-26: Concentration curve statistics for 70kDa fluorescently labelled dextran transport across unseeded NH_3 treated ePTFE membranes exposed to a flow rate of 20µL/min.

Concentration Curve Statistics for Simulated vs Experimental Dextran Transport Studies across Seeded Membranes at 20µL/min

	Area under Curve (AUC, µg.h/mL)	Peak Concentration (C_{max}, µg/mL)	Time of Peak Concentration (t_{max}, hr)	Average Concentration (C_{ave}, µg/mL)
Experimental	11.57	1.17±0.22	3	0.50
Simulation	13.83	1.44	3	0.60

Table 2-27: Concentration curve statistics for 4kDa fluorescently labelled dextran transport across ARPE-19 seeded NH_3 treated ePTFE membranes exposed to a flow rate of 20µL/min.

	Area under Curve (AUC, µg.h/mL)	Peak Concentration (C_{max}, µg/mL)	Time of Peak Concentration (t_{max}, hr)	Average Concentration (C_{ave}, µg/mL)
Experimental	9.05	1.07±0.17	3	0.42
Simulation	11.62	1.22	3	0.50

Table 2-28: Concentration curve statistics for 40kDa fluorescently labelled dextran transport across ARPE-19 seeded NH_3 treated ePTFE membranes exposed to a flow rate of 20µL/min.

	Area under Curve (AUC, µg.h/mL)	Peak Concentration (C_{max}, µg/mL)	Time of Peak Concentration (t_{max}, hr)	Average Concentration (C_{ave}, µg/mL)
Experimental	6.04	0.87±0.25	3	0.28
Simulation	7.27	0.88	3	0.32

Table 2-29: Concentration curve statistics for 70kDa fluorescently labelled dextran transport across ARPE-19 seeded NH_3 treated ePTFE membranes exposed to a flow rate of 20µL/min.

Simulation vs Experimental Concentration Profiles of Dextrans in Receptor Compartment of Kirkstall QV600 exposed to 200µL/min Flow without ARPE-19 cells

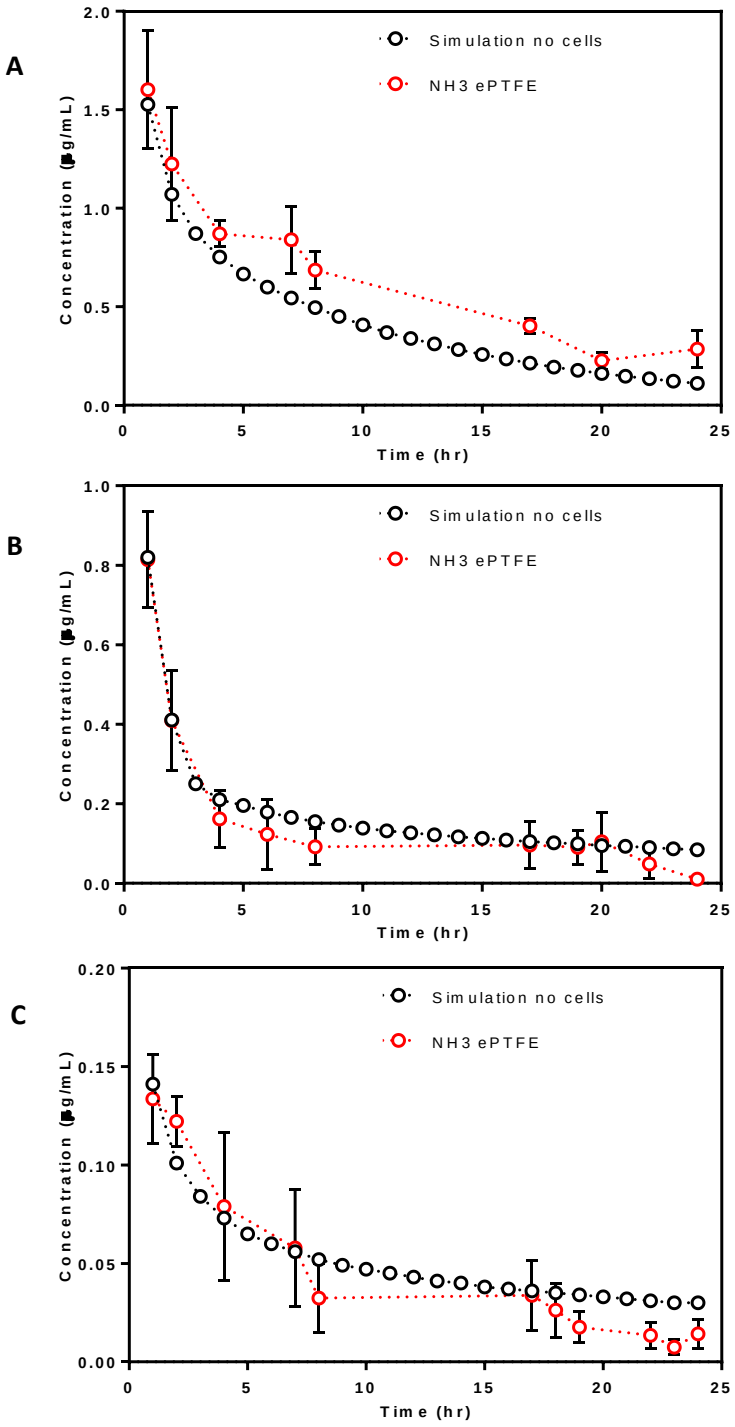

Figure 2-48: Concentration profiles of different molecular weight fluorescently labelled dextrans a) 4kDA, b) 40kDa and c) 70kDa in receptor compartment of Kirkstall QV600 chamber. Studies carried out experimentally (red) and simulated (black) on unseeded NH_3 treated ePTFE membranes. Experimental flow rate = 200µL/min. Data presented as mean ± 1 SD, n=6

Simulation vs Experimental Concentration Profiles of Dextrans in Receptor Compartment of Kirkstall QV600 exposed to 200µL/min Flow with ARPE-19 cells

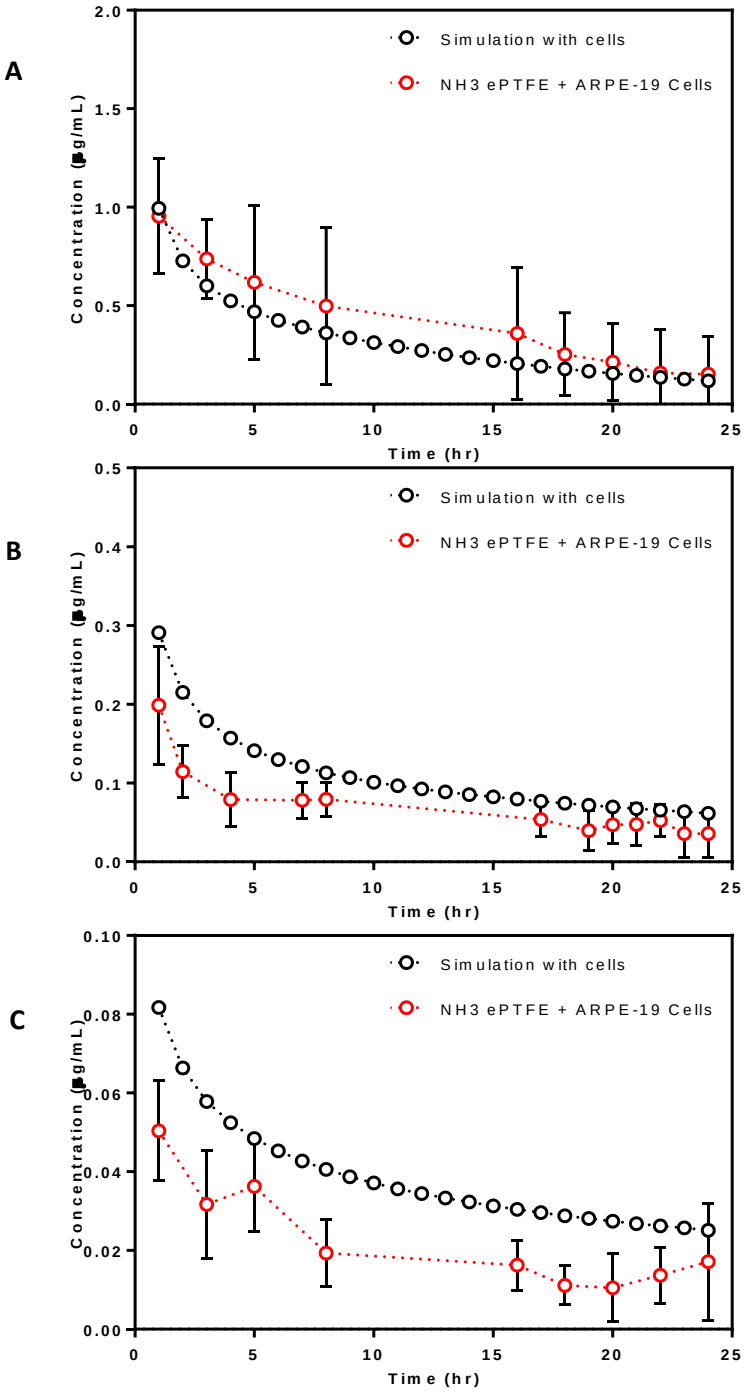

Figure 2-49: Concentration profiles of different molecular weight fluorescently labelled dextrans a) 4kDA, b) 40kDa and c) 70kDa in receptor compartment of Kirkstall QV600 chamber. Studies carried out experimentally (red) and simulated (black) on unseeded NH_3 treated ePTFE membranes. Experimental flow rate = 200µL/min. Data presented as mean ± 1 SD, n=6

Concentration Curve Statistics for Simulated vs Experimental Dextran Transport Studies across Unseeded Membranes at 200µL/min

	Area under Curve (AUC, µg.h/mL)	Peak Concentration (C_{max}, µg/mL)	Time of Peak Concentration (t_{max}, hr)	Average Concentration (C_{ave}, µg/mL)
Experimental	13.70	1.60	1	0.77
Simulation	11.83	1.52	1	0.44

Table 2-30: Concentration curve statistics for 4kDa fluorescently labelled dextran transport across unseeded NH_3 treated ePTFE membranes exposed to a flow rate of 200µL/min.

	Area under Curve (AUC, µg.h/mL)	Peak Concentration (C_{max}, µg/mL)	Time of Peak Concentration (t_{max}, hr)	Average Concentration (C_{ave}, µg/mL)
Experimental	3.03	0.81	1	0.19
Simulation	3.49	0.82	1	0.17

Table 2-31: : Concentration curve statistics for 40kDa fluorescently labelled dextran transport across unseeded NH_3 treated ePTFE membranes exposed to a flow rate of 200µL/min.

	Area under Curve (AUC, µg.h/mL)	Peak Concentration (C_{max}, µg/mL)	Time of Peak Concentration (t_{max}, hr)	Average Concentration (C_{ave}, µg/mL)
Experimental	1.00	0.131	1	0.05
Simulation	1.14	0.14	1	0.05

Table 2-32: Concentration curve statistics for 70kDa fluorescently labelled dextran transport across unseeded NH_3 treated ePTFE membranes exposed to a flow rate of 200µL/min.

Concentration Curve Statistics for Simulated vs Experimental Dextran Transport Studies across Seeded Membranes at 200µL/min

	Area under Curve (AUC, µg.h/mL)	Peak Concentration (C_{max}, µg/mL)	Time of Peak Concentration (t_{max}, hr)	Average Concentration (C_{ave}, µg/mL)
Experimental	9.91	0.95	1	0.44
Simulation	7.30	0.99	1	0.33

Table 2-33: Concentration curve statistics for 4kDa fluorescently labelled dextran transport across seeded NH_3 treated ePTFE membranes exposed to a flow rate of 200µL/min.

	Area under Curve (AUC, µg.h/mL)	Peak Concentration (C_{max}, µg/mL)	Time of Peak Concentration (t_{max}, hr)	Average Concentration (C_{ave}, µg/mL)
Experimental	1.58	0.20	1	0.07
Simulation	2.46	0.29	1	0.10

Table 2-34: Concentration curve statistics for 40kDa fluorescently labelled dextran transport across seeded NH_3 treated ePTFE membranes exposed to a flow rate of 200µL/min.

	Area under Curve (AUC, µg.h/mL)	Peak Concentration (Cmax, µg/mL)	Time of Peak Concentration (tmax, hr)	Average Concentration (Cave, µg/mL)
Experimental	0.48	0.05	1	0.02
Simulation	0.87	0.08	1	0.04

Table 2-35: Concentration curve statistics for 70kDa fluorescently labelled dextran transport across seeded NH_3 treated ePTFE membranes exposed to a flow rate of 200µL/min.

Simulation vs Experimental Concentration Profiles of Dextrans in Receptor Compartment of Kirkstall QV600 exposed to 400µL/min Flow without ARPE-19 cells

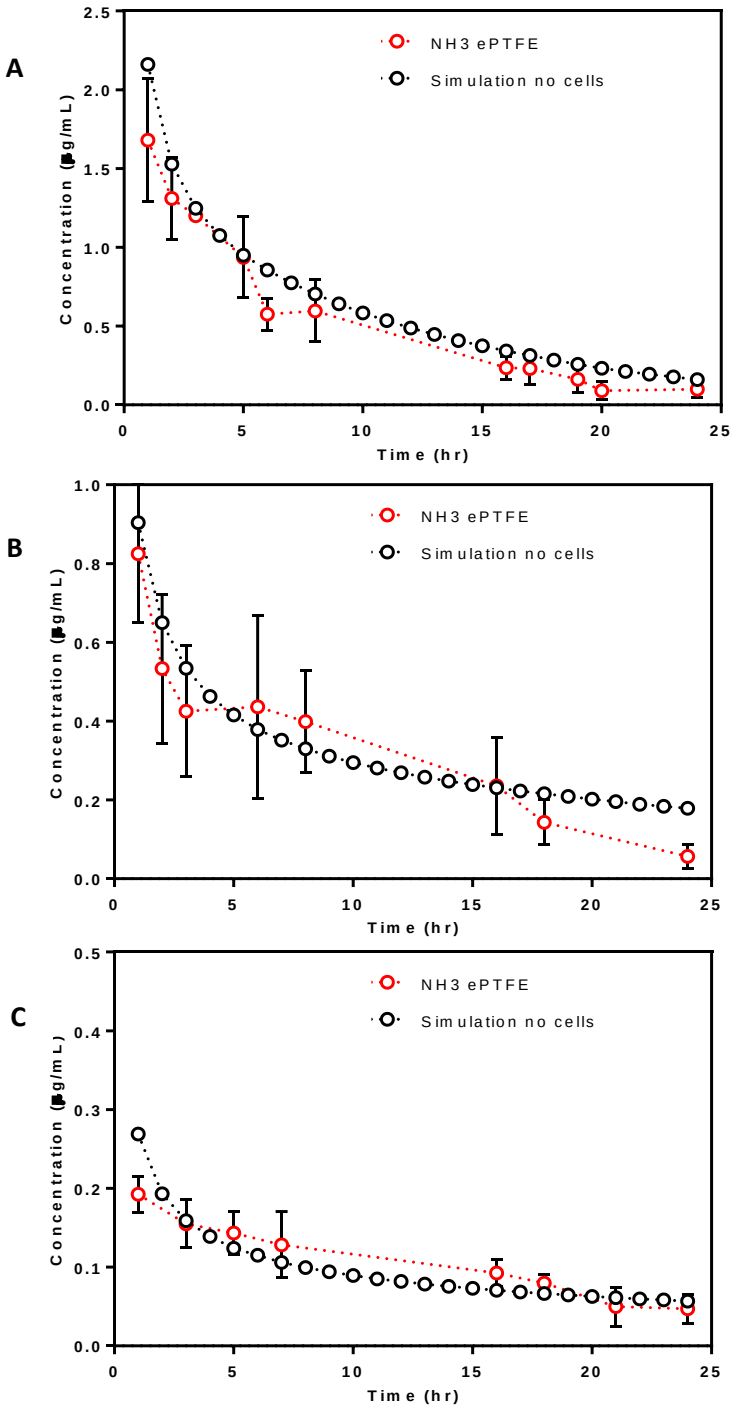

Figure 2-50: Concentration profiles of different molecular weight fluorescently labelled dextrans a) 4kDA, b) 40kDa and c) 70kDa in receptor compartment of Kirkstall QV600 chamber. Studies carried out experimentally (red) and simulated (black) on unseeded NH_3 treated ePTFE membranes. Experimental flow rate = 400µL/min. Data presented as mean ± 1 SD, n=6

Simulation vs Experimental Concentration Profiles of Dextrans in Receptor Compartment of Kirkstall QV600 exposed to 400µL/min Flow with ARPE-19 cells

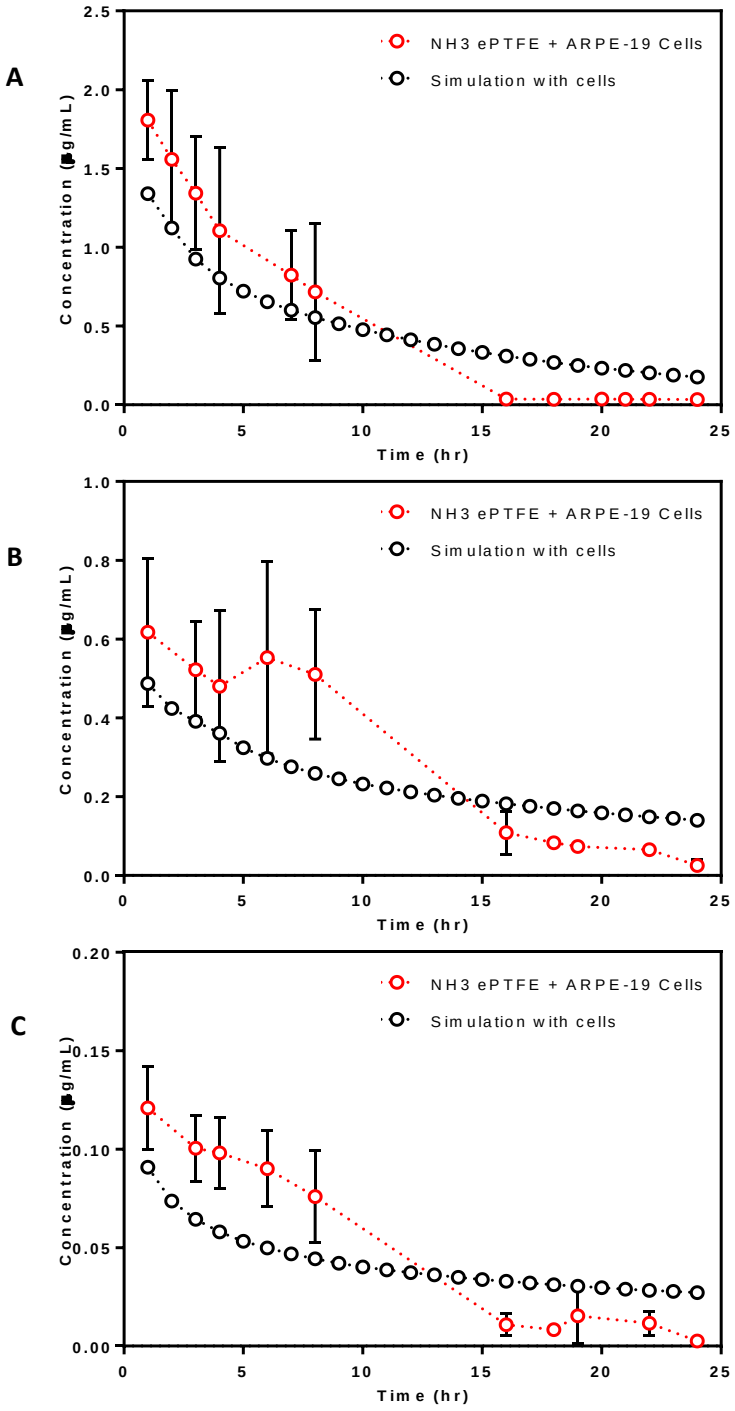

Figure 2-51: Concentration profiles of different molecular weight fluorescently labelled dextrans a) 4kDA, b) 40kDa and c) 70kDa in receptor compartment of Kirkstall QV600 chamber. Studies carried out experimentally (red) and simulated (black) on seeded NH_3 treated ePTFE membranes. Experimental flow rate = 400µL/min. Data presented as mean ± 1 SD, n=6

Concentration Curve Statistics for Simulated vs Experimental Dextran Transport Studies across Unseeded Membranes at 400µL/min

	Area under Curve (AUC, µg.h/mL)	Peak Concentration (C_{max}, µg/mL)	Time of Peak Concentration (t_{max}, hr)	Average Concentration (C_{ave}, µg/mL)
Experimental	11.27	1.70	1	0.62
Simulation	13.11	2.10	1	0.65

Table 2-36: Concentration curve statistics for 4kDa fluorescently labelled dextran transport across unseeded NH_3 treated ePTFE membranes exposed to a flow rate of 400µL/min.

	Area under Curve (AUC, µg.h/mL)	Peak Concentration (C_{max}, µg/mL)	Time of Peak Concentration (t_{max}, hr)	Average Concentration (C_{ave}, µg/mL)
Experimental	6.80	0.90	1	0.38
Simulation	7.21	0.90	1	0.32

Table 2-37: Concentration curve statistics for 40kDa fluorescently labelled dextran transport across unseeded NH_3 treated ePTFE membranes exposed to a flow rate of 400µL/min.

	Area under Curve (AUC, µg.h/mL)	Peak Concentration (C_{max}, µg/mL)	Time of Peak Concentration (t_{max}, hr)	Average Concentration (C_{ave}, µg/mL)
Experimental	2.42	0.19	1	0.10
Simulation	2.20	0.26	1	0.11

Table 2-38: Concentration curve statistics for 70kDa fluorescently labelled dextran transport across unseeded NH_3 treated ePTFE membranes exposed to a flow rate of 400µL/min.

Concentration Curve Statistics for Simulated vs Experimental Dextran Transport Studies across Seeded Membranes at 400µL/min

	Area under Curve (AUC, µg.h/mL)	Peak Concentration (C_{max}, µg/mL)	Time of Peak Concentration (t_{max}, hr)	Average Concentration (C_{ave}, µg/mL)
Experimental	11.32	1.80	1	0.63
Simulation	11.02	1.34	1	0.50

Table 2-39: Concentration curve statistics for 4kDa fluorescently labelled dextran transport across seeded NH_3 treated ePTFE membranes exposed to a flow rate of 400µL/min.

	Area under Curve (AUC, µg.h/mL)	Peak Concentration (C_{max}, µg/mL)	Time of Peak Concentration (t_{max}, hr)	Average Concentration (C_{ave}, µg/mL)
Experimental	6.78	0.62	1	0.30
Simulation	5.46	0.49	1	0.24

Table 2-40: Concentration curve statistics for 40kDa fluorescently labelled dextran transport across seeded NH_3 treated ePTFE membranes exposed to a flow rate of 400µL/min.

	Area under Curve (AUC, µg.h/mL)	Peak Concentration (C_{max}, µg/mL)	Time of Peak Concentration (t_{max}, hr)	Average Concentration (C_{ave}, µg/mL)
Experimental	1.10	0.12	1	0.05
Simulation	0.95	0.09	1	0.04

Table 2-41: Concentration curve statistics for 70kDa fluorescently labelled dextran transport across seeded NH_3 treated ePTFE membranes exposed to a flow rate of 400µL/min.

Simulation vs Experimental Concentration Profiles of Dextrans in Receptor Compartment of Kirkstall QV600 exposed to 2mL/min Flow without ARPE-19 cells

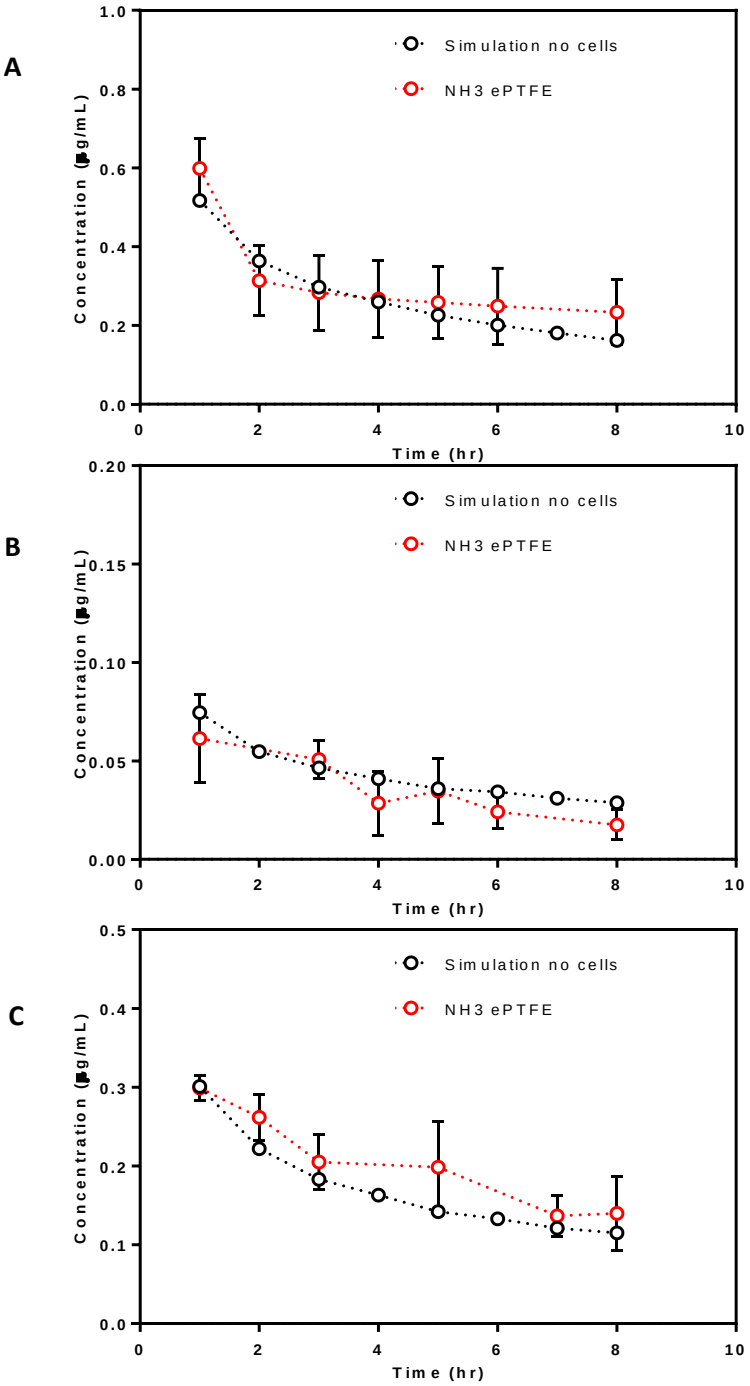

Figure 2-52: Concentration profiles of different molecular weight fluorescently labelled dextrans a) 4kDA, b) 40kDa and c) 70kDa in receptor compartment of Kirkstall QV600 chamber. Studies carried out experimentally (red) and simulated (black) on unseeded NH_3 treated ePTFE membranes. Experimental flow rate = 2mL/min. Data presented as mean ± 1 SD, n=6

Concentration Curve Statistics for Simulated vs Experimental Dextran Transport Studies across Unseeded Membranes at 2mL/min

	Area under Curve (AUC, µg.h/mL)	Peak Concentration (C_{max}, µg/mL)	Time of Peak Concentration (t_{max}, hr)	Average Concentration (C_{ave}, µg/mL)
Experimental	2.02	0.59	1	0.31
Simulation	1.88	0.52	1	0.28

Table 2-42: Concentration curve statistics for 4kDa fluorescently labelled dextran transport across unseeded NH_3 treated ePTFE membranes exposed to a flow rate of 400µL/min.

	Area under Curve (AUC, µg.h/mL)	Peak Concentration (C_{max}, µg/mL)	Time of Peak Concentration (t_{max}, hr)	Average Concentration (C_{ave}, µg/mL)
Experimental	1.39	0.30	1	0.21
Simulation	1.20	0.30	1	0.17

Table 2-43: Concentration curve statistics for 40kDa fluorescently labelled dextran transport across unseeded NH_3 treated ePTFE membranes exposed to a flow rate of 400µL/min.

	Area under Curve (AUC, µg.h/mL)	Peak Concentration (C_{max}, µg/mL)	Time of Peak Concentration (t_{max}, hr)	Average Concentration (C_{ave}, µg/mL)
Experimental	0.25	0.06	1	0.04
Simulation	0.29	0.07	1	0.04

Table 2-44: Concentration curve statistics for 70kDa fluorescently labelled dextran transport across unseeded NH_3 treated ePTFE membranes exposed to a flow rate of 400µL/min.

2.3.2.5 STATIC RELEASE OF IBUPROFEN IN WELL PLATE SIMULATIONS

The concentration profile of ibuprofen was plotted graphically to determine the change in release profile that occurs with a simple change in geometrical arrangement of the SiO and aqueous phases. For each well plate simulation, equal volumes of aqueous and SiO were used however, given the different dimensions of the well plates, the interfacial contact areas decreased as the number of wells in the plate increased. The ibuprofen distribution in the oil domain creates a concentration gradient that tends to its lowest concentration at the interfacial boundary with the aqueous domain. This is most apparent in the 48-well plate simulation. In the 12-well plate, the concentration of ibuprofen is evenly distributed throughout the oil domain from 48hrs onwards, whereas the gradient is maintained in the 24 and 48-well plate up to 72hrs (***Figure 2-53***).

Comparing the quantified percentage release of ibuprofen from the oil into the aqueous in the simulation with the *in vitro* results, the maximum error observed was 15%. This was in the 24-well plate after 24 hours. For the 12-well plate, the difference in percentage release between the simulated and experimental results was 12%, 7% and 7% for 24hr, 48hr and 72hr respectively. Similar low percentage error values were observed in the 48-well plate which had percentage differences of 5%, 5% and 2% at each respective time point. The 24-well plate simulations produced results with the greatest differences in comparison with the *in vitro* data, with the results having 15%, 10% and 7% difference at 24hr, 48hr and 72hr respectively (***Figure 2-55***).

Concentration Fields of Ibuprofen Release in Well Plates over 72 Hours

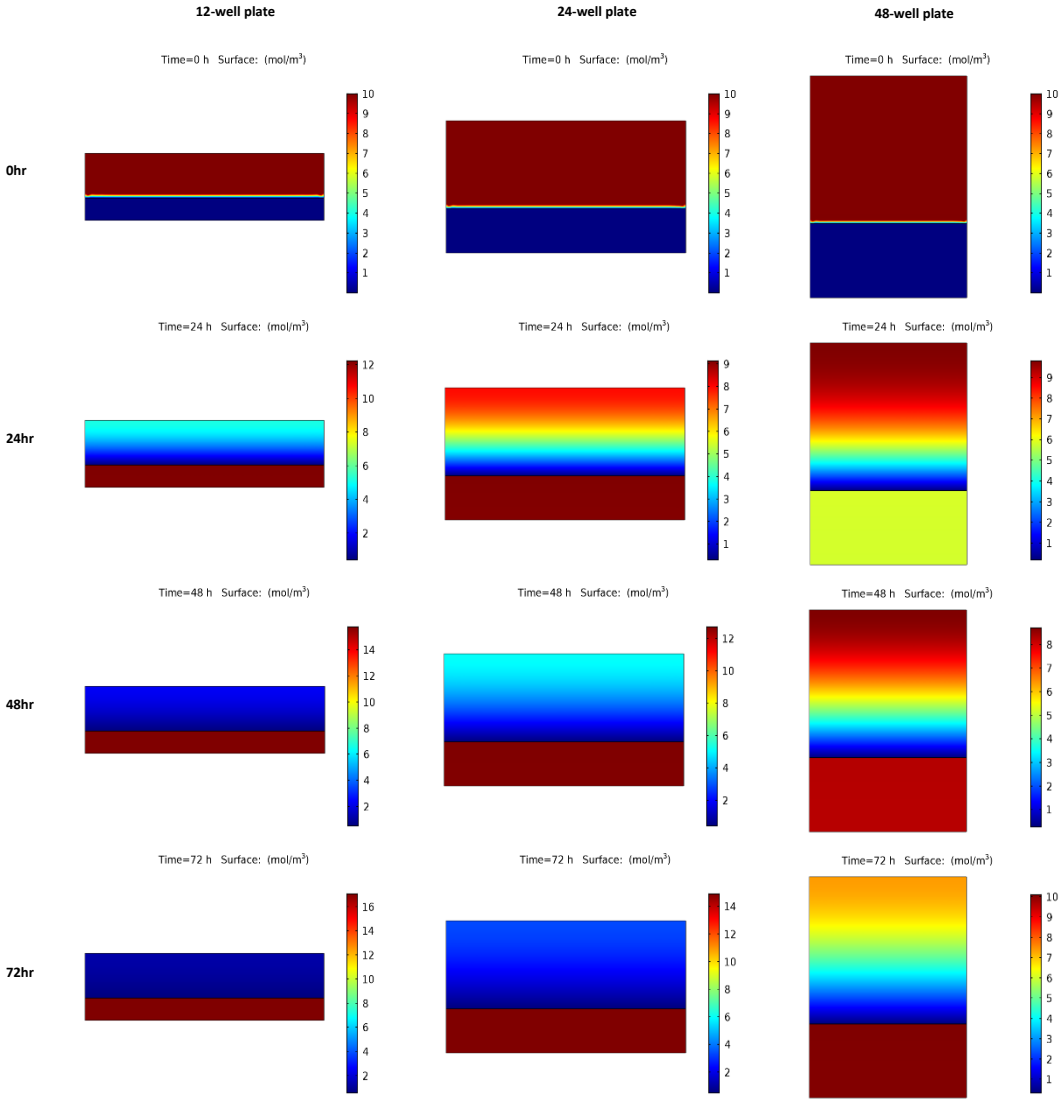

Figure 2-53: Concentration fields of ibuprofen released from silicone oil over 72 hours in a 12-well, 24-well and 48-well plate simulation. Colour scale bar = concentration in mol/m³.

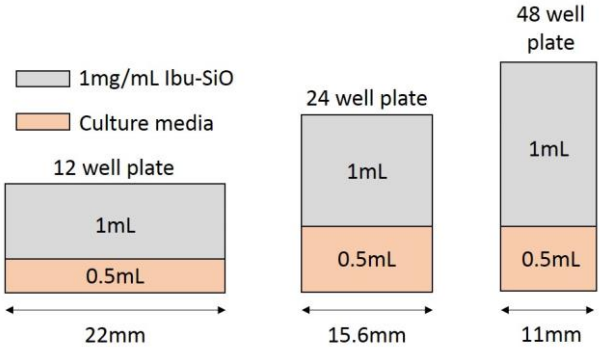

Figure 2-54: Well plate experiment set up.

Simulation vs Experimental Concentration Profile of Ibuprofen Release in Well Plates

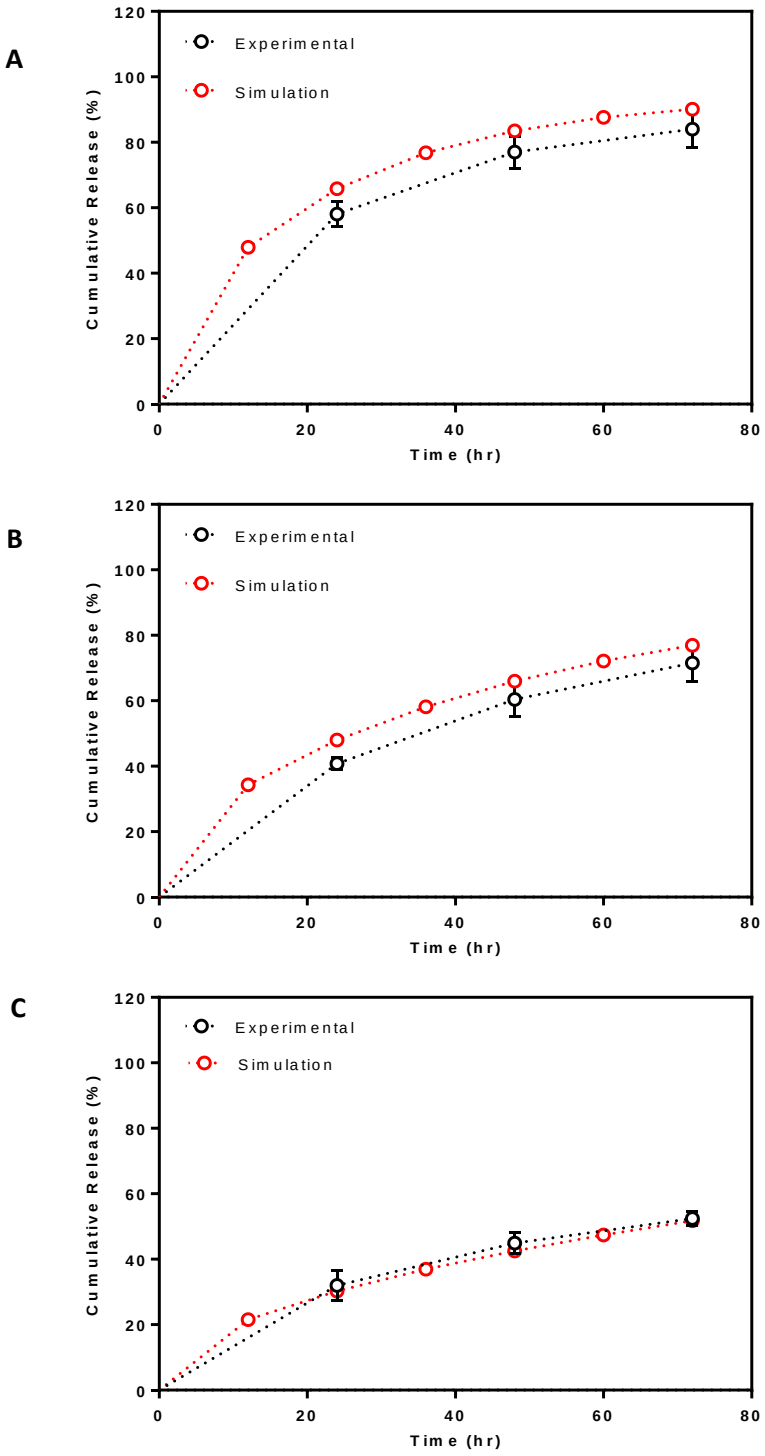

Figure 2-55: Percentage cumulative release of 1mL of 1mg/mL ibu-SiO into 500µL PBS in (a) 12-well plate, (b) 24-well plate, (c) 48-well plate over 72 hours. Studies carried out experimentally (black) and simulated (red). Experimental data presented as mean percentage cumulative release ± 1SD.

2.3.2.6 TRACKING THE FLUID-FLUID INTERFACE AND VELOCITY FIELD DEVELOPMENT IN KIRKSTALL QV600 IBUPROFEN RELEASE STUDIES

Using a moving mesh physics interface to solve for the two-phase (SiO and PBS) system described by this model allows us to track the movement of the interface between the two phases. As the position of this interface could have implications on the flow field and drug release, it was important to be able to trace the movement of this boundary to ensure an accurate representation. As the flow field developed over time, the boundary between the oil domain and the aqueous domain collapsed forming a meniscus between the two phases. This phenomenon is what we observe *in vitro* (photographic image could not be obtained due to translucency of the QV600 chamber) and is expected given the interfacial tension between the two phases described in ***Table 2-22***. After approximately 2 seconds, this system forms a stable arrangement between the two domains and the meniscus remains constant (***Figure 2-56***).

The flow fields formed at 20µL/min, 200µL/min and 400µL/min (***Figure 2-57***) show similarities to those formed in the single phase, membrane system (***Figure 2-44***) shown in section 2.3.2.3. At 20µL/min, however, we see that the low flow rate inlet stream within the aqueous phase appeared to bounce of the oil phase and create a ripple within the primary flow stream. The interaction between the main flow stream and the oil phase also created two recirculating streams within the oil domain itself. This phenomenon is observed for each of the flow rates studied with the split in the two streams shifting towards the inlet as the inlet flow rate increased. Unlike the 2mL/min flow field in the single phase system, the 2mL/min flow profile for the two phase model did not develop large regions of recirculating flow and maintained a single dominating fluid stream from inlet to outlet.

Deformation of the Mesh to Track the Fluid-Fluid Interface

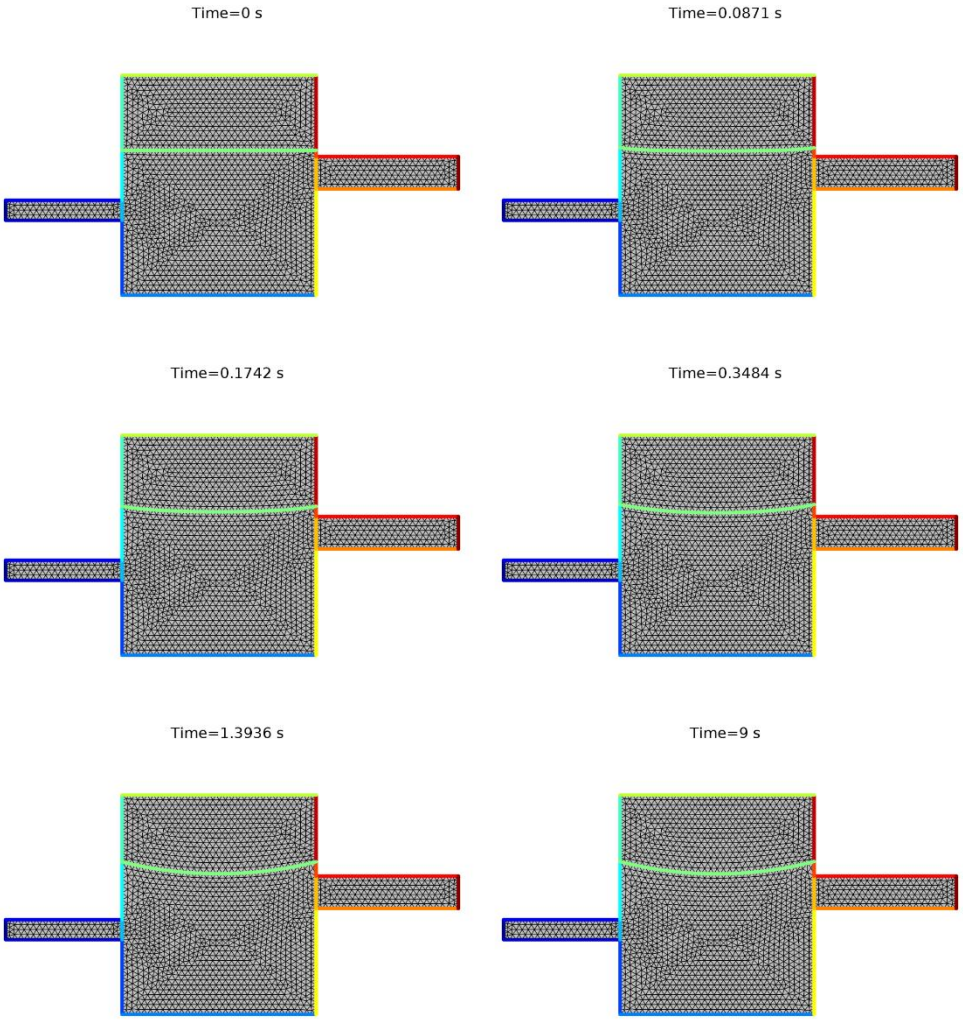

Figure 2-56: Deformation of the mesh over time up to a stable solution indicated by the collapsing of the boundary at the fluid-fluid interface of the two phases (green boundary).

Velocity Fields of Different Flow Rates in the Kirkstall QV600 Ibuprofen Release Studies

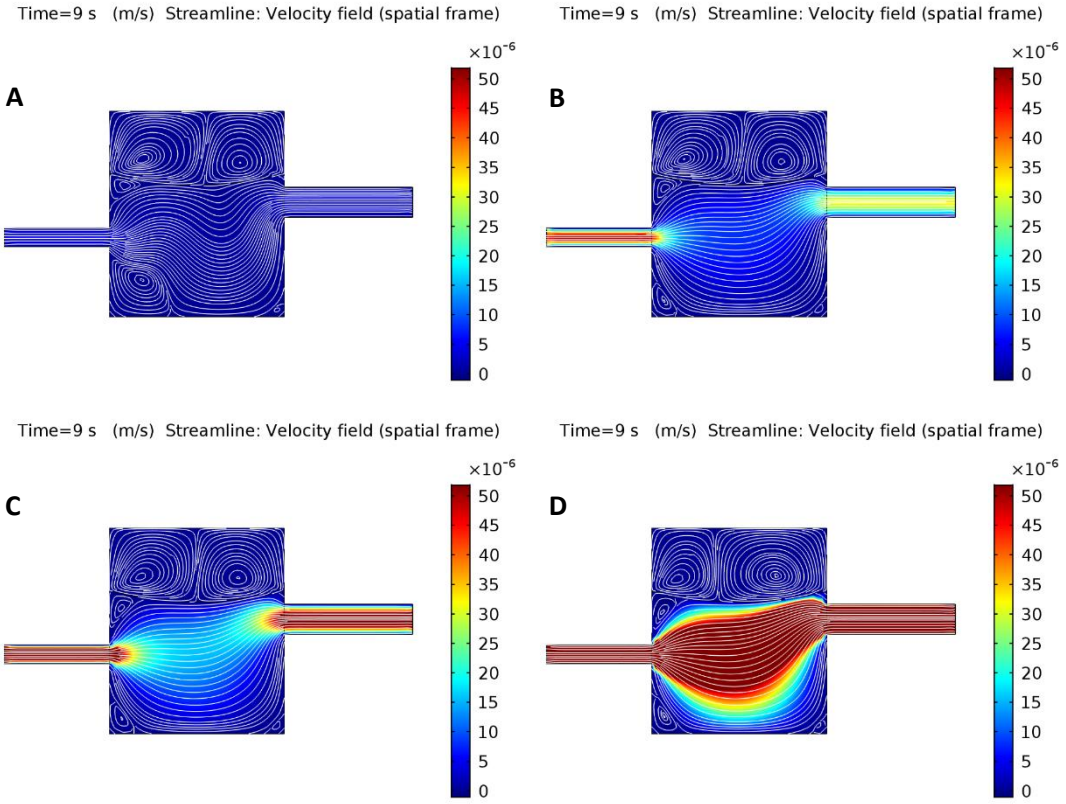

Figure 2-57: Velocity fields for different inlet flow rates used in the Kirkstall QV600 chamber geometry for ibuprofen release studies. Inlet flow rates: (a) 20µL/min, (b) 200µL/min, (c) 400µL/min and (d) 2mL/min. Colour scale bar indicates velocity (m/s). Streamlines show velocity field.

2.3.2.7 CONCENTRATION PROFILES OF IBUPROFEN IN KIRKSTALL QV600 CHAMBER

At the higher flow rates, the concentration of ibuprofen in the aqueous PBS phase showed the same burst release response and exponential decay as the concentration of dextran and this was mirrored in the simulation data. At 20µL/min, there was a rise in concentration up to C_{max} after which a very slow decay in concentration, this was also shown by the computer model which was able to predict the AUC and C_{max} to within 3% and 8% respectively for this given flow rate (***Table 2-45***). The agreement between the simulated and experimental profiles at 200µL/min was also strong for the total exposure in the aqueous domain over the 24 hour time period with AUC data within 8%, however there was a 35% overestimation in maximum concentration within the same domain (***Table 2-46***). Interestingly, at 2mL/min the simulated data underestimated C_{max} by 17% (***Table 2-48***) and appeared to underestimate the concentration in the receptor domain across each time point, again suggesting no correlation between the accuracy of the computer model and the inlet flow rate prescribed to it (***Figure 2-58B, Figure 2-59B, Figure 2-60B, Figure 2-61B***)

The concentration fields within the oil domain showed little difference as the flow rate increased other than to shift the centre of diffusion either towards the outlet (200µL/min and 400µL/min) or towards the inlet (2mL/min) (***Figure 2-58***, ***Figure 2-59***, ***Figure 2-60***, ***Figure 2-61***). For each flow rate the ibuprofen was never completely cleared from the oil domain by the final 72 hour time point. The simulation predicted that a small region of oil at the top of the domain, in contact with the exterior wall of the chamber through to the centre of the domain, maintained a low concentration of ibuprofen.

Concentration Fields and Receptor Domain Profile of Ibuprofen in the Kirkstall QV600 Chamber at 20µL/min

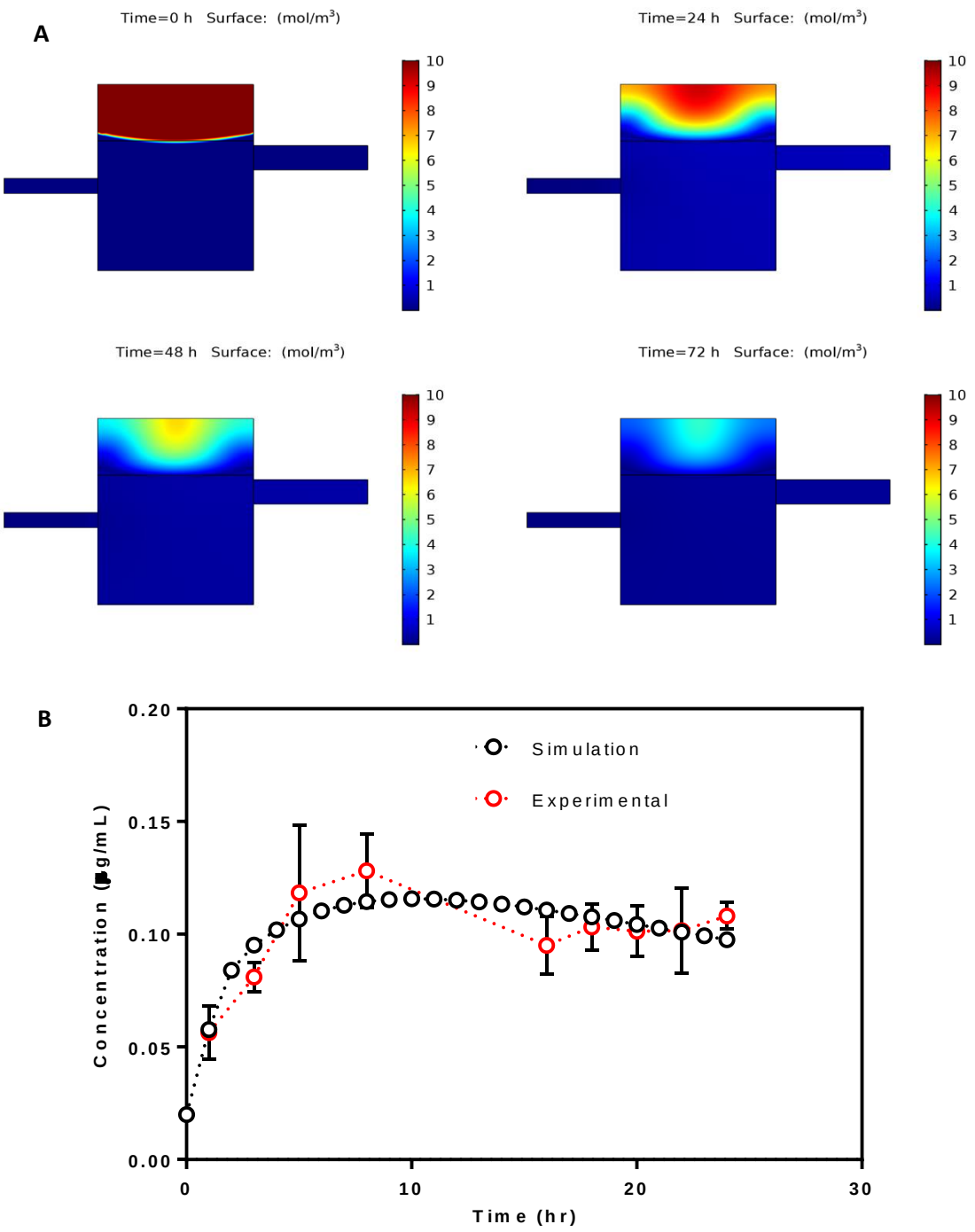

Figure 2-58: (a) Concentration field solution for ibuprofen concentration across the Kirkstall QV600 chamber at 0, 24, 48 and 72 hr. Colour scale bar indicates concentration in mol/m³. (b) Experimental vs simulated concentration profiles of ibuprofen in receptor compartment of Kirkstall QV600 chamber. Flow rate = 20µL/min. Experimental data presented as mean concentration ± 1 SD, n = 6

Concentration Fields and Receptor Domain Profile of Ibuprofen in the Kirkstall QV600 Chamber at 200µL/min

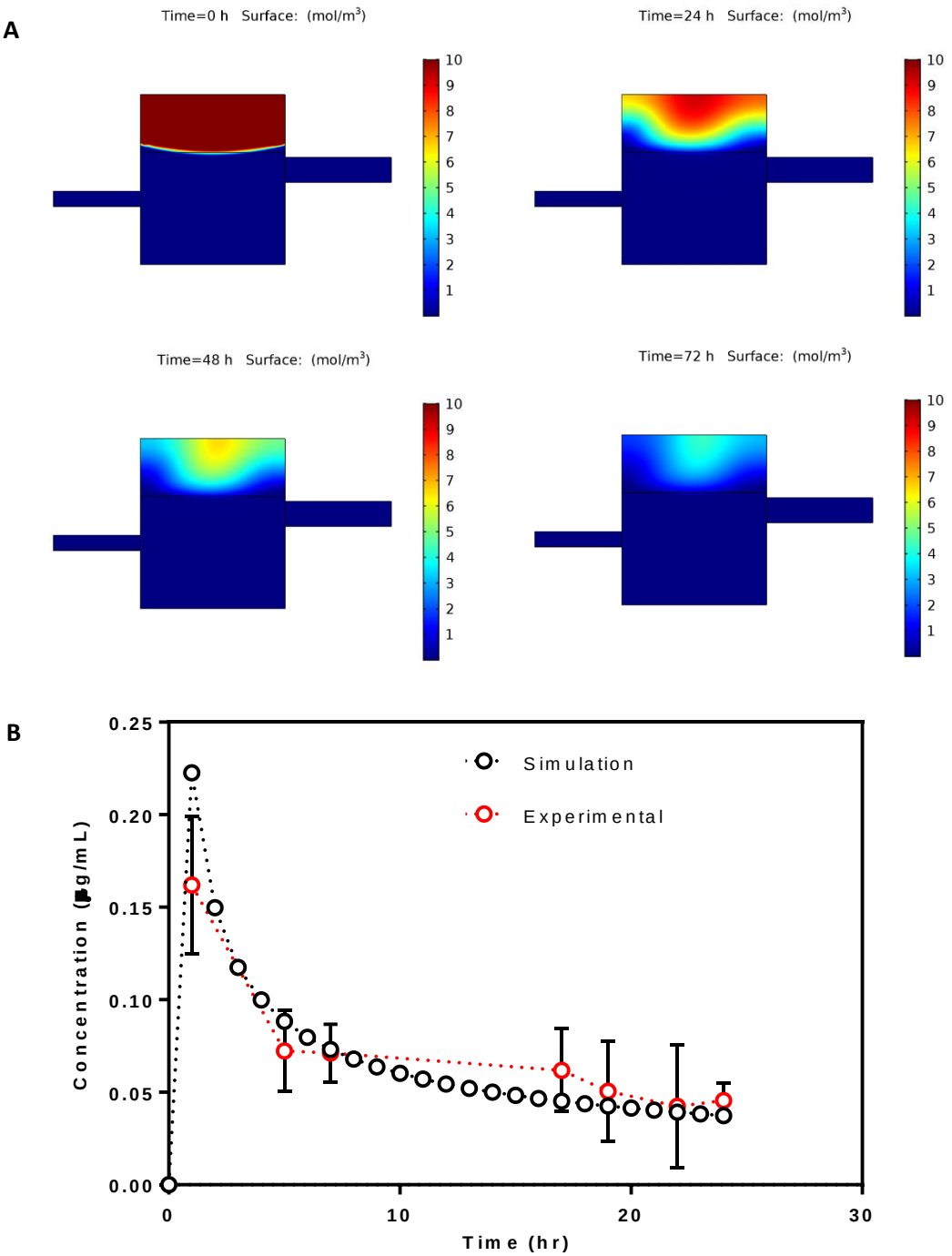

Figure 2-59: (a) Concentration field solution for ibuprofen concentration across the Kirkstall QV600 chamber at 0, 24, 48 and 72 hr. Colour scale bar indicates concentration in mol/m³. (b) Experimental vs simulated concentration profiles of ibuprofen in receptor compartment of Kirkstall QV600 chamber. Flow rate = 200µL/min. Experimental data presented as mean concentration ± 1 SD, n = 6.

Concentration Fields and Receptor Domain Profile of Ibuprofen in the Kirkstall QV600 Chamber at 400µL/min

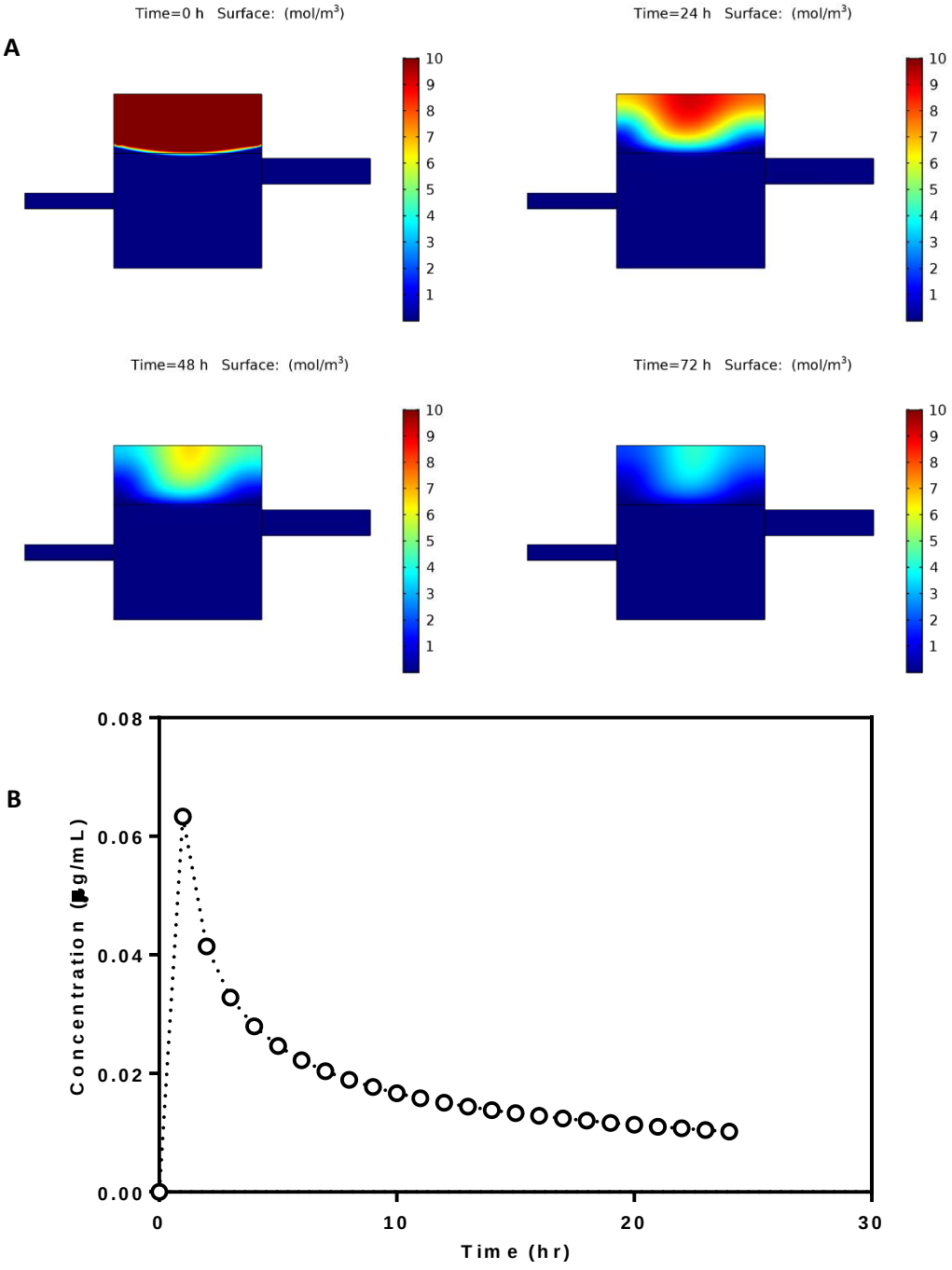

Figure 2-60: (a) Concentration field solution for ibuprofen concentration across the Kirkstall QV600 chamber at 0, 24, 48 and 72 hr. Colour scale bar indicates concentration in mol/m³. (b) Simulated concentration profile of ibuprofen in receptor compartment of Kirkstall QV600 chamber. Flow rate = 400µL/min.

Concentration Fields and Receptor Domain Profile of Ibuprofen in the Kirkstall QV600 Chamber at 2mL/min

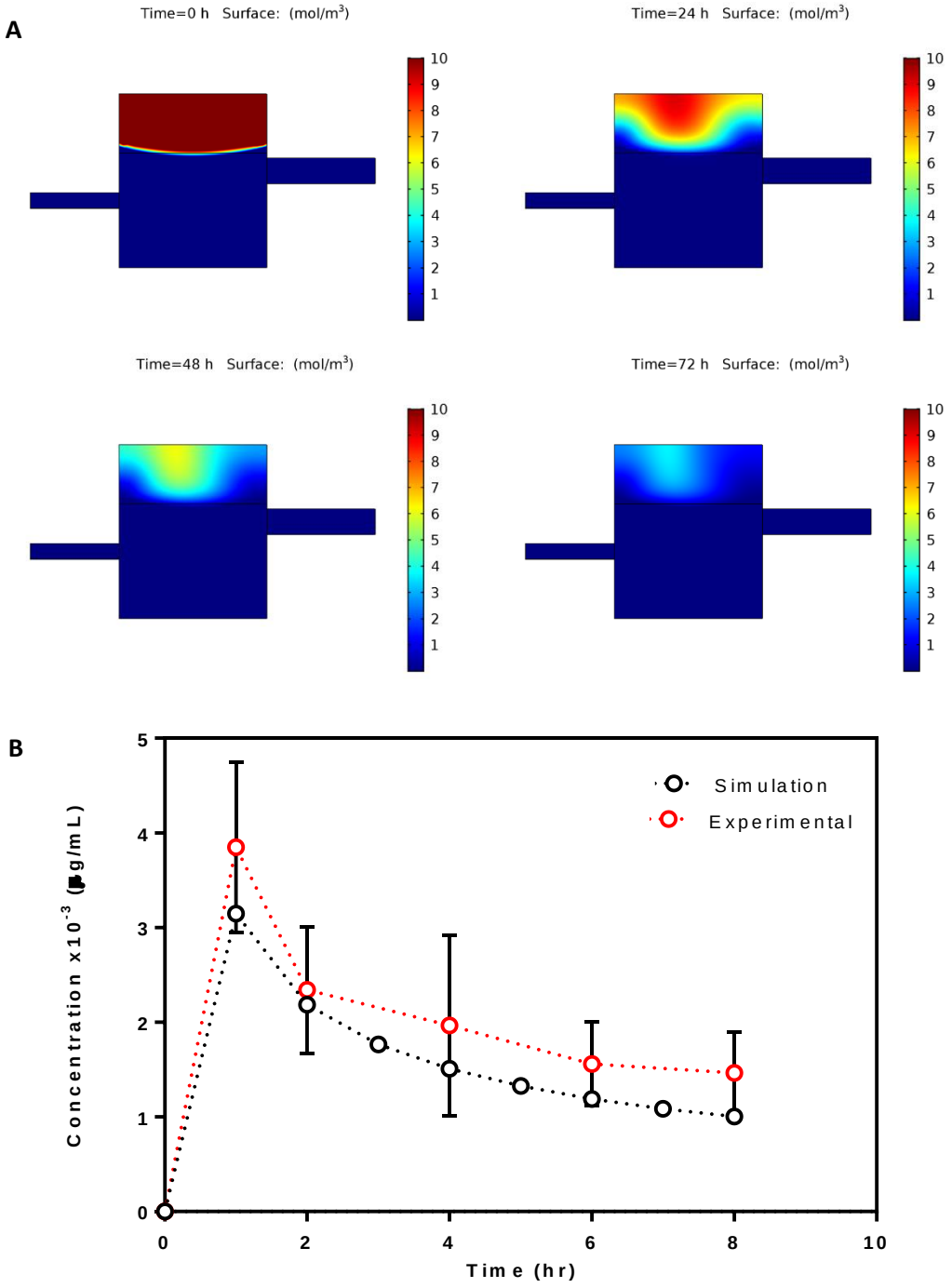

Figure 2-61: (a) Concentration field solution for ibuprofen concentration across the Kirkstall QV600 chamber at 0, 24, 48 and 72 hr. Colour scale bar indicates concentration in mol/m³. (b) Experimental vs simulated concentration profiles of ibuprofen in receptor compartment of Kirkstall QV600 chamber. Flow rate = 2mL/min. Experimental data presented as mean concentration ± 1 SD, n = 6.

Concentration Curve Statistics for Simulated vs Experimental Ibuprofen Release Studies across a Range of Flow Rates

	Area under Curve (AUC, µg.h/mL)	Peak Concentration (C_{max}, µg/mL)	Time of Peak Concentration (t_{max}, hr)	Average Concentration (C_{ave}, µg/mL)
Experimental	2.41	0.13	8	0.10
Simulation	2.48	0.12	10	0.10

Table 2-45: Concentration curve statistics for ibuprofen release from silicone oil in the Kirkstall QV600 chamber exposed to a flow rate of 20µL/min.

	Area under Curve (AUC, µg.h/mL)	Peak Concentration (C_{max}, µg/mL)	Time of Peak Concentration (t_{max}, hr)	Average Concentration (C_{ave}, µg/mL)
Experimental	1.62	0.16	1	0.07
Simulation	1.64	0.22	1	0.06

Table 2-46: Concentration curve statistics for ibuprofen release from silicone oil in the Kirkstall QV600 chamber exposed to a flow rate of 200µL/min

	Area under Curve (AUC, µg.h/mL)	Peak Concentration (C_{max}, µg/mL)	Time of Peak Concentration (t_{max}, hr)	Average Concentration (C_{ave}, µg/mL)
Simulation	0.46	0.06	1	0.02

Table 2-47: Concentration curve statistics for ibuprofen release from silicone oil in the Kirkstall QV600 chamber exposed to a flow rate of 400µL/min

	Area under Curve (AUC, µg.h/mL)	Peak Concentration (C_{max}, µg/mL)	Time of Peak Concentration (t_{max}, hr)	Average Concentration (C_{ave}, µg/mL)
Experimental	0.02	0.003	1	0.001
Simulation	0.01	0.003	1	0.001

Table 2-48: Concentration curve statistics for ibuprofen release from silicone oil in the Kirkstall QV600 chamber exposed to a flow rate of 2mL/min.

2.4 DISCUSSION

2.4.1 SUCCESSFUL GROWTH OF ARPE-19 CELL MONOLAYERS ON AMMONIA GAS PLASMA TREATED EPTFE MEMBRANES

ARPE-19 cells are a non-immortalised spontaneously arisen human RPE cell line with characteristics which make them a useful tool in *in vitro* modelling. It is a well-established and well-characterised cell line which demonstrates the normal phenotype of primary RPE cells *in vivo* and has been shown to express RPE-specific markers such as RPE65 and CRALBP. A major benefit of the ARPE-19 cell line for this present study is that it is able to form differentiated polarised monolayers which allow for the evaluation of the transport of molecules and drugs through the cell monolayer barrier [177, 178]. Ultimately, in order to build a truly representative *in vitro* model of the outer blood retinal barrier, a more appropriate cell type would need to be investigated, such as primary RPE cells, or a co-culture model incorporating other cell types found within the outer BRB structure, such as those found in the choroidal vasculature, but this was beyond the scope of this project.

In vivo, the RPE cells sit atop of a thin layer of extracellular matrix, known as Bruch's membrane, which separates the epithelial layer from the choroid. The integrity of this membrane is vital in supporting an intact, functional monolayer of healthy RPE cells. Previous studies involving models of the outer blood retinal barrier have used materials such as amniotic membrane [104, 179], fibrin gel [180], and poly(ethylene terephthalate) [181] with varying success. Expanded polytetrafluoroethylene (ePTFE) is a porous, synthetic material that has been widely used in medical devices and biomaterials for many years and there have been previous studies to assess its suitability as a transplantable replacement for the native Bruch's membrane (BM). Its material properties make it an ideal candidate as a substitute for the BM. It is biocompatible, stable, flexible and porous although 'as received' ePTFE is hydrophobic and does not promote cell adhesion which is an undesirable property for this study [182, 183]. There are methods available to overcome this problem which involve surface modification of the ePTFE to alter the surface chemistry and provide more favourable cell support whilst also maintaining the bulk properties of the material which make it an appropriate substrate.

It has been shown that ammonia gas plasma treatment of ePTFE increases the hydrophilicity of the membrane and promotes the growth of both ARPE-19 cells and human primary RPE

(hRPE) cells [146, 150, 184]. The plasma technology allows the fibrous, porous structure of ePTFE membrane to be maintained whilst varying the chemistry of the surface to enhance desirable properties in the material, for example decreased water contact angle [184]. The principle of this method involves defluorination of the fluoropolymer surface which then allows incorporation of polar groups following storage in distilled water, these polar groups on the surface are what contribute to increased ability of the cells to adhere [185, 186]. This study utilised ammonia gas plasma treated ePTFE membranes and compared the growth of ARPE-19 cells on these membranes with their growth on tissue culture plastic, with the aim of determining the time required for the ARPE-19 cells to form stable monolayers required to study the transport of molecules and drugs across the cell/material barrier.

Similarities in the growth curves of the ARPE-19 cells grown on NH_3 treated ePTFE membranes and the TCP were observed. Although the cell number was lower on the membranes at each time point measured over the 14 days, the difference was not statistically significant suggesting that the growth of the cells was not dependant on the culture substrate. These results corroborate the results of a study by Krishna et al. who also showed a small decrease in cell numbers on NH_3 treated ePTFE compared with TCP over 15 days [150]. Both substrates showed an increase in cell number up to day 10 when the numbers appear to plateau which is an indication that the ARPE-19 cells have formed a stable monolayer and have reduced their growth rate although some overgrowth of the cells was observed in the phase contrast images of the cells cultured on TCP at 14 days. Due to the opacity of the NH_3 treated ePTFE membranes, the phenotype of the cells grown on this substrate was observed using immunofluorescence.

To determine the integrity of the epithelial monolayer barrier, the cells were stained for the tight junctional protein zonula occludin-1 (ZO-1). ZO-1 is a transmembrane protein found on the peripheral membranes of epithelial cells and is vital in the formation of tight junctions required for cell-cell adhesion. There are over 40 different proteins that are involved in the formation of tight junctions. ZO-1 is one of a group of intracellular plaque proteins which provide support between the transmembrane proteins and the actin cytoskeleton [187]. Both substrates exhibited positive staining of ZO-1 across the entirety of the substrate at day 10, with clear, distinct expression at the cell borders suggesting cell-cell adhesion and intact barrier formation of the monolayer. This qualitative analysis of the barrier was further supported by the TEER results which increased to day 10 after which there was a plateau. Other studies have shown similar results with the reported time to reach maximum TEER

ranging from 7 days to 14 days [163, 188]. The TEER of ARPE-19 cells grown on filter membranes has been shown to reach a maximum of 50-100 Ω/cm^2 in culture although the addition of supplements to the culture medium can increase this value further [141, 163]. This study has shown that ARPE-19 cells can reach a TEER of 59.4 Ω/cm^2 after 10 days when cultured on NH_3 treated ePTFE membranes in DMEM-F12 medium supplemented with 2% FBS. Given the values for TEER obtained using these conditions, in comparison to those reported in the literature, and the positive expression of ZO-1 across the monolayer, day 10 was determined as the point at which the cells had formed a functional barrier and could be used in dynamic flow cultures and permeability studies.

2.4.2 THE INTEGRITY OF ARPE-19 CELL MONOLAYERS CULTURED UNDER FLOW CONDITIONS IS DEPENDENT ON THE FLOW RATE OF THE CULTURE MEDIUM

In vivo, the vascular requirements of retina are supplied by two types of capillary; (1) the central retinal capillaries and (2) the choriocapillaris. The choriocapillaris is a network of capillaries which sit adjacent to the Bruch's membrane and serve to provide the nutritional needs of the RPE cell layer. The retinal-facing side of these capillaries is fenestrated and supports the transport of nutrients to the RPE as well as the clearance of waste products away from the cells [189, 190]. The flow of plasma within these vessels provides the clearance mechanism for waste products produced by the RPE cells which are secreted basally across the Bruch's membrane. Previous studies have reported the flow rate within the choriocapillaris to be 9.45mL/hr or 160µL/min [191] and disruptions or alterations in the flow have been attributed to problems with homeostasis within the RPE [192, 193]. Few studies have investigated the *in vitro* culture of ARPE-19 cells in the presence of fluid flow however there have been studies that show the benefits of flow in other epithelial cells types [194, 195].

In these studies, ARPE-19 cells grown on NH_3 treated modified ePTFE membranes for 10 days were then cultured within microfluidic bioreactor chambers for a further 24 hours. Culture medium was perfused through the system and the basal side of the membranes was exposed to a range of medium flow rates. In comparison with the static cultures, exposing the cultures to flow had no effect on the number of cells regardless of the flow rate, suggesting the flow had no influence on the growth rate of the cells nor detached any of the cells and removed

them from the system. However, the metabolic activity of the cells was decreased in the cultures exposed to the highest flow rate of 400µL/min. Given that there was no decrease in cell number, the decrease in metabolic activity suggests that the highest flow rate has a different effect on the cells. This could be because the cells have formed a fully stable monolayer quicker and require less metabolic turnover or the higher flow may have had some detrimental effect on the cells. It would be interesting to investigate this further to gain a better understanding of the effects of basal flow on the cellular activity. This was echoed in the ability of the cells to maintain the integrity of their monolayer barrier. After 24 hours exposure to 400µL/min, the TEER of the monolayers significantly decreased in comparison to the static cultures and clusters of the mesenchymal cell marker, αSMA also appeared across the monolayers. The presence of αSMA within polarised epithelial cell cultures suggests the cells are undergoing a process known as epithelial-mesenchymal transition (EMT)[196]. During EMT, polarised epithelial cells whose basal surface normally remains in contact with the basement membrane undergo biochemical changes which allow the cells to assume a mesenchymal phenotype and increases there proliferative and migratory capacity [197]. This behaviour is seen in RPE cells in patients with proliferative vitreoretinopathy.

At 400µL/min, the fluid creates greater shear stresses on the basal surface of the ARPE-19 cell monolayer than the lower flow rates. This is due to the increased velocities which are established from the higher flow causing greater shear forces at the boundaries within the chamber. Previous studies have shown that continuous exposure to abnormally high fluid shear stresses causes alterations in the structure of epithelial cell monolayers and organisation of the tight junction proteins [195, 198]. It has also been suggested that high shear stresses act as a stimulus which can trigger the EMT process [199]. However, at lower flow rates, significant increases in the TEER were observed and many other studies have reported decreased permeability and improved barrier function after exposing cultures to fluid shear stresses. Venkatamarana et al. show that low level shear stresses enhanced the epithelial barrier function of human bronchial epithelial cells [200]. Similar results have been shown in endothelial cultures as well, with Cucullo et al. showing upregulation of tight junction proteins following exposure to low level shear stresses [201].

The results suggest that the introduction of flow to ARPE-19 cultures can enhance the barrier function of the monolayer up to a limiting point after which the shear stresses created cause a breakdown in the monolayer. The effects of flow therefore become important when

investigating the permeability of the barrier as different flow rates have different effects. This study only calculated the permeability of the cultures after 10 days in static culture. In order to produce permeability and diffusion coefficients to use in a computer model which is a true representation of the barriers, the coefficients would also need to be calculated post- exposure to fluid flow. These experiments were not done in this study.

2.4.3 FLUORESCENTLY LABELLED DEXTRANS TRANSPORTED THROUGH THE MEMBRANES EXHIBIT DIFFERENT CONCENTRATION PROFILES DEPENDANT ON FLOW RATE

This study aimed to provide data which could be used to validate a complementary computer simulation of the system based on input parameters defined by the experimental conditions. The parameter which was easily measureable across both the *in vitro* and computer models was concentration in the receptor compartment of the chamber over time. At 2 hour intervals, samples were taken from the receptor compartment and the concentration of FD in the compartment at that time point was measured, this was repeated over 24 hours. Given the nature of the study, there were certain time points at which samples were unable to be taken due to time of day and also in an attempt to minimise contamination risk. This is one of the motivations behind using computer simulations for such studies as they allow data to be obtained which may be unable to be obtained in the physical experiment.

The permeability of the RPE/ePTFE complex affects the elimination rate of drugs from the vitreous cavity. In order to predict the permeabilities of new drugs and compounds, a systemic data approach on the permeability of a range of molecules as a function of their size is needed. There are other features of compounds which affect their permeability across the barrier, these include charge and lipophilicity, however these were not investigated here. This study investigated the permeability of three different molecular weight FITC-conjugated dextrans: 4kDa, 40kDa and 70kDa. The results from the static transport studies showed that 4kDa and 40kDa FD were able to move through the barrier, to the point of equilibrium, regardless of the presence of cells. The passage of 70kDa FD was considerably decreased in comparison to the smaller molecules, this was to be expected as previous studies have reported 70kDa to be the limit at which diffusion can occur across RPE cells [202]. The results for permeability achieved in this study are in keeping with those found in the literature and so the values obtained from the static experiments were carried forward for use in the

computational simulations [202, 203]. It is important to note that RPE cells are able to transport larger molecules across the OBRB via mechanisms such as active transport. Studies have shown that RPE cells are able to transport dextran as big as 155kDa [184, 204], however only passive diffusion was of interest for this study.

Introducing flow to the permeability experiments allowed the investigation of its impact on the clearance of the molecules away from the cell layer, analogous to the choriocapillaris flow present *in vivo*. The results showed that changing the flow rate can alter the concentration profile in the receptor chamber. At the lowest flow rate, the concentration of FD in the receptor compartment rose to a peak concentration over the first 3-4 hours after which the FD is continuously cleared from the chamber, this was consistent across all molecular sizes of FD. In pharmacokinetics, this concentration profile is normally seen in plasma samples taken after a single oral dose of a drug, i.e. an administration technique which requires absorption into the bloodstream. In this case there is an initial absorption phase up to the maximum concentration which is followed by an elimination phase [205]. This pattern was not repeated at the higher flow rates. The 200µL/min to 2mL/min experiments had concentration profiles comparable to those seen after a single intravenous dose, i.e. the drug is immediately administered to the bloodstream, a constant elimination phase. These results suggest that at very low flow rates, the diffusion of the dextran is the overriding transport physics within the system. At higher flow rates, the convection of the molecules in the fluid flow field dominates. This could be an important factor to consider when designing dynamic drug release and transport studies. In order to understand how compounds are transported through the *in vivo* environment, these dynamic factors need to be accounted for in *in vitro* models.

Previous studies have tried to determine which structure within the outer BRB provides the greatest barrier to compound movement across it. Miller et al. showed that the choroidal resistance, including the Bruch's membrane, provided only 10% of the resistance measured across a choroid-RPE complex isolated from bovine samples [206]. They suggest that it is the tight junctions between the RPE cells which provide the greatest resistance to transport across the barrier. In the presence of an ARPE-19 cell monolayer, the concentration in the receptor compartment is consistently lower than in the acellular membrane experiments. The exception to this pattern was the experiments conducted at 400µL/min. Here the concentration curves of the membrane and membrane/cell complex cross at points and similar concentrations are observed in the chambers. This could be attributed to the

breakdown of the tight junctions between the cells caused by the shear stress from the fluid flow as shown in section 2.2.3.2. The decrease in TEER observed and the distortion in ZO-1 staining at the cell-cell borders imply a loss of barrier functionality of the monolayer which would increase permeability of the barrier and allow a greater concentration of FD to move into the receptor compartment.

2.4.4 IBUPROFEN CONTAINING SILICONE OIL AS AN IMPLANTABLE DRUG DELIVERY DEVICE

Silicone oil (SiO) tamponades are currently used clinically to replace the vitreous following complicated or severe cases of retinal detachment, particularly in patients who have a high risk of developing fibrotic diseases such as proliferative vitreoretinopathy (PVR) following treatment. The placement of the tamponade creates an aqueous exclusion zone around the wound site as the SiO bubble maintains contact with the retina. The exclusion of aqueous fluid hinders its movement into the subretinal space and looks to prevent any inflammatory factors found within the aqueous from entering the wound site and initiating the inflammation process, which can lead to the migration of RPE cells into the vitreous cavity. It has been proposed that adjunctive drug treatments could improve outcomes in patients treated for RD and PVR. Repeated intravitreal injections of therapeutic drugs into the vitreous of the eye is currently one of the best clinical approaches to attaining sustained exposure of drugs in the posterior segment for the treatment of such conditions. By incorporating therapeutic agents into the silicone oil tamponades it may allow the oil to serve a subsidiary purpose as an extended-release drug delivery device, which could prolong therapeutic levels of the drug at the back of the eye compared with the current techniques. The majority of drugs that have been studied as potential treatments for PVR, such as triamcinolone, daunomycin and growth factor inhibitors are water soluble and therefore have poor solubility in SiO [37]. Ibuprofen is a lipophilic drug and thus is readily soluble in SiO. It is classified as a non-steroidal anti-inflammatory drug (NSAID) and although it has yet to be studied as a treatment in PVR, its characteristic anti-inflammatory response and lipophilic nature made it a suitable candidate for this study [207].

The results observed in the release of ibuprofen from silicone oil in static well plates (section 2.2.3.5) showed that in a 12-well plate, the majority of the ibuprofen had been released from the silicone oil into the PBS after 72 hours. Where the PBS had been replenished at each 24

hour time point, the cumulative percentage release of ibuprofen was 98% after 72 hours compared with 84% in those experiments where the PBS was not replenished. *In vivo*, aqueous humor turnover in the anterior segment is estimated to occur at approximately 2.4µL/min [208] therefore it is likely that the replenishment of the PBS in the well every 24 hours more accurately represents the concentration gradient that would be found *in vivo*. In those conditions, the percentage release of ibuprofen from the SiO over 72 hours is equal to 98%, 82% and 58% in the 12-well, 24-well and 48-well plates respectively. In each case, the volumes of ibu-SiO and PBS in each well were equal, however, due to the dimensions of the wells, the interfacial contact areas between the two fluids decreased as the number of wells in the plate increased. This decrease in interfacial contact area reduces the area across which diffusion of the ibuprofen can take place which gives rise to the differences in cumulative release of the drug over the 72 hours. This is an important factor to consider when scaling experiments of this nature and highlights the need for consistency in the testing of such drug delivery materials. This is one of the motivations of developing complementary *in silico* models of such systems as they can provide estimations of changes in release profiles across vast ranges of different parameters in a more time efficient manner. In comparison with a study conducted by Steffansen et al. which also investigated the release of a lipophilic drug, 5-flurouracil (5FU), from silicone oil, the release of ibuprofen is much slower in comparison to the half-life of 3.5 hours that they report [91]. However, treatment courses for PVR are normally conducted over a 6-8 week period, therefore the release of ibuprofen from SiO would need to be extended in order to make this a viable technology. Cauldbeck et al. showed that by modifying the SiO to include solubilised copolymers, the release of ibuprofen as well as another lipophilic drug, retinoic acid (RA), which has anti-proliferative effects, can be extended up to 9 days for ibu and as long as 72 days for RA [209]. Additionally, the same group they have shown that polymeric modification of the drug, in this case all-trans retinoic acid (atRA), can also extend the release up to a clinically relevant 7 weeks [71]. In both of these studies, the release experiments were conducted in 24-well plates. It would interesting in the future to investigate modified SiO/drug systems using the *in silico* models, which, could potentially aid in predicted and identifying the most suitable modifications in a more time and cost-effective manner, assuming that the degradation and release mechanisms of the systems were well characterised.

Static release experiments cannot truly represent the natural dynamic environment of drug movement that occurs *in vivo*. Studying the ibu-SiO device within the Kirkstall QV600

chamber allows us to observe the flow-dependent release and clearance of the ibuprofen from the SiO. The results observed in this study show that the inlet flow rate of the flow field present can alter the concentration profile of ibuprofen within the PBS containing receptor compartment. As with the dextran movement across the membrane discussed in section 2.4.3, at the lowest flow rate, 20µL/min, there was a sharp increase in concentration over the first 8 hours after which there was a very slow decrease in concentration of the following 16 hours which appears to plateau over the later time points. In contrast, the higher flow rates show a burst release and then constant decay in concentration. This change in release profile could be important to consider in terms of maintaining a therapeutic range of ibuprofen in the target area. One of the limitations of these experiments is that the release of ibu from SiO across a cell barrier was unable to be measured. The proteins present within the culture media needed to maintain a healthy, viable cell monolayer, produce peaks in the UV absorbance spectrum used to measure ibu concentration within the samples. These peaks interfere with the signal produced by the ibu in the sample and produce incomprehensible results. For this reason the release of ibu was measured into PBS. Future work should incorporate the desirable features of both of the systems described in this study, i.e. the dextran permeability and the ibuprofen release from SiO. Using an ibuprofen detection method that can measure the concentration in culture medium would allow the cells to be maintained within the chamber but also to measure the ibuprofen release from the SiO across the cell barrier.

2.4.5 AGREEMENT BETWEEN SIMULATED AND EXPERIMENTAL RESULTS SHOWS COMPUTER MODELS CAN BE USEFUL PREDICTIVE TOOLS

Computational models, such as the ones incorporating fluid dynamics, present the advantage of accurately describing the system behaviours when its constitutive parameters are varied. Unlike the traditional experiments, after thorough validation and benchmarking, these models can be used to describe complex systems in a fast, inexpensive, accurate and reliable manner. Moreover, a vast parameter field can be tested and considered, enabling the analysis and comparison of different physical processes such as fluid flow or drug transport and diffusion. Computational models have the potential to help towards understanding the complex structure of biological systems and their behaviour. The accuracy of the input parameters and boundary conditions applied to the computational model dictate the accuracy and reliability of the results that the simulation will produce. In this

study, parameters such as the permeability/diffusion coefficients and rheological properties, were determined from data collected experimentally. After collecting all the necessary parameters, these could then be applied to a computer model which includes mechanisms which investigate the evolution of both, dextran diffusion across an ARPE-19 monolayer and NH_3 treated ePTFE membrane, and distribution of ibuprofen concentration across the Kirkstall QV600 chamber.

The fluid flow set up used in this study was designed to emulate the mechanism of elimination of molecules via convectional clearance analogous to the systemic circulation present in choroidal tissue *in vivo*. To validate the computer model, comparisons of the average concentration in the receptor compartment of the Kirkstall QV600 chamber were made between predicted and experimental data. It is important to note that previous studies have used computer models to study drug delivery and distribution in the posterior segment of the eye [130-132] however these studies are mostly theoretical or based on experimental data published by Palestine and Brubaker which investigated the pharmacokinetics of fluorescein in the vitreous of humans [135]. In this study I looked to create an *in silico* model which could predict drug distributions in an *in vitro* model which hopefully could be used in the development of this novel ibu-SiO drug delivery device.

To build a validated model to work from in the study of the SiO, it was decided to first build a permeability model which could predict the movement and transport of dextrans through the ARPE-19 cell/ePTFE membrane. The permeability coefficients of each of the molecular weight FDs used were determined by the static transport experiments (2.2.3.3). These numbers were then applied to the computer model to simulate the transport in the dynamic flow environment. To validate the model, experiments were conducted under the same conditions described in the model and concentration of dextran in the receptor compartment was used as the measureable outcome.

This computer model was able to predict the maximum concentration observed in that chamber to within 15% of the acellular experimental data, with the exception of 70kDa FD at 400µL/min which was as high as 30%. The introduction of cells to the system increased the error observed in C_{max} to 30%, with the exception of 70kDa FD at 200µL/min which reached 46%. Interestingly a study conducted by Hsu et al., which simulated permeability of different molecular weight FITC-dextrans in a static set-up similar to that described in section 2.2.2.12 but across collagen or agarose gel, showed an increase in error between their

simulated and experimental results with increasing molecular weight [210]. In this model the least agreement is seen in those experiments which used 70kDa FD, the highest molecular weight. Also the inclusion of cells decreased the agreement between the simulated and experimental data. It is possible that this is due to the effect culturing the cells under flow has on the barrier functionality of the ARPE-19 cell monolayer. As seen in section 2.2.3.2, it appears that the barrier functionality is increased in the monolayer when the cells were exposed to flow rates up to 200µL/min as increased TEER is observed across the barrier. Conversely, when the flow rate was increased to 400µL/min, there appeared to be impairment of barrier function with decreased TEER and a breakdown in the tight junctions across the monolayer. This simulation does not take these biological effects in to account and is one of the major limitations of the current model. An experiment which could investigate whether this is a source of error would be to conduct the static transport experiments following exposure to flow, to determine the changes in permeability that is caused by the cells' exposure to it, and to use these values to build the computational model in the hope of reducing the error observed. There are studies which have investigated biological effects on epithelial tissues in computer simulations, such as Barber et al. who modelled inflammatory effects on intestinal epithelium in necrotising enterocolitis, [211] and Reijniak et al., who produced computer models to investigate links between epithelial morphogenesis and cancer mutations [212]. In the future I think it would be interesting to combine the computational fluid dynamics models designed in this study with a more computational biology approach to investigate cell dependent changes in transport and clearance of molecules.

To model the release of ibu from SiO the physics controls of the computer model had to be redesigned to allow the interaction of two immiscible fluid phases within the QV600 chamber. COMSOL Multiphysics software provides three methods for tracking interfaces in multi-phase flow models: level set, phase field and moving mesh. Each method has advantages and disadvantages depending on which feature of your model you have most interest in. For this ibu-SiO model, the moving mesh method was applied. COMSOL report that this method is best when tracking the interface between the phases is of importance. It also allows mass transport across the interface which is difficult to implement using the other methods [213]. The latter feature is what made this method most applicable to the simulation in this study as I was interested in the transport of ibuprofen across the two phases. Weisbrod et al. presented a study with similar requirements which modelled the

flow of kerosene in water, and within the kerosene phase was a concentration of acetic acid which diffused in to the water phase over time. They suggest that although the phase field method has improved performance in comparison with the level-set method in terms of flow within multi-phase systems, it is not suitable for applications where mass transfer is required and as such suggest the moving mesh method is most appropriate [214].

The results produced by the simulation showed realistic fluid flow profiles which one could expect to see under the same experimental conditions. At 20µL/min, the flow entering the main chamber bounces of the bottom off the meniscus formed by the oil phase and creates a ripple in the main stream of flow. The interaction of the main stream of flow with the oil domain also creates very low velocity recirculating flow patterns within the oil which are separate to the main flow stream. The movement within the oil could be expected to have implications on the distribution of ibuprofen within the oil phase but it appears that because the velocities are so low that the diffusion of the ibuprofen from the oil still occurs symmetrically out from the centre of the domain. As the inlet velocity increases, more asymmetrical diffusion patterns appear, however, the recirculation velocities within the oil remain very low in comparison with the velocity observed in the main stream of flow and so the distribution of ibu in the oil domain appears to be controlled by the concentration gradient between the two phases. This in turn is controlled by the convection of ibuprofen away from the interface by the fluid flow. The flow profiles in the aqueous phase of the two phase model were not comparable with those seen in the dextran transport model. In that model, the membrane was modelled as a fluid matrix domain whereby the fluid can move through the domain at a retarded rate based on the porosity and permeability of the membrane. For this reason only a small percentage of fluid actually passes through the membrane and interacts with the donor domain. The majority of the flowing fluid sees this as a walled domain and so this reduces the height of the chamber which is the reason for recirculating flows to develop in a turbulent fashion. In the two-phase, oil/PBS model, the force of the aqueous flow is partially absorbed by the oil which causes the recirculation within the oil but also reduces the velocity of the aqueous flow in comparison with the single phase model. This reduction in velocity also removes the secondary recirculating streams which occur in the single phase model.

The Kirkstall QV600 chamber is made of moulded polydimethylsiloxane (PDMS), sometimes referred to as silicone rubber. PDMS is a highly inert elastomer and as such makes it useful in many medical device and implant applications [215, 216]. In terms of its biocompatibility

and chemical stability, it is ideal for use in a microfluidic device, however, to validate the flow profiles observed in the computer model, visual and quantifiable data needs to be collected from the representative experiments. It was not possible to obtain that data in this project. In order to obtain quantitative data in such flow models, particle tracing technologies such as particle image velocimetry (PIV) would need to be implemented. PIV is an optical method used to visualise flow and obtain instantaneous velocity measurements within flow streams using scattered particles suspending within the flow medium. A layer of fluid is illuminated with a 2D light sheet whilst a camera simultaneously captures the illuminated particles within that layer. This is repeated over time to determine displacement of particles over time which allows calculation of the velocity within the field [217, 218]. This method was considered for the QV600 chamber to provide comparison with the computer simulation however, the lack of optical transparency of the chamber and the small scale and volumes used within it made it unsuitable as a subject for PIV. In future I think it would be important to confirm the flow profile within the chamber using an experimental method, not only for this particular study but for any study which intends to use the QV600 chamber for flow models.

As with the dextran transport simulations, to quantitatively validate the computer model of the ibu-SiO device within the QV600 chamber the concentration of ibuprofen in the receptor domain over time was measured. The accuracy to which the model was able to predict the concentration of ibu varied with the inlet flow rate. For the lowest flow rate, 20µL/min, the prediction was within 8% of the C_{max} of the experimental and also predicted the total exposure (AUC) to within 3%. At 200µL/min, which closely resembles the *in vivo* choroidal blood flow rate, the total exposure was within 8%, however there was a 35% overestimation in the C_{max} reached. Conversely at the highest flow rate, which is unrealistic in comparison with the *in vivo* environment, the C_{max} was underestimated by the simulation and there was a very large percentage error in the AUC. However, the values for concentration under these conditions were very low, C_{max} = 0.0039µg/mL, so at the very lower measurement limit of the UV-Vis spectrophotometer. Also the differences in absolute value of C_{max} was 0.0007µg/mL, which is negligible in comparison to the 1mg/mL initial concentration present in the SiO.

2.4.6 LIMITATIONS OF THE MODEL

In Vitro Model

The design of the *in vitro* model used in this study uses a human RPE cell line, ARPE-19, cultured on a synthetic Bruch's membrane replacement, NH_3 treated ePTFE. ARPE-19 cells have been used as a model for the RPE in many studies however they have limitations in terms of the comparability with *in vivo* RPE. It has been suggested that they more resemble an aged or pathologic RPE which lack natural pigmentation, whereas primary human RPE cells or foetal primary RPE cell have be shown to have greater barrier functionality and express increased levels of RPE markers [219]. Also, other cell types are involved in the outer blood retinal barrier which have not been considered here. Choroidal endothelial cells occupy the basal side of the Bruch's membrane and it has been shown that the incorporation of an endothelial cell layer, human umbilical vein-derived endothelial cells (HUVECs), within a similar in vitro model of the OBRB decreased the permeability of the barrier to 4kDa FITC-dextran [104]. In order to establish a more robust and representative model of the OBRB, future work should investigate the inclusion of a choroidal endothelial cell type.

Computer Model

From section 2.2.3.2, it can be seen that culturing of ARPE-19 cells under flow conditions can have either beneficial or detrimental effects on the barrier functionality and phenotype of the cells. The current computer model does not consider these alterations in parameters created by the biology of the cells and thus does not adapt to the changing conditions. Additionally, metabolism and active transport of compounds by the cells is not considered. This is particularly important in the assessment of drug transport across the barrier. It would be interesting in the future to combine a mathematical model of cell behaviour and metabolism with the fluid dynamics of drug clearance to provide a full picture of the movement of drugs through such a system.

The current model is conducted under 2 dimensional conditions and provides a planar projection of the mechanisms occurring within the system. Although good agreement was seen between the simulated and experimental results, this could be a source of error as the model extrapolates the concentration results out into 3 dimensions. Ultimately the model would need to be built in 3D to provide the most accurate representation of the *in vitro* model.

As robust and mathematically stringent as computer models are able to be built, they will never be able to provide a fully accurate representation of a biological environment due to the variability and continually dynamic environment of nature. What they are able to do is provide estimated predictions of results across a vast number of parameters in a fast and inexpensive manner. In terms of developing drug delivery devices such as the ibu-SiO described here, it allows us to vary conditions such as initial concentration, drug permeability and material properties and produce estimations which can narrow the range of expensive and time consuming experimental work that would otherwise need to be conducted. Ultimately it would be of interest to apply the knowledge and understanding of drug release from SiO gained from these complementary *in silico* and *in vitro* models to build a computational model of the eye which could help us predict how this system might work *in vivo* in a human eye.

CHAPTER 3

MODELLING AQUEOUS FLOW AND SACCADIC EYE MOVEMENTS

3.1 AIMS AND OBJECTIVES

AIM

To design complimentary *in vitro* models and computer simulations for use in the study release and transport of ibuprofen from a silicone oil tamponade through models of the eye that mimic aqueous flow movements and saccadic eye movements.

OBJECTIVES

- Develop and optimise a geometrically relevant *in vitro* model of aqueous flow.
- Study the effects of release of ibuprofen from a silicone oil tamponade within this model.
- Develop, optimise and validate a complimentary CFD model of the *in vitro* model.
- Determine whether the CFD model can be used to predict molecule concentrations across the *in vitro* model.
- Experimentally simulate the effects of saccadic eye movements on the release of ibuprofen.

3.2 IN VITRO MODEL OF AQUEOUS FLOW AND SACCADIC EYE MOVEMENTS

Following tamponade surgery, three different phase interfaces occur within the patient's eye; the silicone oil-retina interface, the retina-aqueous interface and the silicone oil-aqueous interface. The movement of the aqueous phase around the silicone oil could have implications for the release of the ibuprofen from the tamponade.

Chapter 2 investigated the clearance of molecules across the outer blood retinal barrier model. The other mechanism of drug clearance from the posterior segment is via aqueous outflow in to the anterior segment and out through either the trabecular meshwork or uveo-scleral vasculature. The aqueous fluid is secreted by the ciliary body to the posterior segment and flows into the anterior chamber. The path taken by the fluid creates interaction between the aqueous fluid and the vitreous or vitreous substitute and this interaction could have implications on drug release profiles and concentrations.

Another mechanism which can induce movement of fluids within the eye is saccades. Saccadic eye movements are rapid movements which abruptly change the point of fixation and also include the rapid eye movements that occur during sleep. These saccades last no longer than 100ms, the reported response time of the visual system, however, the duration, amplitude and velocity varies with each movement [220]. Saccades can occur up to amplitudes of 90°, however the majority occur below 20°with peak velocities in this range reaching up to 500°/second. The acceleration and jerk nature of saccades distinguish them from other types of eye movement, such as smooth pursuit movements, and are likely to affect the distribution of drugs within the posterior segment [221].

The following studies investigate the effects of flow around the Ibu-SiO oil and the subsequent differences in ibuprofen release profiles that occur due to either laminar flow around the oil (to represent aqueous outflow) or using simulated saccadic movements. These studies were done using two different *in vitro* models which have both previously been used to investigate the motion effects on the emulsification of silicone oils.

3.2.1 THE SPHERICAL EYE MODEL

Models of the eye were made by machining spheres of equivalent size to the eye into Perspex blocks with 0.8mm diameter inlet and outlet ports at the equator of the spheres. The model was made in two halves which were held together with screws. These models had previously been used by Fawcett et al. to study the emulsification of silicone oil tamponades [222]. The design of the model (***Figure 3-1***) allows for injection of the tamponade via the ports whilst enabling fluid flow to be introduced via the ports. The model simplifies the geometry of the eye to assume it adopts a spherical shape, however the volume the sphere can hold is designed to be equal to that of the human eye, 5mL. The model allowed a bubble of silicone oil to be surrounded by an aqueous phase, equivalent to the phase interface seen *in vivo*. The existence of the ports allowed fluid to be perfused through the system, therefore enabling the study of a dynamic fluid environment. Although the geometry is simplified in comparison to the *in vivo* eye, it is still a better representation in comparison to the previous Kirkstall QV600 chamber used. A disadvantage of this model, however, is it is not designed to be used for cell culture. Therefore all experiments using this model are in the absence of any cells.

3.2.2 EYE-ON-A-CHIP MODEL

The eye-on-a-chip model was designed by the fluid engineering group at the University of Hong Kong again to be used to investigate the emulsification of silicone oil tamponades (***Figure 3-2***). This model provides a two-dimensional (2D) projection the cross-section of the human eye. Over recent years the development of microfluidic cell culture platforms has seen a drastic increase, with these technologies reporting to provide a greater representation of the dynamic microenvironments of organs *in vivo*. These 'organ-on-a-chip' models have been successfully used to study organs such as kidney [223], heart [224] and lungs [225], however relatively little work has been done with eye-on-a-chip devices, in particular, the posterior segment.

The device used in these studies was previously used to study the effects of eye movements on the emulsification of a range of silicone oil tamponades. The design of this device is described by Chan et al. and includes a medium perfusion channel around the outside of a central inner chamber, connected by a series of micro-channels. Both the perfusion channel and the central inner chamber have individual inlet and outlet ports for independent control

of medium perfusion and injection of silicone oil. The purpose of the perfusion channel is to allow to exchange of nutrients through the micro-channels to and from retinal cells which can be cultured in the inner chamber. The geometry also includes an exclusion area within the inner chamber, representative of the lens [226].

The eye-on-a-chip device is another model which provides an opportunity to study drug release from silicone oil tamponades. Combining the results from the different models used in all of these studies should provide a greater understanding of drug release profiles of this delivery method.

In Vitro Spherical Eye Model and Eye-on-a-chip Model

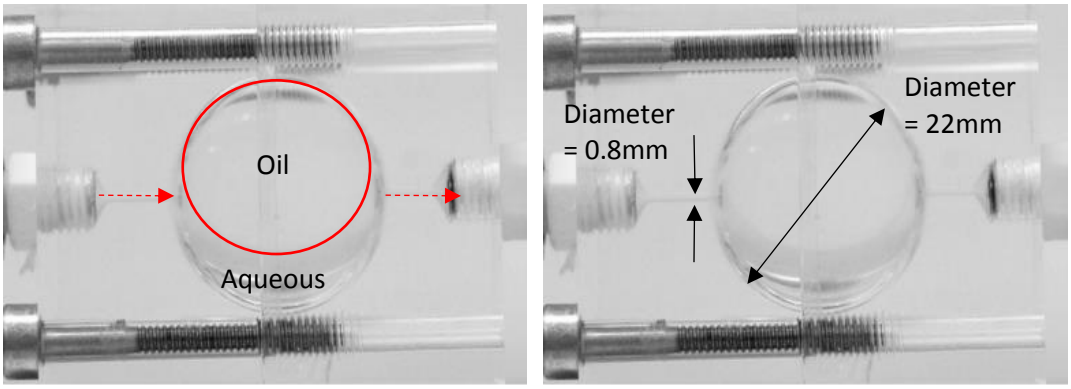

Figure 3-1: Spherical Eye Model.

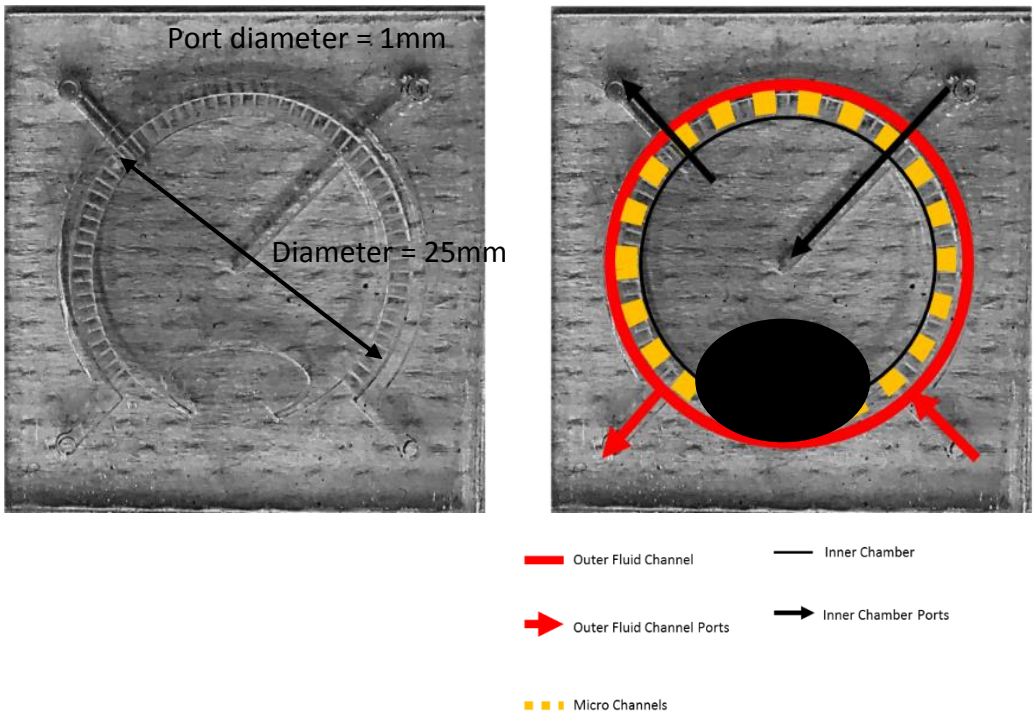

Figure 3-2: Eye-on-a-chip model and schematic diagram. Detailed description of device design is described by Chan et al. [226].

3.2.3 MATERIALS AND METHODS

3.2.3.1 VISUALISING THE FLOW IN THE SPHERICAL EYE MODEL

To fill the spherical model for use, the walls of the sphere were first coated with 1% bovine serum albumin (BSA) solution (diluted in PBS) (Sigma, A4161). The 1% BSA solution was injected into the sphere via the inlet port until filled and kept at room temperature for 30 minutes to allow the protein in the solution to adsorb to the wall. The adsorption of the protein onto the wall of the Perspex reduces any shear effects on the silicone oil caused by the roughness of the wall. After 30 minutes, the BSA solution was syringed out of the system. The system was then flushed through with distilled water (ddH_2O) after which the sphere was filled with fresh ddH_2O. Once filled with, 3.5mL of Ibu-SiO was injected via syringe in through the outlet port of the system, with care taken to ensure that only one continuous stream of oil was injected to produce a single bolus of Ibu-SiO.

The inlet port of the spherical chamber was connected to a syringe pump (Harvard Apparatus, PHD ULTRA 2.0.4) with 1mm diameter silicone tubing. The pump was set to infuse a tracer dye, 0.1% Methylene Blue (Sigma, M9140) diluted in distilled water, at a range of flow rates to evaluate the flow profile in the chamber. A dilution of 0.1% methylene blue in ddH_2O produces a solution with equal density and viscosity as water so the dye has no impact on the fluid properties of the solution. Flow rates of 20µL/min, 200µL/min and 2mL/min and 20mL/min were investigated at room temperature. Images of the chamber were taken every 2 seconds using a Nikon D3500 digital SLR camera.

3.2.3.2 STATIC RELEASE OF IBUPROFEN FROM SILICONE OIL IN SPHERICAL EYE MODEL

The release of Ibuprofen (Ibu) from silicone oil (SiO) was measured over time to determine a static release profile within the model. As in section 2.2.2.14, an experimental concentration of 1mg of Ibu (Tokyo Chemical Industry UK, I0415) was added to 1mL of 1000c.st silicone oil (Fluoron Ltd) and the mixture was stirred for a minimum of 72 hours in a sealed flask. Following stirring, the Ibu-SiO was filtered in a Class II biological safety hood to sterilise and stored at RT. The model was primed and filled using the same method as described in section 3.2.3.1 with PBS used as the aqueous solution as opposed to ddH_2O to maintain consistency across the release experiments. These studies used 4.5mL of Ibu-SiO. All static release experiments were carried out at RT and 37^{o}C.

After 24 hours, the PBS in the chamber was removed using a syringe, 3 x 100µL samples were taken from the PBS and transferred to UV transparent cuvettes (UVette, Eppendorf) and the Ibu concentration was measured using a UV spectrophotometer (SPECTROstar Nano, BMG Labtech) $\lambda_{absorption}$ = 264nm. The system was then cleaned and refilled and left for 48 hours, after which samples were taken. The whole process was then repeated again for 72 hours. Each of these time frames were repeated in triplicate. The concentration in the samples was determined by comparison with a standard curve and used to calculate the cumulative percentage release of ibuprofen from the oil. The results are presented as mean percentage release ± 1 SD, n=3.

3.2.3.3 Release of Ibuprofen from Silicone Oil under Laminar Flow in Spherical Eye Model

The spherical eye chamber was used to investigate the effects of dynamic flow on the release of Ibu from SiO. As in section 3.2.3.1, a syringe pump was used to produce PBS flow through the model. The system was set up in a single pass formation, with the outlet port open, allowing the waste PBS to flow into a collection pot. The use of the syringe pump to implement the flow became unsuitable for the long term nature of these studies due to the limited volume held by a syringe, thus the peristaltic pump from section 2.2.2.8 was used to allow continuous perfusion of PBS without the interruption caused by the need to change the syringe. In order to produce a steady stream of aqueous without the silicone oil bolus interfering, only 3.5 mL of ibu-SiO was injected into the system. After 24 hours, the flow was stopped and the PBS was removed from the sphere. Three 100µL samples were taken from the PBS and transferred to individual UV-clear cuvettes. The system was then cleaned and reset and the process repeated for 48 and 72 hours. Flow rates of 20µL/min, 200µL/min, 400µL/min and 2mL/min were investigated. For 2mL/min, the experiments were conducted over 8 hours to prevent leakage from the system.

The UV light absorption of the samples was measured using a UV spectrophotometer (SPECTROstar, BMG Labtech) $\lambda_{absorption}$ = 264nm. The absorption of each of the samples was compared to a standard curve and the concentration of the ibu present in each sample was determined. After simulating these experiments using a computer model, described in 3.3, the results suggested that the dominating features of the concentration profile occurred in the first 8 hours of flow. Therefore, the experiments were repeated with samples taken at 2, 4, 6 and 8 hours. All studies were repeated in triplicate at 37^{o}C, results are presented as mean concentration at each time point ±1 SD.

3.2.3.4 Release of Ibuprofen from Silicone Oil under Saccadic Simulation in Spherical Eye Model

Normal saccadic eye movements in humans produce fluid flow and shear stress profiles which could have implications for the oil-aqueous interface of the silicone oil tamponade, thus potentially having an effect on the release profile of drugs from the oil. A mechanical device designed to generate motion to simulate saccadic eye movements by Chan et al. at the University of Hong Kong, in collaboration with the University of Liverpool, was used with the spherical eye model to investigate the effects of this motion on the release of ibuprofen from a silicone oil tamponade [227].

The system had three principle parts; a stepper motor C4/MD2 Step Motor System, Arrick Robotics, Tyler, TX), a shaft encoder (Baumer Electric AG, Frauenfeld, Switzerland), and a data acquisition device (National Instruments Corp., Austin, TX). A platform was attached to the shaft of the stepper motor to allow the model to be fixed in position and provide rotational motion in a single plane. In order to execute repetitive motions, with specified angular displacement, velocity and acceleration, a dedicated software program was used to send instructions to the machinery and the shaft encoder enabled the actual motion being performed to be recorded. The system was instructed to execute movements with an amplitude of 10^{o}, angular velocity of 390^{o}/s and a duration of 50ms. These values were based on typical velocity profiles of the most frequent saccades observed in healthy, adult humans.

The spherical eye models were filled with PBS and 4.5mL ibu-SiO as previously described with the inlet and outlet ports sealed and the model fixed to the rotating platform (Figure 3-3). The movement program was executed and the models were exposed to the motion for 24 hours. The PBS was then removed from the model and 3 x 100µL samples were taken. These studies were undertaken at the University of Hong Kong and so a NanoDrop^{c} UV spectrophotometer was used to measure the UV absorbance of 10 x 2µL samples from each of the 100µL taken at wavelength 264nm. The process was repeated with the models fixed to the machinery for 48 and 72 hours. All studies were repeated in triplicate at RT. The concentration in the samples was determined by comparison with a standard curve and used to calculate the cumulative percentage release of ibuprofen from the oil. The results are presented as mean percentage release ± 1 SD, n=3.

Spherical Eye Model on Saccadic Simulator Device

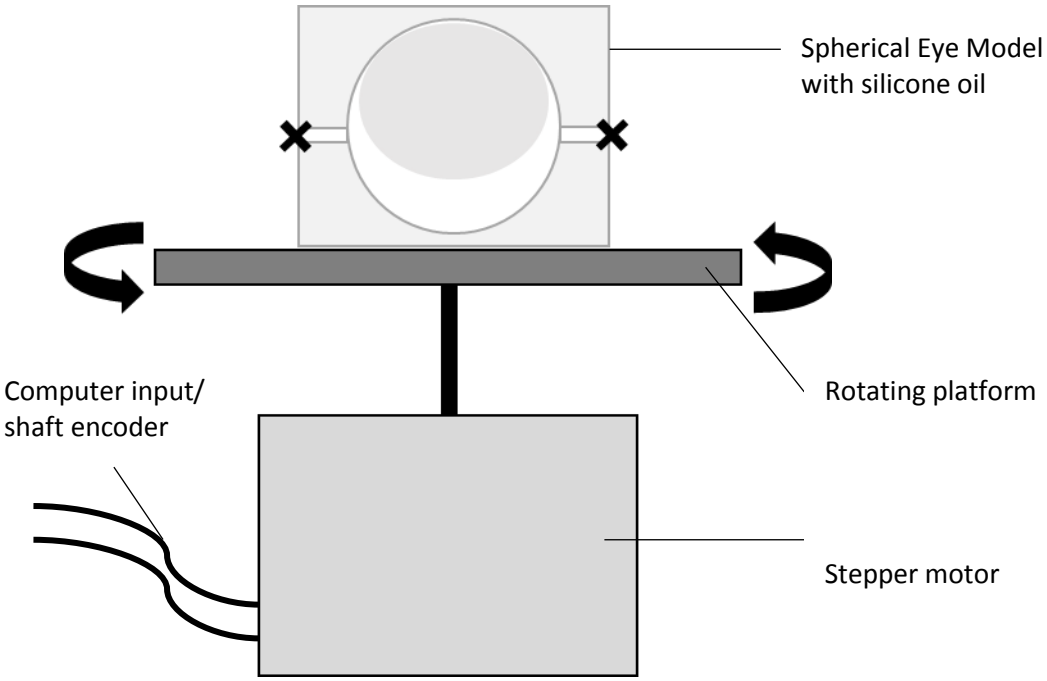

Figure 3-3: Schematic of spherical eye model on saccadic simulator.

3.2.3.5 MANUFACTURING THE EYE-ON-A-CHIP MODEL

Computer-aided design software (AutoCAD 2014, Autodesk, USA) had previously been used to create the inner geometry of the eye-on-a-chip model by the Fluid Engineering group at the University of Hong Kong. The chip device was composed of five layers of 1mm thick poly(methyl methacrylate)(PMMA) which each had an individual part of the inner structure laser engraved (model VLS2.30; Universal Laser Systems, USA) into them. Each layer of the chip was cleaned with lens tissue and the five layers were then stacked in a specific order to complete the chip. The layers were bonded by applying chloroform solution to the edges and once completed, compressed air was forced through each port to remove any dust from the channels. The chips were then flushed with sterile PBS solution to ensure none of the channels were blocked and stored at RT until use.

The main chamber of the device, designed to hold the silicone oil tamponade, was a 25mm diameter circle with an indentation to represent the lens. These dimensions are representative of the cross-section of the posterior segment of the human eye. Surrounding

the central chamber were a series of 100µm wide microchannels, designed to join the outer perfusion channel with the central chamber. The outer perfusion channel allowed the aqueous phase to be injected around the outside of the inner chamber and enable its removal for sampling.

3.2.3.6 Static Release of Ibuprofen from Silicone Oil in Eye-on-a-Chip Model

As with the spherical eye model, the inner walls of the chips were first coated with 1% bovine serum albumin (BSA) solution (diluted in PBS) (Sigma, A4161). The 1% BSA solution was injected into the central chamber and the perfusion channel via the inlet port until filled and kept at room temperature for 30 minutes to allow the protein in the solution to adsorb to the wall. This again was to reduce any shear effects on the silicone oil caused by the roughness of the wall. After 30 minutes, the BSA solution was syringed out and the chip was flushed with fresh PBS. After the chips were primed, sterile PBS solution was injected in both the aqueous inlet port and SiO inlet port to fill the chips. Once filled, the aqueous ports were sealed with Parafilm (Sigma, P7793) and 500µL of 1mg/mL ibu-SiO was injected into the central chamber via the SiO inlet port using an 18G needle. The ports to the central chamber were then sealed with Parafilm.

The release of ibuprofen into the surrounding aqueous was measured over 24, 48, 72 ad 168 hours. A 30µL sample was taken from the perfusion channel of each chip and the UV absorption of each sample was measured by analysing 10 x 2µL drops from each sample with a Nanodrop^{C} UV spectrophotometer. The concentration of Ibuprofen present in each of the samples was determined by comparison with the standard curve. Concentration gradient effects were investigated with experiments being carried out with the PBS completely replaced following sample removal, or just the 30µl sample volume replaced with fresh PBS. Experiments were carried out in triplicate with 3 chips used in each experiment and results are presented as the mean cumulative release ± 1 SD.

3.2.3.7 Release of Ibuprofen from Silicone Oil under Saccadic Simulation in Eye-on-a-Chip Model

The same method was used to simulate saccadic eye movements in eye-on-a-chip model as described for the spherical eye model in section 3.2.3.4. Once filled using the method described above, the chips were mounted onto the rotating platform and exposed to the motion for 24, 48, 72 ad 168 hours with the PBS in the chips either replenished every 24

hours or with only the sample volume replaced. A 30µL sample was taken from the perfusion channel of each chip and the UV absorption of each sample was measured by analysing 10 x 2µL drops from each sample with a Nanodrop^{C} UV spectrophotometer. The concentration of Ibuprofen present in each of the samples was determined by comparison with the standard curve. Experiments were carried out in triplicate with 3 chips used in each experiment and results are presented as the mean cumulative release ± 1 SD.

3.2.3.8 STATISTICS

GraphPad Prism statistical analysis software was used to analyse all data.

Two-way ANOVA

- Release profile of ibuprofen in spherical eye model under static conditions.
- Effects of saccadic simulation on ibuprofen release in spherical eye model.
- Effects of saccadic simulation on ibuprofen release in eye-on-a-chip model.

A two-way ANOVA was used because for each experiment there were two factors to consider: concentration and time. For each case the factors were treated as within subjects. Bonferroni's post hoc test was used. A minimum significance level of $P < 0.05$ was set for each experiment.

3.2.4 RESULTS

3.2.4.1 FLOW PROFILE IN SPHERICAL EYE MODEL AT DIFFERENT LAMINAR FLOW RATES

Dye studies were conducted to analyse the pattern and path that the fluid took when exposed to laminar flow of different flow rates. These dye experiments were designed to imitate mass transfer in the posterior segment of the eye which is caused by aqueous flow around the silicone oil tamponade. This flow is necessary to clear the drug away from the tamponade following release. Methylene blue solution diluted 0.1% in ddH_2O was infused through the system and the dye was traced through the chamber using a series of images taken 2 seconds apart using a digital camera.

For the lowest flow rate studied, 20µL/min, the dye entered the main chamber from the inlet port and traced a path through the aqueous phase along the circumference of the sphere before being cleared out of the outlet port (***Figure 3-4***). This pattern was observed for flow rates of 200µL/min and 2mL/min also (***Figure 3-4***), with the infused dye replacing the initial aqueous phase earlier as the flow rate increased. At 2mL/min, the centre of the silicone oil bolus is dragged towards the outlet under the force of the flow. This drag creates dissymmetry within the system, however the oil is still not forced out through the outlet as the flow reaches equilibrium. An extremely high flow rate of 20mL/min was also studied to observe what would happen to the silicone oil tamponade under extreme flow. After 4 seconds of aqueous flow, the silicone oil began to be removed from the chamber through the outlet under the force of the fluid, showing destruction of the system (***Figure 3-4***).

Visualisation of Flow through Spherical Eye Model

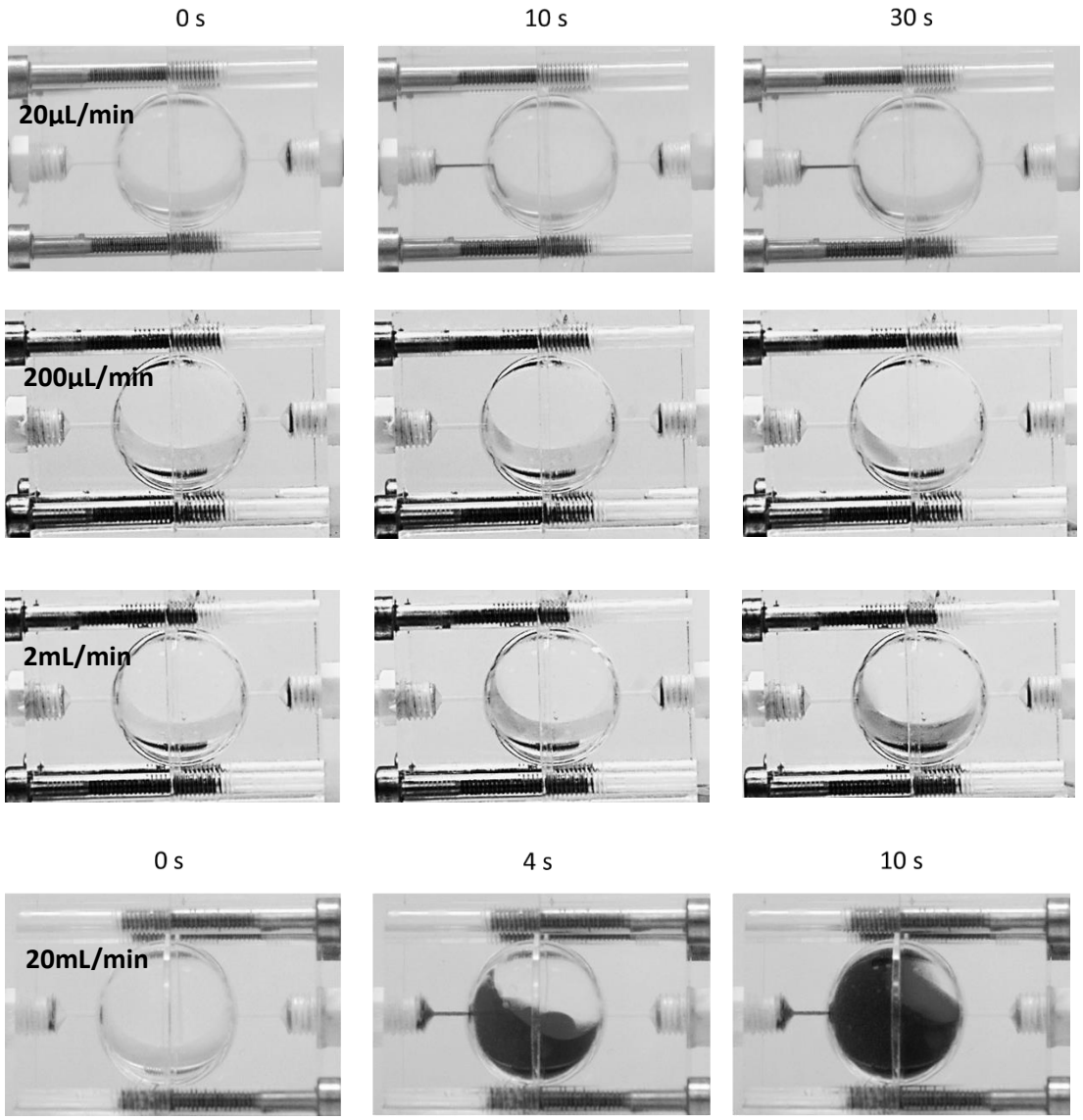

Figure 3-4: Visualisation of flow within the model at flow rate 20µL/min, 200µL/min, 2mL/min and 20mL/min visualised using dye. Up to 2mL/min, dye moves circumferentially around the oil bolus. At an exaggerating rate of 20mL/min, the system is destroyed and the oil is removed via the outlet port.

3.2.4.2 RELEASE OF IBUPROFEN IN SPHERICAL EYE MODEL UNDER STATIC CONDITIONS

To understand the release of ibuprofen from silicone oil in a more geometrically relevant system, release studies were conducted in the spherical eye model under static conditions. The release of ibuprofen was measured every 24 hours for 72 hours and release at both RT and 37^{o}C was investigated.

In PBS, ibuprofen has a saturation limit of 2mg/mL [228]. For the volume ratio of PBS to silicone oil used the saturation limit of ibuprofen in PBS in this model, equates to 44.4% release. For both temperatures, there was an initial burst release of ibuprofen after the first 24 hours, 24.2% at RT and 32.3% at 37^{o}C, after which the release rate appeared to slow as the concentration approached the saturation limit. As expected, the percentage release appeared to be higher at each time point for those experiments conducted at 37^{o}C. When tested with a repeated measures ANOVA with temperature (RT vs 37°C) as a between and time as a within-subjects factor, temperature returned a statistically significant main effect ($F(1, 5) = 42.07$, $p = 0.0013$), time also did ($F(2, 10) = 63.5$, $p < 0.0001$) and the time x temperature interaction was statistically significant ($F(2, 10) = 6.26$, $p = 0.0173$). Bonferroni's post hoc test indicated that the only significant difference in percentage release was seen after 24 hours ($p=0.0013$). Release at both temperatures reached near saturation after 72 hours, 41% and 42.5% for RT and 37^{o}C respectively (***Figure 3-5***).

Release Profile of Ibuprofen in Spherical Eye Model under Static Conditions

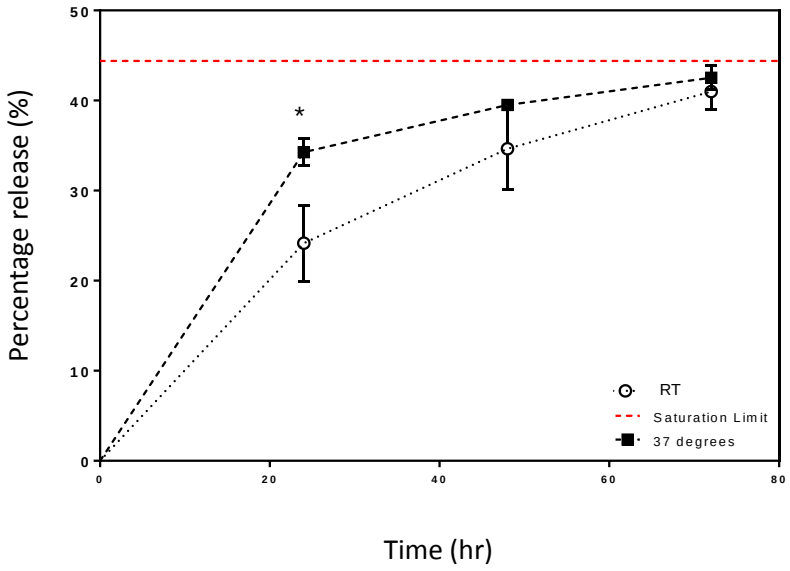

Figure 3-5: Release profiles of ibu from SiO in spherical eye model. Release presented as cumulative percentage release of Ibu into PBS over time at RT (circles) and 37°C (squares). Data presented as mean ± 1SD, n=6. * p = 0.0013 (Repeated measures Two-way ANOVA; Bonferroni post hoc test).

3.2.4.3 RELEASE OF IBUPROFEN FROM SPHERICAL MODEL UNDER LAMINAR FLOW

Fresh PBS was continuously perfused through the system at different flow rates and the concentration of ibuprofen released into the PBS was measured. At each time point the flow was stopped and the PBS from inside the spherical model was removed and the concentration of ibuprofen measured.

At the lowest flow rate, 20µL/min, the concentration in the PBS rose to a peak over the first 8 hours after which there was a small drop in concentration by 24 hours followed by a continuous decrease up to 72 hours. At 200µL/min, the concentration peaked at 4 hours after which there was an immediate steep elimination phase up to 24 hours where the concentration in the PBS was close to zero. This trend was followed for 400µL/min also, however the time to reach the peak concentration of 40.4µg/mL was only 2 hours. For 2mL/min, the peak concentration was also reached after 2 hours but the elimination of the drug from the aqueous phase appeared to be complete by 8 hours.

The peak concentrations followed the same pattern as seen in the Kirkstall QV600 experiments described in 2.2.3.4. The highest peak concentration was seen under 20µL/min, which reached C_{max}=132µg/mL compared with 2mL/min which reached a peak of only 24.5µg/mL. The difference between 200µL/min and 400µL/min was not as extreme with the C_{max}=49.6 and 40.4µg/mL (***Figure 3-6***).

3.2.4.4 STATIC VS SACCADIC SIMULATION RELEASE OF IBUPROFEN IN SPHERICAL EYE MODEL

Saccadic eye movements occur at a frequency of approximately 0.5Hz in the human adult eye and this movement will influence the aqueous flow around the silicone oil tamponade and thus affect the release of drugs. These saccadic movements were simulated using a mechanical device which allows a specific velocity profile to be defined and produces movements which reflect the *in vivo* environment.

The percentage release in both the static experiments and those exposed to saccadic movements reached near saturation limit (44.4%) after 72 hours with percentage release reaching 43.7% in the saccadic models and 41.0% in the static models. The burst release was more apparent in the experiments exposed to motion with 32.6% released after 24 hours compared with just 24.2% in the static models. When tested with a repeated measures ANOVA with group (static vs saccade) as a between and time as a within-subjects factor,

group returned a statistically significant main effect ($F(1, 5) = 11.79$, $p = 0.018$), time also did ($F(2, 10) = 77.87$, $p < 0.0001$) but the time x group interaction was not statistically significant ($F(2, 10) = 1.49$, $p = 0.272$). Bonferroni's post hoc test indicated that the only significant difference in percentage release was seen after 24 hours ($p=0.016$). (***Figure 3-7***).

Concentration Profiles of Ibuprofen released from Silicone Oil in Spherical Eye Model exposed to different Flow Rates

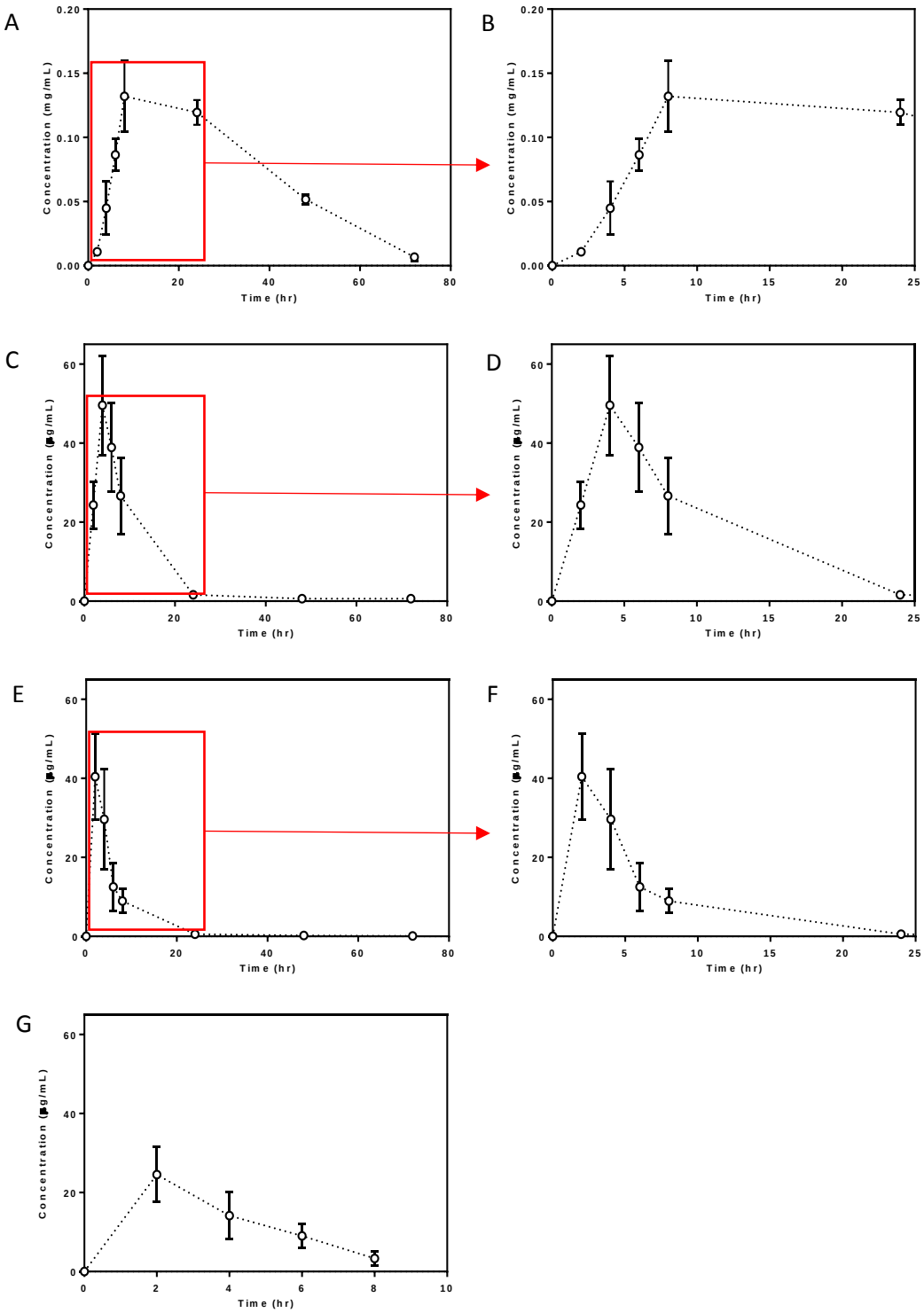

Figure 3-6: Concentration profiles of ibuprofen released from silicone oil into aqueous phase in spherical eye model exposed to flow rates (a,b) 20µL/min, (c,d) 200µL/min, (e,f) 400µL/min and (g) 2mL/min. Data presented as mean ± 1 SD, n=6.

Concentration Curve Statistics of Ibuprofen released from Silicone Oil into Aqueous Phase in Spherical Eye Model exposed to different Flow Rates

Flow Rate	Area under Curve (AUC, µg.hr/mL)	Peak Concentration (C_{max}, µg/mL)	Time of Peak Concentration (t_{max}, hr)	Average Concentration (C_{ave}, µg/mL)
20µL/min	5183	132	8	56.5
200µL/min	521.0	49.6	4	17.8
400µL/min	262.7	40.41	2	11.6
2mL/min	98.8	25.5	2	10.21

Table 3-1: Concentration curve statistics for Ibuprofen released from silicone oil exposed to flow rates of 20µL/min, 200µL/min, 400µL/min and 2mL/min. 2mL/min only conducted over 8 hours therefore AUC and C_{ave} are not comparable with other flow rates.

Concentration Profiles of Ibuprofen released from Silicone Oil in Spherical Eye Model exposed to Saccadic Simulation

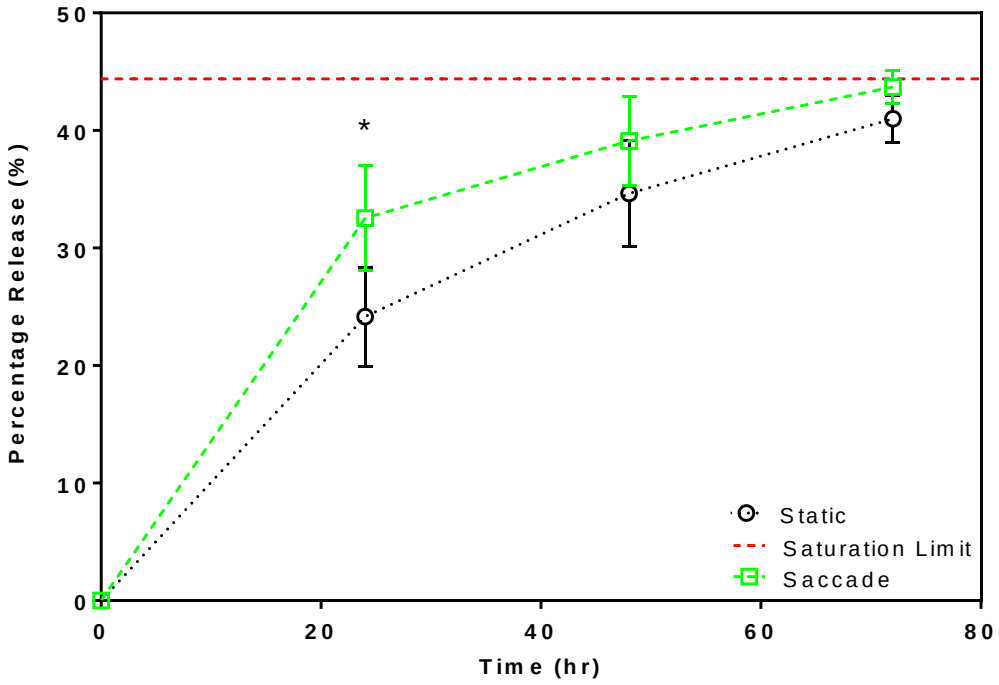

Figure 3-7: Release profiles of ibu from SiO in spherical eye model under static conditions (black) and saccadic simulation (green). Release presented as cumulative percentage release of Ibu into PBS over time. Data presented as mean ± 1 SD, n=6. * p = 0.016 (Two-way ANOVA; Bonferroni post hoc test).

3.2.4.5 STATIC VS SACCADIC SIMULATION R RELEASE OF IBUPROFEN IN EYE-ON-A-CHIP MODEL

The same movement patterns used on the spherical eye model were also investigated in the eye-on-a-chip (EOC) device. The EOC held different volume ratios in comparison to the spherical eye models with 600µL of ibu-SiO in the central chamber and 100µL of PBS in the channels. This put the saturation limit in the PBS at 41.6% release. Alongside the studies into saccadic motion effects, the release under non-saturation conditions were also investigated with the PBS phase replenished every 24 hrs. For both studies, the percentage release failed to reach saturation limit by 72 hours and so the studies were extended to look at the release over 7 days (168 hours).

In the experiments where only the sample volume was replaced every 24 hours, a repeated measures ANOVA was conducted using group (static vs saccade) as a between and time as a within-subjects factor. Group returned a statistically significant main effect ($F(1, 5) = 58.44$, $p = 0.0006$), time also did ($F(3, 15) = 120.6$, $p < 0.0001$) but the group x temperature interaction was not statistically significant ($F(3, 15) = 1.56$, $p = 0.240$). Release at both temperatures reached near saturation after 72 hours, 41% and 42.5% for RT and 37^{o}C respectively and Bonferroni's post hoc test indicated there was a significant difference in the release percentage at each time point excluding over the first 24 hours (48 hrs, $p = 0.0097$. 72 hrs, $p = 0.0016$. 168 hrs, $p = 0.0004$). This is the opposite trend to that seen in the spherical eye model in the previous section. At 24 hours, percentage release reached in the saccadic models was 12.0% compared with 7.1% in the static models. After 168 hours, the static models had still failed to reach the saturation limit of 41.6% with only 28.8% released, whereas the chips exposed to saccadic motion had reached a mean cumulative percentage release of 40.5% (***Figure 3-8***).

A repeated measures ANOVA was conducted using group (static vs saccade) as a between and time as a within-subjects factor for chips which had the PBS replenished every 24 hours. Group returned a statistically significant main effect ($F(1, 5) = 12.79$, $p = 0.0186$), time also did ($F(2, 10) = 78.90$, $p < 0.0001$) but the group x temperature interaction was not statistically significant ($F(2, 10) = 1.478$, $p = 0.274$). Bonferroni's post hoc test revealed a statistically significant difference ($p=0.0129$) in release after 24 hours with 12.7% ibuprofen released following saccadic simulation in comparison to just 8.3% release in the static models. However, for each time point after 24 hours, the release of ibuprofen under both conditions showed the same pattern with a slight decrease in cumulative percentage release in the

static models and no statistically significant difference between the two(48 hrs, p = 0.846. 72 hrs, p = 0.648. 168 hrs, p = 0.269) . Given that the PBS was replenished daily, the saturation limit was not reached. Interestingly, even after 168 hours neither condition reached 100% release of ibuprofen, the cumulative percentage release only reached 57.7 and 51.7% for static and saccadic conditions respectively (***Figure 3-9***).

Concentration Profiles of Ibuprofen released from Silicone Oil in Eye-on-a-Chip Model exposed to Saccadic Simulation

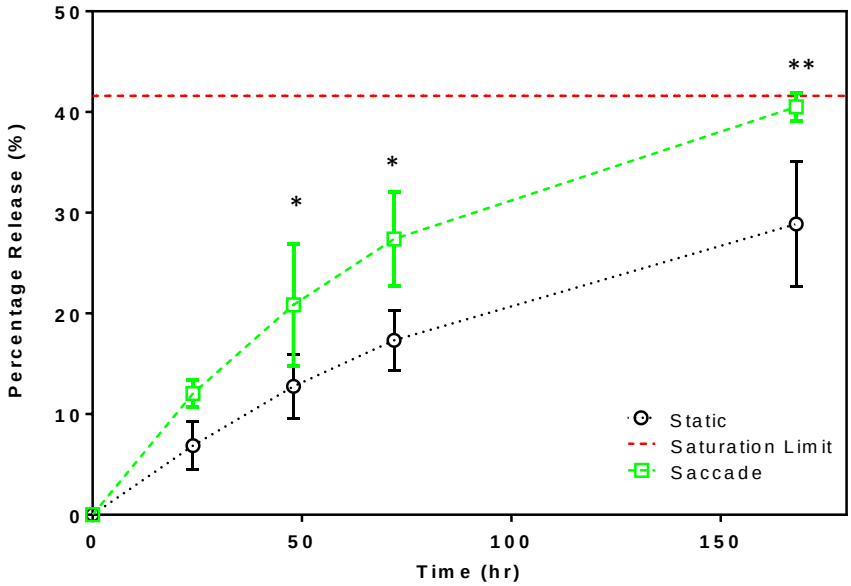

Figure 3-8: Release profiles of ibu from SiO in eye-on-a-chip model under static conditions (black) and saccadic simulation (green). Release presented as cumulative percentage release of Ibu into non-replenished PBS over time. Data presented as mean ± 1 SD, n=9. * p < 0.01, **p < 0.001 (Repeated measures Two-way ANOVA; Bonferroni post hoc test).

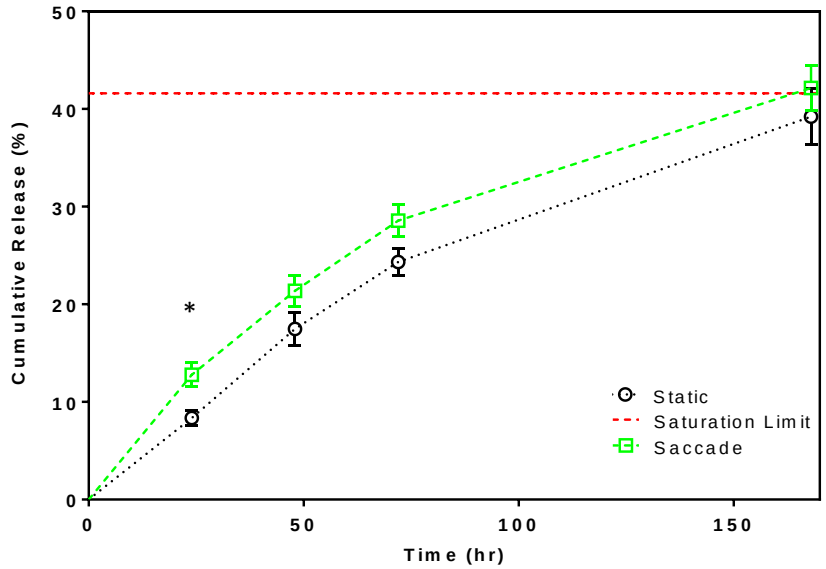

Figure 3-9: Release profiles of ibu from SiO in eye-on-a-chip model under static conditions (black) and saccadic simulation (green). Release presented as cumulative percentage release of Ibu into PBS replenished every 24 hrs over time. Data presented as mean ± 1 SD, n=9. *p < 0.01 (Repeated measures Two-way ANOVA; Bonferroni post hoc test).

3.3 COMPUTATIONAL MODEL OF AQUEOUS OUTFLOW

As in chapter 2, all of the computational analysis in this study was conducted using COMSOL Multiphysics software. The data from the *in vitro* models above were used to validate the computer simulations described in this section, however, modelling of the simulated saccadic motions was not investigated to due limitations of time, therefore only the static release in the spherical model and EOC was studied as well as the laminar flow studies in the spherical model. Future work would be needed to investigate the implementation of the saccadic velocity profile into the COMSOL Multiphysics simulations. Again, by building a computational model using experimentally derived data and boundary conditions it is possible to predict and optimise the conditions of the drug release studies. These computer models could be valuable tools for a more time and cost effective method for developing this drug delivery method.

3.3.1 METHODS

3.3.1.1 PHYSICAL AND MATHEMATICAL DESCRIPTION OF THE AQUEOUS OUTFLOW MODELS

Spherical Eye Model

The model built was based on a two-dimensional (2D) projection of the spherical eye model using COMSOL Multiphysics finite element analysis software. Using the schematic diagrams, the input geometry was built within the software (Figure 3-10). The models were composed of two physics elements: (1) a laminar flow interface, to compute the velocity flow and pressure fields of the fluid flow that occurs across the spherical chamber, and (2) a diluted species interface, which is able to calculate the concentration field of a dilute solute in a solvent i.e. the ibuprofen release from the silicone oil into PBS. These simulations required the use of the laminar flow moving mesh physics interface to track the movement of the interface between the silicone oil phase and the aqueous PBS phase within the spherical chamber, this physics interface was previously discussed in section 2.3.1.5.

The transport of diluted species physics used in these models follows the same principles as described in 2.3.1.5. The simulation solves for the diffusion and convection in the two different fluids. An additional expression for the partition coefficient is included in the mass transport between the two phases. To satisfy the convective terms of the mass balance equation, the solution for the laminar flow, moving mesh physics node was used to describe

the velocity field in the model in order to solve for the concentration filed of the ibuprofen across the model.

Eye-on-a-Chip Model

Only the static studies were conducted for the eye-on-a-chip (EOC) model in the computational simulations. This made the physics of the model less complex as no laminar flow interface was required. The solution for the EOC model was, therefore, purely based on the transport of diluted species physics interface. Also, given the complex geometry of the model, it was not able to be built within the software so the geometry was imported into COMSOL from the CAD file originally used for laser engraving the chips (***Figure 3-11***).

COMSOL Geometry for the Spherical Eye Model and Eye-on-a-Chip Model

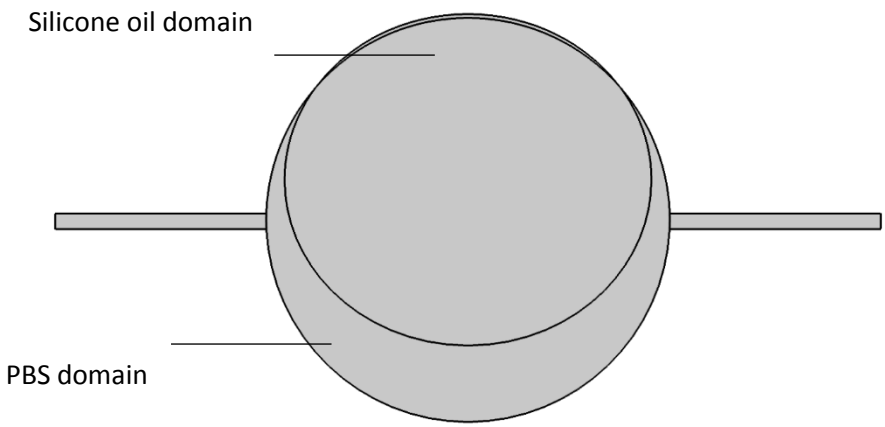

Figure 3-10: Input geometry for spherical eye model.

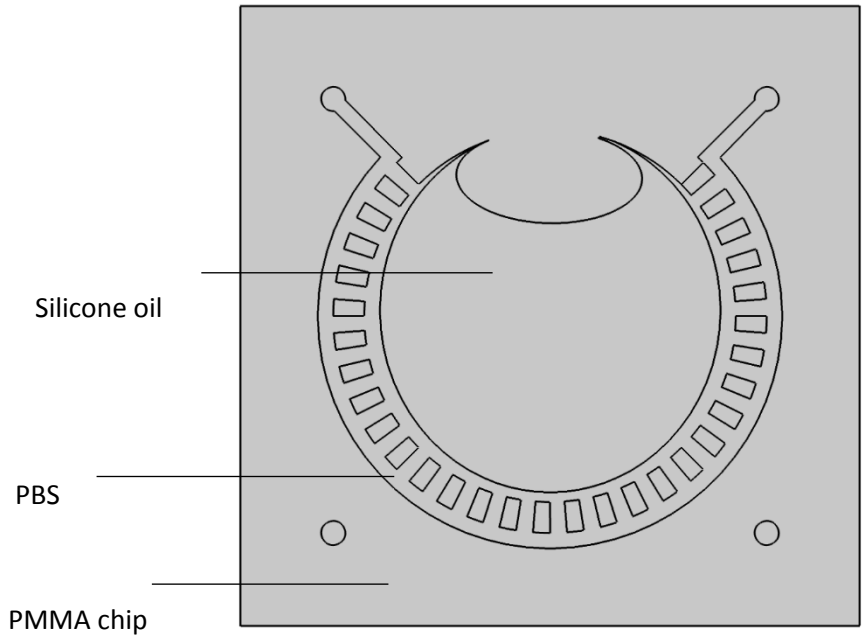

Figure 3-11: Input geometry for eye-on-a-chip model.

3.3.1.2 Input Parameters for Ibuprofen Release Experiments

The input parameters were either defined experimentally or calculated. The values for the partition coefficient of Ibuprofen and the interfacial tension of 1000 c.st silicone oil and PBS were taken from the literature. All the input parameters used for both the spherical eye model and eye-on-a-chip model were identical to those used in the ibuprofen release simulations in the Kirkstall QV600 model from chapter 2. This is because all of the components and physics systems of each of the models were identical, it was just the geometries which were different. Therefore the input parameters for spherical model and EOC can be found in chapter 2, ***Table 2-22***.

3.3.1.3 Boundary Conditions used for Ibuprofen Release Experiments

The boundary conditions used in the spherical eye model were the same as were applied in the Kirkstall QV600 geometry (2.3.1.8). No slip conditions were applied to the exterior boundary walls and those walls in contact with the fluid-fluid interface were assigned a Navier slip condition. This condition allows the fluid-fluid interface to move along the wall.

The inlet was assigned to the left hand port and outlet to the right and the conditions were as previously describes and the same flow rates were investigated as with the Kirkstall QV600: 20µL/min, 200µL/min, 400µL/min and 2mL/min. A volume force was also implemented across the entire geometry to account for gravity in the system.

Both the spherical eye model and EOC used two transport of diluted species nodes to investigate the release of ibuprofen from the silicone oil: one for the oil phase and one for the aqueous phase. As in the previous model, a no flux condition was applied on the exterior boundary walls of the geometry. An outflow condition was applied to the right hand wall of the outlet port of the chamber to allow the removal of ibuprofen via the fluid flow field. The appropriate diffusion coefficients as described in ***Table 2-22*** were applied to each fluid domain and a pointwise constraint equal to that previously described was applied at the fluid-fluid interface. This pointwise constraint takes into account the concentration at the interfaces and solves for the mass flux across that boundary using a function of the concentration gradient and the partition coefficient.

3.3.1.4 MESH USED FOR SPHERICAL EYE MODEL AND EYE-ON-A-CHIP MODEL

For the spherical eye model release studies, the mesh was made up of 17510 free triangular elements (***Figure 3-12***). A grid independence test was carried out to ensure the mesh was refined enough to produce accurate results. The velocity at two points within the well was compared across a range of increasingly finer meshes to evaluate the accuracy of the results compared with the finest mesh. A percentage error of 5% or less compared with the finest mesh was deemed sufficiently accurate. This was achieved at 17510 elements and this mesh was used for all spherical eye model simulations.

Again, for the EOC a grid independence test was carried out. The concentration at two points within the centre of the chamber were compared across a range of mesh element numbers from an extremely coarse mesh of 944 elements to an extremely fine mesh of 14383 elements. The percentage different in concentration at the two points compared with the most refined mesh was used to evaluate the accuracy of the results. A percentage error of 5% or less was deemed accurate enough. This was reached at 4345 elements and this mesh was used for all the following simulations (***Figure 3-13***).

Meshes generated for Spherical Eye Model and Eye-on-a-Chip Model

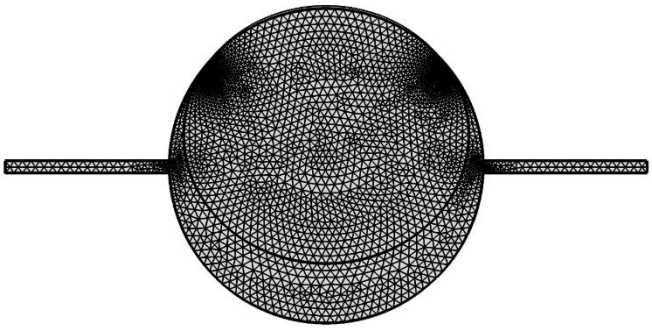

Figure 3-12: Mesh generated for spherical eye model used in ibuprofen release simulations. Mesh consists of 17510 free triangular elements.

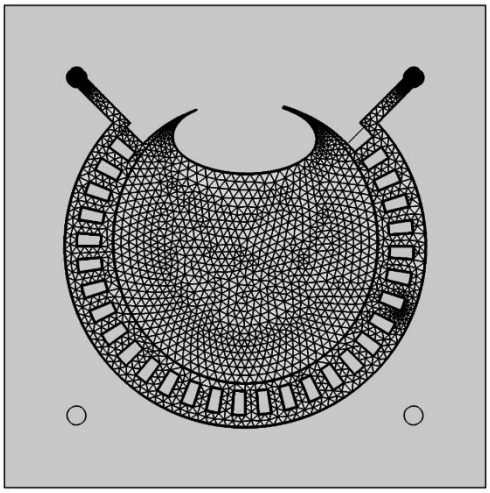

Figure 3-13: Mesh generated for eye-on-a-chip model used in ibuprofen release simulations. Mesh consists of 4345 free triangular elements.

3.3.2 RESULTS

3.3.2.1 GRID INDEPENDENCE TESTS

Analysing the effects of altering the density of the meshes allows for a suitable mesh to be built that minimises the number of elements to save on computational power, and therefore time needed to produce a solution, without compromising on the accuracy of the results.

The simulations were run at decreasing mesh densities and the value of the velocities (spherical eye model) or concentrations (EOC model) at two points within the model were compared to the finest mesh and the density at which the error between the solutions and the solutions of the finest mesh reached ≤5% were determined to have reached an acceptable solution.

As with the Kirkstall QV600 model, the percentage difference in solution decreases with increasing number of elements in the mesh. For the spherical eye model, the least dense mesh consisted of 506 elements and the densest mesh consisted of 17510 elements. None of the less refined meshes produced velocity results within the accuracy limit in comparison with the finest mess, therefore the mesh which was used consisted of 17510 elements (***Figure 3-14***).

With the eye-on-a-chip model, all of the less dense meshes produced concentration results within 5% of the finest mesh for a point within the oil domain of the model, however, it was only when the mesh was refined to 4345 elements that the results for a point in the aqueous phase of the model fell below the error limit. This mesh was used for the remaining simulations (***Figure 3-15***).

Grid Independence Tests for Ibuprofen Release Studies in Spherical Eye Model and EOC

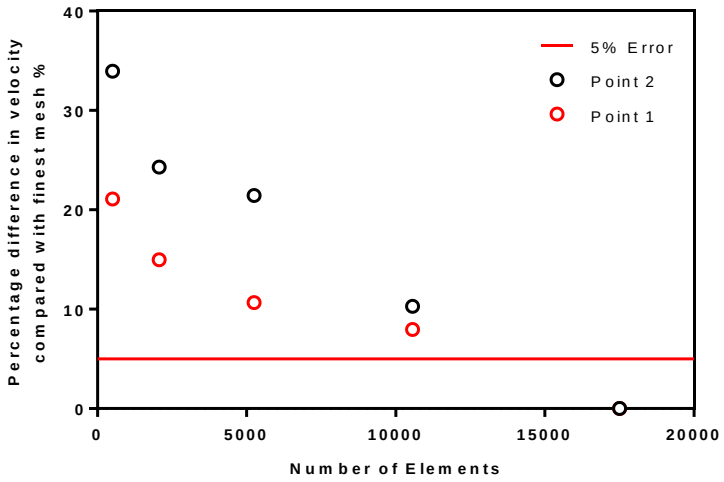

Figure 3-14: Percentage difference in velocity at two points in the centre of the spherical eye model compared with the finest mesh (17510 elements). A <5% error was deemed to be acceptable mesh density.

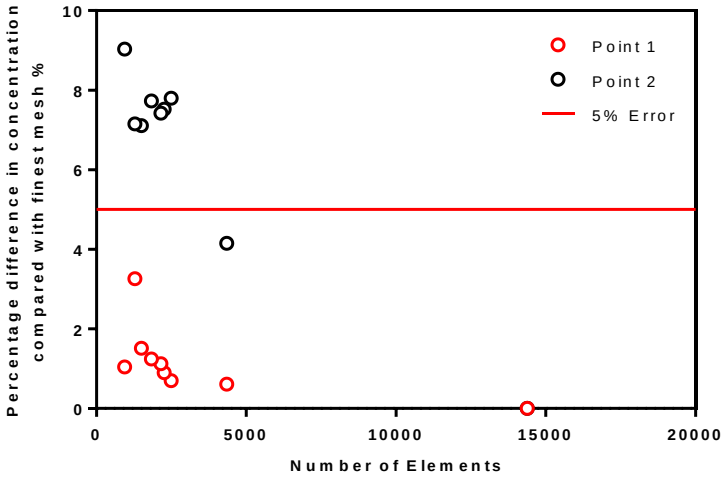

Figure 3-15: Percentage difference in velocity at two points in the centre of the eye-on-a-chip compared with the finest mesh (14383 elements). A <5% error was deemed to be acceptable mesh density.

3.3.2.2 STATIC RELEASE PROFILES IN SPHERICAL EYE MODEL

The concentration profile of ibuprofen was plotted graphically to determine the points of highest concentration and the percentage release of ibuprofen was compared to the *in vitro* results for validation.

Ibuprofen distribution in the oil domain showed release from the periphery of the silicone oil bubble with the concentration decreasing to the centre of the bubble over time, excluding the portion of the bubble that was in contact with the wall of the sphere, which maintains the highest concentration of ibuprofen within the oil domain at each time point. In the aqueous phase, the distribution of ibuprofen was concentrated in the 'corners' of the model in the region of the geometry with the smallest surface area. Over time, the distribution moves down towards the bottom of the aqueous phase as well as spreading further down the ports of the geometry (***Figure 3-16A***).

Comparing the release profiles of the *in vitro* and simulated results, the difference in percentage release was 3.6%, 0.9% and 0.6% for 24hr, 48hr and 72hr respectively. Both conditions neared the saturation limit (44.6%) after 72 hours, 41.0% for the *in vitro* data and 41.6% in the simulation. The simulated data also suggested a sharp release of ibuprofen over the first 5 hours (***Figure 3-16B***). Further *in vitro* experiments need to be done to investigate the release profile over these shorter time periods.

Simulation vs Experimental Release Profile of Ibuprofen Release in Static Spherical Eye Model

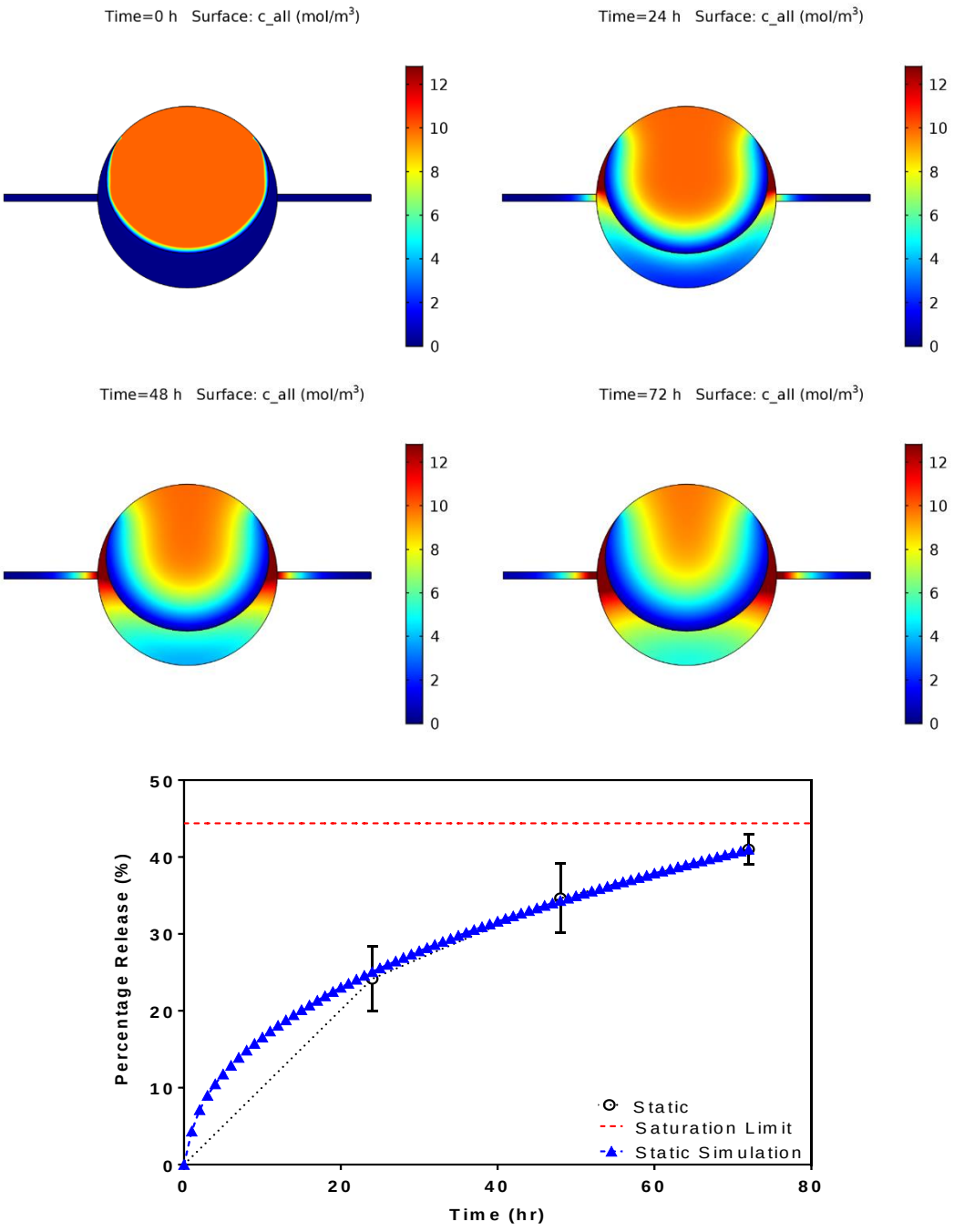

Figure 3-16: *(a) Concentration field solution for ibuprofen concentration across the spherical eye model at 0, 24, 48 and 72 hr. Colour scale bar indicates concentration in mol/m³. (b) Experimental (black) vs simulated (blue) release profiles of ibuprofen in aqueous phase of static spherical eye model. Experimental data presented as mean cumulative release ± 1 SD, n = 6.*

3.3.2.3 DEVELOPMENT OF VELOCITY PROFILES IN SPHERICAL EYE MODEL

Inlet flow rates of 20µL/min, 200µL/min, 400µL/min and 2mL/min were investigated in the simulations to coincide with the *in vitro* experiments. For each flow rate, the streamlines showed the flow field forming a steady stream from inlet to outlet in the aqueous phase around the silicone oil bubble. With increasing inlet flow rate, the peak velocities within the geometry increased but the stream beneath the silicone oil bubble is maintained. At the 'corners' between the aqueous and oil phase there were small regions of recirculating aqueous which became more influenced by the main stream of flow as the flow rate increased. At the highest flow rate, 2mL/min, secondary flows started to form at the exit point of the inlet port and the force of the fluid flow out of the inlet port pushed the silicone bubble towards the outlet (***Figure 3-17***).

Within the silicone oil domain, there appeared to be a very low velocity circulation. At 20µL/min this circulation is split across the oil domain. As the inlet flow rate increased, the center of the circulation shifts further towards the outlet whilst maintaining its uniformity through the domain. The circulation velocity is much lower in comparison to the main stream of flow through the system.

Velocity Fields of Different Flow Rates in the Spherical Eye model

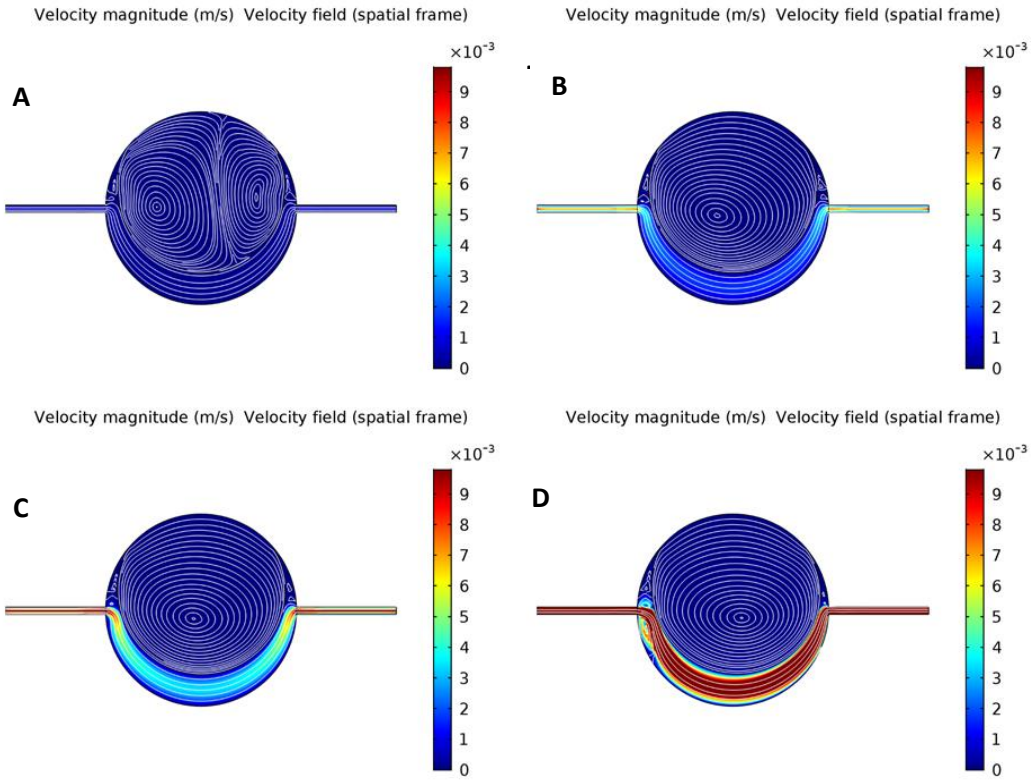

Figure 3-17: Velocity fields for different inlet flow rates used in the spherical eye model geometry for ibuprofen release studies. Inlet flow rates: (a) 20µL/min, (b) 200µL/min, (c) 400µL/min and (d) 2mL/min. Colour scale bar indicates velocity (m/s). Streamlines show velocity field.

3.3.2.4 CONCENTRATION PROFILES OF IBUPROFEN IN SPHERICAL EYE MODEL EXPOSED TO VARYING FLOW RATES

The concentration in the aqueous phase of the spherical model showed similar profile patterns as observed in the Kirkstall QV600 chamber at the respective inlet flow rates. The simulations were run over 72hrs, but in each case, the defining features of the concentration profiles were observed over the first 24 hours. Each flow rate showed the concentration of ibuprofen within the silicone oil domain decreasing over time with the diffusion occurring from a central point which appeared to be defined by the centre of the flow circulation within the oil domain shown in section 3.3.2.3 (***Figure 3-17***).

At 20µL/min, in the 'corner' areas, the ibuprofen concentration becomes trapped in the recirculating flow and is not cleared via the main stream of flow. The diffusion within the oil domain is focussed around two concentration centres which match the centres of the circulating flow within the oil. Over time, ibuprofen is released from the oil domain and cleared from the system in the main stream of flow via the outlet port, however, the concentration in the main flow stream is extremely low in comparison with other regions of the system (Figure 3-18A). The concentration data from within the aqueous phase shows the same profile pattern as the *in vitro* data. There is a rise in ibuprofen concentration in the PBS up to 13 hours, after which the elimination phase begins and the drug is cleared from the system. The simulated peak concentration reached 128µg/mL, a 3% decrease in comparison to the *in vitro* data (***Figure 3-18B***).

For 200µL, 400µL and 2mL/min, there was a spike in concentration, reached after 5hr, 3hr and 2hr respectively. Following the spike, the elimination phase began. For each flow rate, the simulated data produced C_{max} results within 20% of the *in vitro* values and the T_{max} data was within one hour.

The concentration fields showed similar patterns to the 20µL/min fields. The region at the 'corners' had increased concentration where ibuprofen had become trapped in the secondary recirculating flow. The diffusion of ibuprofen from the silicone oil was targeted around the point where the centre of the circulating flow within the oil was positioned. As the flow was increased, this centre shifted further towards the outlet (***Figure 3-19, Figure 3-20 and Figure 3-21***). Only at 2mL/min after 72hrs does the ibuprofen appear to be completely cleared from the silicone oil bubble (***Figure 3-21***).

Concentration Fields and Receptor Domain Profile of Ibuprofen in the Spherical Eye Model at 20µL/min

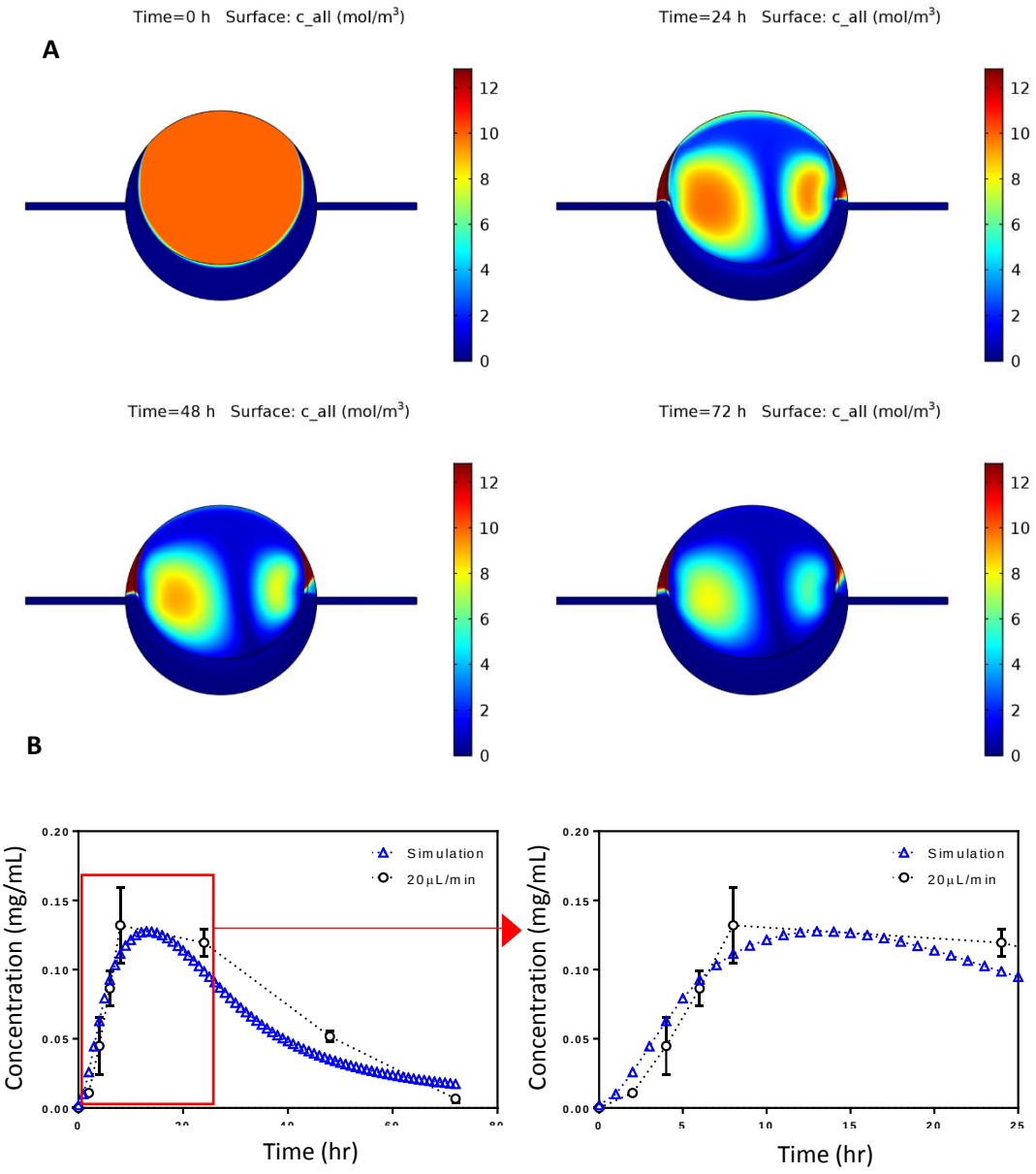

Figure 3-18: (a) Concentration field solution for ibuprofen concentration across the spherical eye model at 0, 24, 48 and 72 hr. Colour scale bar indicates concentration in mol/m³. (b) Experimental vs simulated concentration profiles of ibuprofen in aqueous phase of spherical eye model. Flow rate = 20µL/min. Experimental data presented as mean concentration ± 1 SD, n = 6.

Concentration Fields and Receptor Domain Profile of Ibuprofen in the Spherical Eye Model at 200µL/min

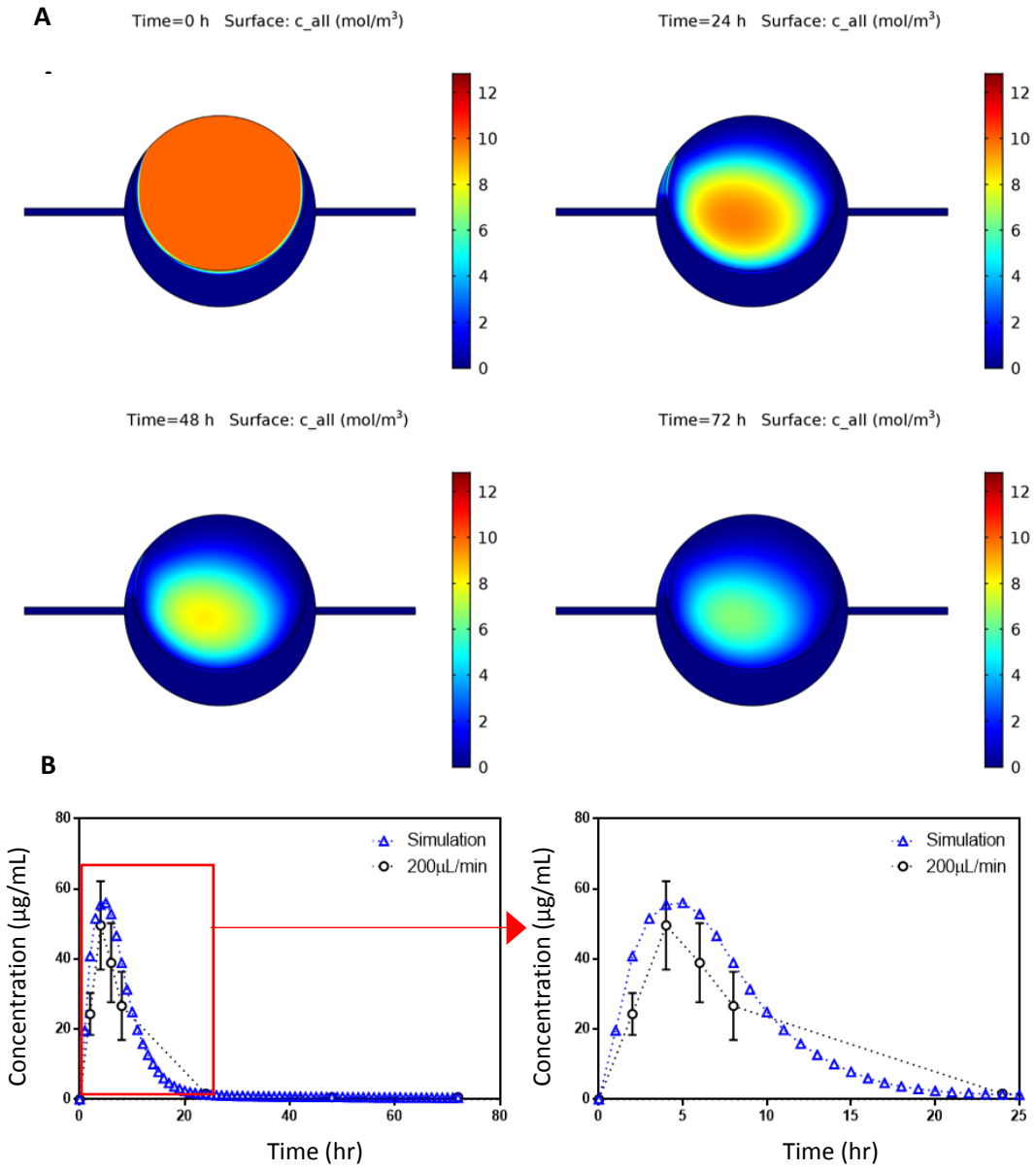

Figure 3-19: (a) Concentration field solution for ibuprofen concentration across the spherical eye model at 0, 24, 48 and 72 hr. Colour scale bar indicates concentration in mol/m³. (b) Experimental vs simulated concentration profiles of ibuprofen in aqueous phase of spherical eye model. Flow rate = 200µL/min. Experimental data presented as mean concentration ± 1 SD, n = 6.

Concentration Fields and Receptor Domain Profile of Ibuprofen in the Spherical Eye Model at 400µL/min

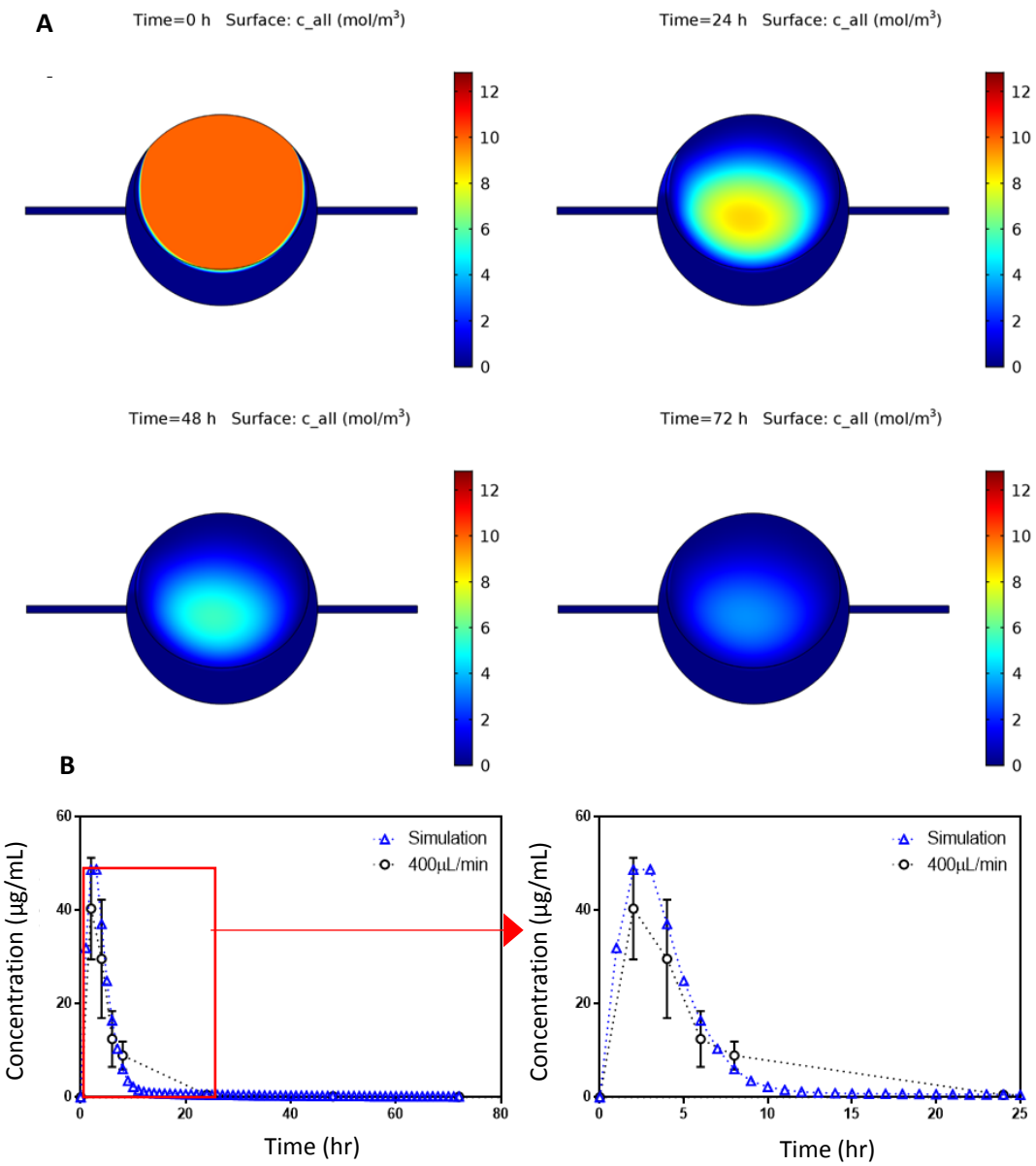

Figure 3-20: (a) Concentration field solution for ibuprofen concentration across the spherical eye model at 0, 24, 48 and 72 hr. Colour scale bar indicates concentration in mol/m³. (b) Experimental vs simulated concentration profiles of ibuprofen in aqueous phase of spherical eye model. Flow rate = 400µL/min. Experimental data presented as mean concentration ± 1 SD, n = 6.

Concentration Fields and Receptor Domain Profile of Ibuprofen in the Spherical Eye Model at 2mL/min

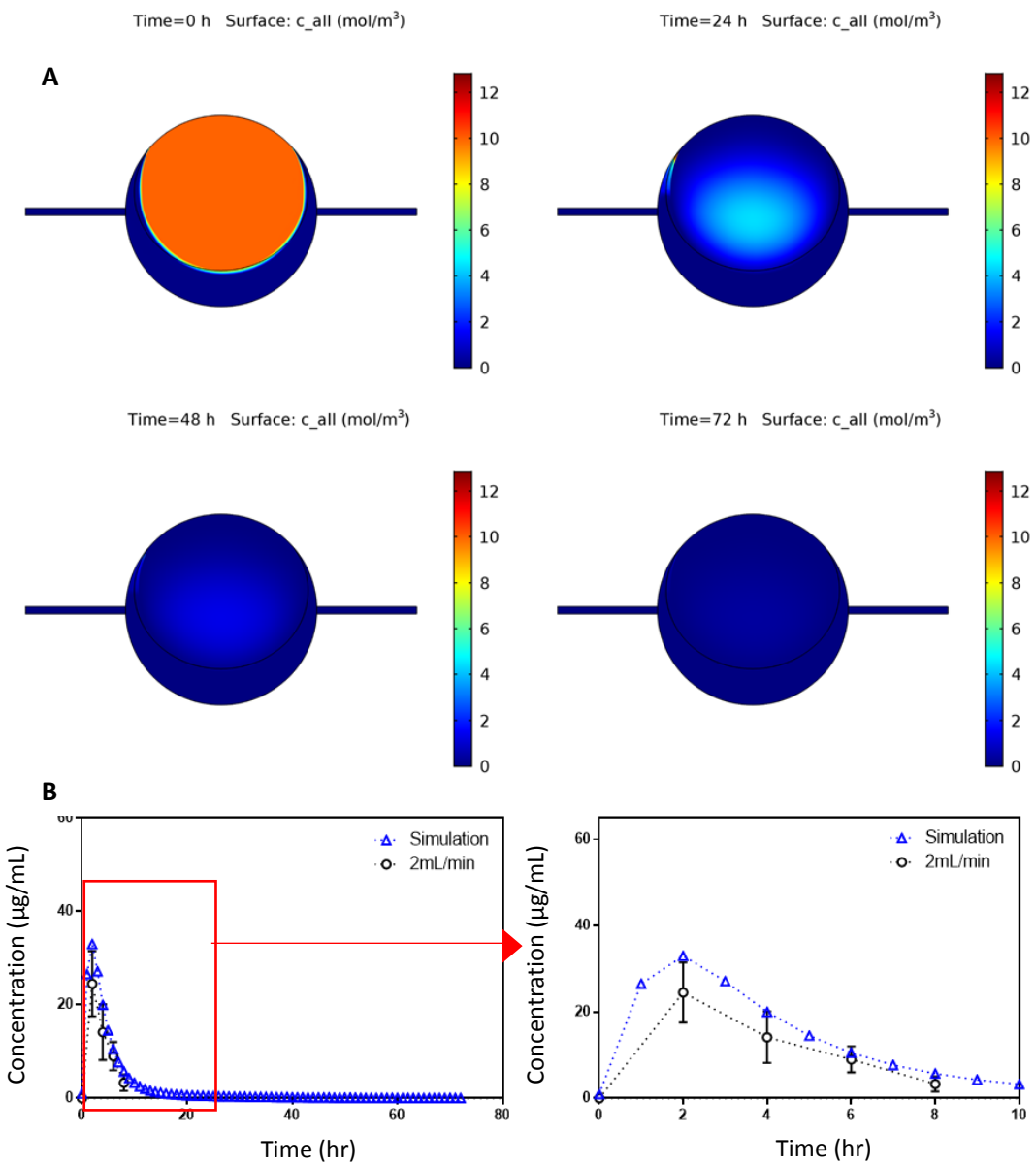

Figure 3-21: (a) Concentration field solution for ibuprofen concentration across the spherical eye model at 0, 24, 48 and 72 hr. Colour scale bar indicates concentration in mol/m³. (b) Experimental vs simulated concentration profiles of ibuprofen in aqueous phase of spherical eye model. Flow rate = 2mL/min. Experimental data presented as mean concentration ± 1 SD, n = 6.

Concentration Curve Statistics for Simulated vs Experimental Dextran Transport Studies across Seeded Membranes at 200µL/min

	Area under Curve (AUC, µg.h/mL)	Peak Concentration (C_{max}, µg/mL)	Time of Peak Concentration (t_{max}, hr)	Average Concentration (C_{ave}, µg/mL)
Experimental	5103	132	8	56.5
Simulation	4439	128	13	59.9

Table 3-2: Concentration curve statistics for ibuprofen release from silicone oil in spherical eye model exposed to a flow rate of 20µL/min.

	Area under Curve (AUC, µg.h/mL)	Peak Concentration (C_{max}, µg/mL)	Time of Peak Concentration (t_{max}, hr)	Average Concentration (C_{ave}, µg/mL)
Experimental	521	50.0	4	17.8
Simulation	545	55.9	5	7.5

Table 3-3: Concentration curve statistics for ibuprofen release from silicone oil in spherical eye model exposed to a flow rate of 200µL/min.

	Area under Curve (AUC, µg.h/mL)	Peak Concentration (C_{max}, µg/mL)	Time of Peak Concentration (t_{max}, hr)	Average Concentration (C_{ave}, µg/mL)
Experimental	262	40.4	2	11.6
Simulation	257	48.1	3	3.5

Table 3-4: Concentration curve statistics for ibuprofen release from silicone oil in spherical eye model exposed to a flow rate of 400µL/min.

	Area under Curve (AUC, µg.h/mL)	Peak Concentration (C_{max}, µg/mL)	Time of Peak Concentration (t_{max}, hr)	Average Concentration (C_{ave}, µg/mL)
Experimental	98.8	25.5	2	10.2
Simulation	177.1	31.1	2	2.4

Table 3-5: Concentration curve statistics for ibuprofen release from silicone oil in spherical eye model exposed to a flow rate of 2mL/min.

3.3.2.5 STATIC RELEASE PROFILES IN EYE-ON-A-CHIP MODEL

The static release of ibuprofen was also evaluated in the EOC model. As in the static results for the spherical eye model, the ibuprofen diffuses out from the centre of the silicone oil bubble. The concentration initially decreases at the periphery and the highest concentration is maintained at the centre of the oil domain, over time the region of high concentration decreases in size as the ibuprofen moves into the aqueous phase. The concentration in the aqueous phase increases over time but appears to be constant across that phase of the model. After simulating 7 days of diffusion, the percentage release appears to plateau however the plateau is reached well before the 41% saturation limit. The release profile shows a greater burst release than that observed from the *in vitro* data which has an almost linear release pattern in comparison. The differences in percent release were 236%, 110%, 67% and 12% for 24, 48, 72 and 168hr respectively (

Figure 3-22).

Concentration Fields across EOC Model over 7 days

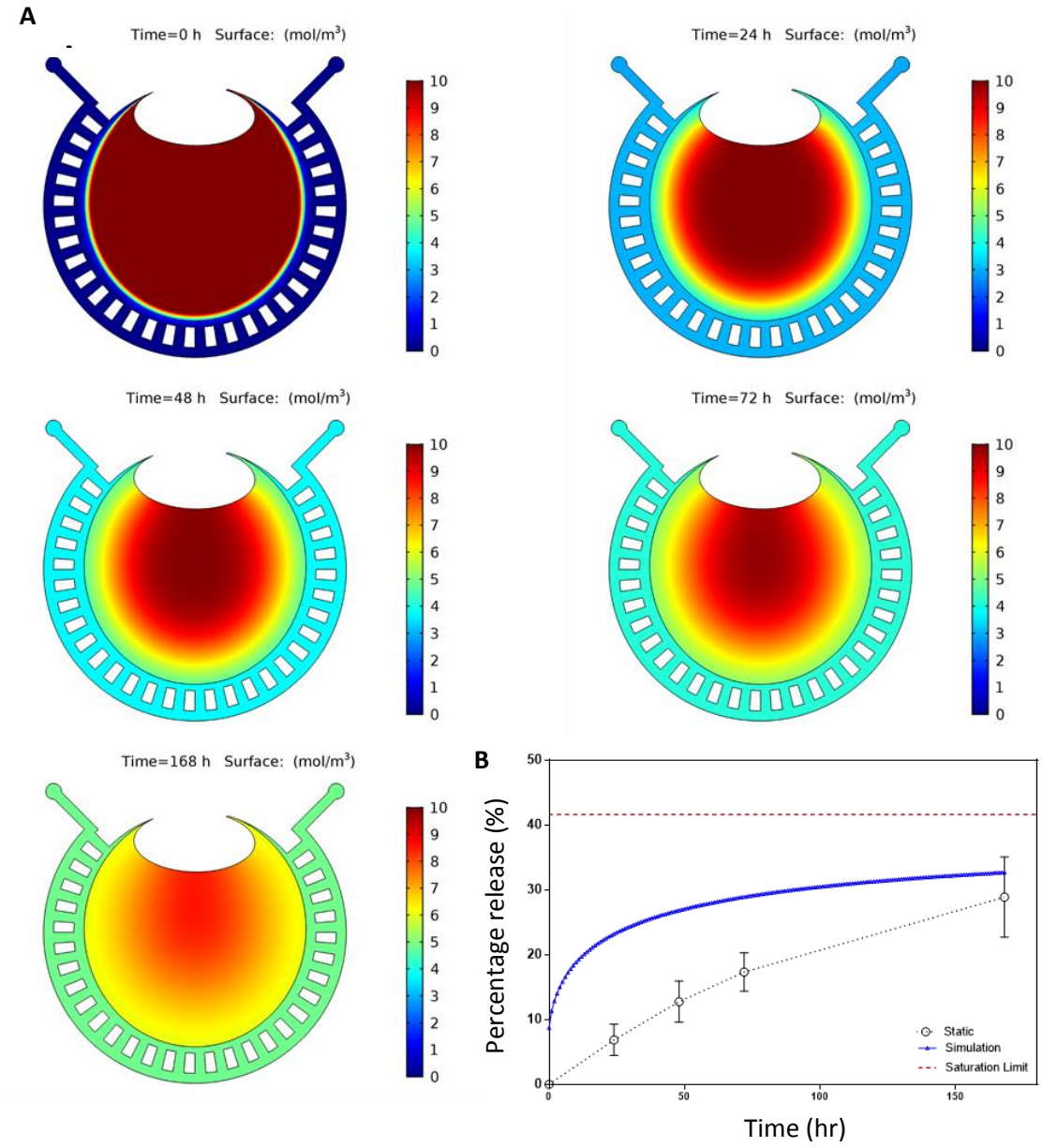

Figure 3-22: (a) Concentration field solution for ibuprofen concentration across the eye-on-a-chip model at 0, 24, 48, 72 and 168 hr. Colour scale bar indicates concentration in mol/m³. (b) Experimental vs simulated concentration profiles of ibuprofen in aqueous phase of EOC model. Experimental data presented as mean concentration ± 1 SD, n = 9.

3.4 DISCUSSION

Following a vitrectomy and the replacement of the vitreous humour with a silicone oil tamponade, any remaining void within the vitreous cavity is replaced with aqueous humour which migrates from the anterior segment of the eye. The interaction between these two liquid phases, the silicone oil tamponade and aqueous humour, could have implications for the release of any drugs solubilised within the oil phase.

Utilising the silicone oil tamponade as a drug reservoir, it is expected that once any drug is released from the oil it will undergo the same clearance mechanisms as drugs injected intravitreally, i.e. anteriorly via aqueous outflow or posteriorly through the blood retina barrier. Bulk flow of aqueous humour within both segments of the eye and its subsequent drainage has been shown to act as a major drug elimination route following intravitreal injections [229]. Dynamic factors such as this produce some of the greatest barriers to drug delivery in the posterior segment and are often overlooked in *in vitro* models. The spherical eye model used in these studies was initially designed to investigate contact angles and interfacial tensions of substances used for tamponades in retinal detachment surgery [222]. The spherical geometry and presence of inlet and outlets ports made an appropriate model for evaluating aqueous flow around the ibuprofen-silicone oil tamponade and ultimately the clearance of ibuprofen away from the oil.

Dye studies were conducted to illustrate the flow profile within the model with a range of flow rates from 20µL/min to 20mL/min. These studies showed that at lower flow rates (20µL/min to 2mL/min), the aqueous fluid, in this case PBS, flowed circumferentially around the silicone oil from the inlet port to the outlet port, with the dye ultimately diffusing throughout the entire aqueous phase. The pattern of fluid flow was comparable for each of the lower flow rates however the velocities within the model were obviously greater as flow rate increased, indicated by the dye reaching the outlet of the model in less time. The flow profiles broadly mimic the mass transfer within the model and show the path that any ibuprofen released from the silicone oil would be expected to take through the model. The consistency of the flow profiles at lower flow rates could be an important factor to consider when comparing the model with the *in vivo* environment. Secretion of aqueous from the ciliary body into the vitreous *in vivo* is reported to occur at a rate of 2-3µL/min [96, 230, 231], the lowest flow rate investigated in these studies was 20µL/min. One of the limitations of using a syringe pump to generate the flow is that they are displacement controlled devices

which use micro-stepping motors and therefore producing a consistently precise flow field is difficult, particularly at very low flow rates. Similar problems are observed with peristaltic pumps, therefore flow rates from 20µL/min to 2mL/min were selected to provide consistent smooth flow which could be generated with both pump types to allow comparison across the models. Using the systematic data collected across these flow rates it could be possible to extrapolate the data to gain an understanding of the flow profiles at lower flow rates such as 2µL/min. The highest flow rate investigated, 20mL/min, produced a fluid flow force which caused the silicone oil bubble to be removed from the system. This unrealistically high flow rate was not used in any drug release studies but was used to illustrate the destruction of the system.

The flow profiles produced in the *in vitro* models were able to be reproduced by the computational simulations. Qualitatively, the simulated flow profiles showed the same circumferential flow around the tamponade from inlet to outlet but one of the advantages of the computational models is they are able to provide more information about the profile which is unable to be seen in the *in vitro* experiments. Technologies such as PIV discussed in chapter 2 are available to visualise flow fields, however this was outside of the scope of the project. From the streamlines present in the simulated data, stagnant areas of recirculating aqueous can be observed between the main stream of flow and the point at which the silicone oil is in contact with the walls of the sphere, excluding the aqueous from the top region of the geometry. These secondary flows appear to have no interaction with the primary stream of flow, this is important in terms of clearance of ibuprofen from these regions. From the corresponding concentration projections it can be seen, particularly at 20µL/min, that where the flow is recirculating in the velocity profile, the concentration of ibuprofen is very high. This suggests, that once released from the silicone oil tamponade, the ibuprofen becomes trapped and accumulates in these areas. As the flow rate increases, this accumulation is dissipated and the concentration of ibuprofen is completely removed from the aqueous phase of the system. Given that the flow rates of aqueous in the eye are very low, should any stagnant areas of aqueous flow present themselves, there is a risk that drug accumulation could occur within these regions which could ultimately lead to toxicity in the adjacent tissues.

Within the EOC device, these regions of accumulation did not present in the computer simulations. This is surprising, particularly at the point at which the oil meets the wall of the device which produces a ‘corner’ region where one would expect a build up to occur. In

addition, the percentage error between the simulated and in vitro results for release of ibuprofen were very high in this model. Although the simulated percentage release achieved at the final time point was within 12% of the in vitro results, the profile of release up to that point was not comparable. It is possible that this could be attributed to the method of input geometry for this particular device. For the model simulations of the Kirkstall QV600 and the spherical eye model, the geometry was built within the COMSOL Multiphysics software based on dimensions from schematic diagrams. The geometry for the EOC model was imported from a CAD file used to manufacture the chips. Following the import of the geometry, it appears resolution is lost between the micro-channels of the chip which in vitro have a width of 100µm. In the simulation geometry it is clear that these micro-channels have a much greater width which therefore increases the interfacial contact area of the SiO and aqueous phase which we have previously shown increases the rate of diffusion in the model as seen by the results for release within the well plates. One limitation of the software is that it is difficult to create very complex and intricate geometries within the software itself and it is therefore useful that CAD files are able to be imported. However in this instance, resolution of small scale features was lost. In the future it would be necessary to create the intricate EOC geometry within the COMSOL software to ensure accuracy in its assembly and produce results within a smaller error of the experimental data.

With the spherical eye model, which is a much simpler geometry, the simulation was able to produce results within 5% of the in vitro data for static experiments and 20% for the flow conditions. For most of the experimental conditions, the simulation overestimated the C_{max} in each case, with the exception of the 20µL/min conditions which predicted a C_{max} 3% lower. Similar observations occur in work presented by Kavousanakis et al., and Jooybar et al. who model the distribution of drugs within the posterior segment of eye following intravitreal injection or sub-scleral implantation [131, 132]. Although the technologies are different, similar physics methods are used to solve the computational models and both report an overestimation in C_{max} for the drugs used in comparison with experimental data of fluorescein kinetics in the vitreous, provided by Palastine and Brubaker [135]. For use as a predictive tool in the development of this drug delivery technology, which hopefully can minimise the use of animal models in any future work, it seems more beneficial for the model to produce an over prediction within the accepted range in error as opposed to an underestimation as administering a potential toxic dose would have greater consequences than a potential sub-therepeutic dose.

The flow mechanics of the vitreous chamber have been studied before both theoretically and experimentally using chambers similar to the spherical eye model used in this study. The majority of these studies investigate the effects of saccadic movements on the fluid dynamics of the vitreous cavity. Saccades are quick movements of the eye that abruptly change the point of fixation and as such are thought to have the most important role in inducing motion in the vitreous chamber [220]. The following have been identified as the characteristic features of a saccadic eye movement: (1) very high angular acceleration, (2) less severe deceleration but effective halting of the movement, (3) a peak angular velocity between 400-600˚s^{-1} [232]. David et al. conducted a theoretical investigation into the effects of small oscillatory movements of the eyeball on movement of the vitreous. They found that for low frequencies of rotation, the vitreous would act as a solid body under motion, as the frequency increases the centre of the sphere would remain stationary with increasing motion as you move out radially from the centre [233]. The results of this study were used by Repetto et al. as a comparison for the observations in flow profiles within their spherical, poly(methyl methacrylate) model of the vitreous chamber under simulated saccadic eye movements [234]. After reaching satisfactory agreement between the theoretical and experimental data, they proceeded to conduct further theoretical studies in to the effect of these movements on other potential vitreous fluids such as silicone oil. The result of this study suggested that using low viscosity silicone oils as tamponade agents reduced the shear stress effects on the wall of their model caused by saccadic motion and would minimise stress on the retina following tamponade placement [234]. Similarly, Chen et al. have used a poly(methyl methacrylate) spherical eye chamber in studies which investigate the flow of heavy SiO and emulsification of different viscosity SiO during simulated saccadic eye movements [227, 235]. The chambers used in these studies were spherical in design as with the model used in this study. In reality the vitreous chamber is not perfectly spherical and a major geometrical feature is the indentation caused by the position of the lens within the eye. Stocchino et al. used an experimental set up based on the work of Repetto et al. [234] but modified their eye chamber to exhibit this indentation feature. They found that inclusion of the indent caused an additional circulation stream to form within the vitreous cavity fluid, at the back of the indentation [236]. This additional flow feature could result in an altered distribution of ibu within the SiO and so in future it would be interesting to study these effects in a more geometrically accurate eye model. One other model, known as the PK-Eye model, was designed by Awaad et al. and included both an anterior and posterior chamber in an attempt to investigate ocular drug clearance via the anterior aqueous outflow pathway. This model

had a posterior cavity and anterior cavity separated by dialysis membrane and they conducted dye studies to show the flow regime after either injection into the posterior region or anterior region and clearance through the anterior segment. This model did not account for lens indentation but did show that dye would not penetrate into the anterior chamber unless flow was present to clear it away [114]..

The saccadic movement profile used in our study was based on the one described by Chan et al. used to investigate emulsification effects on silicone oils [226]. The profile is described in section 3.2.3.4, and the comparison with typical saccades observed in healthy human adults is shown in Table 3-3.This movement pattern was used to observe differences in the percentage release of ibu from SiO when exposed to saccadic movements in comparison to static controls. In the spherical eye model there was an increase in percentage release of the drug over each 24 hour time point when exposed to saccadic simulation, however the only statistically significant difference was seen at 24 hours with 8.4% more released in the moving samples compared with the static models. It was expected that the saccadic movements would increase the rate at which ibu was released as the mechanical action of the motion moves the aqueous more around the silicone oil bolus and therefore transports ibu already released into the aqueous away from the source of the concentration, i.e. the SiO, into the bulk of the aqueous phase and maintains a greater concentration gradient at the interface of the two phases. The effects of the saccadic motion were more obvious in the results observed in the EOC model where there was a statistically significant increase in percentage release of ibu at 48, 72 and 168 hours. Given the dimensions of the micro-channels within the chip device, it is possible that the physical movement of the aqueous phase which the saccadic simulation provides, clears these micro-channels of ibu which could accumulate within them, and moves it into the outer perfusion channel. A limitation of this system, is that natural human saccadic motion is not periodical and the amplitude of the movement can vary from very small, such as when we reading, to very large, looking around a room. However it does allow us to investigate the effects of the motion in a controlled and reproducible manner. Further studies into the effects of changing the profile of this motion on the drug release profile could be interesting to investigate.

There have been theoretical studies investigating saccadic motion on vitreous movement and its implications in drug delivery in the posterior segment. These studies model the transport of drug injected into the vitreous humour of humans and the subsequent diffusion of the drugs out into other tissues. They predict that dispersion of drugs through the vitreous

is much more efficient when exposed to saccadic motion compared to purely diffusion alone in a static system [237, 238]. Kathawate et al. actually describe a mathematical model of drug diffusion through vitreous substitutes, including silicone oil, but do not include flow induced by saccadic motion in their model design. They also model intravitreal injection of the drugs into the silicone oil as opposed to simulating the oil as drug reservoir. Their results show that diffusion, not convection, is the overriding physics of the system when higher viscosity fluids such as SiO are used, however minimal convective terms are used in the model [239]. Unfortunately, time restrictions prevented the inclusion of saccadic motion boundary conditions into the model generated in this study and so there is no simulated data to compare to the experimental work, but in the future I think having a validated predicted simulation of ibu distribution within SiO based on the influence of saccadic motion could prove a cost and time effective tool to use in the development of this drug delivery system.

Although the majority of the results presented in this study are within the tolerated 15% error between simulated and experimental results, I believe that the consistency could be improved and the error reduced by expanding the complexity of the model in to three dimensions (3D), which would be the next step in developing the computer models in to predictive tools. However this work has been able to produce a computational model of a spherical eye model, used in vitro in the development of this novel silicone oil tamponade drug delivery device, and validated this model using comparison with relevant experimental data. It has also shown that saccadic motion has a role to play in ibuprofen release from silicone oil which could be an important consideration taking this technology forward.

	Human	Device
Amplitudes (˚)	5-15	10
Max. angular velocity (˚/s)	300-400	390
Duration (ms)	50	50

Table 3-3: Characteristics of human saccades vs device simulated saccades. Human values from [240, 241].

CHAPTER 4

DISCUSSION, CONCLUSIONS AND FUTURE STUDIES

4.1 DISCUSSION

The retinal pigmented epithelium (RPE) is a highly specialised monolayer of cells located at the back of the retina which plays a vital role in homeostasis and maintenance of the retinal tissue. Along with the Bruch's membrane and choroidal endothelium, it makes up the outer blood retinal barrier (OBRB) which is the structure that separates the neural retinal layer from the choroidal vasculature and regulates the passage of molecules and waste products in and out of the outer retina. Damage to the RPE cell layer can cause a breakdown in the barrier function of the OBRB and ultimately lead to sight threatening complications. Retinal detachment (RD) is one such condition, whereby the inner neuroretina becomes detached from the underlying RPE layer. RD is classified as an ophthalmic emergency and requires urgent treatment to avoid further complications and prevent loss of vision. Complications can include conditions such as proliferative vitreoretinopathy (PVR), a fibrotic disease in which aqueous penetrates the sub-retinal space allowing cytokines and inflammatory factors into the wound site which can cause migration of the RPE into the vitreous cavity. In complicated or severe cases of RD, the most common treatment method is a vitrectomy followed by the insertion of a tamponade to fill the vitreous cavity. The surgery involves removing the natural vitreous and replacing it with either a gas or silicone oil tamponade. The purpose of the tamponade is to maintain contact with the damaged area of the retina and exclude any aqueous from the wound site which could cause an inflammatory response. It seems that there is an opportunity for this tamponade system to gain a supplementary function as a drug delivery device which could further prevent the likelihood of complications developing.

Silicone oil is currently the only tamponade agent available for long term administration as it does not dissipate over time like a gas tamponade does. Utilising the silicone oil tamponade as a drug reservoir to provide sustained drug delivery in the posterior segment has been studied in the past with varying success. One limitation of this technology is that many of the drugs used in the treatment of proliferative diseases are water soluble and therefore poorly soluble in SiO. The success of such a drug delivery device is dependent on the compatibility of drugs that it can be used with, and whether the device can deliver a therapeutic dose over a reasonable period of the necessary treatment time, in the case of PVR this would be 6-8 weeks [242]. Previous studies have investigated the use of lipophilic drugs such as 5-fluoruracil, retinoic acid and α-tocopherol [71, 91, 209, 243]. Ibuprofen is a non-steroidal

anti-inflammatory drug (NSAID) which is lipophilic in nature and therefore readily soluble in SiO. Solubilising ibuprofen within the SiO could produce a drug delivery reservoir with anti-inflammatory capabilities. One previous study has investigated the release of ibuprofen from a silicone oil tamponade and there is scope to for the study of this technology to be taken further [209].

One method of analysing the vast range of potential parameters of a system, such as a new drug delivery device, in a time and cost effective manner is to implement computational simulations. Finite element analysis (FEM) is a numerical method that has applications in solving mathematical physics and engineering problems such as fluid flow and mass transport. This method provides analytical solutions for complex systems which are described by partial differential equations by dividing the larger system into discrete smaller parts, elements. The solutions from the simple equations which describe each element are then assembled in to a larger set of equations which are used to provide a solution for the entire problem. COMSOL Multiphysics is a finite element analysis simulation software which has had widespread use in solving scientific and engineering research problems. One of the benefits of this software is its ability to model multiple physics interfaces simultaneously, making it ideal to study drug transport under the influence of fluid flow.

The aim of this study was to design computational simulations based on complementary *in vitro* systems which could accurately predict the *in vitro* behaviour of a novel tamponade drug delivery system. This drug delivery system was designed around 1000c.st silicone oil, a material that is currently used in vitreoretinal surgery, with solubilised ibuprofen, an anti-inflammatory drug commonly used in pain relief. The hypothesis was that computer models built using experimentally derived parameters from simple *in vitro* experiments would be able to accurately predict the release behaviour of ibuprofen from silicone oil in more complex *in vitro* experiments across a number of model designs. The rationale behind this hypothesis is that numerically based computer simulations have been used for many years to analyse complex physical behaviours, including drug transport and delivery, and their success is ultimately determined by the accuracy of the input parameters and boundary conditions. Therefore obtaining experimentally validated computational simulations of the release behaviour of ibu from SiO in a number of *in vitro* models will allow us to analyse a vast range of input parameters in a more time and cost effective fashion and eventually use these simulations as predictive tools to further develop this technology in the hope of

ultimately contributing to the rapid and cost-effective development of a new drug delivery device that is appropriate for clinical use.

In the present study I was able to create a computer model which showed good agreement between simulated and experimental results for the passage of different molecular weight dextrans across a model of the outer blood retinal barrier which consisted of a human RPE cell line, ARPE-19, and a synthetic Bruch's membrane replacement, NH_3 treated ePTFE. In addition to this I was able to show that ARPE-19 cells withstand culture in the presence of media flow and, when subjected to flow rates up to 200µL/min, barrier functionality is increased compared with static cultures. The results showed however, that there was a threshold limit as to the speed of flow which they can withstand. At 400µL/min, there was a loss of barrier function and a breakdown in the tight junction network. This breakdown in the monolayer barrier obviously had implications for the permeability of dextran across it and therefore agreement of the computer simulated and experimental results was decreased under these conditions as one of the limitations of the computer model is it does not take into account biological changes within the barrier and so assumes a constant permeability across each time point. These findings appear to corroborate a previous study which cultured ARPE-19 cells under flow. Yeste et al. showed reduced permeability of dextran in ARPE-19 cells cultured in a microfluidic chip device with a flow rate of 100µL/min [111]. On the contrary, Chen at al. showed no statistically significant difference in dextran permeability in ARPE-19 cells cultured under media flowing at a rate of 0.8µL/min in their microfluidic device, however the flow rate within this device is so low that it is likely the cells are exposed to very little force from the flow [112].

Using the knowledge gained from modelling the transport of dextran, I was then able to build a computer model which could predict the release of ibuprofen from a silicone oil reservoir under the same flow rates in two different *in vitro* models. Within these two models, the computer simulated results showed strong agreement with the *in vitro* data. Similarly, the computer model was able to accurately predict the release within static conditions in well plates and a spherical eye model. The time scale of study (72 hours) was based on work by Cauldbeck et al. who showed that 100% of ibuprofen freely solubilised in silicone oil was released after 3 days within a 24-well plate [209]. This study has shown that the time-dependent percentage release of ibu from SiO varies dependent on the interfacial contact area of the silicone oil and aqueous phase, however the computer model can be used to predict this release behaviour and can therefore be used as a predictive tool to narrow the

range of experimental study required. It is important to consider the geometrical requirements of such a drug delivery device which is why three different *in vitro* models were used in this study.

Each of the *in vitro* models used in this study have their own advantages and disadvantages and utilising all three gives a greater understanding of how the mechanisms of different model designs affect ibuprofen release from SiO. The Kirkstall QV600 chamber provided the means of being able to design an OBRB model with RPE cells incorporated to investigate permeability of this barrier and transport across it. Although not investigated here, it would also allow the same OBRB model to be used to assess the release of ibu from SiO across the cell/synthetic BM barrier using the basolateral media flow as an analogy to choroidal blood flow. Therefore this system has benefits in modelling the posterior clearance mechanism which intravitreal drugs are exposed to *in vivo*. The disadvantages of this model are that it is geometrically inaccurate and currently only explores the permeability limitation provided by the RPE and not the choroidal endothelium. The spherical eye model provides a more geometrically accurate model of the eye, however it is not designed to accommodate cell culture. It could be possible to grow cells within the model in the future, however work would need to be done on optimising the attachment of the cells to the walls of the model and maintaining sterility could prove difficult. This spherical chamber with the two ports is more suitable in modelling the aqueous outflow pathway that intravitreal drugs could follow *in vivo*.

The computer models of two of these models showed comparable results, however within the third model, the eye-on-a-chip device, the results were not as agreeable. The EOC device was initial developed to investigate the emulsification of different silicone oils [226]. This device provides both a better geometrical representation of the eye and the ability to sustain cell culture but in a 2D chip configuration. There seems to be much debate recently regarding the suitability of microfluidic chip devices as models but they do have advantages in terms of reproducibility and high-throughput nature. The percentage release at the final time point was equal between the simulated and experimental results, however the release profile up to that final time point was not equivalent. This could be because the input geometry within the computer model did not accurately match the *in vitro* specification. This further highlights the point made previously that the computer model is only as good as the information that is applied to it. Previous studies have looked to simulate the release mechanics of drugs injected intravitreally within the posterior segment of the eye. The

majority of these study the transport of drugs within the natural vitreous of the eye. One paper has investigated drug movement in silicone oil within the eye but again only following intravitreal injection. These computer models are theoretical and although they employ a more geometrically representative model of the eye, the data cannot be experimentally validated due to the nature of the study and the requirement to investigate human eyes *in vivo*. Most of these papers base their input parameters on work conducted by Palestine and Brubaker who investigated fluorescein kinetics in the vitreous [135] and in order to prove the accuracy and reliability of computer models, more experimental data needs to made available for comparison. The difficulty in validated computer models of the human eye comes from the inability to run *in vivo* tests for obvious ethical reasons. *In vivo* tests would be able to determine the true permeability of all of the ocular tissues as well as the *in situ* flow dynamics that occur within the eye, though this would not be achievable without invasive measurement techniques. One benefit of computer models is that they are able to provide us information which we are unable to see or collect under experimental conditions, however it is important that there is some way of validating the simulated results in order to produce models which can be believed.

For this study I aimed to produce computer models that could be experimentally validated, so the computer models were designed around *in vitro* models which were accessible and would be used in the early stages of the development of the ibu-SiO device. Using the validated models built in this study, it is now possible to explore more variables such as different drugs, alternative tamponade materials and more complex drug release mechanisms quickly and at reduced cost compared with experimental investigation. Ultimately any alterations in the design of the device would need to be tested experimentally, however the computer models should be able to be used as predictive tools to identify and narrow the range of experimental conditions which need to be studied, saving time and cost.

4.2 CONCLUSIONS

- ARPE-19 cells are able to survive when exposed to basolateral media flow in the Kirkstall QV600 culture chamber depending on the flow rate applied.

- High flow rates affect TEER and cell phenotype, reducing the barrier functionality of ARPE-19 cells cultured on NH_3 treated ePTFE membranes.

- The concentration of dextran on the basolateral side of the ARPE-19/transwell membrane displays a different profile depending on the flow rate of the media used to clear it away from the barrier.

- Results from computer models of the flow within the QV600, designed using data from static dextran transport assays, showed agreement with experimental data from equivalent flow experiments.

- Computer model does not consider biological changes within the cell layer, therefore there is a decrease in agreement in cellular models in comparison with the acellular models.

- Saccadic eye movements increase the rate at which ibuprofen is released from the silicone oil.

- Release rate of ibuprofen varies with interfacial contact area between the silicone oil phase and aqueous phase.

- Computer models of the QV600 and a spherical eye model are able to predict the release profiles of ibuprofen from silicone oil under flow used to simulate drug clearance.

4.3 FUTURE STUDIES

- Develop a more complex model of the outer blood retinal barrier, including choroidal endothelial cells and primary human cells, to make it more physiologically relevant. This would provide a more realistic view of the transport of molecules across the barrier.

- Investigate the release and transport of ibuprofen from silicone oil across the cellular model. This would require finding alternative measurement techniques for detecting the concentration of ibuprofen, however it would lead to a greater understanding of the clearance of the drug away from the RPE layer.

- Further develop the computer models used in this study to incorporate mathematical descriptions of the biological changes which occur within the cell layer. This would create time dependent changes in key parameters, such as permeability, which could reduce the error observed between the simulated and experimental results.

- Investigate the suitability of ibuprofen as a treatment for fibrotic retinal pathologies to determine whether this drug is appropriate for use in this delivery system.

- Expand the simulations into 3 dimensions (3D), again to reduce errors in agreement, and ultimately apply the knowledge gained from the *in vitro* and simulated data to a 3D model of the human eye.

REFERENCES

1. Forrester, J.V., et al., *The Eye: Basic Sciences in Practice*. 2015: Elsevier Health Sciences.

2. Gregory, R.L., *Eye and brain: The psychology of seeing, 5th ed*. Eye and brain: The psychology of seeing, 5th ed. 1997, Princeton, NJ, US: Princeton University Press. ix, 277-ix, 277.

3. Remington, L.A., *Chapter 4 - Retina*, in *Clinical Anatomy and Physiology of the Visual System (Third Edition)*, L.A. Remington, Editor. 2012, Butterworth-Heinemann: Saint Louis. p. 61-92.

4. Kolb, H. *Simple Anatomy of the Retina*. The Organization of the Retina and Visual System 2011 [cited 2018 5 July]; Available from: https://webvision.med.utah.edu/book/part-i-foundations/simpleanatomy-of-the-retina/.

5. Kawamura, S. and S. Tachibanaki, *Rod and cone photoreceptors: molecular basis of the difference in their physiology.* Comp Biochem Physiol A Mol Integr Physiol, 2008. **150**(4): p. 369-77.

6. Sim, et al., *The Retinal Pigment Epithelium: Something More than a Constituent of the Blood-Retinal Barrier—Implications for the Pathogenesis of Diabetic Retinopathy.* Journal of Biomedicine and Biotechnology, 2010. **2010**: p. 15.

7. Strauss, O., *The retinal pigment epithelium in visual function.* Physiol Rev, 2005. **85**(3): p. 845-81.

8. Hamann, S., *Molecular mechanisms of water transport in the eye*, in *International Review of Cytology*. 2002. p. 395-431.

9. Moseley, H., et al., *Routes of clearance of radioactive water from the rabbit vitreous.* British Journal of Ophthalmology, 1984. **68**(3): p. 145-151.

10. Baehr, W., et al., *The retinoid cycle and retina disease.* Vision Research, 2003. **43**(28): p. 2957-2958.

11. Rozanowska, M., et al., *The role of retinal pigment epithelium melanin in photoinduced oxidation of ascorbate.* Photochem Photobiol, 1997. **65**(3): p. 472-9.

12. Bavik, C., et al., *Visual Cycle Modulation as an Approach toward Preservation of Retinal Integrity*. Vol. 10. 2015. e0124940.

13. Streilein, J.W., *Ocular immune privilege: the eye takes a dim but practical view of immunity and inflammation.* J Leukoc Biol, 2003. **74**(2): p. 179-85.

14. Antonetti, D.A., et al., *Molecular mechanisms of vascular permeability in diabetic retinopathy.* Semin Ophthalmol, 1999. **14**(4): p. 240-8.

15. Campbell, M. and P. Humphries, *The Blood-Retina Barrier*, in *Biology and Regulation of Blood-Tissue Barriers*, C.Y. Cheng, Editor. 2013, Springer New York: New York, NY. p. 70-84.

16. Curcio, C.A. and M. Johnson, *Chapter 20 - Structure, Function, and Pathology of Bruch's Membrane*, in *Retina (Fifth Edition)*, S.J. Ryan, et al., Editors. 2013, W.B. Saunders: London. p. 465-481.

17. Nickla, D.L. and J. Wallman, *The multifunctional choroid.* Progress in retinal and eye research, 2010. **29**(2): p. 144-168.

18. Anderson, J.M. and C.M. Van Itallie, *Physiology and function of the tight junction.* Cold Spring Harb Perspect Biol, 2009. **1**(2): p. a002584.

19. Georgiadis, A., et al., *The Tight Junction Associated Signalling Proteins ZO-1 and ZONAB Regulate Retinal Pigment Epithelium Homeostasis in Mice.* PLOS ONE, 2011. **5**(12): p. e15730.

20. Inai, T., J. Kobayashi, and Y. Shibata, *Claudin-1 contributes to the epithelial barrier function in MDCK cells.* Eur J Cell Biol, 1999. **78**(12): p. 849-55.

21. Valle, B.L. and P.J. Morin, *Chapter 13 - Claudins in Cancer Biology*, in *Current Topics in Membranes*, A.S. L. Yu, Editor. 2010, Academic Press. p. 293-333.

22. Litchfield, T.M., S.J.O. Whiteley, and R.D. Lund, *Transplantation of Retinal Pigment Epithelial, Photoreceptor and other Cells as Treatment for Retinal Degeneration.* Experimental Eye Research, 1997. **64**(5): p. 655-666.

23. Ambati, J., et al., *Age-related macular degeneration: etiology, pathogenesis, and therapeutic strategies.* Surv Ophthalmol, 2003. **48**(3): p. 257-93.

24. Abdelfattah, N.S. and S.R. Sadda, *Dry AMD Progression in Wet AMD.* 2018.

25. Rutar, M. and J.M. Provis, *Role of chemokines in shaping macrophage activity in AMD*, in *Retinal Degenerative Diseases*. 2016, Springer. p. 11-16.

26. Excellence, N.I.f.H.a.C. *Age-related macular degeneration*. 2018 [cited 2019 04/06]; Available from: https://www.nice.org.uk/guidance/ng82/chapter/Context.

27. Morimura, H., et al., *Mutations in the RPE65 gene in patients with autosomal recessive retinitis pigmentosa or leber congenital amaurosis.* Proceedings of the National Academy of Sciences, 1998. **95**(6): p. 3088-3093.

28. Sheridan, C., P. Hiscott, and I. Grierson, *Retinal Pigment Epithelium Differentiation and Dedifferentiation*, in *Vitreo-retinal Surgery*, B. Kirchhof and D. Wong, Editors. 2005, Springer Berlin Heidelberg: Berlin, Heidelberg. p. 101-119.

29. Ivanisevic, M., L. Bojic, and D. Eterovic, *Epidemiological study of nontraumatic phakic rhegmatogenous retinal detachment.* Ophthalmic Res, 2000. **32**(5): p. 237-9.

30. Excellence, N.I.f.H.a.C. *Retinal Detachment*. 2015 [cited 2019 04/06]; Available from: https://cks.nice.org.uk/retinal-detachment#!backgroundSub.

31. Go, S., C.B. Hoyng, and C.W. Klaver, *Genetic risk of rhegmatogenous retinal detachment: A familial aggregation study.* Archives of Ophthalmology, 2005. **123**(9): p. 1237-1241.

32. Li, D.Q. and N. Choudhry, *Tractional retinal detachment secondary to diabetic retinopathy.* JAMA Ophthalmology, 2018. **136**(10): p. e183507.

33. Baino, F., *Towards an ideal biomaterial for vitreous replacement: Historical overview and future trends.* Acta Biomater, 2011. **7**(3): p. 921-35.

34. Kang, H.K. and A.J. Luff, *Management of retinal detachment: a guide for non-ophthalmologists.* BMJ, 2008. **336**(7655): p. 1235-1240.

35. Amer, R., H. Nalci, and N. Yalcindag, *Exudative retinal detachment.* Surv Ophthalmol, 2017. **62**(6): p. 723-769.

36. Sternfeld, A., et al., *Advantages of diabetic tractional retinal detachment repair.* Clinical ophthalmology (Auckland, N.Z.), 2015. **9**: p. 1989-1994.

37. Sadaka, A. and G.P. Giuliari, *Proliferative vitreoretinopathy: current and emerging treatments.* Clinical ophthalmology (Auckland, N.Z.), 2012. **6**: p. 1325-1333.

38. Chiba, C., *The retinal pigment epithelium: An important player of retinal disorders and regeneration.* Experimental Eye Research, 2014. **123**: p. 107-114.

39. Jin, Y., et al., *TRAUMATIC PROLIFERATIVE VITREORETINOPATHY: Clinical and Histopathological Observations.* RETINA, 2017. **37**(7): p. 1236-1245.

40. Pastor, J.C., *Proliferative vitreoretinopathy: an overview.* Surv Ophthalmol, 1998. **43**(1): p. 3-18.

41. Heriot, W.J. and R. Machemer, *Pigment epithelial repair.* Graefes Arch Clin Exp Ophthalmol, 1992. **230**(1): p. 91-100.

42. Tamiya, S. and H.J. Kaplan, *Role of epithelial–mesenchymal transition in proliferative vitreoretinopathy.* Experimental Eye Research, 2016. **142**: p. 26-31.

43. Pastor, J.C., E.R.g. de la Rúa, and F. Martín, *Proliferative vitreoretinopathy: risk factors and pathobiology.* Progress in retinal and eye research, 2002. **21**(1): p. 127-144.

44. Feltgen, N. and P. Walter, *Rhegmatogenous retinal detachment--an ophthalmologic emergency.* Deutsches Arzteblatt international, 2014. **111**(1-2): p. 12-22.

45. Zaidi, A.A., R. Alvarado, and A. Irvine, *Pneumatic retinopexy: success rate and complications.* The British journal of ophthalmology, 2006. **90**(4): p. 427-428.

46. Chan, C.K., et al., *Pneumatic retinopexy for the repair of retinal detachments: a comprehensive review (1986-2007).* Surv Ophthalmol, 2008. **53**(5): p. 443-78.

47. Lam, R.F., et al., *Pars Plana Vitrectomy and Perfluoropropane (C3F8) Tamponade for Retinal Detachment Due to Myopic Macular Hole: A Prognostic Factor Analysis.* American Journal of Ophthalmology, 2006. **142**(6): p. 938-944.e2.

48. Sinawat, S., et al., *Air vs perfluoropropane gas in pneumatic retinopexy: a randomized noninferiority trial.* Arch Ophthalmol, 2010. **128**(10): p. 1243-7.

49. *The repair of rhegmatogenous retinal detachments. American Academy of Ophthalmology.* Ophthalmology, 1996. **103**(8): p. 1313-24.

50. Hatef, E., et al., *Pneumatic retinopexy versus scleral buckle for repairing simple rhegmatogenous retinal detachments.* The Cochrane database of systematic reviews, 2015. **5**(5): p. CD008350-CD008350.

51. Valldeperas, X. and J. Lorenzo-Carrero, *Vitreous Tamponades in Highly Myopic Eyes*. Vol. 2014. 2014. 420380.

52. Joussen, A.M. and D. Wong, *The concept of heavy tamponades-chances and limitations.* Graefes Arch Clin Exp Ophthalmol, 2008. **246**(9): p. 1217-24.

53. Vaziri, K., et al., *Tamponade in the surgical management of retinal detachment.* Clinical ophthalmology (Auckland, N.Z.), 2016. **10**: p. 471-476.

54. Krzystolik, M.G. and D.J. D'Amico, *Complications of intraocular tamponade: silicone oil versus intraocular gas.* Int Ophthalmol Clin, 2000. **40**(1): p. 187-200.

55. Barca, F., T. Caporossi, and S. Rizzo, *Silicone Oil: Different Physical Proprieties and Clinical Applications.* BioMed Research International, 2014. **2014**: p. 7.

56. Kim, Y.K., B. Gunther, and H. Meinert, *A new, heavier-than-water silicone oil: a solution of perfluorohexyloctane in polydimethylsiloxane.* Eur J Ophthalmol, 2005. **15**(5): p. 627-37.

57. Williams, R.L., et al., *Novel heavy tamponade for vitreoretinal surgery.* Invest Ophthalmol Vis Sci, 2013. **54**(12): p. 7284-92.

58. Valone, J., Jr. and M. McCarthy, *Emulsified anterior chamber silicone oil and glaucoma.* Ophthalmology, 1994. **101**(12): p. 1908-12.

59. Miller, J.B., T.D. Papakostas, and D.G. Vavvas, *Complications of emulsified silicone oil after retinal detachment repair.* Semin Ophthalmol, 2014. **29**(5-6): p. 312-8.

60. Kim, R.W. and C. Baumal, *Anterior segment complications related to vitreous substitutes.* Ophthalmol Clin North Am, 2004. **17**(4): p. 569-76, vi.

61. Scott, I.U., et al., *Outcomes of complex retinal detachment repair using 1000- vs 5000-centistoke silicone oil.* Arch Ophthalmol, 2005. **123**(4): p. 473-8.

62. Caramoy, A., et al., *Development of Emulsification-Resistant Silicone Oils: Can We Go Beyond 2000 mPas Silicone Oil?* Investigative Ophthalmology & Visual Science, 2011. **52**(8): p. 5432-5436.

63. W Allinson, R., *Adjuvant 5-FU and heparin prevent PVR*. Vol. 109. 2002. 829-30; author reply 830.

64. Joondeph, B.C., et al., *Liposome-encapsulated 5-fluorouracil in the treatment of proliferative vitreoretinopathy.* Ophthalmic Surgery, Lasers and Imaging Retina, 1988. **19**(4): p. 252-256.

65. Borhani, H., et al., *Suppression of experimental proliferative vitreoretinopathy by sustained intraocular delivery of 5-FU.* International Ophthalmology, 1995. **19**(1): p. 43-49.

66. Annane, D., et al., *Corticosteroids for treating sepsis.* Cochrane database of systematic reviews, 2015(12).

67. Liang, H., Y. Hui, and Y. Cai, *Triamcinolone acetonide in the prevention of experimental proliferative vitreoretinopathy.* [Zhonghua yan ke za zhi] Chinese journal of ophthalmology, 1994. **30**(2): p. 122-124.

68. Chen, W., et al., *Midterm results of low-dose intravitreal triamcinolone as adjunctive treatment for proliferative vitreoretinopathy.* Retina, 2011. **31**(6): p. 1137-1142.

69. Jonas, J.B., et al., *Intravitreal injection of crystalline cortisone as adjunctive treatment of proliferative diabetic retinopathy.* American journal of ophthalmology, 2001. **131**(4): p. 468-471.

70. Sunalp, M., et al., *Effects of cytotoxic drugs on proliferative vitreoretinopathy in the rabbit cell injection model.* Current eye research, 1984. **3**(4): p. 619-623.

71. Cauldbeck, H., et al., *Modulated release from implantable ocular silicone oil tamponade drug reservoirs.* Journal of Polymer Science Part A: Polymer Chemistry, 2018. **56**(8): p. 938-946.

72. Ricciotti, E. and G.A. FitzGerald, *Prostaglandins and inflammation.* Arteriosclerosis, thrombosis, and vascular biology, 2011. **31**(5): p. 986-1000.

73. Zhang, W., M.R. Prausnitz, and A. Edwards, *Model of transient drug diffusion across cornea.* Journal of Controlled Release, 2004. **99**(2): p. 241-258.

74. Souza, J.G., et al., *Topical delivery of ocular therapeutics: carrier systems and physical methods.* Journal of Pharmacy and Pharmacology, 2014. **66**(4): p. 507-530.

75. Hughes, P.M., et al., *Topical and systemic drug delivery to the posterior segments.* Advanced Drug Delivery Reviews, 2005. **57**(14): p. 2010-2032.

76. London, N.J.S., et al., *Determining the effect of low-dose isotretinoin on proliferative vitreoretinopathy: the DELIVER trial.* British Journal of Ophthalmology, 2018: p. bjophthalmol-2018-312839.

77. Maurice, D., *Practical issues in intravitreal drug delivery.* Journal of Ocular Pharmacology and therapeutics, 2001. **17**(4): p. 393-401.

78. Choonara, Y.E., et al., *A review of implantable intravitreal drug delivery technologies for the treatment of posterior segment eye diseases.* Journal of Pharmaceutical Sciences, 2010. **99**(5): p. 2219-2239.

79. Danckwerts, M. and R. Fassihi, *Implantable Controlled Release Drug Delivery Systems: A Review*. Vol. 17. 1991. 1465-1502.

80. Musch, D., et al., *Treatment of cytomegalovirus retinitis with a sustained-release ganciclovir implant*. Vol. 124. 1997. 716.

81. Patel, A., et al., *Ocular drug delivery systems: An overview.* World journal of pharmacology, 2013. **2**(2): p. 47-64.

82. Akbarzadeh, A., et al., *Liposome: classification, preparation, and applications.* Nanoscale research letters, 2013. **8**(1): p. 102-102.

83. Fishman, P., et al., *Liposome-encapsulated3H-5FU in rabbits.* International Ophthalmology, 1989. **13**(5): p. 361-365.

84. Assil, K.K., et al., *Liposome suppression of proliferative vitreoretinopathy. Rabbit model using antimetabolite encapsulated liposomes.* Investigative Ophthalmology & Visual Science, 1991. **32**(11): p. 2891-2897.

85. Hou, H., et al., *A Novel Approach of Daunorubicin Application on Formation of Proliferative Retinopathy Using a Porous Silicon Controlled Delivery System:*

PharmacodynamicsOcular Pharmacodymamics of pSi-DNR. Investigative Ophthalmology & Visual Science, 2015. **56**(4): p. 2755-2763.

86. Peyman, G.A., et al., *Clearance of microsphere-entrapped 5-fluorouracil and cytosine arabinoside from the vitreous of primates.* International Ophthalmology, 1992. **16**(2): p. 109-113.

87. Giordano, G.G., M.F. Refojo, and M.H. Arroyo, *Sustained delivery of retinoic acid from microspheres of biodegradable polymer in PVR.* Investigative Ophthalmology & Visual Science, 1993. **34**(9): p. 2743-2751.

88. Tolentino, F.I., et al., *BCNU in silicone oil in proliferative vitreoretinopathy: I. Solubility, stability (in vitro and in vivo), and antiproliferative (in vitro) studies AU - Chung, Hum.* Current Eye Research, 1988. **7**(12): p. 1199-1206.

89. Arroyo, M.H., et al., *Silicone Oil as a delivery vehicle for BCNU in rabbit proliferative vitreoretinopathy.* Retina, 1993. **13**(3): p. 245-250.

90. Veloso, J.A.A.S., et al., *13-cis-Retinoic Acid in Silicone-Fluorosilicone Copolymer Oil in a Rabbit Model of Proliferative Vitreoretinopathy.* Experimental Eye Research, 1997. **65**(3): p. 425-434.

91. Steffansen, B., P. Ashton, and A. Buur, *Intraocular drug delivery. In vitro release studies of 5-fluorouracil from N1-alkoxycarbonyl prodrugs in silicone oil*. Vol. 132. 1996. 243-250.

92. Urtti, A., *Challenges and obstacles of ocular pharmacokinetics and drug delivery.* Advanced Drug Delivery Reviews, 2006. **58**(11): p. 1131-1135.

93. Urtti, A., et al., *Controlled ocular timolol delivery: systemic absorption and intraocular pressure effects in humans.* Pharmaceutical research, 1994. **11**(9): p. 1278-1282.

94. Urtti, A. and L. Salminen, *Minimizing systemic absorption of topically administered ophthalmic drugs.* Survey of ophthalmology, 1993. **37**(6): p. 435-456.

95. Maurice, D. and S. Mishima, *Ocular pharmacokinetics*, in *Pharmacology of the Eye*. 1984, Springer. p. 19-116.

96. Goel, M., et al., *Aqueous humor dynamics: a review.* The open ophthalmology journal, 2010. **4**: p. 52-59.

97. Bill, A. and S.F. Nilsson, *Control of ocular blood flow.* J Cardiovasc Pharmacol, 1985. **7 Suppl 3**: p. S96-102.

98. Pitkänen, L., et al., *Vitreous is a barrier in nonviral gene transfer by cationic lipids and polymers.* Pharmaceutical research, 2003. **20**(4): p. 576-583.

99. Park, J., et al., *Evaluation of coupled convective–diffusive transport of drugs administered by intravitreal injection and controlled release implant.* Journal of controlled release, 2005. **105**(3): p. 279-295.

100. Shafaie, S., et al., *In Vitro Cell Models for Ophthalmic Drug Development Applications.* BioResearch open access, 2016. **5**(1): p. 94-108.

101. Griffith, L.G. and M.A. Swartz, *Capturing complex 3D tissue physiology in vitro.* Nature reviews Molecular cell biology, 2006. **7**(3): p. 211.

102. Tegtmeyer, S., S. Reichl, and C.C. Muller-Goymann, *Cultivation and characterization of a bovine in vitro model of the cornea.* Pharmazie, 2004. **59**(6): p. 464-71.

103. Gukasyan, H.J., K.-J. Kim, and V.H.L. Lee, *The Conjunctival Barrier in Ocular Drug Delivery*, in *Drug Absorption Studies: In Situ, In Vitro and In Silico Models*, C. Ehrhardt and K.-J. Kim, Editors. 2008, Springer US: Boston, MA. p. 307-320.

104. Hamilton, R.D., A.J. Foss, and L. Leach, *Establishment of a human in vitro model of the outer blood–retinal barrier.* Journal of Anatomy, 2007. **211**(6): p. 707-716.

105. Kubo, Y., S.-i. Akanuma, and K.-i. Hosoya, *Influx Transport of Cationic Drug at the Blood–Retinal Barrier: Impact on the Retinal Delivery of Neuroprotectants.* Biological and Pharmaceutical Bulletin, 2017. **40**(8): p. 1139-1145.

106. Forrester, J., et al., *Cellular proliferation in the vitreous: the use of vitreous explants as a model system.* Investigative ophthalmology & visual science, 1986. **27**(7): p. 1085-1094.

107. Hosoya, K.-i. and M. Tachikawa, *The inner blood-retinal barrier*, in *Biology and Regulation of Blood-Tissue Barriers*. 2013, Springer. p. 85-104.

108. Caldwell, R.B., et al., *Vascular endothelial growth factor and diabetic retinopathy: pathophysiological mechanisms and treatment perspectives.* Diabetes/metabolism research and reviews, 2003. **19**(6): p. 442-455.

109. Beharry, K.D., et al., *Human retinal endothelial cells and astrocytes cultured on 3-D scaffolds for ocular drug discovery and development.* Prostaglandins & Other Lipid Mediators, 2018. **134**: p. 93-107.

110. Skottman, H., et al., *Contacting co-culture of human retinal microvascular endothelial cells alters barrier function of human embryonic stem cell derived retinal pigment epithelial cells.* Experimental Cell Research, 2017. **359**(1): p. 101-111.

111. Yeste, J., et al., *A compartmentalized microfluidic chip with crisscross microgrooves and electrophysiological electrodes for modeling the blood–retinal barrier.* Lab on a Chip, 2018. **18**(1): p. 95-105.

112. Chen, L.J., et al., *Microfluidic co-cultures of retinal pigment epithelial cells and vascular endothelial cells to investigate choroidal angiogenesis.* Scientific Reports, 2017. **7**(1).

113. Pepić, I., et al., *Toward the practical implementation of eye-related bioavailability prediction models.* Drug Discovery Today, 2014. **19**(1): p. 31-44.

114. Awwad, S., et al., *The PK-Eye: A Novel In Vitro Ocular Flow Model for Use in Preclinical Drug Development.* J Pharm Sci, 2015. **104**(10): p. 3330-42.

115. Higuchi, T., *Physical chemical analysis of percutaneous absorption process from creams and ointments.* J. Soc. Cosmet. Chem, 1960. **11**: p. 85-97.

116. Siepmann, J. and F. Siepmann, *Mathematical modeling of drug delivery.* International Journal of Pharmaceutics, 2008. **364**(2): p. 328-343.

117. Ryser, M.D., P.E. Gravitt, and E.R. Myers, *Mechanistic mathematical models: An underused platform for HPV research.* Papillomavirus Research, 2017. **3**: p. 46-49.

118. Zienkiewicz, O.C., et al., *The finite element method*. Vol. 36. 1977: McGraw-hill London.

119. Melenk, J.M. and I. Babuška, *The partition of unity finite element method: basic theory and applications.* Computer methods in applied mechanics and engineering, 1996. **139**(1-4): p. 289-314.

120. Hughes, T.J., *The finite element method: linear static and dynamic finite element analysis*. 2012: Courier Corporation.

121. Hughes, T.J., J.A. Cottrell, and Y. Bazilevs, *Isogeometric analysis: CAD, finite elements, NURBS, exact geometry and mesh refinement.* Computer methods in applied mechanics and engineering, 2005. **194**(39-41): p. 4135-4195.

122. Multiphysics, C., *Comsol.* Inc., Burlington, MA, www. comsol. com, 1994.

123. Chorin, A.J., *Numerical solution of the Navier-Stokes equations.* Mathematics of computation, 1968. **22**(104): p. 745-762.

124. Temam, R., *Navier-Stokes equations: theory and numerical analysis*. Vol. 343. 2001: American Mathematical Soc.

125. Chiogna, G., et al., *Mixing, entropy and reactive solute transport.* Geophysical Research Letters, 2012. **39**(20).

126. Zhang, Y.-h., S.A. Campbell, and S. Karthikeyan, *Finite element analysis of hollow out-of-plane HfO2 microneedles for transdermal drug delivery applications*. Vol. 20. 2018.

127. Loizidou, E.Z., et al., *Evaluation of geometrical effects of microneedles on skin penetration by CT scan and finite element analysis.* European Journal of Pharmaceutics and Biopharmaceutics, 2016. **107**: p. 1-6.

128. Caccavo, D., et al., *Modeling the Drug Release from Hydrogel-Based Matrices.* Molecular Pharmaceutics, 2015. **12**(2): p. 474-483.

129. Sturm, R., *A computer model for the simulation of nanoparticle deposition in the alveolar structures of the human lungs.* Annals of translational medicine, 2015. **3**(19): p. 281-281.

130. Balachandran, R.K. and V.H. Barocas, *Computer Modeling of Drug Delivery to the Posterior Eye: Effect of Active Transport and Loss to Choroidal Blood Flow.* Pharmaceutical Research, 2008. **25**(11): p. 2685-2696.

131. Jooybar, E., et al., *Computational modeling of drug distribution in the posterior segment of the eye: Effects of device variables and positions.* Mathematical Biosciences, 2014. **255**(0): p. 11-20.

132. Kavousanakis, M.E., N.G. Kalogeropoulos, and D.T. Hatziavramidis, *Computational modeling of drug delivery to the posterior eye.* Chemical Engineering Science, 2014. **108**: p. 203-212.

133. Loch, C., et al., *Simulation of drug distribution in the vitreous body after local drug application into intact vitreous body and in progress of posterior vitreous detachment.* Journal of Pharmaceutical Sciences, 2014. **103**(2): p. 517-526.

134. Kotha, S. and L. Murtomäki, *Virtual pharmacokinetic model of human eye.* Mathematical Biosciences, 2014. **253**(0): p. 11-18.

135. Palestine, A.G. and R.F. Brubaker, *Pharmacokinetics of fluorescein in the vitreous.* Invest Ophthalmol Vis Sci, 1981. **21**(4): p. 542-9.

136. Giusti, S., et al., *A novel dual-flow bioreactor simulates increased fluorescein permeability in epithelial tissue barriers.* Biotechnol J, 2014. **9**(9): p. 1175-84.

137. Chandorkar, P., et al., *Fast-track development of an in vitro 3D lung/immune cell model to study Aspergillus infections.* Scientific Reports, 2017. **7**(1): p. 11644.

138. Pagliari, S., et al., *A multistep procedure to prepare pre-vascularized cardiac tissue constructs using adult stem sells, dynamic cell cultures, and porous scaffolds.* Frontiers in physiology, 2014. **5**: p. 210-210.

139. Rashidi, H., et al., *Fluid shear stress modulation of hepatocyte-like cell function.* Archives of toxicology, 2016. **90**(7): p. 1757-1761.

140. Nithiananthan, S., et al., *Physiological Fluid Flow Moderates Fibroblast Responses to TGF-beta1.* J Cell Biochem, 2017. **118**(4): p. 878-890.

141. Dunn, K.C., et al., *ARPE-19, a human retinal pigment epithelial cell line with differentiated properties.* Experimental Eye Research, 1996. **62**(2): p. 155-169.

142. Dunn, K.C., et al., *The human retinal pigment epithelial cell line ARPE-19 is polarized.* Investigative Ophthalmology and Visual Science, 1996. **37**(3).

143. Samuel, W., et al., *Appropriately differentiated ARPE-19 cells regain phenotype and gene expression profiles similar to those of native RPE cells*. Vol. 23. 2017.

144. *Cryopreservation of Mammalian Cells*. ThermoFisher Scientific cited 2018]; Available from: https://www.thermofisher.com/uk/en/home/references/gibco-cell-culture-basics/cell-culture-protocols/cryopreservation-of-mammalian-cells.html.

145. Mason, S.L., et al., *Ocular epithelial transplantation: Current uses and future potential.* Regenerative Medicine, 2011. **6**(6): p. 767-782.

146. Kearns, V.R., et al., *Surface modified expanded-polytetrafluoroethylene (ePTFE) substrates for retinal pigment epithelial growth and implantation.* European Cells and Materials, 2011. **22**(SUPPL.2): p. 54.

147. Grethel, E.J., et al., *Prosthetic patches for congenital diaphragmatic hernia repair: Surgisis vs Gore-Tex.* Journal of Pediatric Surgery, 2006. **41**(1): p. 29-33.

148. Cundiff, G.W., et al., *Risk factors for mesh/suture erosion following sacral colpopexy.* American journal of obstetrics and gynecology, 2008. **199**(6): p. 688. e1-688. e5.

149. DAVID, T.E., *Replacement of chordae tendineae with expanded polytetrafluoroethylene sutures.* Journal of cardiac surgery, 1989. **4**(4): p. 286-290.

150. Krishna, Y., et al., *Expanded polytetrafluoroethylene as a substrate for retinal pigment epithelial cell growth and transplantation in age-related macular degeneration.* British Journal of Ophthalmology, 2011. **95**(4): p. 569-573.

151. Kearns, V.R., R.J. McMurray, and M.J. Dalby, *Biomaterial surface topography to control cellular response: Technologies, cell behaviour and biomedical applications*, in *Surface Modification of Biomaterials: Methods Analysis and Applications*. 2011. p. 169-201.

152. Krishna, Y., et al., *Expanded Polytetrafluoroethylene as a Substrate for Retinal Pigment Epithelial Cell Growth and Transplantation in Age-related Macular Degeneration*. Vol. 95. 2011. 569-73.

153. Chu, P.K., et al., *Plasma-surface modification of biomaterials.* Materials Science and Engineering: R: Reports, 2002. **36**(5): p. 143-206.

154. Pringle, S.D., V.S. Joss, and C. Jones, *Ammonia Plasma Treatment of PTFE Under Known Plasma Conditions.* Surface and Interface Analysis, 1996. **24**(12): p. 821-829.

155. O'Kell, S., et al., *Effects of low-power plasma treatment on polyethylene surfaces.* Surface and Interface Analysis, 1995. **23**(5): p. 319-327.

156. Wilson, D.J., R.L. Williams, and R.C. Pond, *Plasma modification of PTFE surfaces. Part I: Surfaces immediately following plasma treatment.* Surface and Interface Analysis, 2001. **31**(5): p. 385-396.

157. Samuel, W., et al., *Appropriately differentiated ARPE-19 cells regain phenotype and gene expression profiles similar to those of native RPE cells.* Molecular vision, 2017. **23**: p. 60-89.

158. Luo, Y., et al., *Effects of Culture Conditions on Heterogeneity and the Apical Junctional Complex of the ARPE-19 Cell Line.* Investigative Ophthalmology & Visual Science, 2006. **47**(8): p. 3644-3655.

159. Riss, T.L., et al., *Cell Viability Assays*, in *Assay Guidance Manual*, G.S. Sittampalam, et al., Editors. 2004, Eli Lilly & Company and the National Center for Advancing Translational Sciences: Bethesda (MD).

160. Barcellona, M.L. and E. Gratton, *Fluorescence anisotropy of DNA/DAPI complex: torsional dynamics and geometry of the complex.* Biophys J, 1996. **70**(5): p. 2341-51.

161. Kurosaka, D., et al., *TGF-β2 increases α-smooth muscle actin expression in bovine retinal pigment epithelial cells.* Current Eye Research, 1996. **15**(11): p. 1144-1147.

162. Nevala, H., T. Ylikomi, and H. Tähti, *Evaluation of the selected barrier properties of retinal pigment epithelial cell line ARPE-19 for an in-vitro blood-brain barrier model.* Human & Experimental Toxicology, 2008. **27**(10): p. 741-749.

163. Mannermaa, E., et al., *Filter-cultured ARPE-19 cells as outer blood–retinal barrier model.* European Journal of Pharmaceutical Sciences, 2010. **40**(4): p. 289-296.

164. Iloki Assanga, S.B. and L. Luján, *Cell Growth Curves for Different Cell Lines and their Relationship with Biological Activities*. Vol. 4. 2013.

165. Bailey, T.A., et al., *Oxidative Stress Affects the Junctional Integrity of Retinal Pigment Epithelial Cells.* Investigative Ophthalmology and Visual Science, 2004. **45**(2): p. 675-684.

166. Hirata, J., et al., *Oxidative stress regulates expression of claudin-1 in human RPE cells.* Central European Journal of Biology, 2014. **9**(5): p. 461-468.

167. Scuderi, S., et al., *Ameliorative effect of PACAP and VIP against increased permeability in a model of outer blood retinal barrier dysfunction.* Peptides, 2013. **39**: p. 119-124.

168. Chen, L.-J., et al., *Microfluidic co-cultures of retinal pigment epithelial cells and vascular endothelial cells to investigate choroidal angiogenesis.* Scientific reports, 2017. **7**(1): p. 3538-3538.

169. Chen, H.-C., et al., *Wnt signaling induces epithelial-mesenchymal transition with proliferation in ARPE-19 cells upon loss of contact inhibition.* Laboratory investigation; a journal of technical methods and pathology, 2012. **92**(5): p. 676-687.

170. Li, H., et al., *Snail involves in the transforming growth factor beta1-mediated epithelial-mesenchymal transition of retinal pigment epithelial cells.* PLoS One, 2011. **6**(8): p. e23322.

171. K. Batchelor, G., *On Steady Laminar Flow with Closed Stream Lines at Large Reynolds Number*. Vol. 1. 1956. 177-190.

172. Eckhardt, B., et al., *Turbulence Transition in Pipe Flow.* Annual Review of Fluid Mechanics, 2007. **39**(1): p. 447-468.

173. Durlofsky, L. and J. F. Brady, *Analysis of the Brinkman Equation as a Model for Flow in Porous Media*. Vol. 30. 1987. 3329-3341.

174. Day, M.A., *The no-slip condition of fluid dynamics.* Erkenntnis, 1990. **33**(3): p. 285-296.

175. Coron, J.-M., *On the controllability of 2-D incompressible Navier Stokes equations with the Navier slip boundary conditions*. Vol. 1. 1996. 35-75.

176. Scheytt, T., et al., *1-Octanol/Water Partition Coefficients of 5 Pharmaceuticals from Human Medical Care: Carbamazepine, Clofibric Acid, Diclofenac, Ibuprofen, and Propyphenazone.* Water, Air, and Soil Pollution, 2005. **165**(1): p. 3-11.

177. Dunn, K.C., et al., *ARPE-19, A Human Retinal Pigment Epithelial Cell Line with Differentiated Properties.* Experimental Eye Research, 1996. **62**(2): p. 155-170.

178. Sonoda, S., et al., *A protocol for the culture and differentiation of highly polarized human retinal pigment epithelial cells.* Nature protocols, 2009. **4**(5): p. 662-673.

179. Hamilton, R.D. and L. Leach, *Isolation and Properties of an In Vitro Human Outer Blood-Retinal Barrier Model*, in *The Blood-Brain and Other Neural Barriers: Reviews and Protocols*, S. Nag, Editor. 2011, Humana Press: Totowa, NJ. p. 401-416.

180. Chung, M., et al., *Wet-AMD on a Chip: Modeling Outer Blood-Retinal Barrier In Vitro.* Advanced Healthcare Materials, 2018. **7**(2): p. 1700028.

181. Haneef, A.S. and S. Downes, *Assessing the Suitability of Electrospun Poly(Ethylene Terephthalate) and Polystyrene as Cell Carrier Substrates for Potential Subsequent Implantation as a Synthetic Bruch's Membrane.* International Journal of Polymeric Materials and Polymeric Biomaterials, 2015. **64**(6): p. 320-332.

182. Cassady, A.I., N.M. Hidzir, and L. Grøndahl, *Enhancing expanded poly(tetrafluoroethylene) (ePTFE) for biomaterials applications.* Journal of Applied Polymer Science, 2014. **131**(15).

183. Batniji, R.K., et al., *Tissue response to expanded polytetrafluoroethylene and silicone implants in a rabbit model.* Archives of Facial Plastic Surgery, 2002. **4**(2): p. 111-113.

184. Kearns, V.R., et al., *The formation of a functional retinal pigment epithelium occurs on porous polytetrafluoroethylene substrates independently of the surface chemistry.* Journal of Materials Science: Materials in Medicine, 2017. **28**(8): p. 124.

185. Williams, R.L., D.J. Wilson, and N.P. Rhodes, *Stability of plasma-treated silicone rubber and its influence on the interfacial aspects of blood compatibility.* Biomaterials, 2004. **25**(19): p. 4659-4673.

186. Pu, F.R., et al., *Effects of plasma treated PET and PTFE on expression of adhesion molecules by human endothelial cells in vitro.* Biomaterials, 2002. **23**(11): p. 2411-2428.

187. McNeil, E., C.T. Capaldo, and I.G. Macara, *Zonula Occludens-1 Function in the Assembly of Tight Junctions in Madin-Darby Canine Kidney Epithelial Cells.* Molecular Biology of the Cell, 2006. **17**(4): p. 1922-1932.

188. Abe, T., et al., *Interleukin-1β and Barrier Function of Retinal Pigment Epithelial Cells (ARPE-19): Aberrant Expression of Junctional Complex Molecules.* Investigative Ophthalmology & Visual Science, 2003. **44**(9): p. 4097-4104.

189. Bernstein, M.H. and M.J. Hollenberg, *Fine Structure of the Choriocapillaris and Retinal Capillaries.* Investigative Ophthalmology & Visual Science, 1965. **4**(6): p. 1016-1025.

190. *Physiology of the eye, Francis Heed Adler, The C. V. Mosby Company, St. Louis by John A. Alexander.* The Australian Journal of Optometry, 1965. **48**(7): p. 216-219.

191. Ranta, V.-P., et al., *Barrier analysis of periocular drug delivery to the posterior segment.* Journal of Controlled Release, 2010. **148**(1): p. 42-48.

192. Flower, R.W., A.W. Fryczkowski, and D.S. McLeod, *Variability in choriocapillaris blood flow distribution.* Investigative Ophthalmology & Visual Science, 1995. **36**(7): p. 1247-1258.

193. Flower, R.W., et al., *Theoretical investigation of the role of choriocapillaris blood flow in treatment of subfoveal choroidal neovascularization associated with age-related macular degeneration.* American Journal of Ophthalmology, 2001. **132**(1): p. 85-93.

194. Martin, K.C., et al., *Symmetry-breaking in branching epithelia: cells on micro-patterns under flow challenge the hypothesis of positive feedback by a secreted autocrine inhibitor of motility.* Journal of Anatomy, 2017. **230**(6): p. 766-774.

195. Flitney, E.W., et al., *Insights into the mechanical properties of epithelial cells: the effects of shear stress on the assembly and remodeling of keratin intermediate filaments.* FASEB journal : official publication of the Federation of American Societies for Experimental Biology, 2009. **23**(7): p. 2110-2119.

196. Zeisberg, M. and E.G. Neilson, *Biomarkers for epithelial-mesenchymal transitions.* The Journal of Clinical Investigation, 2009. **119**(6): p. 1429-1437.

197. Kalluri, R. and R.A. Weinberg, *The basics of epithelial-mesenchymal transition.* The Journal of clinical investigation, 2009. **119**(6): p. 1420-1428.

198. Maggiorani, D., et al., *Shear Stress-Induced Alteration of Epithelial Organization in Human Renal Tubular Cells.* PLOS ONE, 2015. **10**(7): p. e0131416.

199. Liu, S., et al., *Fluid shear stress induces epithelial-mesenchymal transition (EMT) in Hep-2 cells.* Oncotarget, 2016. **7**(22): p. 32876-32892.

200. Sidhaye, V.K., et al., *Shear stress regulates aquaporin-5 and airway epithelial barrier function.* Proceedings of the National Academy of Sciences of the United States of America, 2008. **105**(9): p. 3345-3350.

201. Cucullo, L., et al., *The role of shear stress in Blood-Brain Barrier endothelial physiology.* BMC neuroscience, 2011. **12**: p. 40-40.

202. Pitkänen, L., et al., *Permeability of Retinal Pigment Epithelium: Effects of Permeant Molecular Weight and Lipophilicity.* Investigative Ophthalmology & Visual Science, 2005. **46**(2): p. 641-646.

203. Steuer, H., et al., *In vitro model of the outer blood–retina barrier.* Brain Research Protocols, 2004. **13**(1): p. 26-36.

204. Wade, J.S. and T.A. Desai, *Planar microdevices enhance transport of large molecular weight molecules across retinal pigment epithelial cells.* Biomedical microdevices, 2014. **16**(4): p. 629-638.

205. Shargel, L., S. Wu-Pong, and A.B.C. Yu, *Applied biopharmaceutics & pharmacokinetics*. 2005, New York: Appleton & Lange Reviews/McGraw-Hill, Medical Pub. Division.

206. Miller, S.S. and J.L. Edelman, *Active ion transport pathways in the bovine retinal pigment epithelium.* The Journal of Physiology, 1990. **424**(1): p. 283-300.

207. Bushra, R. and N. Aslam, *An overview of clinical pharmacology of Ibuprofen.* Oman medical journal, 2010. **25**(3): p. 155-1661.

208. PL, G.B.K., *Aqueous humor hydrodynamics*, in *Adler's Physiology of the Eye*, H. WM, Editor. 2003, Mosby: St. Louis.

209. Cauldbeck, H., et al., *Controlling drug release from non-aqueous environments: Moderating delivery from ocular silicone oil drug reservoirs to combat proliferative vitreoretinopathy.* Journal of Controlled Release, 2016. **244**: p. 41-51.

210. Hsu, H.-H., et al., *A Method for Determination and Simulation of Permeability and Diffusion in a 3D Tissue Model in a Membrane Insert System for Multi-well Plates.* Journal of visualized experiments : JoVE, 2018(132): p. 56412.

211. Barber, J., et al., *A three-dimensional mathematical and computational model of necrotizing enterocolitis.* Journal of theoretical biology, 2013. **322**: p. 17-32.

212. Rejniak, K.A., et al., *Linking Changes in Epithelial Morphogenesis to Cancer Mutations Using Computational Modeling.* PLOS Computational Biology, 2010. **6**(8): p. e1000900.

213. Schlegel, F. *Which Multiphase Flow Interface Should I Use?* [cited 2018 01/12]; Available from: https://www.comsol.com/blogs/which-multiphase-flow-interface-should-i-use/.

214. Weisbrod, K., et al., *Simulation of Mass Transfer in a Microfluidic Experiment Using the Moving Mesh Method*. 2014.

215. Yoo, B.Y., et al., *Dual surface modification of PDMS-based silicone implants to suppress capsular contracture.* Acta Biomaterialia, 2018. **76**: p. 56-70.

216. Park, J.H. and Y.H. Bae, *Hydrogels based on poly(ethylene oxide) and poly(tetramethylene oxide) or poly(dimethyl siloxane): Synthesis, characterization, in vitro protein adsorption and platelet adhesion.* Biomaterials, 2002. **23**(8): p. 1797-1808.

217. Melling, A., *Tracer particles and seeding for particle image velocimetry.* Measurement Science and Technology, 1997. **8**(12): p. 1406.

218. Kaipio, J.P., et al., *21 - Process tomography and estimation of velocity fields*, in *Industrial Tomography*, M. Wang, Editor. 2015, Woodhead Publishing. p. 551-590.

219. Ablonczy, Z., et al., *Human retinal pigment epithelium cells as functional models for the RPE in vivo.* Investigative ophthalmology & visual science, 2011. **52**(12): p. 8614-8620.

220. Purves D, A.G., Fitzpatrick D, et al., *Types of Eye Movements and Their Functions*, in *Neuroscience*. 2001, Sinauer Associates: Sunderland (MA).

221. Leigh, R.J., D.S. Zee, and R.J. Leigh. *The neurology of eye movements*. 2015; Available from: http://site.ebrary.com/id/11041495.

222. Fawcett, I.M., R.L. Williams, and D. Wong, *Contact angles of substances used for internal tamponade in retinal detachment surgery.* Graefe's Archive for Clinical and Experimental Ophthalmology, 1994. **232**(7): p. 438-444.

223. Jang, K.J. and K.Y. Suh, *A multi-layer microfluidic device for efficient culture and analysis of renal tubular cells.* Lab Chip, 2010. **10**(1): p. 36-42.

224. Agarwal, A., et al., *Microfluidic heart on a chip for higher throughput pharmacological studies.* Lab on a chip, 2013. **13**(18): p. 3599-3608.

225. Tavana, H., et al., *Epithelium damage and protection during reopening of occluded airways in a physiologic microfluidic pulmonary airway model.* Biomed Microdevices, 2011. **13**(4): p. 731-42.

226. Chan, Y.K., et al., *In Vitro Modeling of Emulsification of Silicone Oil as Intraocular Tamponade Using Microengineered Eye-on-a-Chip.* Invest Ophthalmol Vis Sci, 2015. **56**(5): p. 3314-9.

227. Chan, Y.K., R.L. Williams, and D. Wong, *Flow Behavior of Heavy Silicone Oil During Eye Movements.* Investigative Ophthalmology & Visual Science, 2014. **55**(12): p. 8453-8457.

228. Levis, K.A., M.E. Lane, and O.I. Corrigan, *Effect of buffer media composition on the solubility and effective permeability coefficient of ibuprofen.* Int J Pharm, 2003. **253**(1-2): p. 49-59.

229. Kim, S.H., et al., *Transport Barriers in Transscleral Drug Delivery for Retinal Diseases.* Ophthalmic Research, 2007. **39**(5): p. 244-254.

230. Brubaker, R.F., *The flow of aqueous humor in the human eye.* Transactions of the American Ophthalmological Society, 1982. **80**: p. 391-474.

231. Toris, C.B., et al., *Aqueous humor dynamics in the aging human eye.* American Journal of Ophthalmology, 1999. **127**(4): p. 407-412.

232. Becker, W., *The neurobiology of saccadic eye movements. Metrics.* Rev Oculomot Res, 1989. **3**: p. 13-67.

233. David, T., et al., *A model for the fluid motion of vitreous humour of the human eye during saccadic movement.* Phys Med Biol, 1998. **43**(6): p. 1385-99.

234. Repetto, R., A. Stocchino, and C. Cafferata, *Experimental investigation of vitreous humour motion within a human eye model.* Phys Med Biol, 2005. **50**(19): p. 4729-43.

235. Chan, Y.K., et al., *Emulsification of Silicone Oil and Eye Movements.* Investigative Ophthalmology & Visual Science, 2011. **52**(13): p. 9721-9727.

236. Stocchino, A., R. Repetto, and C. Cafferata, *Eye rotation induced dynamics of a Newtonian fluid within the vitreous cavity: the effect of the chamber shape.* Phys Med Biol, 2007. **52**(7): p. 2021-34.

237. Bonfiglio, A., et al., *Investigation of the motion of a viscous fluid in the vitreous cavity induced by eye rotations and implications for drug delivery.* Phys Med Biol, 2013. **58**(6): p. 1969-82.

238. Modareszadeh, A., et al., *Saccade movements effect on the intravitreal drug delivery in vitreous substitutes: a numerical study.* Biomech Model Mechanobiol, 2013. **12**(2): p. 281-90.

239. Kathawate, J. and S. Acharya, *Computational modeling of intravitreal drug delivery in the vitreous chamber with different vitreous substitutes.* International Journal of Heat and Mass Transfer, 2008. **51**(23–24): p. 5598-5609.

240. Boghen, D., et al., *Velocity Characteristics of Normal Human Saccades.* Investigative Ophthalmology & Visual Science, 1974. **13**(8): p. 619-623.

241. Knox, P.C., C.R. Weir, and P.J. Murphy, *Modification of visually guided saccades by a nonvisual afferent feedback signal.* Invest Ophthalmol Vis Sci, 2000. **41**(9): p. 2561-5.

242. Joeres, S., B. Kirchhof, and A.M. Joussen, *PVR as a complication of rhegmatogeneous retinal detachment: a solved problem?* The British journal of ophthalmology, 2006. **90**(6): p. 796-797.

243. Larrosa, J., et al., *Antiproliferative effect of intravitreal α-tocopherol and α-tocopheryl-acid-succinate in a rabbit model of PVR*. Vol. 16. 1997. 1030-5.